



The effect of low level diode laser in treatment of recurrent aphthous stomatitis (case study)

Dalia saleem kareem*, Layla M. H. Al-ameri, Ammar saleh Alalawi

Institute of Laser for Postgraduate Studies, University of Baghdad, Baghdad, Iraq

* Email address of the Corresponding Author: Dalia.ugla2102m@ilps.uobaghdad.edu.iq

Article history: Received: 25 Jul. 2024; Revised: 3 Sept. 2024; Accepted: 9 Sept. 2024; Published online: 15 Jun. 2025.

Abstract

Objective: Recurrent Aphthous Stomatitis (RAS) is a common, painful, and recurrent oral condition characterized by ulcer formation. Its pathogenesis is multifactorial, involving genetic, immunological, and environmental factors. conventional methods like topical anesthetics, such as benzocaine. Mouth rinses containing hydrogen peroxide, chlorhexidine, or dexamethasone. Corticosteroid ointments, such as fluocinonide, beclomethasone, or hydrocortisone hemosuccinate, primarily focus on symptom relief rather than cure. Low-level laser therapy (LLLT) has emerged as a promising treatment modality, offering minimal invasiveness and effective healing.

Case Presentation: A 28-year-old female patient presented with a painful ulceration (6*5mm) with edematous border on the lateral surface of her tongue, after clinical examination (ulcer duration and frequency, the number of ulcers present, their shape and size, location, and specific characteristics such as the edges, base, and the condition of the surrounding tissues). and the medical history of the patient diagnosed as Recurrent Aphthous Stomatitis. The condition is treated by using low-level diode laser therapy. using a diode laser 980 nm with the power set at 1W, a non-contact laser application. The distance between the laser probe's tip and the ulcer surface was meticulously maintained at 10mm. A single laser treatment session consisted of four 30-second applications, separated by a 15-second interval. The cumulative laser application time amounted to approximately 120 seconds.

Conclusion: Low-level diode laser therapy significantly reduces pain, lesion size, and edema in RAS patients, while improving patient satisfaction, functional ability, and reducing Interleukin-1 beta (IL1 β), Transforming Growth Factor-beta 1 (TGF β -1) serum levels.

Keywords: Recurrent Aphthous Stomatitis, LLLT, biostimulation.

1. Introduction

Recurrent Aphthous Stomatitis (RAS) is a common, painful, and often debilitating condition characterized by recurrent episodes of oral ulceration without a clearly defined pathogenesis. Three clinical subtypes of RAS have been established based on the magnitude, number, and duration of outbreaks: minor, major, and herpetiform [1]. The etiology of RAS is not clear; however, several factors are known to predispose an individual to the disease. The primary predisposing factors include genetic factors, infections, decreased



immune system integrity, and deficiencies in folic acid, iron, or vitamin B12. Additional predisposing factors include stress, trauma, hormonal factors, and endocrine imbalance [2]. The diagnosis of RAS is based on patient history and clinical symptoms. There is no specific diagnostic test for RAU, though discarding possible underlying systemic causes is essential. It is prudent to request a complete series of laboratory tests, including a complete blood count and evaluation of iron, vitamin B12, and folic acid [3]. Conventional treatment modalities have ranged from topical agents to systemic medications, focusing on symptom relief rather than cure. The introduction of low-level diode laser therapy, particularly at a wavelength of 980 nm, offers a new avenue for managing RAS, combining the benefits of minimal invasiveness with effective healing, pain reduction and may influence the inflammatory response by reducing the concentrations of certain cytokines, including interleukin-1 beta (IL-1 β), tumor necrosis factor-alpha (TNF- α) [4,5]. Recent advancements in LLLT have highlighted its efficacy in reducing pain, ulcer size, and healing time in RAS patients. LLLT acts through photobiomodulation (PBM), stimulating cellular and tissue repair mechanisms, modulating inflammation, and promoting wound healing. The specific use of a 980 nm diode laser has been shown to offer a promising treatment modality, with studies demonstrating significant improvements in clinical outcomes for RAS patients [5]. One of the new interventions in oral medicine is low-level diode laser therapy. This non-invasive method, known as LLLT, has demonstrated the potential to boost the immune system, enhance tissue healing, and alleviate pain in various medical and dental contexts [6]. LLLT uses a coherent and monochromatic laser beam with a specific wavelength and power to deeply penetrate tissues. The laser's photons are absorbed by proteins, triggering biochemical reactions that encourage cell proliferation, tissue regeneration, and improved blood flow. LLLT speeds up wound healing, collagen production, and epithelial cell differentiation while providing pain relief by reducing pain-related stimuli. Although LLLT has multiple biological effects, its precise immunomodulatory mechanism is still not fully understood [7]. This therapy is safe, non-invasive, and shows great promise for a range of medical applications like wound healing. It fosters epithelial cell differentiation and collagen production [8] and pain relief. The analgesic effects of PBM are due to the reduction of inflammation, increased endorphin release, and modulation of nerve conduction. It is used to treat conditions like arthritis and neuropathic pain [9].

This study aimed to evaluate the clinical effectiveness of using a low-level diode laser for treating recurrent aphthous stomatitis. By exploring LLLT's impact on the healing process, pain reduction, and recurrence of lesions, This study aimed to better understanding of the role this novel therapy in managing RAS.

1. Case presentation

A 28-year-old female patient visited the Al-Mamoon Specialized Dental Center seeking dental care. Two days ago, she suffered from a painful ulceration on the lateral left border of her tongue. Upon questioning about her medical, dental, and family history, it revealed a family history of recurrent oral ulceration.

Following this, an intraoral examination was conducted to assess the site (middle part of the lateral left surface of the tongue), size (The size of the ulceration was measured to be 6x5 mm), shape, and texture of the ulcer base (red border and yellow floor). Then, an extra oral examination, including palpation of cervical lymph nodes (no mass or pain), was also performed. The evaluation of pain intensity was accomplished using the Visual Analog Scale (VAS) score, (It is measures pain intensity and consists of a 10cm line, with two end points from 0 to 10, where 0 = no pain, 1-3 = mild, 4-6 = moderate and 7-10 = severe pain) where the patient reported a pain degree of 9.

The Function and satisfaction scores, ranging from 0 to 100, were also evaluated and categorized as poor (0-25), fair (26-50), good (51-75), and excellent (76-100). The patient reported poor function and satisfaction. An initial diagnosis of recurrent aphthous stomatitis was established.

Saliva samples were collected pre-treatment for assessment of serum concentrations of IL1 β and TGF β -1 using the enzyme-linked immunosorbent assay (ELISA-Shanghai YL Biotech Co.)



The treatment was scheduled using the diode laser. The patient provided informed written consent before the treatment procedure. The local ethics committee approved the research (1374, Project Number: 161), which was conducted in accordance with the ethical guidelines outlined in the 1964 Declaration of Helsinki and its subsequent revisions. A dual-wavelength (810nm and 980nm) diode laser (Quick Lase England, UK), 12W dual 4 [810nm 50% + 980nm 50%], was utilized along with fiber optics (FC 400 μ m single file multimode). The wavelength was set at 980nm. Laser output power was set at 1W, operating in continuous mode. The distance between the laser probe's tip and the ulcer surface was meticulously maintained at 10mm. A single laser treatment session consisted of four 30-second applications, separated by a 15-second interval rest without radiation. The cumulative laser application time amounted to approximately 120 seconds with a total of 165 sec single treatment session.

The patient was recalled on days 1, 3, and 7 to assess healing progress and for saliva collection (for the IL1 β and TGF β -1 screening). By day 7, the patient's pain intensity had reduced to 0, and the ulcer size had decreased to 2 mm with no edema, as shown in Table 1 and Figure 1. There was also an improvement in the patient's satisfaction and function scores, along with a reduction in IL1 β and TGF β -1 serum levels.,

Table 1: Clinical evaluation scores

	Pain VAS	Size mm	Edema	Function	Satisfaction	IL1 β	TGF β -1
Pre treatment	9	6*5mm	1	20	20	1.272 pg/L	1.318 pg/L
Follow up							
Day 1	5	5*4mm	1	70	75	1.136 pg/L	1.156 pg/L
Day 3	1	3*1mm	0	85	90	0.904 pg/L	0.967 pg/L
Day 7	0	2mm	0	97	100	0.868 pg/L	0.851 pg/L

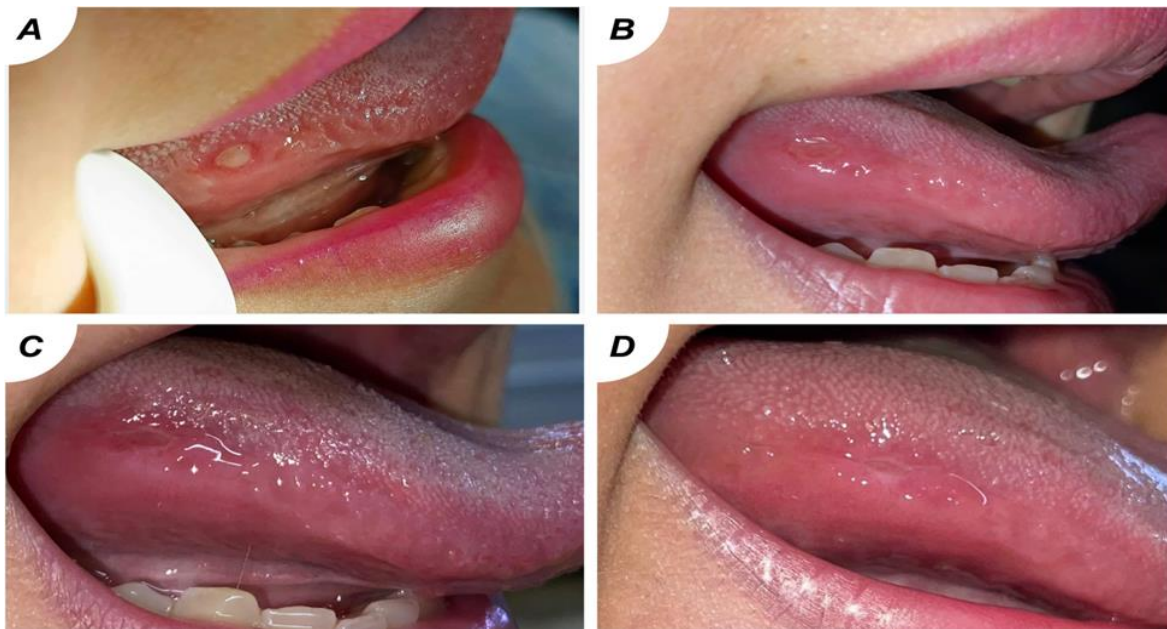


Figure 1: aphthous ulcer; A: before treatment; B: one day after treatment; C: three days after treatment; D: seven days after treatment.

4. Discussion

Low-level laser therapy (LLLT), applying the diode laser, is an emerging therapeutic method for a variety of medical conditions, including the RAS. LLLT works by delivering specific wavelengths of light to targeted tissues, which then absorb the light energy, leading to a series of cellular responses. This process can enhance cell proliferation, reduce pain, and decrease inflammation (10). Findings of this case report align with a meta-analysis by Radithia et al (11), Farista et al (12) in their study, which demonstrated that low-level laser therapy significantly reduces pain scores and healing time in patients with recurrent aphthous stomatitis (RAS).

Soliman et al. (13) and Ghali et al.(14) highlighted the remarkable improvements in healing time, pain reduction, and lesion size associated with diode laser treatment

The significant increase in patient satisfaction reflects the efficacy of LLLT in providing rapid and sustained relief from the symptoms of recurrent aphthous stomatitis since the RAS is associated with poor quality of life and demonstrated by research (15). Balakrishnan et al (16) examined the impact of LLLT on TGF-beta-1 concentrations in gingival crevicular fluids. They observed a significant decrease in TGF-beta1 concentrations from baseline at day 1, continuing through days 7 as well as 30.

The observed reductions in IL-1 β as well as TGF β -1 concentrations could be attributed to a number of mechanisms of LLLT. Also, another study by Oton-Leite et al. (17) applied LLLT for treating oral mucositis and noted a tendency towards decreased concentrations of IL-1beta and TGF-beta in laser-cured group compared to the control. LLLT inhibits the production of pro-inflammatory cytokines, reducing the inflammatory response, which aligns with the observed decreases in IL1 β and TGF β -1. Additionally, LLLT enhances cellular repair mechanisms, accelerating healing and reducing sources of inflammation by stimulating ATP production and other growth factors. Improved microcirculation and blood flow from LLLT help clear inflammatory mediators more efficiently, supporting tissue healing and reducing cytokine levels. Moreover, LLLT modulates the immune response, balancing pro- and anti-inflammatory cytokines to control inflammation and promote faster symptom resolution. In conclusion, the significant reductions in IL1 β and TGF β -1 levels observed in our study,

The efficacy of LLLT in managing RAS by targeting and reducing inflammation. This dual benefit of pain relief and inflammation control makes LLLT a superior therapeutic option for patients with recurrent aphthous stomatitis (18, 19).

5. Conclusion

LLLT significantly reduces pain, lesion size, and edema, greatly improves satisfaction and functional ability, and reduces IL-1 β and TGF β -1 levels in patients with recurrent aphthous stomatitis.

References

- [1] R. C. Del Mazo, G. L. Forcén, and M. E. Aguilar, "Recurrent aphthous stomatitis," *Med. Clin. (Barc.)*, Sep. 12, 2023.
- [2] N. R. Edgar, D. Saleh, and R. A. Miller, "Recurrent aphthous stomatitis: a review," *J. Clin. Aesthet. Dermatol.*, vol. 10, no. 3, p. 26, Mar. 2017.
- [3] F. A. Vale, M. S. Moreira, F. C. Almeida, and K. M. Ramalho, "Low-level laser therapy in the treatment of recurrent aphthous ulcers: a systematic review," *Sci. World J.*, vol. 2015, no. 1, p. 150412, 2015.
- [4] P. L. Tú, P. V. Binh, and Đ. T. Thảo, "Effectiveness of low-level diode laser therapy in recurrent aphthous stomatitis treatment at Can Tho University of Medicine and Pharmacy Hospital in 2020–2022," *Tap Chi Y Duoc Hoc Can Tho*, vol. 12, no. 47, pp. 7–13, May 2022.
- [5] C. Dompe, L. Moncrieff, J. Matys, K. Grzech-Leśniak, I. Kocherova, A. Bryja, et al., "Photobiomodulation—underlying mechanism and clinical applications," *J. Clin. Med.*, vol. 9, no. 6, p. 1724, Jun. 2020.
- [6] N. A. Owaid, H. A. Jawad, and A. A. Maazil, "Evaluation of low-level laser therapy using 785 nm diode laser on the enhancement of chronic wound healing," *Iraqi J. Laser B*, vol. 15, pp. 41–46, 2016.
- [7] Z. Ślebioda and B. Dorocka-Bobkowska, "Low-level laser therapy in the treatment of recurrent aphthous stomatitis and oral lichen planus: a literature review," *Adv. Dermatol. Allergol.*, vol. 37, no. 4, pp. 475–481, 2020.



- [8] F. Abesi and N. Derikvand, "Efficacy of low-level laser therapy in wound healing and pain reduction after gingivectomy: a systematic review and meta-analysis," *J. Lasers Med. Sci.*, vol. 14, 2023.
- [9] B. M. Li, C. K. Zhang, J. H. He, Y. Q. Liu, X. Y. Bao, and F. H. Li, "The effects of photobiomodulation on knee function, pain, and exercise tolerance in older adults: a meta-analysis of randomized controlled trials," *Arch. Phys. Med. Rehabil.*, vol. 105, no. 3, pp. 593–603, Mar. 2024.
- [10] C. Dompe, L. Moncrieff, J. Matys, K. Grzech-Leśniak, I. Kocherova, A. Bryja, et al., "Photobiomodulation underlying mechanism and clinical applications," *J. Clin. Med.*, vol. 9, no. 6, p. 1724, Jun. 2020.
- [11] D. Radithia, F. Y. Mahdani, R. K. Bakti, A. E. Parmadiati, A. Subarnbesaj, S. R. Pramitha, et al., "Effectiveness of low-level laser therapy in reducing pain score and healing time of recurrent aphthous stomatitis: a systematic review and meta-analysis," *Syst. Rev.*, vol. 13, no. 1, p. 192, Jul. 2024.
- [12] S. Farista, B. Kalakonda, and A. S. Ahmed, "Effectiveness of 980 nm diode laser therapy on recurrent aphthous stomatitis," *Int. J. Laser Dent.*, vol. 4, no. 3, pp. 83–86, Dec. 2014.
- [13] H. A. Soliman and D. Mostafaa, "Clinical evaluation of 660 nm diode laser therapy on the pain, size and functional disorders of recurrent aphthous stomatitis," *Open Access Maced. J. Med. Sci.*, vol. 7, no. 9, p. 1516, May 2019.
- [14] H. G. Ghali and B. S. Abdulhamed, "Treatment of recurrent minor aphthous stomatitis using diode laser (940 nm)," *J. Popul. Ther. Clin. Pharmacol.*, vol. 28, no. 2, pp. e99–e112, Jan. 2022.
- [15] C. Rivera, M. Muñoz-Pastén, E. Núñez-Muñoz, and R. Hernández-Olivos, "Recurrent aphthous stomatitis affects quality of life: a case-control study," *Clin. Cosmet. Investig. Dent.*, vol. 14, pp. 217–223, 2022.
- [16] A. Balakrishnan, L. T. Arunachalam, and U. Sudhakar, "Evaluation of TGF- β 1 in gingival crevicular fluid and clinical parameters of smoker and nonsmoker patients treated with low-level laser therapy as an adjunct to scaling and root planing," *Lasers Dent. Sci.*, vol. 6, no. 1, pp. 55–61, Mar. 2022.
- [17] A. F. Oton-Leite, G. B. Silva, M. O. Morais, T. A. Silva, C. R. Leles, M. C. Valadares, J. C. Pinezi, A. C. Batista, and E. F. Mendonça, "Effect of low-level laser therapy on chemoradiotherapy-induced oral mucositis and salivary inflammatory mediators in head and neck cancer patients," *Lasers Surg. Med.*, vol. 47, no. 4, pp. 296–305, Apr. 2015.
- [18] T. O. De Souza, M. A. Martins, S. K. Bussadori, K. P. Fernandes, E. Y. Tanji, R. A. Mesquita-Ferrari, et al., "Clinical evaluation of low-level laser treatment for recurring aphthous stomatitis," *Photomed. Laser Surg.*, vol. 28, suppl. 2, pp. S85, Oct. 2010.
- [19] R. K. Indrastiti, I. I. Wardhany, M. Mandasari, and Y. S. Wimardhani, "Case series of low-level laser therapy for minor ulceration: diverse outcomes related to predisposing factors," *Sci. Dent. J.*, vol. 7, no. 1, pp. 33–38, Jan. 2023.

تأثير ليزر الدايدود المنخفض المستوى في علاج التهاب الفم القلاعي المتكرر

داليا سالم كريم*, ليلي محمد علي العامري, عمار صالح العلوي

معهد الليزر للدراسات العليا، جامعة بغداد، بغداد، العراق

البريد الإلكتروني للباحث*: Dalia.ugla2102m@ilps.uobaghdad.edu.iq

الخلاصة

الهدف: التهاب الفم القلاعي المتكرر (RAS) هو حالة فموية شائعة ومؤلمة ومتكررة تتميز بتكوين القرحة. التسبب في المرض متعدد العوامل، بما في ذلك العوامل الوراثية والمناعية والبيئية. تركز العلاجات التقليدية في المقام الأول على تخفيف الأعراض بدلاً من العلاج. في الأونة الأخيرة، ظهر العلاج بليزر الدايدود منخفض المستوى (LLLT) كطريقة علاجية واعدة، حيث يوفر الحد الأدنى من التدخل والشفاء الفعال.

عرض دراسة الحالة: مريضة تبلغ من العمر 28 عامًا تعاني من تقرح مؤلم على السطح الجانبي للسانها، وتم تشخيصها على أنها التهاب الفم القلاعي المتكرر. لقد عالجت الحالة باستخدام دايدود ليزر منخفض المستوى.

الاستنتاجات: العلاج بالليزر الدايدود منخفض المستوى يقلل بشكل كبير من الألم وحجم الآفة والوذمة لدى مرضى RAS، مع تحسين رضا المرضى والقدرة الوظيفية.





Highly Sensitive Refractive Index Sensor Based on Dual Peak Plasmonic Tapered D-shaped PM-PCF Coated with Gold Nano-Structures

Suaad Sahib Hindal^{1,2,*}, Zainb F. Al-Bawai¹, Aseel I. Mahmood²

¹ Institute of Laser for Postgraduate Studies, University of Baghdad

² Scientific Research Commission, Ministry of Higher Education & Scientific Research, Baghdad, Iraq

* Email address of the Corresponding Author: suad.saheb2101p@ilps.uobaghdad.edu.iq

Article history: Received: 20 Jul. 2024; Revised: 3 Sept. 2024; Accepted: 17 Sept. 2024; Published online 15 Jun. 2025

Abstract

This paper uses the finite element method (FEM) to study a Surface Plasmon Resonance (SPR) refractive index sensor based on D-shaped Polarization Maintaining Photonic Crystal Fiber (PM-PCF). A chemically stable plasmonic material, gold (Au), with hemispherical structures having a radius of 50 nm, is applied to the surface of a D-shaped sensor to create the surface plasmon resonance (SPR) effect, enabling this SPR sensor to detect variation in the surrounding analyte refractive index (RI). The resonance condition will change when the refractive index of the targeted analyte changes, leading to a certain shift in the loss peak. Two resonant peaks are observed, one located in the visible part of the spectrum, and the second in the near-infrared region. Our suggested design offers a high wavelength sensitivity (WS) of 5176 nm/RIU and the spectral resolution for this sensor is 1.93×10^{-5} RIU, for y-polarization. For x-polarization, the wavelength sensitivity of the 1st and 2nd peaks are 1058 nm/RIU and 3764 nm/RIU, respectively. The spectral resolution for the 1st and 2nd peaks is 9.45×10^{-5} RIU and 2.65×10^{-5} RIU, respectively in the high sensing range of 1.34 to 1.41 RIU. The results show that this improves the sensor's ability to detect the refractive index. The proposed SPR sensor design has high sensitivity, high resolution, and high linearity, a promising result that could be used in environmental monitoring, biological detection, physical sensors, and chemical analysis.

Keywords: D-shape PM-PCF; Finite Element Method (FEM); Polarization Maintaining Photonic Crystal Fiber (PCF); Refractive Index Sensor; Surface Plasmon Resonance (SPR)..

1. Introduction

Optical fibers have become an ideal option for sensing applications due to their precision, compact size, high sensitivity, and remote sensing [1]. There exist many types of optical fibers like single-mode fibers [2], multimode fibers [3], No-Core Fibers [4], photonic crystal fibers (PCFs) [5], and nanostructured fibers



[6]. Various sensing approaches are employed in optical fibers such as surface plasmon resonance (SPR), Bragg gratings, interferometers, long-period gratings, and fluorescence [7].

The Fabry-Perot (FP) interferometer usually comprises two mirrors with high reflectivity. The incident light beam reflects multiple times between these mirrors, leading to multiple-beam interference [8]. Fabry-Perot (FP) interferometric sensors stand out among the many optical fibers proposed because they are simple, accurate, adaptable, responsive, and resistant to environmental noise [9].

The working principles of optical fiber FP interferometer sensors are primarily explained by the propagation phase shift equation φ in the interferometer, where $\varphi = \frac{2\pi}{\lambda} \Delta$ (with Δ representing the optical path difference (OPD) and λ denoting the free-space optical wavelength). When a disturbance is introduced to the sensor, the phase difference is affected due to the variation in the OPD of the interferometer. By observing the shift in the phase or wavelength spectrum, the sensing parameter applied to the optical fiber FP interferometer sensor can be accurately determined [10].

Thin film technology is essential in fiber optic sensors by coating reflective surfaces inside the FP cavity or on the fiber surface, which allows for the measurement of specific physical parameters [8].

SPR sensors based on optical fiber garner significant research attention in environmental monitoring, biomedical, food detection, etc., due to features like real-time monitoring, high sensitivity, wide operated wavelength range, and label-free detection [11]. The D-shape plasmonic refractive index (RI) sensors are a typical part of these sensors, which have been functionalized for responding indirectly to diverse factors such as liquid/gas concentration, temperature, and various biological and physicochemical parameters [11, 12]. The performance of these sensors based on an optical fiber is generally evaluated in terms of the following key parameters: sensitivity, resolution and FOM.

The physical-optical phenomenon including excitation of oscillations in electron density at metal-dielectric interfaces when exposed to p-polarized light waves is called Surface Plasmon Resonance (SPR) [12, 13]. This excitation leads to a sharp loss in the propagation spectrum. The peak of the loss is called the resonance frequency or resonance wavelength, which is highly sensitive to the surrounding RI changes [14]. This characteristic makes it widely utilized in biomedical, biological, and chemical monitoring applications [12, 15].

The sensor's performance depends mainly on the plasmonic materials [16]. and Silver (Ag) [17], Gold (Au) [18], Aluminum (Al) [19], and Copper (Cu) [17], etc., are popular plasmonic materials [20]. Silver presents a high resonance peak [21], but at the same time, it experiences oxidation problems when exposed to water. Gold is primarily preferred as a plasmonic material [16, 22]; because of its biocompatibility, chemical stability, and gold exhibits strong surface plasmon resonance in the visible and near-infrared (NIR) spectrum. This makes it highly effective for SPR applications that operate in these wavelength ranges, which are commonly used in optical sensing. Therefore, gold is chosen as the plasmonic material in this work.

The sensitivity of optical fiber sensors is crucial for improving their capability to detect small variations in the surrounding refractive index. In other words, it allows for detecting low analyte concentration and thus enhances the SPR sensor performance [23]. There are many strategies to reach this goal like choosing the type of plasmonic material to get strong SPR resonance. Metal thickness is also a crucial factor. In addition, the shape of nanoparticle material which is used as a plasmonic layer [24]. Different structures of SPR sensors using photonic crystal fibers (PCFs) have been suggested to address the limitations found in multiple optical fiber SPR sensors [25] and fiber gratings [26] which displays poor sensitivity. In this case, the surface plasmons (SPs) are activated by the evanescent wave that passes through the metal film. Photonic crystal fiber provides significant flexibility by modifying the arrangement of air holes in the core and cladding regions. Moreover, PCFs are small, and compact, making them precise for creating miniaturized devices for remote sensing applications. Various structures of PCF have been suggested for the sensors based on SPR, each offering different sensing capabilities and detection ranges [27].



Plasmonic sensors based on PCFs have many applications in measurements and detection. For example but not limited to Refractive Index Sensor (RI)[28], Biomedical applications [29], magnetic field [30], Temperature[31] and many others.

Fiber optic geometry is also a very important factor in enhancing the SPR sensor sensitivity, geometries were introduced like U-shape [32], double side polished U- shape [33], flat tip [34], and D-shape [35].

This type of photonic device has received significant interest from the scientific community. Below, we will mention some of the most recently published work.

In 2020, Meng et al. [36] proposed a D-shaped SPR sensor with dual loss peaks, reaching a maximum sensitivity of 18,900 nm/RIU and 17,500 nm/RIU, respectively of the primary and secondary peaks, within the RI range of (1.35-1.38). The spectral resolutions are 5.291×10^{-6} and 5.714×10^{-6} RIU, respectively. Alok K. Paul et al [27] designed and evaluated of an SPR sensor in a photonic crystal fiber (PCF) platform, where graphene is applied externally to enhanced sensing performance for an aqueous solution. The proposed sensor performance was evaluated using the finite element method-based simulation tool COMSOL Multiphysics. The simulation results indicate that the proposed sensor exhibits identical linear characteristics and achieves a very high figure of merit (FOM) of 2310.11 RIU^{-1} in the very low detection limit of 10^{-3} . The average wavelength sensitivity is 2000 nm/RIU for the analyte RI ranging from 1.331 to 1.339. Mumtaz et al. in 2022 [37], presented an SPR sensor based on optical fiber with extremely high sensitivity for simultaneous dual-parameter measurement. The SPR sensor utilizes a D-shaped fiber coated with a nanolayer of Silver (Ag) and Hematite ($\alpha\text{-Fe}_2\text{O}_3$). This sensor demonstrates an exceptionally high refractive index sensitivity of 8,518 nm/RIU within the RI range of 1.33 to 1.40. The SPR performance indicates its potential for various dual-parameter sensing applications. Ruan et al [38] designed an arc-shaped PCF with high refractive index sensitivity. They use the finite element method (FEM) to create the analyte channel of an open arc-shaped at the top of the fiber, facilitating the detection of the analyte's RI. To stimulate mode coupling, a gold layer is applied inside the arc-shaped structure. The influence of changing the diameters of the air hole rings and thickness of the metallic layer on sensor performance is done. The sensor's maximum sensitivity is 24900 nm/RIU; the spectral resolution is 4.01×10^{-6} RIU; and the figure of merit (FOM) is 661.71 RIU^{-1} . Yu Ying et al [39] designed and evaluated a dual-core D-shaped PCF surface plasmon resonance sensor, which was coated with gold grating using the FEM method. They examined how various PCF structural parameters such as small and large air holes and polishing depths along with grating parameters like grating duty, heights, and periods, influence the sensor's performance. The findings indicate that both the grating and dual-core design are crucial in enhancing the sensor's capabilities. The proposed sensor achieves an average wavelength sensitivity of 994.5 nm/RIU as the analyte's refractive index increases from 1.33 to 1.37. Furthermore, a maximum amplitude sensitivity of 181.049 RIU^{-1} is reported. The resolution of the dual-feature interrogation is determined to be 2.03×10^{-6} RIU, which is better than the wavelength and amplitude interrogations. In 2024, Chen et al. proposed a novel, dual-functional, ultra-sensitive sensor using a D-shaped microchannel PCF for temperature and refractive index (RI) sensing. Its high sensitivity is achieved by incorporating magnesium fluoride (MgF_2) and gold (Au) as plasmonic materials within the channel of a micro-rectangular shape. These simulations reveal a wide detection range, spanning refractive index values from 1.27 to 1.43. The sensor achieves peak sensitivities of 31,800 nm/RIU, a maximum resolution of 3.14×10^{-6} RIU, and a FOM of 211.07 RIU^{-1} in the analyte RI range of 1.27-1.43 [40].

This research paper presents a refractive index (RI) sensor based on a D-shape PM_PCF plasmonic configuration. Gold hemisphere structure is used as plasmonic material. The confinement loss spectrum characteristics of the proposed configuration are analyzed utilizing the finite element method (FEM) accompanied by perfectly matched layers absorbing boundary conditions. Sensitivity, spectral resolution, and figure of merit (FOM) are calculated to assess its sensing capability. This design introduces several enhancements: Sensitivity, Spectral Resolution and FOM, and broader applicability unlike some studies with narrow RI ranges, our design aims for a broad detection range, making it more versatile for various applications.



2. Design Considerations of the Sensor

The suggested design is studied and assessed using the Finite Element Method (FEM) within COMSOL Multiphysics (version 6.1). A two-dimensional D-shape PM-PCF is built, and the radio frequency, electromagnetic waves, and frequency domain (emw) model is selected to calculate the effective RI of core mode and SPR mode. The perfectly matched layer (PML) boundary condition is utilized in this model to enhance the absorption of the reflected light [41], the thickness of the PML layer is ($T_{pml} = 2\mu\text{m}$).

The designed model is a D-shape PM-PCF, and the dimensions and the hole structure of the PM-PCF are the same as the commercial PM-1550-01 from Thorlabs Inc. The Polarization Mode Dispersion (PMD) for this PCF fiber is typically around $0.1 \text{ ps}/\sqrt{\text{km}}$. Figure (1) shows a Scanning Electron Microscope (SEM) image of this fiber.

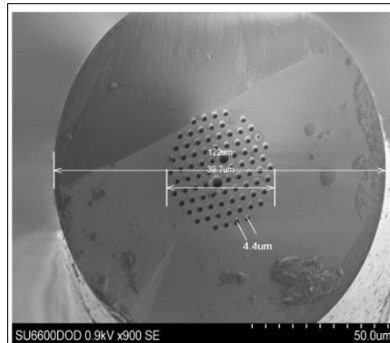


Fig. 1: SEM image of PM-1550-01-PCF

The orientation of light waves in some applications like interferometric sensors needs to be preserved. Thus, the PM-PCF which maintains the polarization state of light propagating through optical fibers, will be an excellent choice to enhance the interaction between the guided modes and the plasmonic surface. This results in higher sensitivity to changes in the refractive index of the surrounding medium. The air holes are arranged in hexagonal shape according to the SEM image, the solid core is encircled by five rows of circular holes. The bare fiber's diameter is $(122 \mu\text{m})$, while the coating's diameter is $230 \mu\text{m}$. The diameter of the holey area which has a hexagonal symmetry is $(d_H = 39.7 \mu\text{m})$, the two holes adjacent to the core have a larger diameter of $(d_L = 4.4 \mu\text{m})$, and the diameter of the other holes is $(d_S = 2.2 \mu\text{m})$. The pitch which is the inter-hole spacing equal to $(P = 4.4 \mu\text{m})$. The same structure and dimensions of air holes are used to build the sensor in this work. The designed optical fiber is tapered to $(d_T = 53.64 \mu\text{m})$ diameter and polished to form the D-shape structure as shown in Figure 2. This thickness was chosen because it is the closest distance to the holes, which are filled with the analyte under study. Consequently, it achieves a strong interaction and, thus, high sensor performance. The vertical distance between the polished side of the structure to the end of the air hole rings is $(V_d = 26.82 \mu\text{m})$.

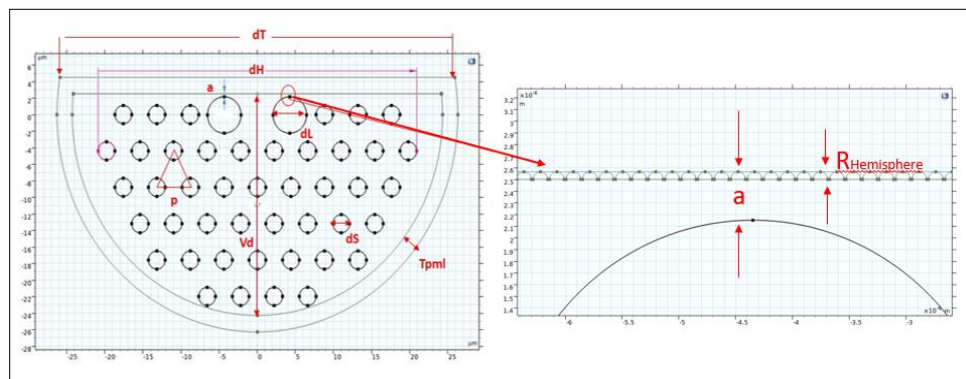


Fig. 2: The dimensions of the D-shape-PM-PCF-SPR Structure

the gold hemisphere structure of a radius ($R_h=50$) nm is applied above the polished designed fiber to form the plasmonic metal layer. The distance between the big hole outer diameter and the edge of the plasmonic layer is ($a=0.35$) μm , the distance equal to (0.4) μm it's measured with the plasmonic structure. The dimensions of the designed structure are shown in table (1).

Table 1 The designed parameter of the proposed structure

Parameter	Description	Value
dT	Tapered diameter	53.64 μm
dH	Hole's region diameter	39.7 μm
dL	The diameter of the big hole	4.4 μm
dS	The small hole diameter	2.2 μm
P	Pitch	4.4 μm
Vd	Vertical Polished distance	26.82 μm
N	No. of air hole rings	5 rings
T_{pml}	PML thickness	2 μm
$R_{\text{Hemisphere}}$	Plasmonic Hemisphere structure radius	50 nm
A	Distance from air hole and polished fiber	0.35 μm

The proposed optical fiber is made of silica (Si). The design aims to detect variations in the analyte's RI (n_a), specifically at values of (1.34, 1.35, 1.36, 1.37, 1.39, 1.41) RIU. The air holes are filled with analyte RI. Figure (3) illustrates the material layout of the designed D-shape PM-PCF-SPR sensor.

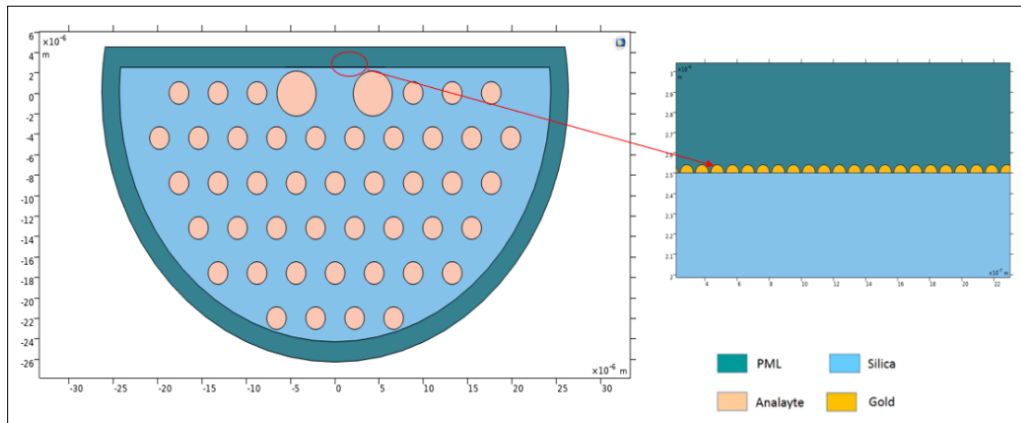


Fig. 3: Schematic illustration of the designed sensor with hemisphere plasmonic structure.

3. Numerical Method

As mentioned before, silica (SiO_2) is the background material for the sensor, and its dispersion can be expressed by the Sellmeier dispersion relation [42]:

$$n_s^2(\lambda) = 1 + \frac{B_1\lambda^2}{\lambda^2 - C_1} + \frac{B_2\lambda^2}{\lambda^2 - C_2} + \frac{B_3\lambda^2}{\lambda^2 - C_3} \quad (1)$$

where n_s is the RI of the proposed sensor's cladding, λ is the wavelength of the incident light in μm , and the values of B_1 , B_2 , B_3 , C_1 , C_2 and C_3 coefficients in the Sellmeier equation [42] are shown in Table 2.

Table 2 Coefficients of the Sellmeier equation for silicon dioxide

B_1	B_2	B_3	$C_1 (\mu\text{m}^2)$	$C_2 (\mu\text{m}^2)$	$C_3 (\mu\text{m}^2)$
0.69616630	0.40794260	0.89747940	0.004679148260	0.01351206310	97.93400250

The plasmonic material selected for SPR excitation in this model is gold, and its permittivity (ϵ_{Au}) for a given wavelength is characterized by the Drude–Lorentz (DL) model [43]:

$$\epsilon_{Au} = \epsilon_{\infty} - \frac{\omega_D^2}{\omega(\omega + j\gamma_D)} - \frac{\Delta\epsilon \cdot \Omega_L^2}{(\omega^2 - \Omega_L^2) + j\Gamma_L\omega} \quad (2)$$

Where, ω is the angular frequency, γ_D is the damping frequency, ω_D is the plasmon frequency, ϵ_{∞} is permittivity at high frequencies which is equal to 5.9673, and $\Delta\epsilon = 1.09$ is the weighting factor. Oscillator strength is $\Omega_L/2\pi = 650.07 \text{ THz}$, and Lorentz's spectral width is [44]:

$$\Gamma_L/2\pi = 104.86 \text{ THz}.$$

The SPR sensor-based PCFs operate due to the mechanism of interactions between surface electrons of the plasmonic material and the evanescent field [45]. When light propagates with a critical angle through the sensor's surface, some leaky modes escape from the air holes array and reach the metal layer covering the sensor's polished surface. This interaction causes a generation of free electrons excited from the sensor surface, due to this interaction, the SPR effect will produce different modes of core and SPP. The resonance will be generated when the frequency of the evanescent field matches the frequency of the free electrons generated from the plasmonic layer material. This phenomenon is characterized by the confinement loss (C_L) which explains the loss in propagation, calculated using Equation (2). The C_L in dB/m given by [42]:

$$C_L = \frac{40\pi}{\ln(10)\lambda} \times \text{Im}(n_{eff}) \times 10^4 \quad (3)$$

Where $\text{Im}(n_{eff})$ the effective RI imaginary part, and λ is the operating wavelength.

The following parameter wavelength sensitivity examines the submitted sensor performance [11], refractive index resolution [46], linearity [47], the figure of merit [16], and Birefringence [16]. The wavelength sensitivity ($S(\lambda)$) in (nm/RIU) is a method to evaluate the sensing performance of the designed sensor, and it is described by [11]:

$$S(\lambda) = \frac{\Delta\lambda_{peak}}{\Delta n_a} \quad (4)$$

Where $\Delta\lambda_{peak}$ indicates the difference in resonance wavelength, and Δn_a represents the variation in the analyte RI.

To evaluate the sensor's detection capability, a resolution (R) parameter is introduced. This parameter is calculated in RIU as follows [46]:

$$R = \Delta n_a \frac{\Delta\lambda_{min}}{\Delta\lambda_{peak}} \quad (5)$$

$\Delta\lambda_{min}$ represents the minimum spectral resolution (equal to 0.1 nm) for calculation [48].

Another metric for evaluating sensor performance is the figure of merit (FOM), the factor that combines sensor sensitivity ($S(\lambda)$) and full width at half maximum (FWHM), which defined as [16]:



$$FOM = \frac{m}{FWHM} \quad (6)$$

Where m represents the slope of two adjacent resonance points, while FWHM represents the full width at half the maximum peak for each detected signal peak.

Finally, maintaining the polarization state is important in sensing. The ease of birefringence is because of the adaptable structural design and optical properties of photonic crystal fiber (PCF). The difference in the refractive index (RI) real parts of the x- and y-polarized core modes is defined as Birefringence (B) [16]:

$$B = |Re(n_{eff}^x) - Re(n_{eff}^y)| \quad (7)$$

4. Simulation Results and Discussion

In this study, PM-PCF is utilized. This approach preserves the light polarization state within the optical fiber, enhancing the sensor's sensitivity to minimal variation in the surrounding refractive index (RI). Additionally, it reduces birefringence which causes undesired polarization states-related effects, thereby improving the sensor's responsiveness.

Generally, the SPR sensor functions owing to the interaction between the evanescent wave and the electrons released from the surface of the plasmonic material (gold). By reducing the outer diameter of the optical fiber and creating a D-shape, the generation of the evanescent field will be enhanced. The surface plasmon wave is generated by interacting with the evanescent field and the metal surface. As the surface plasmon wave transfers forward, a frequency matching occurs between the fundamental mode and SPP mode. The y-polarization core fundamental mode and x-polarization core fundamental mode, and SPR mode in the sensing layer were examined as illustrated in Figure 4.

These images show that the energy of the fundamental mode under x- and y-polarization is not solely confined to the core, but a portion of this energy transfers to the surface of the nanomaterial, made of Au Hemisphere structures. This energy then facilitates the coupling of the fiber fundamental core mode and SPR mode, which may lead to strong electromagnetic field coupling that is likely to enhance the sensor's sensitivity.

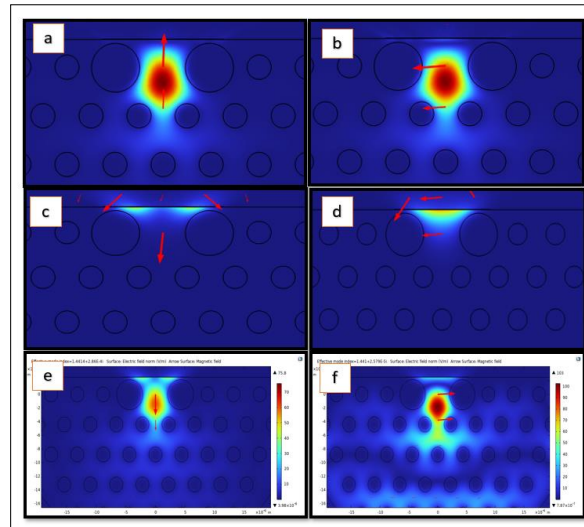


Fig. 4: The electric field distributions of (a) fundamental y-polarized mode, (b) fundamental x-polarized mode, (c) SPP y-polarized mode, (d) SPP x-polarized mode, (e) phase matching mode for y-polarized, and (f) phase matching mode for x-polarized

Both y- and x-polarization fundamental modes exist in the core, with birefringence on the order of 10^{-4} which higher than that of conventional PM fibers. This feature makes PM-PCF valuable in fiber optic sensing, and other advanced optical applications where precise control over polarization is required. In this study, both y- and x-polarized modes are considered. Two resonance peaks are observed in the spectra of confinement loss because of the resonance coupling of two distinct higher-order SP modes with the fundamental core mode of the D-shape-PM-PCF. Figure 5 illustrates the dispersion relation of the y-polarized fundamental mode and SPP mode loss spectra for the analyte's RI equal to 1.34 RIU.

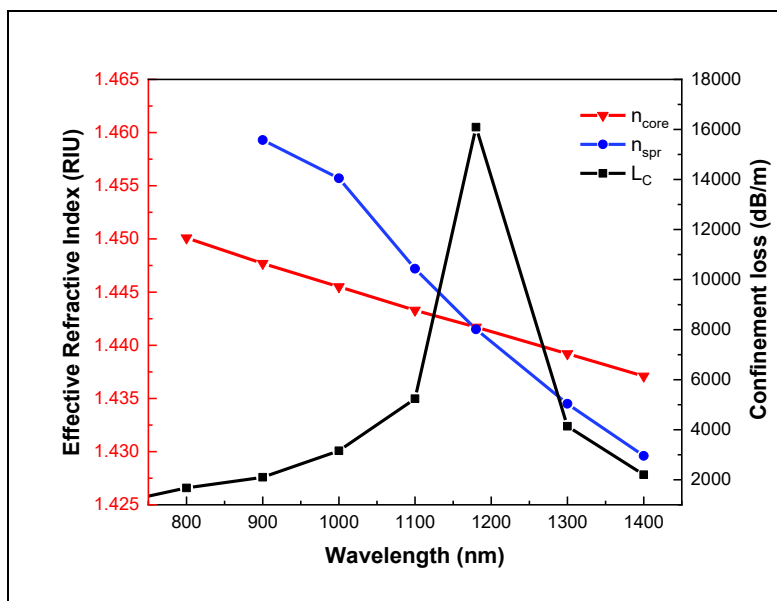
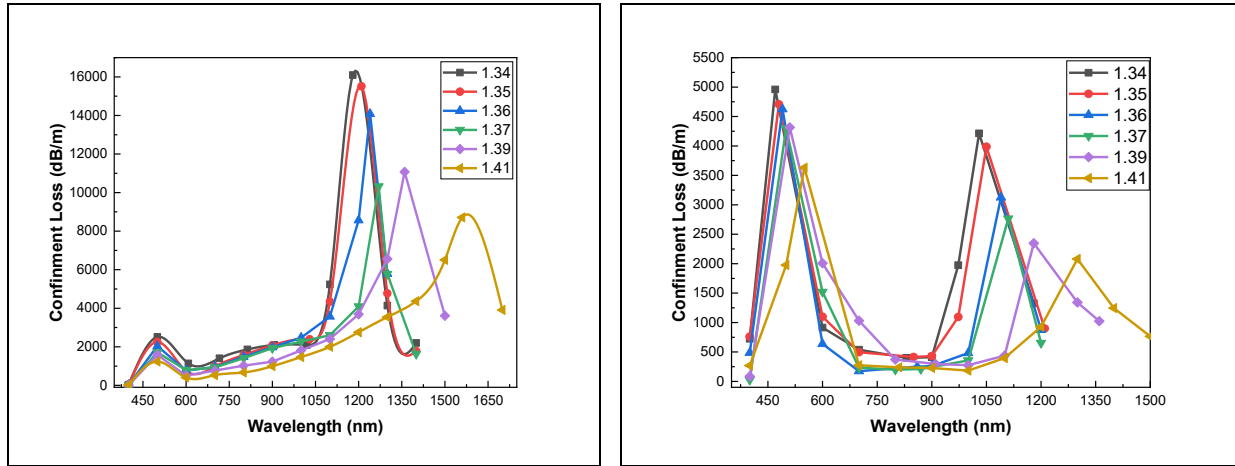


Fig. 5: The Dispersion relationship of the y-polarized core-guided mode, SPP mode, and loss spectra, for analyte RI = 1.34 RIU

The y-polarization loss curve, which initially increases with wavelength, reaches a maximum peak at the resonant wavelength and decreases with further wavelength increase. The resonant wavelength is detected at 1180nm, where the peak coincides with the intersection of the two dispersion curves. This intersection, where the effective RI of the core mode and refractive index of the SPP mode of the sensor are equal, signifies the phase-matching coupling phenomenon.

The confinement loss of the fundamental core mode dependence on wavelength for various analyte refractive indices in both x-polarization and y-polarization are depicted in Figure 6. This figure illustrates how the wavelength sensitivity varies with the analyte's refractive index (RI) for both x- and y-polarization modes. The sensitivity changes in response to variations in refractive index and peak wavelength. According to Equation (4), sensitivity rises if the RI analyte variation decreases or the peak wavelength variation increases, and vice versa. The scanning wavelength is chosen before and after 1550nm, this is because in plasmonic sensors different modes of surface plasmon polaritons can be excited at various wavelengths. Also, the dispersion properties of gold plasmonic material change significantly with wavelength. Gold has distinct plasmonic responses in the visible (around 500 nm) and near-infrared (NIR) regions (around 1100 nm). The material's dielectric function, which varies with wavelength, can lead to different resonance conditions at these wavelengths. This resonance wavelength could be shifted due to the changing of the surrounding refractive index [23].



(a)

(b)

Fig. 6: Confinement loss spectra of different analyte refractive indices (a) for y- y-polarization, (b) for x-polarization

From the dispersion relation of the fundamental core in the y-polarization mode and plasmonic modes shown in Figure 6, two loss peaks were observed. The reason behind the appearance of two peaks could be due to the interaction of different SPP modes with the core fundamental mode. Also, this multiple peaks appearance could be due to the complexity of the plasmonic layer shape [49]. These peaks shift towards longer wavelengths, and their intensity decreases as the RI of the analyte increases for the 2nd peak of y-polarization and both peaks of x-polarization, as clear in Figure 6. The loss curve amplitude in the 1st peak of y-polarization increases as the RI of analytes decreases [50]. These behaviors provide ample information about the variation in the analyte RI.

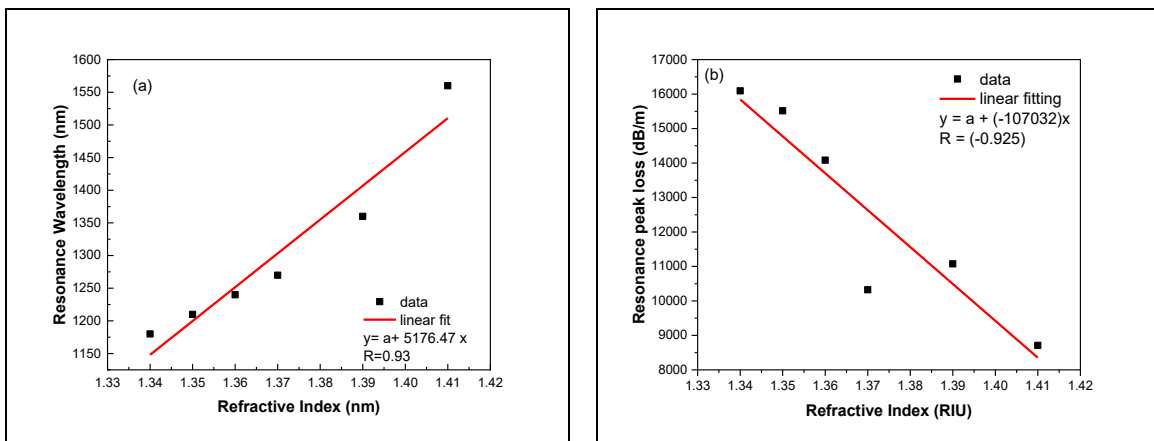


Fig.7: A linear fit that represented (a) the resonance wavelengths and (b) the loss peak intensity, as a function of the analyte RI. (For Y-polarization)

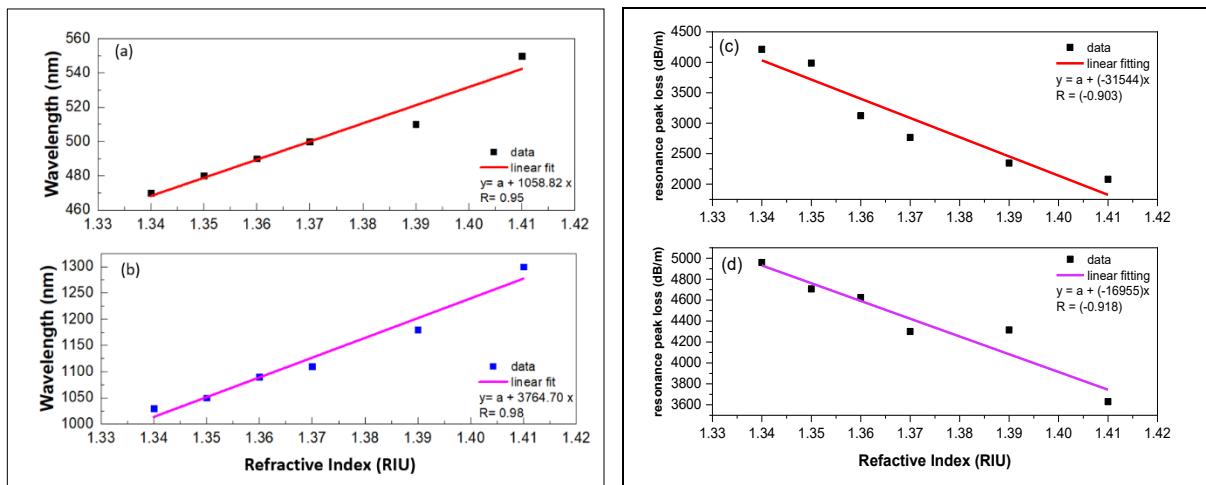


Fig.8: A linear fit that represented (a, b) the resonance wavelengths and (c, d) the loss peak intensity, as a function of the analyte RI for P1 and P2. (For X-polarization)

Variation in the analyte's RI causes a shift in the resonance wavelength because it affects the distribution of the sensor's electric field. The decrease in peak intensity results from the increased surface plasmon resonance mode attenuation as the analyte's refractive index rises. Combining polarization-maintaining photonic crystal fibers with surface plasmon resonance principles leads to the design of sensors that are highly sensitive to variation in RI and maintain the polarization state of light, ensuring precise and stable measurements.

A linear relationship exists between both the resonance wavelength and peak intensity with the analyte's refractive index within the range of 1.34 RIU to 1.41 RIU for Y-polarization and X-polarization mode, as depicted in Figures 7 and 8.

These figures demonstrate that the two resonance loss peaks exhibit high sensitivity to the filled analyte's refractive index (1.34-1.41) RIU. The loss peak will continuously shift to longer wavelengths as the analyte's RI rises, enabling the detection of the analyte's RI through analysis of the loss spectrum. So, the D-PM-PCF-SPR structure is suitable for refractive index sensing applications. The relationship between the analyte's refractive index and the SPR wavelength for y-polarization for the 2nd peak is expressed by $y = a + (5.176)x$ which shows high linearity $R = 0.93$.

The relationship between the analyte's refractive index and the SPR wavelength for x-polarization for both peaks are expressed by $y = a + (1.058)x$ for 1st peak, and $y = a + (3.764)x$ for 2nd peak, respectively. Both peaks have high linearity $R = 0.95$ for 1st peak and $R = 0.98$ for 2nd peak, respectively.

For RI values ranging from 1.34 to 1.41, the maximum wavelength sensitivity of the peak is 5176 nm/RIU, and the spectral resolution for this sensor is 1.93×10^{-5} RIU, for y-polarization. For x-polarization and the same range of RI, the maximum sensitivity of the 1st and 2nd peaks is 1058 nm/RIU and 3764 nm/RIU, respectively. The spectral resolution for the 1st and 2nd peaks is 9.45×10^{-5} RIU and 2.65×10^{-5} RIU, respectively.

The figure of merit (FOM) is regarded as a crucial factor for assessing the sensor performance and quality because it measures the sensor sensitivity and efficiency to detect minor variations in the surrounding

refractive index. FWHM measures the width of a sensor's response curve at half its peak, characterizing its resolution or bandwidth. A higher FOM indicates an improved signal-to-noise ratio for the sensor and thus reducing signal noise. Table (3) presents the FOM values for different refractive indices RIs in both x- and y-polarization. The proposed SPR sensor has an FWHM of 50.99 at n_a of 1.37 and a maximum FOM of 101.5 for the y-polarization mode.

Table 3 illustrates the FOM in (RIU⁻¹) calculation for the proposed sensor

n_a (RIU)	FOM (RIU ⁻¹)	
	X-polarization mode P1	Y-polarization mode P2
1.34	13.5	34.2
1.35	13.6	27.7
1.36	11.6	64
1.37	12.9	46.7
1.39	10.3	50.8
1.41	9.5	24

Table 4 provides a comparative analysis of the maximum sensitivity and spectral resolution of the proposed sensor and others in recent published work.

Table 4. Performance comparison with other SPR fiber-based sensors

Ref. No.	Type and shape of the plasmonic material	WS (nm/RIU)	Resolution (RIU)	Detection range (RIU)
[51]	Gold / thin layer	2200	3.75×10^{-5}	1.33 - 1.36
[27]	Graphene / thin layer	2000	5×10^{-5}	1.331 - 1.339
[52]	Gold and molybdenum disulfide / thin layers	5100	1.96×10^{-5}	1.19 - 1.40
[39]	Gold / Grating	994.5	2.03×10^{-6}	1.33 - 1.37
[53]	Gold / Nanoparticles	3157.98	3.16×10^{-5}	1.281- 1.39
[54]	Gold / thin layer	1000	1×10^{-4}	1.33 - 1.37
This work	Gold / Hemisphere structure	For x-polarization, P1: 1058	9.45×10^{-5}	1.34 – 1.41
		P2: 3764 For y- polarization, P2: 5176	2.65×10^{-5} 1.93×10^{-5}	

5. Conclusion

In conclusion, this study presents a new SPR-based PM-PCF sensor. Due to its chemical stability, gold was utilized as a plasmonic material with hemispherical structures on the surface of the D-shaped sensor to induce the SPR effect. Numerical analyses were conducted using Finite Element Method (FEM) in the frequency domain. Our suggested design offers a high wavelength sensitivity (WS) of 5176 nm/RIU and the spectral resolution for this sensor is 1.93×10^{-5} RIU, for y-polarization. For x-polarization, the wavelength sensitivity of the 1st and 2nd peaks are 1058 nm/RIU and 3764 nm/RIU, respectively. The spectral resolution for the 1st and 2nd peaks is 9.45×10^{-5} RIU and 2.65×10^{-5} RIU, respectively in the high sensing range of 1.34 to 1.41 RIU. Y-polarization was used for better performance of the proposed sensor,



due to high confinement loss and Figure of Merit (FOM). The sensor demonstrates excellent spectral resolution allowing for precise measurement of refractive index changes within the specified range. These findings could affect highly sensitive and high-resolution refractive index sensing applications, such as biosensors and environmental monitoring systems.

References

- [1] W. Luo, B. Liu, J. Liu, T. Wu, Q. Liu, M.-Y. Wang, *et al.*, “Tapered side-polished microfiber sensor for high sensitivity hCG detection,” *IEEE Sensors Journal*, vol. 22, pp. 7727–7733, 2022.
- [2] H. A. Mohammed, S. A. Rashid, M. H. A. Bakar, S. B. A. Anas, M. A. Mahdi, and M. H. Yaacob, “Fabrication and characterizations of a novel etched-tapered single mode optical fiber ammonia sensors integrating PANI/GNF nanocomposite,” *Sensors and Actuators B: Chemical*, vol. 287, pp. 71–77, 2019.
- [3] V. T. Huong, N. T. T. Phuong, N. T. Tai, N. T. An, V. D. Lam, D. H. Manh, *et al.*, “Gold nanoparticles modified a multimode clad-free fiber for ultrasensitive detection of bovine serum albumin,” *Journal of Nanomaterials*, vol. 2021, p. 5530709, 2021.
- [4] H. J. Taher, “The influence of no-core fiber length on the sensitivity in fiber optic strain sensor,” *Iraqi Journal of Laser*, vol. 20, pp. 13–20, 2021.
- [5] Y. Liu, H. Chen, Y. Guo, M. Wang, X. Meng, X. Jing, *et al.*, “Ultra-high sensitivity plasmonic sensor based on D-shaped photonic crystal fiber with offset-core,” *Optik*, vol. 221, p. 165309, 2020.
- [6] D. M. Kim, J. S. Park, S.-W. Jung, J. Yeom, and S. M. Yoo, “Biosensing applications using nanostructure-based localized surface plasmon resonance sensors,” *Sensors*, vol. 21, p. 3191, 2021.
- [7] M. Elsherif, A. E. Salih, M. G. Muñoz, F. Alam, B. AlQattan, D. S. Antonysamy, *et al.*, “Optical fiber sensors: Working principle, applications, and limitations,” *Advanced Photonics Research*, vol. 3, p. 2100371, 2022.
- [8] C. Ma, D. Peng, X. Bai, S. Liu, and L. Luo, “A review of optical fiber sensing technology based on thin film and Fabry–Perot cavity,” *Coatings*, vol. 13, p. 1277, 2023.
- [9] M. R. Islam, M. M. Ali, M.-H. Lai, K.-S. Lim, and H. Ahmad, “Chronology of Fabry–Perot interferometer fiber-optic sensors and their applications: a review,” *Sensors*, vol. 14, pp. 7451–7488, 2014.
- [10] Y.-J. Rao, Z.-L. Ran, and Y. Gong, *Fiber-Optic Fabry–Perot Sensors: An Introduction*, CRC Press, 2017.
- [11] F. Xue, Y. Yao, P. Xu, J. Luo, L. Li, L. Zhang, *et al.*, “Ultra-high sensitive refractive index sensor based on D-shaped photonic crystal fiber with graphene-coated Ag-grating,” *Heliyon*, vol. 9, 2023.
- [12] C. Liu, J. Lü, W. Liu, F. Wang, and P. K. Chu, “Overview of refractive index sensors comprising photonic crystal fibers based on the surface plasmon resonance effect,” *Chinese Optics Letters*, vol. 19, p. 102202, 2021.
- [13] H. Huang, Z. Zhang, Y. Yu, L. Zhou, Y. Tao, G. Li, *et al.*, “A highly magnetic field sensitive photonic crystal fiber based on surface plasmon resonance,” *Sensors*, vol. 20, p. 5193, 2020.
- [14] R. B. Schasfoort, *Handbook of Surface Plasmon Resonance*, Royal Society of Chemistry, 2017.
- [15] D. Wang, W. Li, Q. Zhang, B. Liang, Z. Peng, J. Xu, *et al.*, “High-performance tapered fiber surface plasmon resonance sensor based on the graphene/Ag/TiO₂ layer,” *Plasmonics*, vol. 16, pp. 2291–2303, 2021.
- [16] P. Bing, Q. Liu, G. Wu, S. Yuan, Z. Li, H. Du, *et al.*, “A plasmonic sensor based on D-shaped dual-core microchannel photonic crystal fiber,” *Plasmonics*, vol. 17, pp. 1471–1478, 2022.
- [17] R. Zakaria, M. Mahbub, and C. Lim, “Studies of surface plasmon resonance effect on different metallic layers of silver (Ag) and copper (Cu) with molybdenum trioxide (MoO₃) for formaldehyde sensor,” *Results in Optics*, vol. 11, p. 100374, 2023.
- [18] M. R. Sardar and M. Faisal, “Numerical analysis of highly sensitive twin-core, gold-coated, D-shaped photonic crystal fiber based on surface plasmon resonance sensor,” *Sensors*, vol. 23, p. 5029, 2023.
- [19] D. Kumar, M. Khurana, M. Sharma, and V. Singh, “Analogy of gold, silver, copper and aluminium based ultra-sensitive surface plasmon resonance photonic crystal fiber biosensors,” *Materials Today: Proceedings*, 2023.
- [20] A. Khaleque, E. G. Mironov, J. H. Osório, Z. Li, C. M. Cordeiro, L. Liu, *et al.*, “Integration of bow-tie plasmonic nano-antennas on tapered fibers,” *Optics Express*, vol. 25, pp. 8986–8996, 2017.



- [21] S. A. S. Sunny, T. Ahmed, S. M. Hiam, and A. K. Paul, "Highly sensitive externally metal coated plasmonic refractive index sensor based on photonic crystal fiber," *Optik*, vol. 243, p. 167482, 2021.
- [22] L. F. Abdulrazak, M. B. Hossain, M. S. Islam, A. F. Alkhateeb, I. M. Mehedi, S. Roy, et al., "Plasmonic sensor based on microstructure PCF: performance analysis with outside detecting approach," *Optical and Quantum Electronics*, vol. 54, p. 58, 2022.
- [23] C. Caucheteur, T. Guo, and J. Albert, "Review of plasmonic fiber optic biochemical sensors: improving the limit of detection," *Analytical and Bioanalytical Chemistry*, vol. 407, pp. 3883–3897, 2015.
- [24] M. Tu, T. Sun, and K. Grattan, "Optimization of gold-nanoparticle-based optical fibre surface plasmon resonance (SPR)-based sensors," *Sensors and Actuators B: Chemical*, vol. 164, pp. 43–53, 2012.
- [25] Q. Wang, X. Jiang, L.-Y. Niu, and X.-C. Fan, "Enhanced sensitivity of bimetallic optical fiber SPR sensor based on MoS₂ nanosheets," *Optics and Lasers in Engineering*, vol. 128, p. 105997, 2020.
- [26] S. Cai, H. Pan, Á. González-Vila, T. Guo, D. C. Gillan, R. Wattiez, et al., "Selective detection of cadmium ions using plasmonic optical fiber gratings functionalized with bacteria," *Optics Express*, vol. 28, pp. 19740–19749, 2020.
- [27] A. K. Paul, M. A. Mollah, M. Z. Hassan, N. Gomez-Cardona, and E. Reyes-Vera, "Graphene-coated highly sensitive photonic crystal fiber surface plasmon resonance sensor for aqueous solution: Design and numerical analysis," in *Photonics*, p. 155, 2021.
- [28] Y. Fei, B. Luo, M. An, T. Hu, W. Lin, and H. Jia, "Highly sensitive surface plasmon resonance refractive index sensor based on D-shaped dual-core photonic crystal fiber with ITO film," *Plasmonics*, pp. 1–15, 2023.
- [29] S. Jain, K. Choudhary, and S. Kumar, "Novel materials-based photonic crystal fiber sensor for biomedical applications," *Plasmonics*, pp. 1–14, 2023.
- [30] W. Zhou, X. Qin, M. Lv, L. Qiu, Z. Chen, and F. Zhang, "Design of plasmonic photonic crystal fiber for highly sensitive magnetic field and temperature simultaneous measurement," *Micromachines*, vol. 14, p. 1684, 2023.
- [31] Q. Liu, S. Hou, J. Dong, J. Lei, G. Wu, and Z. Yan, "D-shaped microstructure fiber temperature sensor based on surface plasmon resonance," *Japanese Journal of Applied Physics*, vol. 62, p. 096002, 2023.
- [32] B. S. Boruah and R. Biswas, "Localized surface plasmon resonance based U-shaped optical fiber probe for the detection of Pb²⁺ in aqueous medium," *Sensors and Actuators B: Chemical*, vol. 276, pp. 89–94, 2018.
- [33] C. Teng, P. Shao, S. Li, S. Li, H. Liu, H. Deng, et al., "Double-side polished U-shape plastic optical fiber based SPR sensor for the simultaneous measurement of refractive index and temperature," *Optics Communications*, vol. 525, p. 128844, 2022.
- [34] L.-X. Kong, Y.-X. Zhang, W.-G. Zhang, Y.-S. Zhang, T.-Y. Yan, P.-C. Geng, et al., "Lab-on-tip: Protruding-shaped all-fiber plasmonic microtip probe toward in-situ chem-bio detection," *Sensors and Actuators B: Chemical*, vol. 301, p. 127128, 2019.
- [35] J. Wang, W. Liu, L. Yang, J. Lv, Q. Yin, Q. Liu, et al., "Symmetrical dual D-shape fiber for waveguide coupled surface plasmon resonance sensing," *Optik*, vol. 287, p. 171162, 2023.
- [36] X. Meng, J. Li, Y. Guo, S. Li, Y. Wang, W. Bi, et al., "An optical-fiber sensor with double loss peaks based on surface plasmon resonance," *Optik*, vol. 216, p. 164938, 2020.
- [37] F. Mumtaz, M. Roman, B. Zhang, L. G. Abbas, M. A. Ashraf, M. A. Fiaz, et al., "A simple optical fiber SPR sensor with ultra-high sensitivity for dual-parameter measurement," *IEEE Photonics Journal*, vol. 14, pp. 1–7, 2022.
- [38] H. P. Li, J. Ruan, X. Li, Q. Q. Zhang, J. J. Chen, T. He, et al., "High-sensitivity refractive index sensor of arc-shape photonic crystal fiber based on surface plasmon resonance," *Progress in Electromagnetics Research C*, vol. 137, pp. 29–38, 2023.
- [39] Y. Ying, Y. Xia, S. Cheng, D. Shan, Z. Gao, G. Si, et al., "High performance dual-core D-shaped PCF refractive index sensor coated with gold grating," in *Photonics*, p. 473, 2023.
- [40] L.-Q. Chen, Y.-C. Wu, Y. Liu, H. Y. Cai, and J. Liu, "Highly sensitive dual-function sensor for refractive index and temperature using D-shaped microchannel photonic crystal fiber," *Optics Express*, vol. 32, pp. 12405–12418, 2024.
- [41] M. Koshiba, Y. Tsuji, and M. Hikari, "Finite element beam propagation method with perfectly matched layer boundary conditions," *IEEE Transactions on Magnetics*, vol. 35, pp. 1482–1485, 1999.



- [42] X. Yan, R. Fu, T. Cheng, and S. Li, "A highly sensitive refractive index sensor based on a V-shaped photonic crystal fiber with a high refractive index range," *Sensors*, vol. 21, p. 3782, 2021.
- [43] M. R. Islam, M. M. I. Khan, F. Mehjabin, J. A. Chowdhury, M. Islam, A. J. Yeasir, et al., "Design of a dual spider-shaped surface plasmon resonance-based refractometric sensor with high amplitude sensitivity," *IET Optoelectronics*, vol. 17, pp. 38–49, 2023.
- [44] X. Chen, L. Xia, and C. Li, "Surface plasmon resonance sensor based on a novel D-shaped photonic crystal fiber for low refractive index detection," *IEEE Photonics Journal*, vol. 10, pp. 1–9, 2018.
- [45] W. Li, Y. Chen, J. Xu, M. Jiang, and H. Zou, "A dual-core surface plasmon resonance-based photonic crystal fiber sensor for simultaneously measuring the refractive index and temperature," *Crystals*, vol. 13, p. 972, 2023.
- [46] H. Qiu, W. Li, C. Zhu, J. Xu, J. Li, and G. Bai, "A high-sensitivity D-shaped photonic crystal fiber surface plasmon resonance sensor for low refractive index detection," *Journal of Optics*, pp. 1–9, 2023.
- [47] Y. Li, H. Chen, H. Li, Z. Gao, X. Fan, and Q. Chen, "Highly sensitive methane gas sensor based on Au/UVCFS films coated D-shaped photonic crystal fiber," *Physica Scripta*, vol. 98, p. 065533, 2023.
- [48] A. K. Paul, A. K. Sarkar, A. B. S. Rahman, and A. Khaleque, "Twin core photonic crystal fiber plasmonic refractive index sensor," *IEEE Sensors Journal*, vol. 18, pp. 5761–5769, 2018.
- [49] Z.-K. Fan, S.-B. Fang, S.-G. Li, and Z.-Y. Wei, "Refractive index sensor based on high-order surface plasmon resonance in gold nanofilm coated photonic crystal fiber," *Chinese Physics B*, vol. 28, p. 094209, 2019.
- [50] K. Ahmed, M. A. AlZain, H. Abdullah, Y. Luo, D. Vigneswaran, O. S. Faragallah, et al., "Highly sensitive twin resonance coupling refractive index sensor based on gold-and MgF₂-coated nano metal films," *Biosensors*, vol. 11, p. 104, 2021.
- [51] M. R. Hasan, S. Akter, A. A. Rifat, S. Rana, and S. Ali, "A highly sensitive gold-coated photonic crystal fiber biosensor based on surface plasmon resonance," in *Photonics*, p. 18, 2017.
- [52] X. Guo, Y. Wang, T. Sang, G. Yang, and Q. Yao, "SPR sensor based on a concave photonic crystal fiber structure with MoS₂/Au layers," *Materials*, vol. 16, p. 5523, 2023.
- [53] M. A. Fakhri, E. T. Salim, S. M. Tariq, R. K. Ibrahim, F. H. Alsultany, A. A. Alwahib, et al., "A gold nanoparticles coated unclad single mode fiber-optic sensor based on localized surface plasmon resonance," *Scientific Reports*, vol. 13, p. 5680, 2023.
- [54] A. A. Rifat, G. A. Mahdiraji, Y. Shee, M. J. Shawon, and F. M. Adikan, "A novel photonic crystal fiber biosensor using surface plasmon resonance," *Procedia Engineering*, vol. 140, pp. 1–7, 2016.
- [55] F. J. Moaen and H. R. Humud, "Raman scattering enhancement by silver nanostructures prepared by electrical exploding wire technique," *Iraqi Journal of Science*, pp. 2017–2024, 2022.

متحسس عالي الحساسية لمعامل الانكسار المعتمد على بلازمونات مزدوجة القمة في الليف البصري الفوتوني مديم الاستقطاب ذو الشكل D والمغطى بهياكل ذهب نانوية

سعاد صاحب هندال^{1,2*} ، زينب فاضل مهدي¹ ، أسيل إبراهيم محمود²

¹معهد الليزر للدراسات العليا/ جامعة بغداد

²هيئة البحث العلمي / وزارة التعليم العالي والبحث العلمي

البريد الإلكتروني للباحث*: suad.saheb2101p@ilps.uobaghdad.edu.iq

الخلاصة: يدرس هذا البحث متحسس تأثير رنين البلازمون السطحي (SPR) استناداً إلى الألياف البلورية الفوتونية المديمة للاستقطاب (PM-PCF) بشكل D باستخدام طريقة العناصر المحددة. وباستخدام عنصر الذهب (Au) كمادة بلازمونية



وبتراكيب نصف كروية لها نصف قطر يبلغ 50 نانومتر على سطح المتحسس ذو الشكل D لإنتاج تأثير الرنين البلازموني السطحي (SPR)، مما يتيح للمتحسس اكتشاف التغيرات في معامل انكسار العنصر المحيط. ستتغير قيم الانحلال عندما تتغير معامل انكسار العنصر المطلوب الكشف عنه، مما يؤدي إلى زحزحة معين في ذروة الفقد. حيث تم ملاحظة قمتي رنين، الأولى في الجزء المرئي من الطيف، والثانية في منطقة الأشعة تحت الحمراء القريبة. التصميم المقترح يُظهر حساسية عالية للطول الموجي (WS)، حيث بلغت (5176 نانومتر/وحدة معامل الانكسار) والدقة الطيفية لهذا المتحسس هي (1.93×10^{-5}) وحدة معامل الانكسار، لأنماط المحور الصادي للاستقطاب. وبالنسبة لأنماط الاستقطاب للمحور السيني، فإن الحساسية القصوى للقيمة الأولى والثانية هي (1058 نانومتر/وحدة معامل الانكسار) و (3764 نانومتر/وحدة معامل الانكسار)، على التوالي. الدقة الطيفية للقيمة الأولى والثانية هي (9.45×10^{-5}) وحدة معامل الانكسار و (2.65×10^{-5}) وحدة معامل الانكسار. على التوالي وفي ضمن مدى معاملات الانكسار من 1.34 إلى 1.41 وحدة معامل انكسار. تُظهر النتائج أن هذا التصميم حسن قدرة التحسس على كشف التغير في معاملات الانكسار. التصميم المقترح للمتحسس يتصف بحساسية ودقة وخطية عالية، وهي نتيجة واعدة يمكن استخدامها في مراقبة البيئة والكشف البيولوجي والمتحسسات الفيزيائية والتحليل الكيميائي.





Enhance the efficiency of [CeO₂(NP)/Cu(NP)] PEC cell photoanode for hydrogen production by laser illumination

Sally A. Al-Ani*, and Mohamed K. Dhahir

Institute of Laser for Postgraduate Studies, University of Baghdad, Baghdad, Iraq

* Email address of the Corresponding Author: Sally.Abdulrazaq1101a@ilps.uobaghdad.edu.iq

Article history: Received: 2 Sept. 2024; Revised: 9 Oct. 2024; Accepted: 14 Oct. 2024; Published online: 15 Jun. 2025.

Abstract

This research introduces a novel approach to enhancing solar-to-hydrogen (STH) efficiency by applying laser illumination with the assistance of a UV source to illuminate the photoanode in photoelectrochemical (PEC) cells, representing a significant departure from conventional methods relying solely on solar light. The photoanode was fabricated using a (CeO₂ and Cu) nanoparticles thin film through the drop-casting method, the materials were chosen for their favorable optical and electronic properties, which are key in improving the hydrogen production rate. What sets this study apart is the innovative use of laser illumination, which allows for more precise and concentrated light absorption that match the materials' absorption peaks compared to the broad spectrum of traditional sunlight. The structural properties of the materials were examined using X-Ray diffraction (XRD), (FE-SEM) to get the cross-sectional image and the optical properties were characterized by the UV-VIS-NIR spectrophotometer. Photoelectrochemical measurements were carried out by linear sweep voltammetry in the dark and under illumination condition AM 1.5 G of 100 mW/cm². Our findings reveal that under laser and UV illumination, the PEC cell substantially improves photocurrent density and efficiency by 12.3%, outperforming traditional solar light irradiation with an efficiency of 5.5%. This work sets a new direction for PEC cell optimization by demonstrating the effectiveness of laser-assisted light in boosting hydrogen production, representing a significant step forward in renewable energy research.

Keywords: Water splitting, PEC, Thin film, hydrogen production.

1. Introduction

The increasing global demand for renewable energy solutions has intensified research into alternative methods for sustainable energy production. One promising avenue is hydrogen generation through photoelectrochemical (PEC) water splitting, a process that converts solar energy into chemical energy by splitting water into hydrogen and oxygen. Hydrogen, as a clean and highly energy-dense fuel, plays a critical role in the emerging hydrogen economy, with its potential to replace fossil fuels in various sectors. [1,2]. However, a major challenge in PEC systems lies in enhancing the solar-to-hydrogen (STH)



conversion efficiency, which remains limited by several factors including material performance, light absorption, and charge carrier dynamics[3]. These systems typically involve the use of a photoelectrochemical (PEC) cell, where a semiconductor photoanode absorbs sunlight, generating electron-hole pairs that drive the water-splitting reaction [4]. The efficiency of this process is often limited by the photoanode's ability to absorb light, separate charge carriers, and catalyze the water oxidation reaction. In fact, the rate at which light is absorbed by the photoanode material is thought to be the key to enhanced hydrogen generation. It is estimated that the UV portion of sunlight on Earth makes up just 4%. Consequently, to achieve maximum efficiency, the photoresponse of the working electrode's (photoanode) absorption must reach the visible light area. Realizing the full potential of solar energy conversion technologies can be attributed to the importance of creating effective photoanode materials for PEC cells, such as thin film composites and inventive designs [5].

Historically, solar light has been the primary source of illumination in PEC systems, with pioneering works dating back to the early 1970s when Fujishima and Honda first demonstrated water splitting using a TiO₂ photoanode under ultraviolet light. Since then, efforts to improve efficiency have focused on optimizing the materials and structures of photoanodes, including the development of thin films, nanostructured surfaces, and doped semiconductors [6]. CeO₂ (ceria), for instance, has emerged as a highly attractive material due to its high oxygen vacancy concentration, superior charge storage capability, dielectric property, and stability in water oxidation reactions. Coupled with copper (Cu) nanoparticles, the CeO₂-Cu combination offers improved conductivity and enhanced charge separation, making it an effective photoanode material for PEC applications [7,8]. On the other hand, Cu nanoparticles (NP) have excellent plasmonic properties including the surface plasmon resonance effect that spans the UV-visible region of the optical spectrum [9,10].

In recent years, there has been a growing interest in exploring alternative light sources to further enhance the efficiency of PEC cells [11]. Laser illumination, which provides highly focused, coherent, and monochromatic light, represents a novel approach to boosting photoactivity. Unlike conventional solar light, which covers a broad and less concentrated spectrum, laser light can be precisely tuned to the absorption characteristics of the photoanode material, leading to more efficient photoexcitation and charge generation. This precise control over the light source opens new possibilities for overcoming the limitations posed by traditional sunlight, such as poor energy concentration.

This study seeks to explore the innovative application of laser illumination in PEC water splitting, using a [CeO₂(NP)/Cu(NP)] thin film photoanode fabricated by the drop-casting method. By comparing the performance of this system under both laser and traditional solar light, we aim to assess the extent to which laser illumination can enhance STH efficiency. This work not only builds on the historical advancements in PEC technology but also introduces a novel illumination strategy that could redefine the approach to maximizing hydrogen production in solar-driven systems.

2. Experimental

Fabrication of the (P) photoanode: The P photoanode is a two-layer thin film of CeO₂ (NP) and Cu (NP) drop-casted on a glass substrate coated with fluorine tin oxide (FTO). The CeO₂ is a 99.9% pure powdered nanoparticle that was bought from (HONGWUNEMATERIAL). A 0.2 g quantity of cerium dioxide (CeO₂) nanoparticles was dispersed in 25 mL of deionized (DI) water to form the suspension. The mixture was magnetically stirred for 1 hour at room temperature to ensure proper dispersion of CeO₂ particles. A micropipette was used to drop-cast 10 drops of the CeO₂ suspension onto the clean (1 × 1) cm² FTO substrate at the conductive face to form the first layer. Then, the film was allowed to dry on a hot plate. The 99.99% pure Cu nanoparticles were supplied by (Nanjing Nano Technology Co., Ltd.).

The second layer was formed by dispersing 0.2 g of copper (NP) in 25 mL of deionized (DI) water. The suspension was stirred continuously for one hour to achieve a uniform mixture. Following the Cu (NP) suspension preparation, 10 drops were drop-cast onto the pre-formed CeO₂ layer and dried on a hot plate.



3. Characterizations

3.1 X-Ray Diffraction Measurement (XRD)

XRD characterization was used for materials identification to confirm their structural properties. The X-ray diffraction patterns of CeO₂ (NP) and Cu (NP) were obtained using (Aeris – Malvern Panalytical's X-ray diffractometer). The scanning was over the required range for 2 θ values (15 – 75) o with $\pm 0.02^\circ$ 2 θ peak position accuracy. Peaks of crystalline phases were compared with those of standard compounds of the materials with previous research.

3.2 Optical Analysis

In order to investigate the optical properties of the designed photoanode, the UV-VIS-NIR-1800 (SHIMADZU, Japan) spectrophotometer was used. This instrument was computerized with a CRT screen and keyboard to operate the input value. The absorption spectra were characterized with a wavelength range of (190–1100) nm.

3.2 Photoelectrochemical Characteristics

To study the photoelectrochemical performances of the P photoanode as an efficient photonode, it was tested by an electrochemical workstation (ER466, EDAQ company Australia, potentiostat). Ag/AgCl serves as the reference electrode, Pt serves as the counter electrode, and the designed photoanode (P) serves as the working electrode in the three-electrode system. Regular testing at room temperature used a 125 mL quartz cell with 2g KOH in DI water with PH 9, which served as the electrolyte. The linear sweep voltammetry curve was recorded with a scan starting at (0-1) V versus (Ag/AgCl).

J-V curves were obtained at a rate of 100 mW/s and at a frequency of 20 kHz at the corresponding program. The light-emitting diode (LED) Source (42 W, Zethors H7) illuminated the photoanode under an AM 1.5 G condition of (100) mW/cm².

4. Results and discussion

The structural information of CeO₂ (NP) and Cu (NP) was characterized by powder X-ray diffraction (XRD) patterns. Figure 1A displays the pattern of the CeO₂ nanoparticles. It revealed all of the major peaks of CeO₂ which coincided with lattice planes (111), (200), (220), (311), (222), and (400) and were positioned at 2 θ = 28.5°, 33.0°, 47.5°, 56.3°, 59.1° and 69.4°. These findings are in line with previous studies on CeO₂ nanoparticles [12,13]. An XRD diffractogram of copper nanoparticles is shown in Fig. 1 B. Typical lines indexed as (111), (200), and (220) that were found at diffraction angles of 43.3°, 50.4°, and 74.1°, respectively, correspond to the copper nanoparticles diffraction peaks. That matches the references [14,15]. Using Field emission scanning electron microscopy FE-SEM, cross-sectional images of the fabricated photoanode have been acquired and displayed in Fig. 2, which shows a recorded thickness ranging between 9.0 and 12.3 μ m for the thin film photoanode, including the two layers of CeO₂ (NP) and Cu(NP) with approximately equal thickness for each layer. The absorption enhancement was evaluated through an examination of the absorption spectra of the photoanodes P. As observed from the P's Fig. 3, the bilayer [CeO₂(NP)/Cu(NP)] thin film revealed an optimal light absorption, demonstrated by the three peaks in the visible range (446nm, 646 nm and 709) in addition to the peak of (294 nm) in the UV region. It is important to mention that, among the above peaks of P, the (446) nm is the intensive one. It's clearly that the peak at the UV region, (294) nm related to CeO₂ (NP) layer. While the rest of the peaks are belong to the Cu nanoparticles, which are form the second layer of the P photoanode. This could be in line with reported researches for the absorption peak of Cu (NP) which is around 570 nm [16,17].



The presence of more than one peak in the visible range of absorption spectrum related to the incorporation of a dielectric semiconductor CeO_2 with a plasmonic Cu nanostructure, related to higher efficiency. Because one of the pathways that surface plasmon resonance (SPR) might boost semiconductor photocatalytic activity is by increasing light absorption through metallic enhancement [18,19].

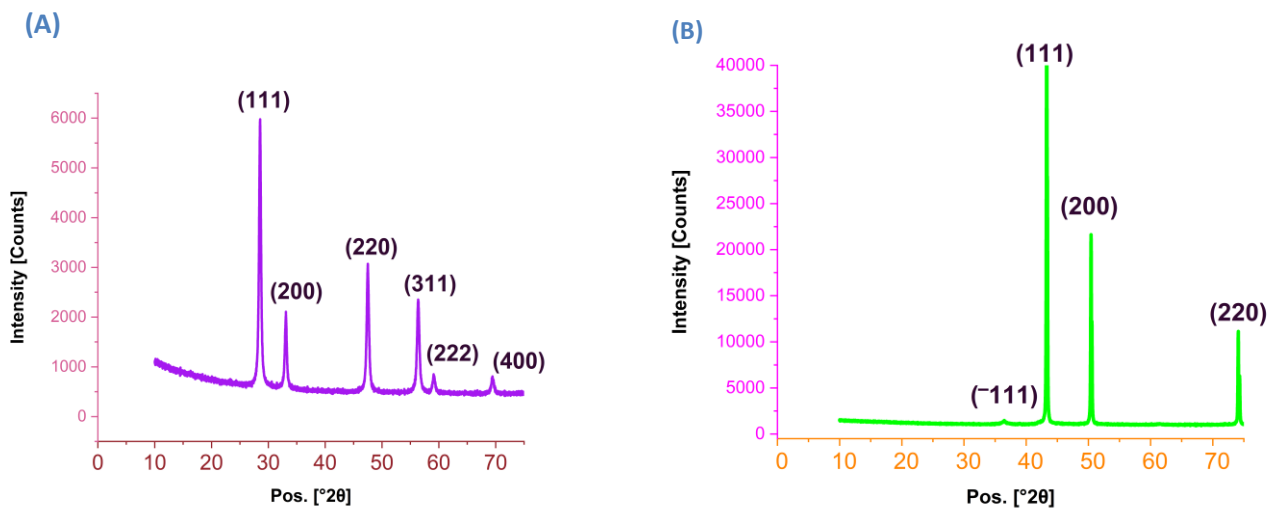


Fig. 1: XRD pattern (A) of CeO_2 NP; (B) of Cu NP.

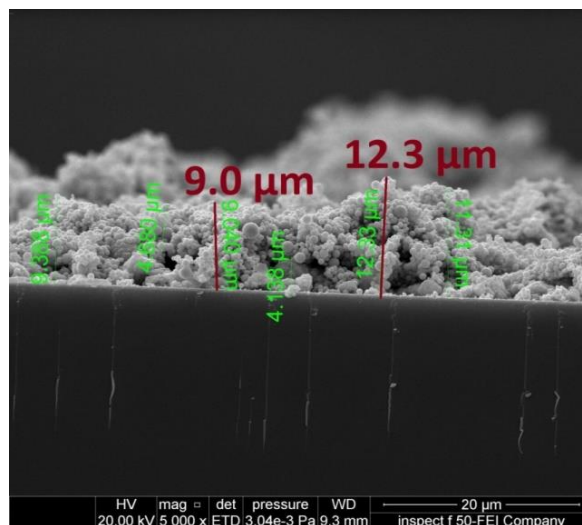


Fig. 2: Cross-sectional FE-SEM image of the (P) photoanode [FTO/ CeO_2 (NP) /Cu (NP)].

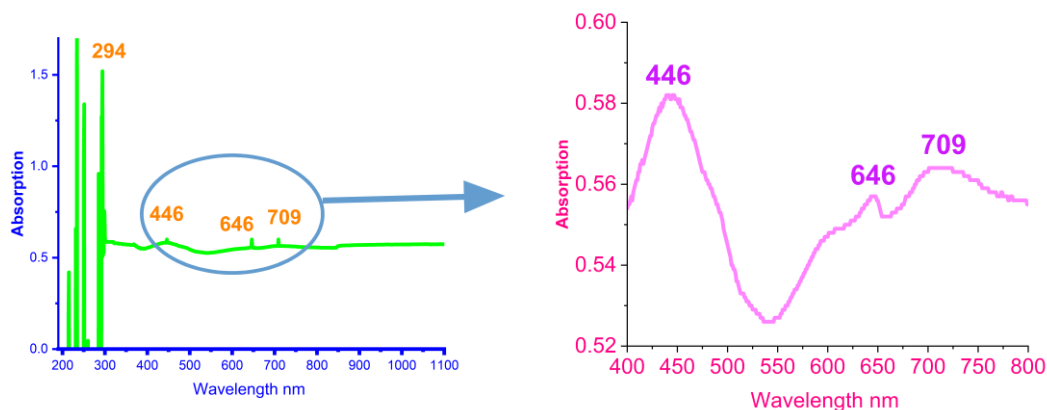


Fig. 3: Absorption spectrum of the (P) photoanode [FTO/CeO₂ (NP) /Cu (NP)]. indicates its absorption peaks at both UV and VIS regions.

Based on these findings, it can be said that the materials chosen for the fabricated photoanode allowed for maximal absorption to be regulated beyond the UV region and cover the visible region of the solar spectrum. The investigation of Dark current measurement, which reflects the baseline current in the absence of light, was the first step in determining the photoelectrochemical performance of the P photoanode. To confirm that incident light independently is the source of the observed photocurrent, to ensure it is not influenced by other factors, and to aim for accurate assessments of PEC performance. As a working electrode, the fabricated photoanode (P) was tested with a scan starting at (0-1) V versus Ag/AgCl in darkness. The dark current density of the P working electrode increased from (3.2×10^{-3} to 5.0×10^{-3}) mA. cm⁻² when the Cu (NP) were added as a second layer in the thin film fabricated. An increase in conductivity is connected to this rise. The low current observed in the P suggests that there aren't numerous defects in the electrode fabrication, which would otherwise cause recombination losses and decreased photoactivity. Due to the differentiation between photocurrent (produced by light-induced processes) and non-photoinduced currents, high dark current may indicate insufficient electrode quality or defective manufacturing. The low dark current in our experiment led to a higher effective efficiency, and stability, which could have an impact on the PEC cell's overall performance.

It was decided that one should utilize the comparison principle in order to achieve the best and most accurate evaluation of the photoelectric response of the the designed photoanode. By examining the LED illumination influence on the P photoanode [FTO/CeO₂(NP)/Cu(NP)] and investigating its behavior, it was found that P exhibited a current density of 23.0 mA.cm⁻² at 0.99 V vs. Ag/AgCl as displayed in Fig. (4) The positive photogenerated current value indicated that the P photoanode was an n-type semiconductor [20,21]. It is noteworthy to emphasis that the LED source (42 W, Zethors H7) was used to simulate the full solar spectrum [22], meaning that the results obtained accurately showed how this photoanode behave under solar spectrum characteristics.

It was assumed that a new strategy should be followed to improve hydrogen production, where an illumination procedure was adopted, including illumination of the (P) photoanode separately by laser sources with wavelengths of 473 nm, 532 nm, and 632 nm(DPSS laser model MBL-FN-473nm-200mW-15050466, Diode laser 532nm -150mW- Shanghai Dream Laser Technology and Diode laser 632nm). This procedure's principal objective is to examine how these lasers' wavelengths affect the photoanode's current reading by utilizing the idea that the absorption peak of an electrode or substance can be matched to the wavelength of incident light to achieve maximal absorption. The laser wavelengths were chosen closer to each of the P absorption peaks in the visible range. The laser with the best result was then chosen in order to be used as the primary source in the following stage. The results recorded in Fig. (5) illustrated that the 473 nm laser yielded the highest current density of (37.2) mA.cm⁻² at 0.99 V vs. Ag/AgCl, while the 632

nm laser recorded the lowest current density of (29.1) mA.cm⁻² at 0.99 V vs. Ag/AgCl. Conversely, the 532 nm laser revealed a value of (33.1) mA.cm⁻², which fell in between the 473 and 632 nm lasers.

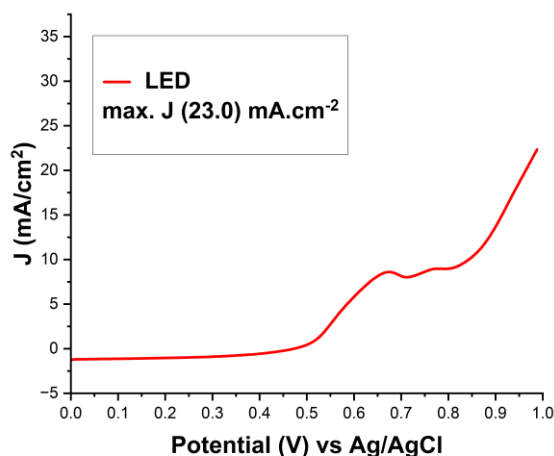


Fig. 4: I-V curve of the P photoanode [FTO/CeO₂ (NP) /Cu (NP)] tested by linear sweep voltammetry under AM 1.5G Illumination of LED source.

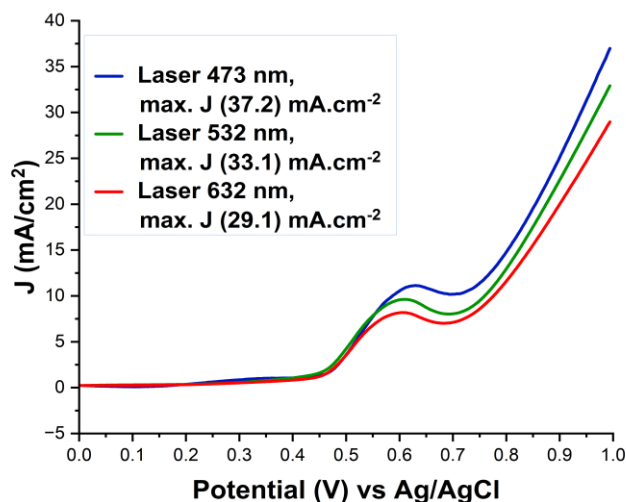


Fig. 5: I-V curve of the P photoanode [FTO/CeO₂ (NP) /Cu (NP)] tested by linear sweep voltammetry under AM 1.5G Illumination of 473 nm, 532 nm and 632 nm lasers sources (separately).

These findings align with the absorption peaks which identified in Fig. (3) as the maximum peak reported at 446 nm, a higher photocurrent value associated with laser 473 nm was observed. Consequently, due to its highest effect, the 473 nm laser was selected and used in the following step of the new procedure which was carried out by simultaneously exposing the P photoanode to a UV source of 6 W which has a wavelength of around 290 nm and a laser beam with a wavelength of 473 nm under AM 1.5 G illumination condition. The photocurrent density of the P photoanode increased significantly to (51.1) mA.cm⁻² at 0.99 V vs. Ag/AgCl, which emphasizing the benefits of the photoanode modification and procedure that were employed. Many factors contributed to this rise in current density, including the high conductivity of Cu

(NP), the materials' nanostructure, which enhanced the operative surface area, and the strong SPR effect, which was primarily responsible for the high measured current. The surface plasmon resonance (SPR) effect produced by Cu nanoparticles (NPS) on the dielectric semiconductor CeO₂ extends the light adsorption edge, encourages charge separation, and improves hydrogen generation [8,21,23-25]. This result demonstrates the significant improvement obtained when compared to that of the influence of LED on the P photoanode. This comparison is clear in Fig.(6), the high increment from (23.0) mA.cm⁻² to (51.1) mA.cm⁻² at 0.99 V vs. Ag/AgCl shows that employing a laser 473 nm + UV source might boost current by roughly (28.1) mA.cm⁻². A closer look at the same figure reveals that while the photoanode P is illuminated by different sources, its behaviour is similar but not identical. While as can be seen in Fig. (5) where the illumination source is comparable since it is a laser with a different wavelength, the behavior is completely identical with a rise in the photoelectric response. All the results of photocurrent densities for the P fabricated photoanode are illustrated in Table 1.

Table 1: illustrates the photocurrent density at 0.99 V vs. Ag/AgCl of the P photoanode with the illuminated sources and their represented readings.

Result Symbol	Illumination source	Thin film components on a (1*1) cm ² FTO substrate	Photocurrent density at 0.99 V vs. Ag/AgCl J (mA.cm ⁻²)
R1	LED	CeO ₂ (NP)/Cu(NP)	23.0
R2	Laser 473 nm	CeO ₂ (NP)/Cu(NP)	37.2
R3	Laser 532 nm	CeO ₂ (NP)/Cu(NP)	33.1
R4	Laser 632 nm	CeO ₂ (NP)/Cu(NP)	29.1
R5	Laser 473 nm + UV source	CeO ₂ (NP)/Cu(NP)	51.1

The Solar-to-Hydrogen efficiency (η) of all the resulting current densities is presented in Table 2. And in a 3-electrode PEC configuration, when an external bias is applied between the working (WE) and the counter electrodes (CE), conversion efficiency is usually evaluated using the following equation [26,27]:

$$\eta = [I (1.23 - E \text{ bias}) / J \text{ light}] \times 100\% \quad (1)$$

Where, (I) is photocurrent density at the given potential observed from the experiment (mA.cm⁻²), E bias is the used potential, 1.23 is the criterion of potential of water splitting, and J light refers to the intensity of the irradiating light at 100 mW/cm² for AM 1.5 G standard.

Table 2: The results of the calculated Solar-to-Hydrogen efficiencies for the P photoanode illuminated by different sources.

Result Symbol	Illumination source	Thin film components on a (1*1) cm ² FTO substrate	Solar-to-Hydrogen efficiency (η)
R1	LED	CeO ₂ (NP)/Cu(NP)	5.5 %
R2	Laser 473 nm	CeO ₂ (NP)/Cu(NP)	8.9 %
R3	Laser 532 nm	CeO ₂ (NP)/Cu(NP)	7.9 %
R4	Laser 632 nm	CeO ₂ (NP)/Cu(NP)	7.0 %
R5	Laser 473 nm + UV source	CeO ₂ (NP)/Cu(NP)	12.3 %



To visually compare values of all result calculated efficiencies, Fig. (6) provides information on the percentage efficiency of the photoconversion process. The Solar-to-Hydrogen efficiency of the P fabricated photoanode [CeO₂(NP)/Cu(NP)] which was illuminated by employing (laser 473 nm + UV source) is much higher than other resulted efficiencies, which implies that P have a strong ability for hydrogen production when the new procedure employed in comparison to traditional illumination represented by the LED source as it doubled increasing from (5.5%) to (12.3%). Moreover, the response at lower efficiencies is also considerably good results at the same time. This leads in overall good performance of the PEC cell

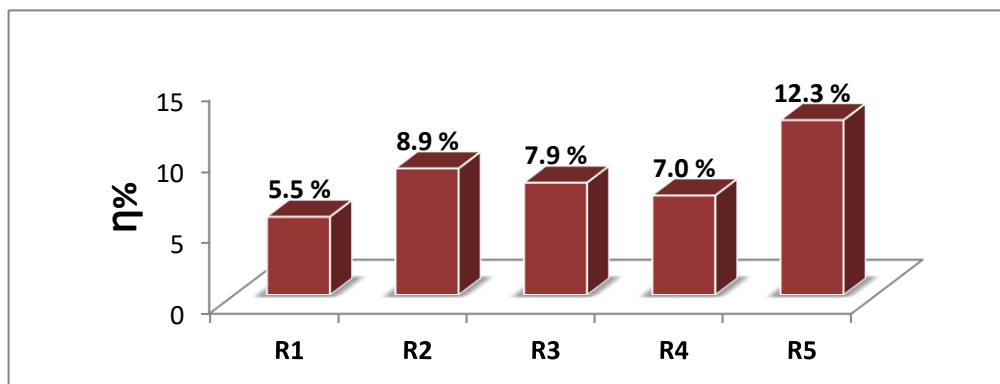


Fig. 6: Diagram illustrating the calculated efficiency for each outcome as: R1 of LED source, R2 of Laser 473 nm, R3 of Laser 532 nm, R4 of Laser 632 nm, and R5 of Laser 473 nm + UV source.

5. Conclusions

An efficient and low-cost photoanode for PEC cells was designed and fabricated. Its absorption was successfully controlled and enhanced to cover the UV and visible regions. Fine materials were selected and deposited on an FTO substrate by drop-casting technique. The first photoanode layer was formed by cerium oxide nanoparticles, which were then cast with copper nanoparticles to form the second layer. Advanced procedures were used to illuminate this photoanode by using laser and UV sources, resulting in higher photoconversion efficiency. The strategy was examined by comparisons with a conventional light source (LED) by linear scanning voltage with AM1.5 G of (100) mW/cm². The photoanode illuminated by the LED source was shown to record a current density of (23.0) mA.cm⁻² at 0.99 V vs Ag/AgCl. While an impressive result recorded to the implementation of our new procedure. As the photoanode is first illuminated by three laser sources separately with wavelengths matching the photoanode absorption Peaks in the visible region. The higher current density was recorded for the 473 nm laser source of (37.2) mA.cm⁻² at 0.99 V vs. Ag/AgCl. The second step of the new procedure of illumination the P photoanode [CeO₂/Cu(NP)] by 473 nm laser + UV source which enhanced the current density up to (51.1) mA.cm⁻² at 0.99 V vs. Ag/AgCl. This result show the validity of the strategy that was adopted and the hypothesis that was taken into considered when carrying out this investigation, and demonstrated the high performance of the PEC cell configuration with these electrodes designed to produce hydrogen via the water splitting process, which can be expressed in a practical and clear way through the high recorded Solar-to- Hydrogen efficiency of up to 12.3 %.

References

- [1] G. Z. Alwan, W. J. Aziz, and R. S. Sabry, "Producing hydrogen energy using Cr₂O₃-TiO₂ nanocomposite with animal (chitosan) extract via photocatalysis," *Iraqi J. High. Pure Appl. Sci.*, vol. 35, no. 4, 2022.
- [2] M. G. C. Zoontjes, "Visible-light-induced water splitting on a chip," M.Sc. thesis, Univ. of Twente, 2015.
- [3] T. Hisatomi, J. Kubota, and K. Domen, "Recent advances in semiconductors for photocatalytic and photoelectrochemical water splitting," *Chem. Soc. Rev.*, vol. 43, no. 22, pp. 7520–7535, 2014.



- [4] C. Ros, T. Andreu, and J. R. Morante, "Photoelectrochemical water splitting: a road from stable metal oxides to protected thin film solar cells," *J. Mater. Chem. A*, vol. 8, pp. 10625–10669, 2020.
- [5] Z. K. Ali and M. A. Mahdi, "Preparation of silicon nanowires photocathode for photoelectrochemical water splitting," *Iraqi J. Phys.*, vol. 4, pp. 66–68, 2022.
- [6] A. Fujishima and K. Honda, "Electrochemical photolysis of water at a semiconductor electrode," *Nature*, vol. 238, pp. 37–38, 1972.
- [7] D. Channei, A. Nakaruk, S. Phanichphant, P. Koshy, and C. C. Sorrell, "Cerium dioxide thin films using spin coating," *J. Chem.*, vol. 2013, pp. 2–4, 2013.
- [8] E. Kusmierek, "A CeO₂ semiconductor as a photocatalytic and photoelectrocatalytic material for the remediation of pollutants in industrial wastewater: a review," *Catalysts*, vol. 10, p. 1435, 2020.
- [9] P. Zhang, H. Liu, and X. Li, "Photo-reduction synthesis of Cu nanoparticles as plasmon-driven non-semiconductor photocatalyst for overall water splitting," *Appl. Surf. Sci.*, vol. 535, p. 147720, 2021.
- [10] F. G. Hamzah and H. R. Humud, "Signature of plasmonic nanostructures synthesised by electrical exploding wire technique on surface-enhanced Raman scattering," *Iraqi J. Sci.*, vol. 62, pp. 167–179, 2021.
- [11] Q. Zhang, D. T. Gangadharan, Y. Liu, Z. Xu, M. Chaker, and D. Ma, "Recent advances in light management for photoelectrochemical water splitting: from plasmonics to photonic structures," *J. Materiomics*, vol. 3, no. 1, pp. 33–50, 2017.
- [12] K. Nusrath and K. Muraleedharan, "Synthesis, characterization and thermal decomposition kinetics of cerium oxalate rods," *Devagiri J. Sci.*, vol. 2, no. 1, pp. 118–120, 2016.
- [13] E. Kumar, P. Selvarajan, and K. Balasubramanian, "Preparation and studies of cerium dioxide (CeO₂) nanoparticles by microwave-assisted solution method," *Recent Res. Sci. Technol.*, vol. 2, no. 4, pp. 37–41, 2010.
- [14] U. S. Shenoy and A. N. Shetty, "Simple glucose reduction route for one-step synthesis of copper nanofluids," *Appl. Nanosci.*, vol. 4, pp. 47–54, 2014.
- [15] Y. Suresh, S. Annapurna, G. Bhikshamaiah, and A. K. Singh, "Green luminescent copper nanoparticles," *IOP Conf. Ser.: Mater. Sci. Eng.*, vol. 149, p. 012187, 2016.
- [16] M. C. Crisan, M. Teodora, and M. Lucian, "Copper nanoparticles: synthesis and characterization, physiology, toxicity and antimicrobial applications," *Appl. Sci.*, vol. 12, p. 141, 2022.
- [17] Y. Fan, D. Li, M. Deng, Y. Luo, and Q. Meng, "An overview on water splitting photocatalysts," *Front. Chem. China*, vol. 4, no. 4, 2009.
- [18] J. Li and N. Wu, "Semiconductor-based photocatalysts and photoelectrochemical cells for solar fuel generation: a review," *Catal. Sci. Technol.*, vol. 5, no. 3, 2014.
- [19] S. Cho, J. Jang, K. Lee, and J. S. Lee, "Research update: strategies for efficient photoelectrochemical water splitting using metal oxide photoanodes," *APL Mater.*, vol. 2, p. 010703, 2014.
- [20] W. Ismail, G. Ibrahim, M. A. Habib, O. K. Alduaij, M. Abdelfatah, and A. El-Shaer, "Advancement of physical and photoelectrochemical properties of nanostructured CdS thin films toward optoelectronic applications," *Nanomaterials*, vol. 13, p. 1764, 2023.
- [21] M. L. Gaur, P. P. Hankare, K. M. Garadkar, S. D. Delekar, and V. M. Bhuse, "CdSe thin films: morphological, optoelectronic and photoelectrochemical studies," *J. Mater. Sci. Mater. Electron.*, 2013. [Online]. DOI: 10.1007/s10854-013-1572-9.
- [22] W. Jo and R. J. Tayade, "New generation energy-efficient light source for photocatalysis: LEDs for environmental applications," *Ind. Eng. Chem. Res.*, vol. 53, no. 6, pp. 2073–2084, 2014.
- [23] M. Hamid, Y. Zengin, and I. Boz, "Surface plasmon resonance-enhanced photocatalytic water-splitting for improved visible-light-driven H₂ generation using Ag-modified twin crystal Cd_{0.5}Zn_{0.5}S photocatalysts," *Catal. Commun.*, vol. 187, p. 106841, 2024.
- [24] Sh. Khanam and K. Rout, "Plasmonic metal/semiconductor heterostructure for visible light enhanced H₂ production," *ACS Omega*, vol. 7, pp. 25466–25475, 2022.
- [25] S. Wang, P. Liu, C. Meng, Y. Wang, L. Zhang, L. Pan, Z. Yin, N. Tang, and J. Zou, "Boosting photoelectrochemical water splitting by Au@Pt modified ZnO/CdS with synergy of Au–S bonds and surface plasmon resonance," *J. Catal.*, vol. 408, pp. 196–205, 2022.
- [26] Z. Liu, K. Guo, X. Zhang, T. Hong, and B. Wang, "Integrated CO₂ capture and photocatalytic conversion by a hybrid adsorbent/photocatalyst material," *Appl. Catal. B*, vol. 179, pp. 61–68, 2015.
- [27] Y. Qiu, Z. Pan, H. Chen, D. Ye, L. Guo, Z. Fan, and S. Yang, "Current progress in developing metal oxide nanoarrays-based photoanodes for photoelectrochemical water splitting," *Sci. Bull.*, vol. 64, no. 18, pp. 1348–1380, 2019.



تحسين كفاءة قطب الخلية الفوتوكهروكيميائية [CeO₂(NP)/Cu(NP)]

لانتاج الهيدروجين بواسطة اضاءة الليزر

سالي عبد الرزاق العاني*، محمد كريم ظاهر

معهد الليزر للدراسات العليا، جامعة بغداد، بغداد، العراق

البريد الإلكتروني للباحث*: Sally.Abdulrazaq1101a@ilps.uobaghdad.edu.iq

الخلاصة

يقدم هذا البحث نهجاً جديداً لتعزيز كفاءة تحويل الطاقة الشمسية إلى هيدروجين (STH) من خلال تطبيق الإضاءة بالليزر بمساعدة مصدر الأشعة فوق البنفسجية لإضاءة الأنود الضوئي في الخلايا الكهروضوئية (PEC)، مما يمثل انعطافاً كبيراً عن الطرق التقليدية التي تعتمد فقط على ضوء الشمس. تم تصنيع الأنود الضوئي باستخدام فيلم رقيق من الجسيمات النانوية لأكسيد السيريوم والنحاس (Cu و CeO₂) من خلال طريقة الصب بالتنقيط، وقد تم اختيار المواد لخصائصها البصرية والإلكترونية المواتية، والتي تعد مفتاحاً لتحسين معدل إنتاج الهيدروجين. ما يميز هذه الدراسة هو الاستخدام المبتكر لإضاءة الليزر، مما يسمح بامتصاص الضوء بشكل أكثر دقة وتركيزاً يتوافق مع ذروات امتصاص المواد مقارنة بالطيف الواسع لأشعة الشمس التقليدية. تم فحص الخصائص البنيوية للمواد باستخدام حيود الأشعة السينية (XRD) و (FE-SEM) للحصول على صورة مقطعية وتم وصف الخصائص البصرية بواسطة مطياف UV-VIS-NIR. تم إجراء القياسات الكهروضوئية الكيميائية باستخدام الفولتية الخطية في الظلام وفي ظل ظروف الإضاءة AM 1.5 G من 100 mW / cm². تكشف نتائجنا أنه تحت إضاءة الليزر والأشعة فوق البنفسجية، تعمل خلية PEC على تحسين كثافة التيار الضوئي وكفاءتها بشكل كبير بنسبة 12.3٪، متفوقة على إشعاع الضوء الشمسي التقليدي بكفاءة 5.5٪. يحدد هذا العمل اتجاهاً جديداً لتحسين خلية PEC من خلال إظهار فعالية الضوء بمساعدة الليزر في تعزيز إنتاج الهيدروجين، مما يمثل خطوة مهمة إلى الأمام في أبحاث الطاقة المتجددة..





Circumcision by CO₂ laser 10600nm

Amjed Saeed Yaqob^{1,*}, Ali Fouad Rashid Al-Khazraji², Mardukh Sami Abd²

¹ Department of surgery, Baiji general hospital, salahdin, Iraq.

² Department of Surgery, Al-Yarmouk Teaching Hospital, Baghdad, Iraq.

* Email address of the Corresponding Author: aquarius77doc@gmail.com

Article history: Received: 27 Jul. 2024; Revised: 19 Oct. 2024; Accepted: 28 Oct. 2024; Published online: 15 Jun. 2025.

Abstract

Background: Male Circumcision is one of the most common surgical procedures performed in children. The indications for circumcision differ from country to country and might include both medical and religious ones. Several different surgical procedures for circumcision have been documented, with various results and complications.

Aim of study: to evaluate the safety, effectiveness of the use of CO₂ laser in circumcision and asses any possible post-operative complication(s).

Patients, Materials & Methods: A prospective study was done for 26 patients who were circumcised by using a CO₂ laser at 10600 nm from PLATIN, using continuous wave (CW) power that is set at 6 W with different exposure times during the period from June to August 2022. The patients had been operated under local anesthesia. In all cases, the parents had requested circumcision for religious reasons. The patients were followed up for 14 days, and reported having one or more complications postoperatively (if any).

Results: The patients were grouped into three age groups based on their age: the first group was 6–12 months old, the second group was 13–24 months old, and the final group was 25–36 months old, with a mean age of 14.7 ± 8.7 months. All patients had a single-session operation. Twenty patients (76.92%) had moderate pain, four patients (15.38%) had mild pain, and two patients (7.7%) had severe pain. Twenty patients (76.92%) had no bleeding; six patients (23.07%) had bleeding and were treated conservatively. Twenty-four patients (92.3%) had no infection, and only two patients (7.7%) developed a simple surgical site wound infection. Regarding the edema, four patients (15.4%) suffers of null degree: 12 patients (46.2%) of 1st degree: 8 patients (30.8%) of 2nd degree; and 2 patients (7.6%) of 3rd degree after four hours; while 17 patients (65.4%) suffers of null degree; 5 patients (19.2%) of 1st degree; 3 patients (11.5%) of 2nd degree; and 1 patient (3.9%) of 3rd degree after 7 days. 18 patients (69.2%) were completely satisfied. The operative time is less than that of conventional methods. All the patients were discharged after half an hour.

Conclusion: A CO₂ laser circumcision is a safe and effective procedure, and the device is very beneficial due to precise results with decreased pain, infection, bleeding, and edema following surgery.

Keywords: circumcision, CO₂ laser, 10600nm, gas laser, CO₂ laser circumcision.

1. Introduction

One of the most frequent surgical procedures done on children is male circumcision. The indications for circumcision differ from country to country and might include both medical and religious ones. [1–3].



Several different surgical procedures for circumcision have been documented, with various results and complications. [2, 3].

Indications of circumcision:

- 1- Religious reasons.
- 2- Cultural.
- 3- Public health reasons.
- 4- Medical reasons like phimosis, infection, paraphimosis, balanitis, posthitis, and localized condylomata acuminata [2-6].

This operation can reduce penile cancer rates, enhance penile topical cleanliness, lower the risk of HIV transmission [2, 5], and help reduce cervical cancer rates in female partners [6, 7]. Furthermore, it can improve sexual enjoyment and function for most men with foreskin problems, perhaps reducing coital injuries [8].

Other benefits of circumcision are:

- Reduce the risk of urinary tract infections in circumcised men.
- Reduces the risk of balanoposthitis, an inflammation of the glans and foreskin. [3-6].

Techniques of circumcision

1. The guillotine technique [9].
2. Shield and clamp [10].
3. Excision [11, 10, 12].
4. Electrocautery and Nd:YAG [12, 13, 14].

Complications of circumcision

- 1- Bleeding [11, 10].
- 2- Concealed penis [14].
- 3- Phimosis [14].
- 4- Skin Bridge [14].
- 5- Infection [14].
- 6- Urinary retention [15, 14].
- 7- Fistulas [14].
- 8- Necrosis [14].
- 9- Iatrogenic hypospadias and epispadias [14].

Study objectives: to evaluate the safety, effectiveness and precision of the use of CO₂ laser in circumcision and assess any possible post-operative complication(s)..

2. Patients and Methods

2.1 Patients

This is a prospective study. Twenty-six boys had been enrolled for circumcision in the private clinic in the Salahdin government / Baiji district between June 2022 and August 2022. The age of patients was from six months to 36 months, with the mean age 14.7 ± 8.7 months. They were divided into three groups: the first group, 16 patients aged 6–12 months, the second group, six patients aged 13–24 months, and the last group, four patients aged 25–36 months, as shown in Table 1. All the parents had requested circumcision for religious reasons, following a thorough description of the procedure and a discussion of its potential benefits and complications.

All patients had undergone circumcision under local anesthesia; they were circumcised using a CO₂ laser (PLATIN) using continuous wave (CW) power that is set at 6 W with different exposure times between 2 and 3 minutes.

All the cases were followed up for 14 days after the operations for any possible complication(s) if any.

Pre-operative preparation: Each parent was invited for the procedure after full explanation and discussion regarding the nature of the procedure, the possible advantages and disadvantages and complications



expected. At the conclusion of the discussion, each parents was asked to sign an (Informed consent) indicating their parent agreement.

A case sheet was prepared for the purpose of reviewing each patient's healthcare details and records. Name, Age, any prior surgeries (if any), past medical history of child and family and history of photosensitivity are all considered as part of the patient's history. Operative time were recorded, fix a date of the follow up. All patients were examined one day before the operation, also lab investigations were done, including blood tests for hemoglobin level and viral screening (hepatitis B&C and HIV).

We administered prophylactic antibiotics (amoxicillin"250mg"/ clavulanate "125 mg") 60 minutes before the procedure.

Table 1: the number of patients according to their age

Groups	Age (month)	Number of patients
First	6-12	16
Second	13-24	6
Third	25-36	4
Total	-	26

D: seven days after a treatment.

Case Sheet

Patient name:

Age:

Address:

Record number:

Date of admission:

Surgeon's name:

Assistant's name:

Diagnosis:

Type of surgical procedure:

Surgeon signature:

Past medical history:

Past surgical history:

Systemic review:

History of photosensitivity:

Consent of parents and signature:

Next visit: Next visit:

Next visit: Next visit:

2.1.1 Inclusion criteria:

This study includes all patients who have their parents asked that's their children to have been circumcised.

2.1.2 Exclusion criteria:

Any child who had severe congenital heart disease, any congenital anomaly of genitalia (None was excluded).

2.2 The Material:

The medical laser system and accessories:



2.2.1. Laser system Specification:

The laser system used in this study was a class IV Medical laser system, 10600nm CO₂ laser, which emits laser at a wavelength in the far infrared spectrum. The surgeon configured the laser aperture power output to vary between 0.5 and 70 Watts (max.). The brand "PLATIN" high power medical CO₂ laser system with gas type as working material (figure 2-1). The CO₂ laser for this unit is powered as a continuous or pulsed wave mode and the wavelength is 10600 nm. The laser beam can be coupled efficiently into the articulated arm. The aiming beam is a visible diode 635-660nm (red beam) with a power of < 5mW (class I B diode laser) at laser aperture. Table2 shows Technical Specifications of PLATIN CO₂ laser machine. Figure 1 shows PLATIN CO₂ device.

Table 2: Technical Specifications of PLATIN CO₂ laser device

Technical Specifications	
Laser Type	CO ₂
Model	F12
Wavelength	10600 nm
Maximum Power	70W
Operation Mode	CW and Pulse
Transmission System	Seven articulated arms
Pilot Beam	Red Diode Laser of 635nm, Power < 5 mW
Control Mode	True Color Touch Screen
Voltage/Current Rating	220 VAC, 50/60 Hz
Weight	58 Kg
Power	6 W
Exposure time	(2 – 3) minute



Figure 1: PLATIN CO₂ device.

2.2.2 Equipment

The following items are arranged on a tray with drapes as shown in Figure 2-2. Surgical mosquito, gauze, gloves, syringes (insulin syringe), Winkelman circumcision clamp, lidocaine injection 2 %, EMLA ointment, povidone iodine solution 10 %.



Figure 2: Equipment.

Figure 3 shows the protective goggles used by surgeon and staff



Figure 3: protective goggles used by surgeon and staff.

Figure 4 shows the protective goggles used by patients



Figure 4: protective goggles use by patients.

2.3 Procedure:

EMLA was applied for 30 minutes, and then cleaned. An antiseptic 10% povidone iodine solution applied. For local anesthesia, lidocaine 2% was used (administered at a dose of 0.1 mg/kg and infiltrated subcutaneously as a dorsal penile nerve block), the adhesions on the coronal sulcus were separated, the preputial skin was pulled up, and a straight hemostat or mosquito forceps was applied loosely to the preputium. The power was set at 6 W of continuous wave mode C/W, and the exposure time was 2–3 minutes. A surgical handpiece of CO₂ (10600 nm) was used. Photographs were taken of each patient with a digital camera before and immediately after completing the procedure. Postoperative complication(s): Wound swelling, bleeding, surgical site infection, and pain were evaluated four hours, 24 hours, and seven days following surgery. Surgical dressings had been removed 24 hours following the circumcision, either by relatives at home or by doctors in the hospital.

2.4 Post-operative treatments:

Following the circumcision, an antibiotic ointment was applied three times a day to the wounds, and the five days of therapy that included amoxicillin "250 mg" and clavulanate "125 mg" three times a day, as well as Ibuprofen 8 mg/kg to be used only if needed twice or three times a day.

3. Results and discussion

This is a prospective study. Twenty-six boys had been enrolled for circumcision using a CO₂ laser (PLATIN) using continuous wave (CW) power that is set at 6 W for all cases; the operative time was 11±3 minutes. Depending on laser exposure time as shown in Table 3, the operative time for the first group was 120 sec, for the second group was 180 sec, and for the third group was 240 sec. Table 3 shows the laser power and exposure according to the patients' age group.

Table 3: Power and laser exposure time according to the patients' age group.

Groups	Power (watt)	Laser exposure time(sec.)
First	6	120
Second	6	180
Third	6	240

The patients were surveyed for pain, bleeding, surgical site infection, edema, and satisfaction (parents). Regarding the pain it is divided into mild, moderate and severe, as the parents describes the pain of their children and compared with Faces pain rating scales in which there is 6 faces emoji (first 2 represents the mild pain, the second 2 represents the moderate pain, and the last 2 represents the severe pain). In this study after one hour four patients that represent (15.38%) had mild pain, twenty patients that represent (76.92%) had moderate pain, and two patients that represent (7.7%) had severe pain. As shown in Table 4.

Table 4: Degree of pain post-operatively.

Degree of pain	Number of patients	Percent %
Mild	4	15.38
Moderate	20	76.92
Severe	2	7.7
Total	26	100



Yet, Pain scores after 4 hours, 24 hours, and 7 days were much lower than this, as Table 5 shows. 14 cases (53.8%) suffered from pain at 4 hours, 10 cases (38.5%) developed pain after 24 hours, and two cases (7.7%) developed pain after 7 days.

Table 5: Details of pain at 4, 24 hours, and at 7 days.

Period after surgery	Number of cases	Percent %
At 4 hours	14	53.8
At 24 hours	10	38.5
At 7 days	2	7.7

In this study, bleeding is divided into two degrees: first degree, minimal bleeding without further treatment. Second degree: bleeding that requires wound compression or wound dressing. The bleeding is surveyed after 4 hours and 7 hours.

In this study, twenty patients (76.92%) had no bleeding; six patients (23.07%) had bleeding of the first degree and were treated conservatively. First-degree bleeding occurred at the 4-hour follow-up; there was no bleeding (first degree) at the 7-hour follow-up, and no second-degree bleeding was recorded at all, as shown in Table 6.

Table 6: wound bleeding at 4 hours and 7 hours.

Degree of bleeding	At 4 hours	At 7 hours
No bleeding	20 (76.92%)	0 (0%)
First degree	6 (23.08 %)	0 (0%)
Second degree	0 (0%)	0 (0%)
Total	26 (100%)	0 (0%)

In this study of surgical site infection, Twenty-four patients (92.3%) had no infection, and only two patients (7.7%) developed a simple surgical site wound infection treated by prolonged post-operative treatment for another five days, as shown in Table 7.

Table 7: Surgical wound infection.

surgical site wound infection	Number of cases	Percent
Infected	2	7.7%
Non-infected	24	92.3%
Total	26	100%

Regarding edema and swelling, it is divided into four degrees as follows:

Null degree: no swelling

First degree: minimal swelling

Second degree: swelling less than half the circumference

Third degree: swelling of more than half the circumference

In this study, edema was followed up after 4 hours and after 7 days post-operatively. Table 8 shows the degree of swelling after 4 hours and 7 days after surgery. The percentage of swelling after 4 hours of null

degree, 1st degree, 2nd degree, and 3rd degree was 15.4%, 46.2%, 30.8%, and 7.6%, respectively; and after 7 days, it was 65.4%, 19.2%, 11.5%, and 3.9%, respectively. Regarding the satisfaction, 18 patients (69.2%) were completely satisfied, while those who were not so satisfied, 8 patients (30.8%), were so because of severe pain, infection, edema, and bleeding, as shown in Table 9. Figures 5, 6, and 7 show circumcision after operation, three days, and 10 days, respectively.

Table 8: wound swelling at 4 hours and 7 days after surgery.

Degree of swelling	After 4 hours	After 7 days
	No. of pat., percent %	No. of pat., percent %
Null degree	4, (15.4%)	17, (65.4%)
1 st degree	12, (46.2%)	5, (19.2%)
2 nd degree	8, (30.8%)	3, (11.5%)
3 rd degree	2, (7.6%)	1, (3.9%)
Total	26, (100.0%)	26, (100.0%)

Table 9: Patients' satisfaction.

satisfaction	pain	Infection	edema	Bleeding	No. of patient	percent
satisfied	/	/	/	/	18	69.2%
Not satisfied	2, 7.7%	2, 7.7%	1, 3.9% (4 th degree after 7 days)	3, 11.5% (half cases of bleeding)	8	30.8%
Total	2, 7.7%	2, 7.7%	1, 3.9%	3, 11.5%	26	100%



Figure 5: circumcision directly after the operation.



Figure 6: circumcision directly after three days.



Figure 7: circumcision directly after ten days.

From the result of this study, the CO₂ laser with power 6 W and exposure time ranged (2 – 3) minutes is more precise than other methods and may be due to that CO₂ laser act as a cutting and coagulation action. So, less bleeding had occurred (due to thermal effect). How et al. evaluated the cost of operating time for CO₂ lasers with the traditional approach. The average operating time for the traditional approach was 20 (range 16-21) minutes, whereas the CO₂ laser took 15 (range 13-17) minutes. In this study, the period of operation using the CO₂ laser was 12 minutes, which is consistent with the How et al. study [16]. One of the benefits of CO₂ laser surgery is that it significantly reduces postoperative pain, which improves patient comfort. This study found that individuals treated with the CO₂ laser experienced decreased postoperative pain. This result agrees with the study by Ronchi et al [17]. The CO₂ laser has a coagulation function and was previously reported to reduce postoperative bleeding after circumcision [18]. In this study, six cases suffered from bleeding at 4 hours (23%). These results were in agreement with Gorgulu et al, which showed that the use of a CO₂ laser shortened the operating time and reduced complications related to bleeding, in comparison with the conventional guillotine method [18]. In this study, more cases of edema were found. In the Ronchi et al. study, edema was seen in 7.9% of the patients treated with lasers. The finding is most likely owing to significant thermal injury to the preputial tissues generated by the electrocautery employed for hemostasis in the conventional group. The CO₂ laser has negligible thermal transmission to adjacent

tissue, whereas electrosurgery produces far more mean depths of injury than does the CO₂ laser. As a result, edema in the laser group is lower than with other methods, such as electro-surgery [17].

4. Conclusions

1. The use of a CO₂ laser in circumcision is a very effective and safe device due to its precise results.
2. The CO₂ laser therapy was linked to decreased pain, infection, bleeding, and edema following surgery.
3. The operative time is less than that of conventional methods.

References

- [1] World Health Organization (WHO) (2015). "Neonatal and child male circumcision": http://www.who.int/hiv/pub/malecircumcision/neonatal_child_MC_UNAIDS.pdf
- [2] Asgari SA et al (2012) . "Pediatric suture less circumcision without using skin closure adhesives: a new technique for poor setting". *Urol J* ;9(1):423–8
- [3] Ong CCP, Jacobsen AS, Joseph VT(2002). "Comparing wound closure using tissue glue versus subcuticular suture for pediatric surgical incisions: a prospective, randomized trial". *Pediatr Surg Int*;18:553.
- [4] Dunsmuir WD, Gordon EM. :The history of circumcision". *BJU Int*. 1999;83:1-12.
- [5] Williams N, Kapila L(1993). :Complications of circumcision". *Br J Surg*.;80:1231-6.
- [6] Bhan A (2009). "Advocating the benefits of male circumcision": are doctors well informed? *169 Indian J Med Ethics*.
- [7] Gray RH, Kigozi G, Serwadda D, Makumbi F, Watya S, Nalugoda F, et al(2007). "Male circumcision for HIV prevention in men in Rakai, Uganda: a randomised trial". *Lancet*. 369:657–666.
- [8] Bitega JP, Ngeruka ML, Hategekimana T, Asiimwe A, Binagwaho A(2011). "Safety and efficacy of the PrePex device for rapid scale-up of male circumcision for HIV prevention in resource-limited settings". *J Acquir Immune Defic Syndr*.58: e127–e134.
- [9] S Cheng YZ, Su X, Fang H, Hu J, Wu K, Su R, Ma J(2011). "A clinical comparative study of Chinese Shang Ring circumcision versus conventional circumcision".
- [10] Weiss H, Polonsky J, Bailey R, Hankins C, Halperin D, Schmid G(2007). "Male circumcision: Global trends and determinants of prevalence, safety and acceptability". World Health Organization and the Joint United Nations Programme on HIV/AIDS (UNAIDS). Available from: http://data.unaids.org/pub/Report/2007/jc1360_male_circumcision_en.pdf. [Last accessed on 2012 Dec 01].
- [11] BBC (2009a) "Circumcision of Boys". <http://tinyurl.com/5t2c7se> (Last accessed: April 17 2012.)
- [12] Massry, S.G. (2011). "History of circumcision: a religious obligation or a medical necessity". *J. Nephrol*. 24, S100–S102.
- [13] BBC (2009b) "Jewish Baby Rites". www.bbc.co.uk/religion/religions/judaism/rites/birth.shtml (Last accessed: April 17 2012.)
- [14] Tucker SC, Cerqueiro J, Sterne GD, Bracka "A(2001). Circumcision: A refined technique and 5 year review". *Ann R Coll Surg Engl* 83:121-5.
- [15] Blank S, Brady M, Buerk E, Carlo W, Diekema D, Freedman A, et al(2012). American Academy of Pediatrics, Task force on Circumcision: "Male circumcision". *Pediatrics*130:e756-85.
- [16] How AC, Ong CC, Jacobsen A, Joseph VT(2003). Carbon dioxide laser circumcisions for children. *Pediatr Surg Int*;19(1–2):11–3.
- [17] Ronchi et al (2020). "CO₂ Laser Circumcision versus Conventional Surgical Technique", *Dove Press journal: Research and Reports in Urology*.;12 255–260.
- [18] Gargollo PC, Kozakewich HP, Bauer SB, et al(. 2005). Balanitis xerotica obliterans in boys. *J Urol*. 2005;174:1409–1412.



الختان باستخدام الليزر ثنائي اوكسيد الكربون 10600 نانومتر

امجد سعيد يعقوب*¹, علي فؤاد رشيد², مردوخ سامي عبد²

¹ قسم الجراحة، مستشفى بيجي العام، صلاح الدين، العراق

² قسم الجراحة، مستشفى اليرموك التعليمي، بغداد، العراق

البريد الإلكتروني للباحث*: aquarius77doc@gmail.com

الخلاصة

الخلفية: ختان الذكور هو أحد أكثر الإجراءات الجراحية شيوعاً التي يتم إجراؤها للأطفال. تختلف دواعي الختان من بلد إلى آخر وقد تشمل دواعي طبية ودينية. تم اعتماد العديد من العمليات الجراحية المختلفة للختان، والتي تختلف بالنتائج ومضاعفات.

هدف الدراسة: تقييم سلامة وفعالية استخدام ليزر ثاني أكسيد الكربون في الختان وتقييم أي مضاعفات محتملة بعد الجراحة.

المرضى والمواد والطريقة: هذه دراسة مستقبلية على 26 مريضاً تم ختانهم باستخدام جهاز ليزر ثاني أكسيد الكربون ذو الطول الموجي 10600 نانومتر من شركة PLATIN، باستخدام اعدادات طاقة موجة مستمرة (CW) التي تم ضبطها على قدرة 6 وات مع أوقات مختلفة للتعرض لليزر خلال الفترة من شهر حزيران إلى شهر آب من سنة 2022. خضع المرضى للعملية الجراحية تحت تأثير التخدير الموضعي. وفي كل الحالات كان الأهل قد طلبوا الختان لأسباب دينية. تمت متابعة المرضى لمدة 14 يوماً، واستعلامهم، وتسجيل الإبلاغ عن وجود مضاعفات واحدة أو أكثر بعد العملية الجراحية (إن وجدت).

النتائج: وفقاً لأعمار المرضى، تم تقسيمهم إلى ثلاث مجموعات: المجموعة الأولى كانت تتراوح أعمارها بين 6 و12 شهراً، والمجموعة الثانية كانت تتراوح أعمارها بين 13 و24 شهراً، والمجموعة الأخيرة كانت تتراوح أعمارها بين 25 و36 شهراً، بمتوسط عمر 14.7 ± 8.7 شهراً. خضع جميع المرضى لعملية جراحية في جلسة واحدة. عانى عشرون مريضاً (76.92%) من ألم متوسط، وأربعة مرضى (15.38%) من ألم بسيط، وعانى مريضان (7.7%) من ألم شديد. لم يكن لدى عشرين مريضاً (76.93%) أي نزيف؛ في حين كان لدى ستة مرضى (23.07%) نزيف وقد تم علاجهم بشكل تحفظي. لم يكن لدى أربعة وعشرين مريضاً (92.3%) أي عدوى في مكان العملية، وأصيب مريضان فقط (7.7%) بعدوى جرح بسيطة في مكان العملية. فيما يتعلق بالوذمة، لم يعاني أربعة مرضى (15.4%) من أي وذمة، عانى 12 مريضاً (46.2%) من وذمة من الدرجة الأولى. 8 مرضى (30.8%) من الدرجة الثانية؛ و مريضان (7.6%) من الدرجة الثالثة بعد أربع ساعات من العملية؛ بينما لم يعاني 17 مريضاً (65.4%) من أي وذمة؛ وعانى 5 مرضى (19.2%) من وذمة من الدرجة الأولى؛ و 3 مرضى (11.5%) من الدرجة الثانية؛ ومريض واحد (3.9%) من الدرجة الثالثة بعد 7 أيام. وكان 18 مريضاً (69.2%) راضين تماماً.

كان وقت العملية أقل من الطرق التقليدية. وخرج جميع المرضى الى المنزل بعد نصف ساعة من الانتهاء من العملية.

الاستنتاجات: الختان بالليزر ثاني اوكسيد الكربون تعتبر عملية آمنة وفعالة وجهاز الليزر ثاني اوكسيد الكربون مفيد جداً بسبب النتائج الدقيقة مع انخفاض الألم والعدوى والنزيف والوذمة بعد الجراحة.





The Efficacy of Diode Laser (810-980 nm) as an Adjunct to Non-Surgical Treatment of Periodontitis on *Porphyromonas gingivalis*: A Randomized Split-Mouth Study

Fatima K. Salman*, Layla M. H. AL-ameri

Institute of Laser for Postgraduate Studies, University of Baghdad, Baghdad, Iraq

* Email address of the Corresponding Author: fatima.kadhumi2022m@ilps.uobaghdad.edu.iq

Article history: Received: 5 Nov. 2024; Revised: 24 Dec. 2024; Accepted: 8 Jan. 2025; Published online: 15 Jun. 2025.

Abstract: Periodontitis is a chronic, complex inflammatory condition linked to dysbiotic plaque biofilms and marked by the progressive deterioration of the tooth-supporting structures. *Porphyromonas gingivalis*, a critical periodontal infection, is known to significantly contribute to the onset and advancement of periodontal illnesses by inducing a dysbiotic alteration in the overall, particularly sub-gingival, gram-positive and gram-negative periodontal microbiota. Conventional therapies, including scaling and root planing (SRP), seek to eliminate plaque and tartar from the surfaces of teeth and subgingival areas. Nonetheless, these treatments are accompanied by certain limitations. The advent of diode lasers has demonstrated potential as an adjuvant therapy, possibly improving the results of traditional treatments.

Aim of the study: This study aimed to compare the effectiveness of the diode laser as an adjunctive treatment modality for nonsurgical treatment versus SRP only on the colony-forming unit (CFU) of the *Porphyromonas gingivalis* in patients with periodontitis.

Material and methods: This research was structured as a singular, randomized controlled, split-mouth clinical experiment. Twenty-five persons (11 females and 14 men aged 20 to 56 years) diagnosed with periodontitis, participated in this research. Following primary periodontal treatment, which included dental hygiene guidelines and scaling procedures, each patient underwent two separate treatments on opposing sides of the mouth. The left side was designated as the test group, while the right side was allocated to the control group. Randomization was accomplished by a coin toss to guarantee impartial allocation. In the test group (left side) patients underwent scaling and root planing (SRP) in conjunction with diode laser therapy; in the opposing control group (right side) they received scaling and root planing (SRP) treatment exclusively. The laser was set at a 1.5 W, continuous wave, 400 μm tip, contact, and sweeping technique. 50 Subgingival plaque samples were taken after recording periodontal parameters, plaque index (PI), bleeding on probing (BOP), periodontal pocket depth (PPD), and clinical attachment loss (CAL) at baseline before, immediately after 3 days, 1 week, and 12 weeks post-treatment. Microbiological assessments focused on the colony-forming unit of *Porphyromonas gingivalis* (P.G). Colony-forming units (CFU) were enumerated for each group for 48-72 hours on a suitable culture medium following serial dilution. Clinically isolated bacteria were confirmed by using the biochemical test, microscopic examination, viteck II system, and finally by PCR technique (16S rRNA).

Result: Colony-forming units (CFU) reduced with both forms of treatment and did not return to the initial concentrations three months after therapy. The SRP plus the diode laser group exhibited significantly higher reductions in bacterial levels of *P. gingivalis* at 3 days, 1 week, and 3 months after treatment in comparison to SRP treatments alone.



Conclusion: A notable disparity in the colony-forming units of p.g was detected between the control and test groups. The dual wavelength diode laser can be utilized as an adjunct to non-surgical treatment for those with periodontitis

Keywords: periodontitis, diode laser, SRP, Colony forming unit, Porphyromonas gingivalis.

1. Introduction

Microbial plaques have been established as the principal etiological factor of inflammatory periodontal disease[1-3]. The subgingival oral biofilm contains various periodontopathogenic bacteria, including Porphyromonas gingivalis, Aggregatibacter actinomycetemcomitans, Treponema denticola, and Prevotella intermedia [4]. P. gingivalis, an anaerobic Gram-negative member of the Cytophaga-Bacteroidetes family, belongs to a “red complex” of species associated with chronic periodontal infections [5, 6]. These bacteria secrete toxins that compromise the integrity of periodontal soft and hard tissues and promote the production of deleterious inflammatory cytokines that contribute to the prognosis of periodontal illnesses [7]. The primary objective of periodontal therapy has been to eradicate all bacterial deposits from the tooth surface[1, 8]. Mechanical debridement refers to a professional scaling and root planing (SRP) procedure. that is designed to remove supra and subgingival biofilms and calculus from colonized root surfaces in order to halt and regulate inflammatory processes[9-13]. SRP is unable to eradicate pathogenic bacteria in inaccessible periodontal areas, including deep periodontal pockets, root concavities, and furcation involvement.[14-16] Therefore, it was found that local and systemic antibiotics were essential for the removal of pathogenic microorganisms from tissues[17].

On the other hand, the development of bacterial resistance and adverse effects may result from antimicrobial treatment[1, 18]. Researchers suggested the utilization of lasers in periodontal therapy as a solution to these inconveniences.[19] In periodontal therapy, lasers are beneficial for control of bacteremia, reduction of bacteria, and improvement of periodontal healing in both humans and animals without harming the neighbouring bone and pulp tissues [20]. Lasers were introduced to periodontics as a monotherapy alternative to traditional nonsurgical periodontal therapy, or as an adjunct to traditional scaling and root planing [14, 15]. A pilot study demonstrated that diode laser with an (805)nm wavelength achieved superior bacterial elimination in periodontal pockets compared to scaling and root planing (SRP) alone [21]. Moritz et al. showed that diode laser, when used alongside SRP, enhanced the repair of periodontal pockets through its bactericidal properties. Reports indicate that DL + SRP resulted in a substantial decrease in total bacterial load, specifically P. gingivalis and T. denticola, at six months post-treatment compared to SRP alone[22]. diode laser incorporates a solid-state semiconductor composed of aluminum, gallium, arsenide, and occasionally indium, enabling it to generate laser wavelengths spanning from 810 nm to 980 nm .With its antibacterial characteristics[23], the diode laser system possesses photothermal properties that facilitate the simultaneous removal of granulation tissue and inflamed periodontal tissue (sulcular debridement). This process involves coagulation at a temperature of 60°C, leading to protein denaturation and a decrease in proinflammatory cytokines [24-26]

The aim of this study was to compare the effectiveness of the diode laser as an adjunctive treatment modality for nonsurgical treatment versus SRP alone on bacterial count of the pathogen Porphyromonas gingivalis in patient with periodontitis.

2. Materials and methods

This study comprised 25 adult patients with periodontitis, aged between 20 and 56 years, who attended the Specialist Centre of Dentistry's periodontology division and dental clinics in Al-Muthanna, Iraq, from January 2024 to September 2024. Approval for this work was secured by the Ethical and Scientific Committee of Baghdad University, Institute of Laser for Postgraduate Studies (approval number 464 in 10-10-2023). Written informed consent was obtained from all of the participants.

The inclusion criteria included Patients of both sexes who were systemically healthy, with Periodontitis (interdental clinical attachment loss [CAL] of ≥ 2 nonadjacent teeth, or buccal or oral CAL of ≥ 3 mm with



pocketing of ≥ 4 mm observable at ≥ 2 nonadjacent teeth) [27, 28]. The additional eligibility criteria included patients who had not received any antibiotic therapy within the previous three months, each Patient should possess a minimum of one pocket from the same tooth on every side, and these teeth should exhibit a periodontal clinical attachment loss and pocket depth ≥ 5 mm.

The exclusion criteria encompassed pregnant or lactating patients and persons with chronic diseases, immunocompromised patients, and those who used antimicrobial mouthwash or had a history of smoking.

3. Calculation of Sample size

With a pooled standard deviation of 1.2 units, the study requires a sample size of 22 per group (yielding a total of 44, assuming equal group sizes) to achieve a power of 80% and a significance level of 5% (two-sided) for detecting a true mean difference of -1.027 (i.e., 1.2 - 2.227) BC between the test and control groups based on (Nammour et al., 2021) study [9]. The sample size was increased to 25 for each group to account for the loss of follow-up.

4. Clinical examinations and plaque sampling

Periodontitis Patients received clinical diagnoses, underwent comprehensive oral examinations, and periodontal samples were obtained. Microbial samples were obtained randomly from pockets in the periodontal tissue of both the control and test groups. The two deepest interproximal periodontal sites with probing depths (PD ≥ 5 mm) were selected from the same tooth on each side for subgingival plaque sampling. Subsequently, samples were aggregated for either the group treated just with SRP or the group treated with both SRP and a diode laser. Designated sites were sampled at pretreatment, 3 days post-treatment, 1 week post-treatment, and 3 months post-treatment. The sampling area was isolated using cotton rolls, meticulously scaled supragingivally with a sterile scaler, and cleansed with sterile cotton pellets to avert contamination of the samples by saliva or supragingival plaque [29]. then, the samples were taken with fine sterile Gracey curette[30]. The curette was introduced as deeply as feasible into the pocket without exerting pressure on the tooth surface to prevent the displacement of subgingival plaque into the depths of the pocket. Upon encountering tissue resistance in the apical region of the pocket, subgingival sampling was executed with a singular vertical stroke [31] Figure 1. The bacterial sample was suspended in 1 ml of *P. gingivalis* broth media within a 5 ml screw-capped bottle by vigorously agitating the instrument's tip in the solution. It was then incubated for 24 hours until growth was indicated by turbidity in the broth. Subsequently, it was taken to a lab for the cultivation of bacteria and molecular analysis. The microbiological study included the identification of *Porphyromonas gingivalis* (Pg).



Figure.1: Curette sampling

5. Treatment protocol



Initial appointment (0 days): Comprehensive medical and dental histories were obtained from each participant, and panoramic Radiographs were performed on all participants after their study enrollment. Clinical periodontal measures, including full mouth plaque index (PI)[32], bleeding on probing (BOP)[33], probing pocket depth (PPD)[34], and clinical attachment level (CAL)[34], were assessed utilizing a William periodontal probe. Supragingival scaling was conducted by the same examiner for all patients using ultrasonic equipment (Woodpecker UDS-K, India). All patients received dental hygiene and motivational teaching, reiterated at each appointment.

Baseline appointment (seven days post-initial appointment): assessment of clinical periodontal parameters (Plaque Index, Bleeding on Probing, Pocket Probing Depth, and Clinical Attachment Level), After evaluating periodontal parameters, collection of plaque sample were done.

Afterward, each participant was assigned to one of two treatments: the test group(left side) underwent SRP combined with diode laser therapy. The contralateral control group (right side) received only SRP therapy .Both groups underwent the identical scaling and root planing (SRP) operation for the periodontal pockets as a component of the conventional treatment protocol. Local anesthetic was utilized to provide treatment to all patients. In the designated side for diode laser plus SRP, diode laser treatment was conducted in a single session following instrumentation with an ultrasonic scaler and gracy curette, utilizing a continuous contact-focused mode (810-980 nm) diode laser (Quicklase, Dentalase, U.K.) operating at 1.5W power and employing a 400- μ m flexible glass fiber optic. The insertion of the laser fiber optics required a decrease of 1 mm from the documented pocket depths. The 1 mm reduction improved the penetration of the laser's energy at its apex and the irradiation of damaged tissue in the periodontal pocket.

Nevertheless, it did not cause heat injury to healthy tissues[35]. The laser started working after the fibre reached the calibrated depth and the tip was engaged. The fibre was then placed in gentle contact aligned with the root's area to excise the infected soft tissue lining the compartment. The instrument was thereafter advanced in an apico-coronal direction with a sweeping motion at a constant velocity of 2.5 mm/sec, commencing at the base of the pocket and progressing upward while ensuring contact with the soft tissue within the pocket. The technique was reiterated until the full circumference of the root was irradiated, resulting in renewed bleeding. Each location underwent an irradiation duration of approximately 10 seconds.

Furthermore, this enabled the removal of delicate tissue during laser-assisted curettage. To prevent thermal injury to the root surface, we thoroughly cleaned the root surface with a saline solution after the laser irradiation was complete[36]. The fiber tip was cleansed with moist gauze between treatments of each tooth to avoid the accumulation of debris, and ethanol was applied to the wiping surface for 5 seconds. The tip's termination was tested and cut before and after each subsequent treatment to ensure optimal beam emission.

The contralateral side was treated exclusively with SRP only. The periodontal gracy curettes and an ultrasonic piezoelectric scaler (Woodpecker, UDS-K, India) were employed to conduct the SRP. The entire pocket cementum was treated, and the pockets were manually root-planed from the apical to the coronal direction. This was done with great care. The instrumentation was accomplished until the operator felt the root surfaces were adequately scaled and planned. Conventional periodontal therapy aims to eradicate all local allergens, including calculus, plaque, debris, and toxins. A single practitioner administered the SRP treatments to each patient during a single appointment[35]. The patient, the surgeon, and the dental assistant were required to wear safety glasses during the treatments to prevent the potential ocular harm that could result from laser irradiation. Upon completion of both treatments, patients were instructed to abstain from dental brushing on the day of the therapy. An oral hygiene protocol was subsequently implemented. X-rays were obtained at the baseline and the end of the three-month study period.

Third appointment(Follow-up) immediately 3 days after baseline appointment: collection of plaque sample.
Fourth appointment (follow-up) one week after baseline appointment: collection of plaque sample.



Five appointments (follow-up) 12 weeks after baseline appointment: Assessment of clinical periodontal parameters (Plaque Index, Bleeding on Probing, Probing Pocket Depth, and Clinical Attachment Level), collection of plaque sample.

6. Cultivation of *Porphyromonas gingivalis*

The dental tube samples were thereafter incubated vertically at 37°C for 48 hours, after which a 100 µl aliquot from each sample was streaked over *P. gingivalis* agar (P.GING), an enriched selective medium for the isolation and presumptive identification of *P. gingivalis*[37, 38]. The (P.GING) medium is locally prepared. The formulation consists of Columbia Agar Base, supplemented with 5% sheep blood, 5 µg/ml haemin, and 1 µg/ml vitamin K1 (Himedia), which function as selective agents for the isolation of the fastidious, strictly anaerobic *P. gingivalis* from other periodontopathogens. The chosen media plates were incubated in a hermetically sealed anaerobic jar at 37°C using a gas pack (Oxoid) for a duration of 7 to 14 days [37].

7. Identification and colony counting of *porphyromonas gingivalis*

The preliminary identification of *P. gingivalis* was conducted using standard procedures, encompassing biochemical testing and microscopic examination, as shown in Figure 2. [39], and Vitek II system (bioMérieux, France) [40]. In contrast, the definitive identification was conducted with the polymerase chain reaction (PCR) method[41]. Bacterial enumeration was performed using CFU/ml. A portion of the bacterial suspension (100 microlitres) was disseminated over P.GING agar and grown for 48-72 hours following serial dilutions of 10^1 , 10^2 , 10^3 , and 10^4 in peptone water, and the number of colonies that have between 30 and 300 colonies is counted by using the following equation: Number of CFU/ml = number of CFU x dilution factor[42].

The colonies of *porphyry monas gingivalis* on the P.GING agar were in Black and surrounded by a transparent halo, as shown in Figure 3.

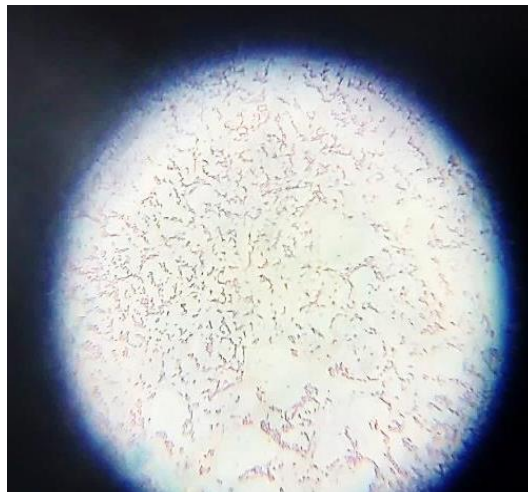


Figure 2: Microscopic examination of *porphyry monas gingivalis* after performing the dying process with gram stain.

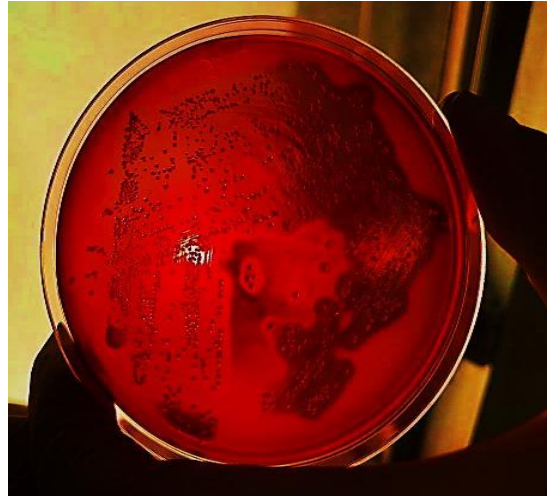


Figure 3: Colonies of *porphyromonas gingivalis* Black colony grown on P.GING at 37°C for 48-72 hrs.

8. Identification of *p.gingivalis* using the Vitek II system

This system was used according to the manufacturing company (bioMérieux, France) by inoculating bacteria on the agar plate. Incubation at (37 °C /48-72 hours) shown in Table (1).

Table.1: Identification of *p.gingivalis* using the Vitek II system

Bionumber: 7537739485441		Selected Organism: Porphyromonas gingivalis				
Organism Quantity:						
Comments:						
Identification Information	Card:	ANC	Lot Number:	2442240403	Expires:	Jan 14, 2025 12:00 AST
	Status:	Final	Analysis Time:	8.10 hours	Completed:	July 20, 2024 16:24 AST
Organism Origin	VITEK 2					
Selected Organism	99% Probability Porphyromonas gingivalis					
	Bionumber: 7537739485441		Confidence: excellent identification			
Analysis Organisms and Tests to Separate:						
Analysis Messages:						
Contraindicating Typical Biopattern(s)						

Biochemical Details																	
4	dGAL	+	5	LeuA	+	6	ELLM	(+)	7	PheA	+	8	ProA	-	10	PyrA	-
11	dCEL	-	13	TyrA	+	15	APPA	-	18	dGLU	+	20	dMNE	+	22	dMAL	+
28	SAC	+	30	ARB	-	33	NAG	+	34	BGLUi	+	36	URE	-	37	BGURi	-
39	BGALi	-	41	AARA	-	42	AGALi	-	43	BMAN	-	44	ARG	+	45	PVATE	-
51	MTE	+	53	ESC	+	54	BdFUC	-	55	BNAGi	-	56	AMANi	-	57	AIFUC	-
59	PHOS	-	60	IARA	-	61	dRIB2	+	62	OPS	-	63	AARAF	-	64	dXYL	+
	GRAM	-		MORPH	-		AERO	-									

9. Molecular Detection of *P. gingivalis*

9.1 DNA extraction

The Genomic DNA Mini Kit (Geneaid, Korea) was employed to isolate DNA from periodontal samples in accordance with the manufacturer's instructions. Immediately after extraction, the DNA samples were stored at -20°C for molecular detection of *P. gingivalis*; for the molecular identification of *P. gingivalis*, a monoplex PCR targeting the 16S rRNA gene amplification was implemented in accordance with [43] using the amplification primers listed in Table 2 and the cycling parameters listed in Table 3.

Table.2: The primer set was employed for the molecular detection of *P. gingivalis*.

	Prime		Primer sequence 5' - - 3'	PCR product
Porphyromonas gingivalis	16S ribosomal RNA gene	F R	ACGGGAATAACGGGCGATAC TGTAAGGGCCGTGCTGATT	766 bp

9.2 Amplification Reaction Protocols

Table .3: Cycling parameters for monoplex PCR of 16S rRNA gene amplification

No.	Phase	Tm (°C)	Time	No. of cycle
1-	Initial Denaturation	95°C	3min	1 cycle
2-	Denaturation-2	95°C	45sec	35cycle
3-	Annealing	60°C	45sec	
4-	Extension-1	72°C	45sec	
5-	Extension-2	72°C	7Min	1 cycle

9.2 Agarose gel electrophoresis

The PCR products were subjected to agarose gel electrophoresis (1.5%) using the following lanes: M (M: 100bp ladder), Figure 4.

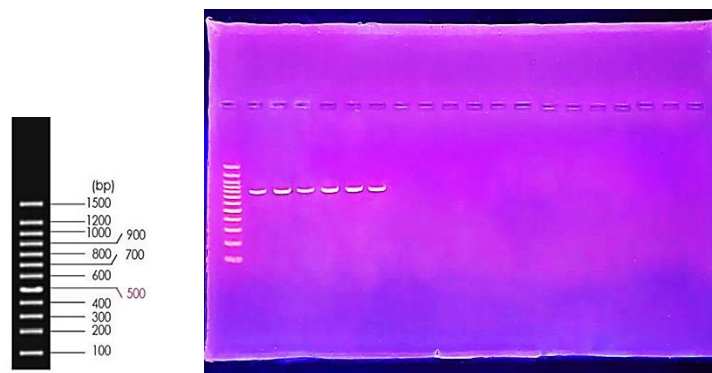


Figure .4: Gene electrophoresis using agarose gels. After staining with red stain, bands were visualized under ultraviolet light after being fractionated by electrophoresis on a 1% agarose gel. Lane: M (M: 100-1500bp ladder).

10. Statistical analysis

Depending on whether the distribution was normal or skewed, the continuous variables were represented as means and standard deviations. Frequency and percentages were employed to represent categorical variables. In order to evaluate the mean differences, the Welch's t-test was implemented for variables that were normally distributed. The differences between serial measurements of periodontal indices were calculated based on repeated measure ANOVA test and post-hoc analysis with holm adjustments. A P-value less than 0.05 was considered statistically significant. The sample size was calculated using G-power software. R software packages (dplyr, gt_summery, and ggplot) were used for data processing, visualization, and statistical analysis ("R version 4.2.2, R Foundation for Statistical Computing, Vienna, Austria").

11. Result

The patient had an average age of 35.3 years and a standard deviation of 10.7 years. This indicates a median age of 32 within 20 to 56 years. The sex distribution revealed that 56.0% of the participants were male (14 individuals), while 44.0% were female (11 individuals), as was detailed in Table(4).

Table .4: Description of the demographic profile of the patients with Periodontitis (N=25).

Characteristic	N = 25 ¹
Age (years)	35.3 ± 10.7
Median (range)	32 (20 - 56)
Sex	
Male	14 (56.0%)
Female	11 (44.0%)
¹ Mean ± SD; n (%)	

The colony forming unit (CFU) of *Porphyromonas gingivalis* was measured in both the control group, which received scaling and root planing (SRP) only, and the test group, which received SRP plus diode laser treatment, over several follow-up periods. At baseline, the CFU was similar between the groups, with the control group showing a count of $2.56e+06 \pm 9.75e+04$ and the test group at $2.51e+06 \pm 7.14e+04$, with no significant difference ($p=0.066$). By the 3rd day, the test group showed a significantly lower CFU ($1.51e+06 \pm 4.61e+04$) compared to the control group ($1.70e+06 \pm 5.30e+04$), with a p-value of <0.001 . This trend continued in the 1st week, where the CFU in the test group decreased further to $4.94e+05 \pm 5.69e+04$, significantly lower than the control group's $6.81e+05 \pm 5.93e+04$ ($p<0.001$). By the 3rd month, the test group CFU declined to $2.99e+05 \pm 5.48e+04$, again significantly lower than the control group's $4.86e+05 \pm 5.89e+04$, with a p-value of <0.001 , indicating the efficacy of diode laser treatment in reducing CFU over time, as was detailed in Table 5.

The CFU of *Porphyromonas gingivalis* showed significant reductions over the follow-up period in both the SRP group and the SRP plus diode laser group. In the SRP group, the baseline CFU was $2.56e+06 \pm 9.75e+04$, which decreased significantly to $1.70e+06 \pm 5.30e+04$ on the 3rd day, $6.81e+05 \pm 5.93e+04$ by the 1st week, and to $4.86e+05 \pm 5.89e+04$ by the 3rd month ($p<0.001$). Similarly, in the SRP plus diode laser group, the CFU started at $2.51e+06 \pm 7.14e+04$ and significantly declined to $1.51e+06 \pm 4.61e+04$ by the 3rd day, $4.94e+05 \pm 5.69e+04$ by the 1st week, and $2.99e+05 \pm 5.48e+04$ by the 3rd month ($p<0.001$). Post-hoc analysis using Tukey's test showed that the differences between all the measurements in each group were statistically significant, as was shown in Table 6 and Figures 3 and 4.



Table 5: Description of CFU/ml of Porphyromonas gingivalis in both control and test groups over the follow-up time.

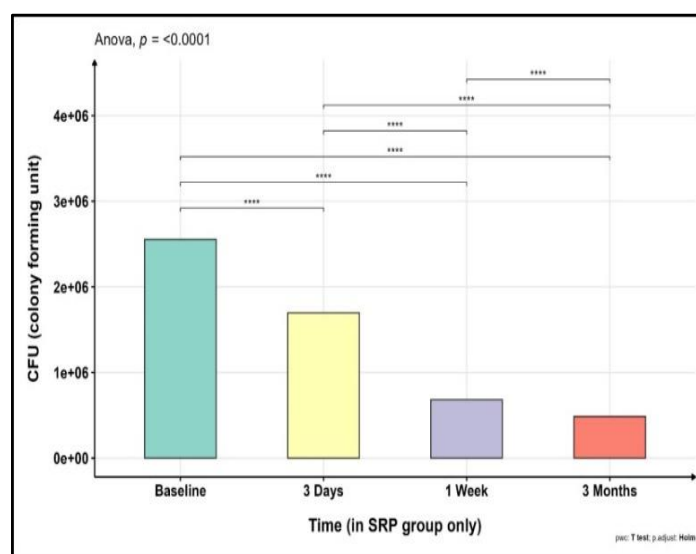
CFU/ML	SRP only, N = 25 ¹	SRP + Diode Laser, N = 25 ¹	P-value ²
At baseline	2.56e+06 ± 9.75e+04	2.51e+06 ± 7.14e+04	0.066
At 3 rd day	1.70e+06 ± 5.30e+04	1.51e+06 ± 4.61e+04	<0.001
At 1 st week	6.81e+05 ± 5.93e+04	4.94e+05 ± 5.69e+04	<0.001
At 3 rd month	4.86e+05 ± 5.89e+04	2.99e+05 ± 5.48e+04	<0.001

¹Mean ± SD
²Welch Two Sample t-test

Table 6: The statistical differences between the CFU/ml over the follow-up time.

Parameter	Baseline ¹	3 rd day ¹	1 st week ¹	3 rd month ¹	P-value ²
SRP Group	2.56e+06 ± 9.75e+04	1.70e+06 ± 5.30e+04	6.81e+05 ± 5.93e+04	4.86e+05 ± 5.89e+04	<0.001
SRP + Diode laser group	2.51e+06 ± 7.14e+04	1.51e+06 ± 4.61e+04	4.94e+05 ± 5.69e+04	2.99e+05 ± 5.48e+04	<0.001

¹Mean ± SD
²Repeated measure ANOVA

**Figure.5:** post-hoc analysis showing the mean CFU/ml in the different follow-up time in the SRP groups (****: p-value <0.0001).

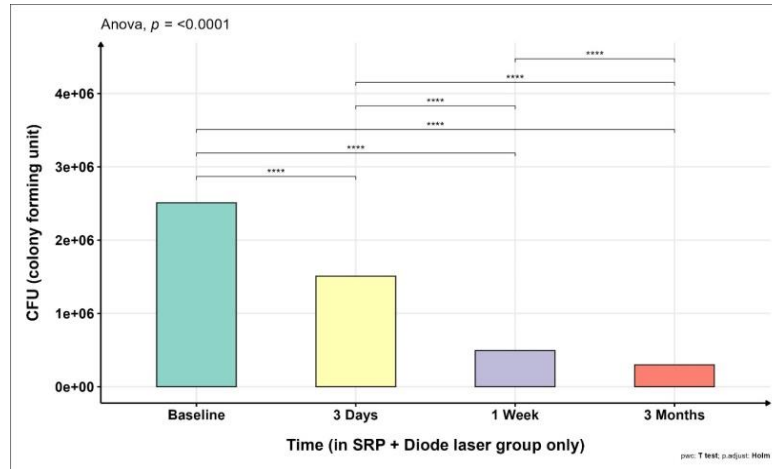


Figure 6: post-hoc analysis showing the mean CFU /ml in the different follow-up times in the SRP with diode laser groups (****: p -value < 0.0001).

12. Discussion

This is the first study that assesses the impact of an 810-980nm diode laser as an addition to periodontal therapy on the colony-forming units of *P. gingivalis* in individuals with periodontitis. The current literature indicates that microorganisms play a substantial role in developing periodontal disease [44]. The efficacy of periodontal therapy is widely acknowledged to rely on the diminishment of periodontal pathogens in the subgingival region. Research indicates that scaling and root planing (SRP) in individuals with periodontitis significantly alters the composition of subgingival microbiota, like that of healthy areas [45]. Nonetheless, these alterations are temporary, particularly in remaining deep sites following periodontal therapy [46]. Recent research indicates that bacteria can infiltrate epithelial cells not only in the periodontal pocket but also in the outer gingiva, so establishing a microbial reservoir may promote post-treatment relapses and the chronicity of periodontitis [47]. Rhemrev et al. illustrate that subgingival mechanical washing alone has a restricted efficacy in eliminating microorganisms[45]. Periodontopathogens remain inside cells outside the pocket epithelium, irrespective of standard periodontal therapy [12]. Numerous studies have demonstrated positive results from this medication regarding clinical and microbiological attributes. The clinical benefits arise from the removal of subgingival plaque and the disruption of the subgingival biofilm, leading to a decrease in bacterial populations. The results of the current investigation demonstrated that the counts of the bacterial species under investigation, particularly *P. gingivalis*, were significantly reduced by SRP alone. These data substantiate the beneficial effects of SRP in reducing the levels of *P. gingivalis* and *T. denticola* that were previously observed[26, 31]. Lasers are integral to periodontal therapy. They aid in eliminating both intra- and extracellular microorganisms[48]. Numerous literature papers reveal that laser irradiation possesses significant bactericidal characteristics [49, 50]. Our microbiologic examination results indicate that Applying a diode laser in combination with the SRP resulted in a substantial drop in bacterial presence. The effectiveness may stem from the thorough elimination of subgingival biofilm and eradication of pathogens from the root pocket[51]. Arisan et al. discovered that scaling and root planing (SRP) with adjunctive laser therapy decreased the total bacterial count in the compromised peri-implant region [52]. Arisan et al. observed an insignificant decrease in *A. a.*, *P. g.*, *T. d.*, and *T. f.* species after one month of follow-up relative to the control group [52]. In our current investigation, the CFU in the test group assessed after 3 days, 1 week, and 3 months was considerably lower compared to SRP alone. Furthermore, we observed a substantial reduction in the quantity of *P. gingivalis* at all follow-up intervals. The decrease in bacterial CFU may be attributed to the superior penetration and affinity of the diode laser's wavelength for the chromophores or pigments in *P. gingivalis*, perhaps leading to rupture of the bacterial cell wall[53]. Chan and Chien: [54] It was proved that the in vivo bactericidal effect of the Nd:YAG laser was the result of the interaction between this wavelength and pigmentation. This suggests that black-pigmented infectious

periodontal bacteria will absorb this energy, as the dark pigment functions as a laser-absorbing chromophore.

The haemoglobin in the soft tissue of periodontal pockets serves as an absorptive chromophore for the high-power diode laser, functioning as an endogenous dye that amplifies the laser's efficacy at this location [55]. These findings align with prior research, demonstrating that short-term decreases in bacterial numbers transpired within three months following medication [9, 56], and bacterial re-colonization occurred after three months [35]. Additional research employing the same treatment procedure and laser parameters, with a greater patient cohort and extended follow-up durations, is essential to validate the efficacy of the therapy suggested in this study. Future research should optimise the session number for each group session to yield sufficient results. A more extensive sample should be analysed to validate the importance and efficacy of the treatment on bacterial CFU.

13. Conclusions

A notable disparity in the colony-forming units of p.g was detected between the control and test groups. The dual wavelength diode laser can be an adjuvant to non-surgical treatment for those with periodontitis.

References

- [1] Y. Chan and C.-H. Lai, "Bactericidal effects of different laser wavelengths on periodontopathic germs in photodynamic therapy," *Lasers Med. Sci.*, vol. 18, pp. 51–55, 2003.
- [2] N. K. Imran, B. G. Ali, and D. Q. Jassim, "Quantitative detection and correlation of Epstein-Barr Virus in plasma with gingivitis and severity of chronic periodontitis by using real-time polymerase chain reaction technique," *J. Baghdad Coll. Dent.*, vol. 26, no. 4, pp. 133–140, 2014.
- [3] B. T. Ali and M. S. Mahmood, "Assessment of salivary total antioxidants capacity levels of patients with chronic periodontitis in comparison to healthy control," *J. Baghdad Coll. Dent.*, vol. 30, no. 1, pp. 58–62, 2018.
- [4] K. Aabed et al., "Is a single session of antimicrobial photodynamic therapy as an adjuvant to non-surgical scaling and root planing effective in reducing periodontal inflammation and subgingival presence of *Porphyromonas gingivalis* and *Aggregatibacter actinomycetemcomitans* in patients with periodontitis?," *Photodiagn. Photodyn. Ther.*, vol. 38, p. 102847, 2022.
- [5] A. Singh et al., "The capsule of *Porphyromonas gingivalis* leads to a reduction in the host inflammatory response, evasion of phagocytosis, and increase in virulence," *Infect. Immun.*, vol. 79, no. 11, pp. 4533–4542, 2011.
- [6] M. I. Alameer, H. R. Abdulbaqi, and D. Martin, "Antibacterial effect of green tea against *Porphyromonas gingivalis*: a literature review," *J. Baghdad Coll. Dent.*, vol. 36, no. 1, pp. 70–78, 2024.
- [7] F. AlAhmari et al., "Effectiveness of scaling and root planning with and without adjunct antimicrobial photodynamic therapy in the treatment of chronic periodontitis among cigarette-smokers and never-smokers: a randomized controlled clinical trial," *Photodiagn. Photodyn. Ther.*, vol. 25, pp. 247–252, 2019.
- [8] L. A. Abdullah et al., "Effectiveness of Diode (810 nm) Laser in Periodontal Parameters and Reduction of Subgingival Bacterial Load in Periodontitis Patients," *J. Contemp. Dent. Pract.*, vol. 24, no. 12, pp. 1008–1015, 2023.
- [9] S. Nammour et al., "Clinical evaluation of diode (980 nm) laser-assisted nonsurgical periodontal pocket therapy: a randomized comparative clinical trial and bacteriological study," *Photobiomodul. Photomed. Laser Surg.*, vol. 39, no. 1, pp. 10–22, 2021.
- [10] T. J. O'Leary, "The impact of research on scaling and root planing," *J. Periodontol.*, vol. 57, no. 2, pp. 69–75, 1986.
- [11] B. Fahad Al Dabbagh and B. Khulood Al Safi, "Clinical evaluation of Er: YAG laser in the treatment of chronic periodontitis in comparison with that of hand and ultrasonic treatment," *Sci. J. Published by the Coll. of Dent.–Univ. of Baghdad*, pp. 78.
- [12] K. Grzech-Leśniak, A. Sculean, and B. Gašpirc, "Laser reduction of specific microorganisms in the periodontal pocket using Er: YAG and Nd: YAG lasers: a randomized controlled clinical study," *Lasers Med. Sci.*, vol. 33, pp. 1461–1470, 2018.
- [13] S. Acharya et al., "Effectiveness of single versus multiple sessions of photodynamic therapy as adjunct to scaling and root planing on periodontopathogenic bacteria in patients with periodontitis," *Photodiagnosis Photodyn. Ther.*, vol. 32, p. 102035, 2020.



- [14] A. A. Odor, E. S. Bechir, and D. A. Forna, "Effect of Hydrogen Peroxide Photoactivated Decontamination Using 940 nm Diode Laser in Periodontal Treatment: A Pilot Study," *Photobiomodulation, Photomed. Laser Surg.*, vol. 38, no. 10, pp. 614–624, 2020.
- [15] F. F. Dakhil et al., "Assisted Non-Surgical Therapy of Periodontal Pockets Utilizing Diode Laser: A Randomized Clinical Trial," *Iraqi J. Laser*, vol. 18, no. 2, pp. 1–6, 2019.
- [16] A. R. Atarchi and Z. R. Atarchi, "Efficacy of a single antimicrobial photodynamic therapy session as an adjunct to non-surgical periodontal therapy on clinical outcomes for periodontitis patients. A systematic review," *J. Bagh. Coll. Dent.*, vol. 35, pp. 76–87, 2023.
- [17] H. Alzoman and H. Diab, "Effect of gallium aluminium arsenide diode laser therapy on *Porphyromonas gingivalis* in chronic periodontitis: a randomized controlled trial," *Int. J. Dent. Hyg.*, vol. 14, no. 4, pp. 261–266, 2016.
- [18] Ş. B. Doğan and G. Akça, "Clinical Evaluation of Diode Laser-Assisted Surgical Periodontal Therapy: A Randomized Split-Mouth Clinical Trial and Bacteriological Study," *Photobiomodulation, Photomed. Laser Surg.*, vol. 40, no. 9, pp. 646–655, 2022.
- [19] F. F. Dakhil and A. S. Mahmood, "Evaluation of clinical effects of a 940nm diode laser as adjunctive therapy in treating periodontal pockets," *Iraqi Dent. J.*, vol. 39, no. 1, pp. 12–15, 2020.
- [20] K. Chandrasekaran et al., "Immediate effects of diode laser (970±15 nm) on microbial load in patients with chronic periodontitis: A split-mouth study," *Indian J. Dent. Res.*, vol. 32, no. 4, pp. 453–458, 2021.
- [21] A. Moritz et al., "Bacterial reduction in periodontal pockets through irradiation with a diode laser: a pilot study," *J. Clin. Laser Med. Surg.*, vol. 15, no. 1, pp. 33–37, 1997.
- [22] E. Kocak et al., "Effect of diode laser application as an adjunct to nonsurgical periodontal therapy on the reduction of red complex microorganisms in type 2 diabetics with chronic periodontitis," *Lasers Med. Sci.*, vol. 35, pp. 1403–1410, 2020.
- [23] Q. K. Abbas and L. M. Al-Ameri, "Photodynamic effect of Rose Bengal activated by low-level laser light on *S. aureus*," *Iraqi J. Laser*, vol. 21, no. 2, pp. 48–57, 2022.
- [24] M. Pawelczyk-Madalińska et al., "Impact of adjunctive diode laser application to non-surgical periodontal therapy on clinical, microbiological and immunological outcomes in management of chronic periodontitis: a systematic review of human randomized controlled clinical trials," *J. Inflamm. Res.*, pp. 2515–2545, 2021.
- [25] S. Mulder-van Staden, H. Holmes, and J. Hille, "In vivo investigation of diode laser application on red complex bacteria in non-surgical periodontal therapy: A split-mouth randomised control trial," *Sci. Rep.*, vol. 10, no. 1, p. 21311, 2020.
- [26] T. A. Kamble et al., "Clinical and Microbiological Evaluation of Diode Laser and Systemic Doxycycline as an Additive to Scaling and Root Planing for Stage II and Stage III Periodontitis Patients," *Cureus*, vol. 16, no. 3, 2024.
- [27] P. N. Papapanou et al., "Periodontitis: Consensus report of workgroup 2 of the 2017 World Workshop on the Classification of Periodontal and Peri-Implant Diseases and Conditions," *J. Periodontol.*, vol. 89, pp. S173–S182, 2018.
- [28] M. S. Tonetti, H. Greenwell, and K. S. Kornman, "Staging and grading of periodontitis: Framework and proposal of a new classification and case definition," *J. Periodontol.*, vol. 89, pp. S159–S172, 2018.
- [29] P. Ingalagi et al., "Detection and comparison of prevalence of *Porphyromonas gingivalis* through culture and Real Time-polymerase chain reaction in subgingival plaque samples of chronic periodontitis and healthy individuals," *J. Oral Maxillofac. Pathol.*, vol. 26, no. 2, pp. 288, 2022.
- [30] I. Darby, J. Mooney, and D. Kinane, "Changes in subgingival microflora and humoral immune response following periodontal therapy," *J. Clin. Periodontol.*, vol. 28, no. 8, pp. 796–805, 2001.

فاعلية الليزر الثنائي (810-980 نانومتر) كمساعد للعلاج غير الجراحي لالتهاب اللثة على بكتيريا بورفيروموناس جينيفاليس: دراسة عشوائية مقسمة على الفم

فاطمة كاظم سلمان*, ليلى محمد حسن العامري

معهد الليزر للدراسات العليا، جامعة بغداد، بغداد، العراق.

البريد الإلكتروني للباحث: fatima.kadhumi2202m@ilps.uobaghdad.edu.iq



الملخص: التهاب اللثة هو حالة التهابية مزمنة ومعقدة ترتبط بالأغشية الحيوية للبلاك المختل وتتميز بالتدهور التدريجي للهياكل الداعمة للأسنان. يُعرف أن بكتيريا *Porphyromonas gingivalis*، وهي عدوى حيوية حرجة في اللثة، تساهم بشكل كبير في بداية وتقدم أمراض اللثة عن طريق إحداث تغيير اختلافي في الميكروبيوتا اللثوية، خاصة تحت اللثة، من البكتيريا الموجبة والسالبة الجرام. تسعى العلاجات التقليدية مثل تنظيف الجذور وتخطيط الجذور (SRP) إلى إزالة البلاك والجير من أسطح الأسنان والمناطق تحت اللثة. ومع ذلك، فإن هذه العلاجات تصاحبها بعض القيود. لقد أظهرت الليزرات الثنائية إمكانية كعلاج مساعد، مما قد يحسن نتائج العلاجات التقليدية.

الهدف من الدراسة: تهدف هذه الدراسة إلى مقارنة فعالية ليزر الصمام الثنائي كطريقة علاجية مساعدة للعلاج غير الجراحي مقابل SRP فقط على CFU للبورفيروموناس اللثوية في المرضى الذين يعانون من التهاب اللثة.

المواد والطرق

تم تنظيم هذا البحث كتجربة سريرية عشوائية محكمة، مقسمة الفم. شارك في هذا البحث خمسة وعشرون شخصًا (11 أنثى و14 ذكرًا) تتراوح أعمارهم بين 20 و56 عامًا) تم تشخيصهم بالتهاب اللثة. بعد العلاج الأولي للثة، والذي شمل إرشادات نظافة الفم وإجراءات التنظيف، خضع كل مريض لعلاجين منفصلين على جانبي الفم المتقابلين. تم تعيين الجانب الأيسر كمجموعة اختبار، بينما تم تخصيص الجانب الأيمن كمجموعة تحكم. تم تحقيق العشوائية عن طريق رمي العملة لضمان التوزيع العادل. في مجموعة الاختبار (الجانب الأيسر) خضع المرضى (SRP) بالتزامن مع علاج الليزر الثنائي؛ في مجموعة التحكم المقابلة (الجانب الأيمن) تلقوا علاج (SRP) فقط. تم ضبط الليزر على موجة مستمرة بقدرة 1.5 واط، طرف 400 ميكرومتر، تقنية التلامس والمسح. تم أخذ 50 عينة من اللوحة تحت اللثة بعد تسجيل معايير اللثة، مؤشر اللويحة (PI)، النزيف عند الفحص (BOP)، عمق جيب اللثة (PPD)، وفقدان التعلق السريري (CAL) في البداية قبل، وبعد 3 أيام، أسبوع واحد، و12 أسبوعًا من العلاج. ركزت التقييمات الميكروبيولوجية على الوحدات المكونة للمستعمرات من *Porphyromonas gingivalis* (P.G). تم تعداد الوحدات المكونة للمستعمرات (CFU) لكل مجموعة لمدة 48-72 ساعة على وسط زراعي مناسب بعد التخفيف التسلسلي. تم تأكيد البكتيريا المعزولة سريريًا باستخدام الاختبار البيوكيميائي، الفحص المجهرى، نظام Vitek II، وأخيرًا بواسطة تقنية PCR

النتيجة: تم تخفيض وحدات تشكيل المستعمرة (CFU) من خلال طريقتي العلاج ولم تعود إلى مستويات خط الأساس بعد ثلاثة أشهر من العلاج. أظهرت مجموعة ليزر SRP+ ليزر دايود انخفاضًا ملحوظًا إحصائيًا في المستويات البكتيرية لـ *P. gingivalis* بعد 3 أيام وأسبوع و3 أشهر بعد العلاج مقارنةً بمعالجات SRP وحدها.

الاستنتاج: تم الكشف عن تباين ملحوظ في وحدات تشكيل مستعمرة p.g بين المجموعتين الضابطة والاختبارية. يمكن استخدام ليزر الصمام الثنائي ذو الطول الموجي المزدوج كمساعد لعلاج اللثة غير الجراحي للمرضى الذين يعانون من التهاب اللثة.



Optical Fiber Sensors Based on Surface Plasmon Resonance: A Comprehensive Review

Dalya H. Abbas^{1,*}, Hanan J. Taher¹, Bushra R. Mahdi²

¹*Institute of Laser for Postgraduate Study, University of Baghdad, Baghdad, Iraq*

²*Ministry of Science, Baghdad, Iraq.*

* *Email address of the Corresponding Author:* dalia.abbas2201p@ilps.uobaghdad.edu.iq

Article history: Received: 22 Oct. 2024; Revised: 31 Dec. 2024; Accepted: 13 Feb. 2025; Published online: 15 Jun. 2025.

Abstract

Surface Plasmon sensor is commonly used in chemistry, biologic, and environments nursing. This type of sensor display strange sympathy depends on surfaces Plasmon resonance (SPRs) or localize surfaces Plasmon resonance (LSPRs) effect, which have a commercial application. In this review, we present current progressing in the fields of surfaces plasmatic sensor, principally in the configuration of planar Meta structure and optical-fiber waveguide. In the Meta structures platforms, the optical sensor depend on LSPRs, hyperbolic dispersions, Fanon resonance, and two-dimension (2Ds) material integrations are presented. The optical-fiber sensor integration with LSPRs/SPRs structure and 2D material are summarizing. In addition, we introduced the current advance in quantum plasmatic sensors beyond the classic shot noisy limitation. The challenge and opportunity in this arena is deliberated. The LSPRs biosensor, enabling Nano scale limitation and manipulations of lights, compromise the enhance sensitivity and electromagnetics energies localizations. The combination of LSPRs and fibers-optics techniques is managed to progress the sensors compacts to reduction and remotes recognizing. These comprehensive reviews explore numerous sensors configuration, fibers categories, and geometric outlines, highlight their benefit in term of sensitivities, integrations, and performances improvements. The fabrication technique effort on non-chemical bond strategy and self-assemble of nanoparticle discusses and provide controlling over nanostructures morphologies and enhanced the sensors performances. Bio-application of fiber-optics LSPRs (FOLSPRs) sensor is comprehensive, definitely in bio-molecular interaction and analyze of protein, pathogen and cell, nucleic acid (DNAs and RNAs). Surfaces modifications and recognition structures are emphasizing for their probable in label-free and real-times bio senses. The challenge and prospect of FOLSPRs sensor is addresses, with the development in sensitivities, fabrications technology, and measurements reliabilities. Integrations with developing technology like Nano-material is highlight as a capable directions for upcoming researches. These reviews provide insight into the advancement and possible application of FOLSPRs sensor, pavement the technique for sensitive and adaptable optical bio-sense platform in several arenas.

Keywords: Optical Fiber Sensors, LSPR, SPRS, Refractive index sensor, Mach–Zehnder Interferometer, Offset Sensor, Concentration.



1. Introduction

Surface Plasmon is combined electrons oscillation that happens at the interfaces among metals with dielectrics, resultant in generate surfaces Plasmon polarities on excitations through lights [1]. This sensation is influence via property of material and incidents lights, permitting to imprisonment with manipulations of lights at Nano-scale [2]. In connection of the oscillate electric fields of the incidents lights with the cooperative motions of electron on the metals surfaces, surface Plasmon could propagated along the metal-dielectrics interfaces, lead to important fields enhancement and the localizations of the electromagnetic energies. If the incidents lights match the wave vectors of the surfaces Plasmon, a depression in the concentration of replicated or transmit lights, identified as the surfaces Plasmon resonances (SPRs) depression, could be observe [3]. This depression is extremely sensitive to change in the refractive indexing (RIs) of the nearby mediums. Therefore, surfaces Plasmon have originate broad applications in label-free and real-times detections of bio-molecular collaboration [4], like DNAs hybridizations and antibody-antigen recognitions, enabled Nano-scales analyzing of biological and chemical interaction over the single property of plasmodia material [5]. The LSPRs is a deviation of the SPRs that occur in nanostructure, such as nanoparticle or periodical array, which have individual plasmodia property [6]. In difference to the SPRs, which relay on macroscopic surface, the LSPRs could be customize by control the sizes, shapes, and compositions of the nanostructure, permitting for tenability of the resonances wavelength and enhance sensitivities [7]. Subsequently, LSPRs sensor is high striking for many requests, include bio-sensing, environment monitor, and Nano-photonic [8]. The combination of the fiber-optic knowledge with the LSPRs has resulting in the advance of compacts and adaptable sensor, simplifying miniaturizations, and remotes recognizing. This advancement is open up novel possibility for high sensitive and compacts optical sensing in several field. Fiber-optic base sensor is gain attentions for their smaller sizes, highly sensitivities, compatibilities with remotes and real-times monitor, and the potentials for multiplex measurement [9]. These reviews aim to offer complete overviews of fiber-optic LSPRs (FOLSPRs) sensor, with a effort on their configuration, type, geometry, fabrications technology, and bio-application. FOLSPRs sensor could be classify into two primary classes: flat headed reflective and straight Transmissive configuration. These conformations offer separate advantage and could be personalized to definite sense requirement, depend on factor like the desire sensitivities, measurements system, and experiment condition [10]. Many fiber type, like single-mode fiber (SMF), multimode fiber (MMF), photonic crystal fiber (PCF), and specialty fiber could be uses in this configuration offering exclusive advantage in term of sensitivities, flexibilities, and integrations with other system. The symmetrical shape employ in FOLSPRs sensor play a important roles in enhance their performances. The LSPRs biosensor with different geometry, include taper, U-types, Ω -types, and D-types shape, efficiently enhanced the sensitivities of the sensor and encounter definite assemblage requirement of succeeding sense structure. Besides, these reviews investigate diverse fabrications technology utilizes in the developments of FOLSPRs sensor. This technique contain top-down fabrications of periodical Nano-structure by focus ions beams (FIBs) or electrons beams lithograph (EBLs), surfaces homemade of nanoparticle, and bottoms-up nanostructure films transfer technique [11, 12]. This fabrications technology permit for precise controlling over the surfaces morphologies of the nanostructure, additional enhances the performances of the sensor. Additionally, the different bio-application of FOLSPRs sensor is reconnoitered; include their utilizations in the detections and analyzing of biomolecule, like protein, DNAs, and virus [13]. Definite surfaces modifications and detections scheme is deliberated in details. The possible application of FOLSPRs sensor in medicals diagnostic, environment monitor, and foods protection is explored [14]. The challenge and prospect in the developments of FOLSPRs sensor could be highlight. This challenge included improves the sensors sensitivities, optimize the fabrications technique, and enhance the reliabilities and reproducibility of sensors measurement. Possible area is upcoming researches and advancement, like the integrations of FOLSPRs sensor with technology like nanomaterial is outline as well. Generally, the purposes of these review is to afford a comprehensive understand of FOLSPRs sensor, the fabrications technique, and the widely ranges of bio-application. Through discovering diverse geometry, fabrications technology, and application, this reviews aim to



contributed the advancements and adoptions of FOLSPRs sensor in field like humans health, drugs screen, foods protection, and environment nursing.

2. Principle of SPR

In general, when the light waves are incident into light dense mediums from a light sparse medium with the angles larger than critical angles, the phenomenon identified as whole reflections take place. Within this situation, even if the light waves not penetrated the critical interfaces among the two medium, it generate an evanescent waves along with the directions comparable to the critical interfaces. As the space from the critical surfaces increased, an exponent declined might be realized in difficult amplitude of the electric and magnetic field with the waves that is evanescent [15]. Figure 1 shows that the incidence of free electrons gas in the metals permits it to behave like plasma. If the incident light interacts with the metals, it induces longitudinal oscillation in the electron gas. Resultant in the oscillation, the formations of charge density waves result in the generations of a surface plasma wave that travel along the metal-dielectric contacts [16]. The intensity of the monitor reflects light is considerably reduced as results of the resonances amongst the metal surface plasma waves and the evanescent waves [17]. The SPRs is the names give to this phenomenon. The outline of reflect light intensity will exhibit a trough when the relate wavelengths (or angles) match the resonance wavelengths (or resonance angles) [18].

Surface Plasmon resonance happens if the photon of incident light hit metal surfaces (usually gold surfaces). At a definite angle of incidence, a slice of the light energy combines over the metal coating with the electron in the metal surface layers, which then transfer due to excitations. The electron movement is now named Plasmon, and they propagated parallel to the metal surfaces. The Plasmon oscillations in turn produce electrical fields whose range is about 300 nm from the boundaries among the metal surfaces and tester solutions. In a profitable SPRs biosensors conformation, incident light is used by employing a high-reflective index glass prism in the geometry of the attenuate total reflections (ATRs) technique. The definite SPRs angles, at which resonance occurs, on the conditions of the constant light source wavelength and metal thin surfaces, are reliant on the refractive index of the material nearby the metal surfaces. Therefore, when there is a smaller variation in the reflective index of the sensing medium (e.g., over biomolecule attachment), Plasmon not be molded. Finding is thus accomplish by computing the change in the reflect light achieved on a detectors. Additionally, the quantity of surface concentrations could be quantified by monitoring reflect light intensities or tracking the resonance angles shift. Typically, an SPRs biosensors has a detection limits on the order of 10 pg/mL.

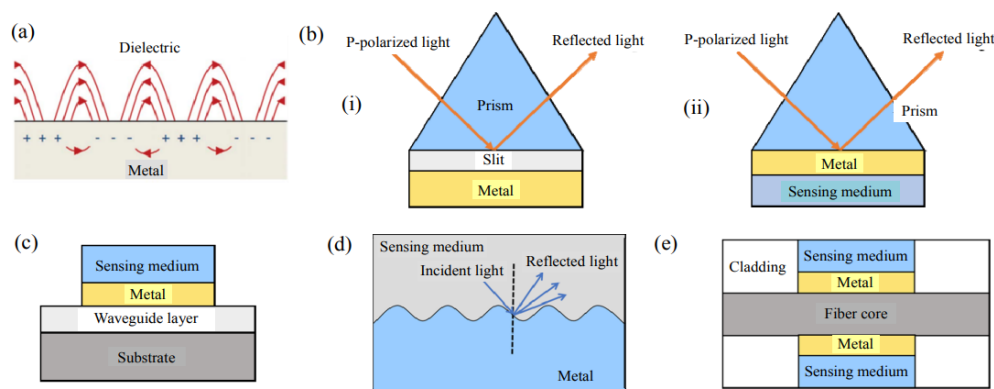


Figure 1: Schemes structure of SPRs: (a) SPRs on a planar metals films; (b) prism-couple excitations SPRs; (c) waveguides couplings devices; (d) gratings-couple SPRs excitations structures; (e) optics fibers types SPRs sensors.

The partitioning amongst the wavelengths and angles is mostly base on whether detections systems use wavelengths interrogations or angles interrogations. The sensors are sensitive to RIs of mediums attach to surfaces of metals films, and the resonances angles will be diverse if the property of surfaces mediums

changed or if the quantity of attachments changed. The incident lights could be decomposed into S-polarized (TE waves) and P-polarized (TM waves), and this type of polarized light is perpendicular. Surface Plasmon wave is not excited by the electric fields of S-polarized light due to it is transverse to interfaces and has no impact on the migration of free electrons with the metals; the electric fields of P-polarized light are perpendicular to the interfaces, that could be induced surface charge and forms SPR phenomena, which confine to the surfaces. Consequently, the essential conditions for producing SPRs are the presence of P-polarized light at incident lights [17].

3. Surface plasmon-based sensors

The advantages of optical fiber-coupled SPRs sensor [18] over other SPRs sensor is that they are modest to use, take up relative small spaces, are highly sensitive, and exceptionally stable. Consequently, in current time, further researchers devoted themselves to these studies to advance their performances. Physically improve fiber optic SPRs sensor sensitivity so far, numerous types of optical fiber structures, mostly D-type probe, U-type probe, and taper probe. The key type of optical fiber is single-mode fiber (SMF), multimode fiber (MMF), photonic crystal fiber (PCF), plastic optical fiber (POF), and fiber Bragg grating (FBG).

3.1 Surface Plasmon Resonance

A. Plasmon Oscillation

There is a thick assembly of negatively charged free electrons in the conductors and an equal charge of positive ions lattices. Then, positive ions have an infinite larger mass compared to this free electron, hence, rendering to the jellium model, this ion could be replaced by a positive constant background. Though, the whole charge density in the conductors still remains to be zero. When the density of free electrons is locally reduced by applying an external field on the conductors, so that the movement of free electrons might take place, the negatively charged free electron is not screened by the background and they initiate to be attracted by the positive ion background. These attractions act as heavy forces for free electrons and they move to positive regions and accumulate with a density larger than required to attain charge neutrality. Nowadays, at this point, the Coulomb repulsions among the moving free electrons act as a restoring force and produce motions in differing directions. The result of these forces set up the longitudinal oscillation among the free electrons. This oscillation is recognized as plasma oscillation. A plasmon is a quantum of the plasma oscillations. The existence of plasma oscillations has been verified in electron energy-loss experiments [19, 20].

B. Surface Plasmon

The metal-dielectric interfaces support plasma oscillation. This charged density oscillation in the metal-dielectric interfaces are recognized as surface plasma oscillation. The quantum of this oscillation is denoted as surface plasmon. This surface plasmon is complemented through the longitudinal (TM or p-polarized) electric fields, that decay exponentially in metals and dielectrics. Because of these exponential declines of field intensity, the fields have their extreme at metal-dielectric interfaces themselves. These properties of surface plasmon being TM-polarized and exponential decline of electric fields are created by solving Maxwell's equations for metal-dielectric type of refractive index distributions. Through the solutions of Maxwell's equations, one could display that the surface plasmon wave propagation constant is continuous over the metal-dielectric interfaces.

C. Surface Plasmon Excitation by Light



The maximal propagations constant of the light wave at frequencies propagate over the dielectrics mediums is given by frequencies, the propagations constants of surfaces Plasmon is larger than that of the light wave. Therefore, the directs lights not excited the surfaces Plasmon at a metals-dielectrics interfaces and is referred to as non-radiated surfaces Plasmon. Consequently, in order to excited the surfaces Plasmon, the momentums and therefore the waves vectors of the excite lights in dielectrics mediums must be increases. The further momentums should be informed to lights waves to develop the surfaces Plasmon excites at metals-dielectrics interfaces. The common ideas after this configurations is coupling of surfaces Plasmon waves with the evanescent waves, that is setup because of ATRs at the bases of a couple prisms when a lights beams is incidents at an angles bigger than the critical angles at prisms-air interfaces [21]. The natural of evanescent waves is recognized to have the propagations constants along the interfaces and to decline exponential in the dielectrics mediums nearby to metals layers.

3.2 *Fibers-Optics SPRs Sensors*

Outline of optical fiber in the SPRs sense systems are depend on the logic reasons that direction of lights in optic fiber is also depend on total internal reflections (TIRs). Meanwhile, a prism is use in SPRs sense systems to produce TIRs at the prisms-metals interfaces; hence, couple prisms use in the SPRs theories could be convenient replace by the cores of an optical fiber to designing the fibers-optics SPRs sensors. Amongst another main reason are the advantage of optical fiber by couple prisms like modest and flexible designing, miniaturizes sensor systems, and ability of remotes sensor. Generally, the silicon clad from a definite smaller portions of the fibers cores is eliminate and is coated with a metals layers, that additional enclosed by a dielectrics sense layers. The TIRs take place for the ray propagation with an angle in the ranges changing from the critical angles (depend on the numeric apertures of the fibers and the lights wavelengths) around 90. Therefore, the evanescent fields are produced, that excite the surfaces Plasmon at the fibers cores-metals layers interfaces. These couple of evanescent fields with surfaces Plasmon intensely depends on lights wavelengths, fibers parameter, fibers geometries, and metals layers property. As an example, couplings mechanisms will be unlike for singles-mode and multimode optic fiber because of have many modes of transmissions property depend on a numbers of mode in fibers which will supporting. Likewise, straights fibers and taper fibers will shows changed strength of lights couple due to this fiber will display many penetrations depth of evanescent fields because of have many geometric configuration. The taper fibers show a substantive variant in evanescent fields penetrations along the taper sense regions lengths while an un-taper fibers exhibit uniforms penetrations of evanescent fields along the sense regions. Additional, penetrations of the evanescent fields and, hence, strengths of lights couple with surfaces Plasmon depend on an important fibers parameters recognized as numeric apertures that relate to lights reception limits of the fibers. Besides, different prisms-bases SPRs geometric, the numbers of reflection for utmost of the angle is larger than one for fibers-bases SPRs sensors geometric. Nearby its angles, the numbers of reflection for some rays depend on another fibers parameter, specifically, sense regions lengths, and fibers cores diameters. The numbers of reflection straight affect the SPRs curves widths, hence, performances parameter (SNRs and sensitivity) of the sensors depend on fibers property. This different aspect relate to fiber optic and geometric property along with their advantage and disadvantage Lastly, the spectrums of lights transmits after pass over SPRs sensor regions is detects at the other ends. The sense is accomplish by observe the wavelengths correspond to the dips in the spectrums. These wavelengths are named as the resonances wavelengths. Plots of resonances wavelengths with the refractive indexes of the sense layers give the calibrations curves of the fibers-optics SPRs sensors. Different prisms-bases SPRs sensors where angular interrogations technique is usage, the spectral interrogations technique is uses in the fibers-optics SPRs sensors due to the fibers-optics sensors all the guide mode is launch in the fibers [22].



4. Geometric structure of folsprs sensor

FOLSPRs sensor is commonly usages for sensitive detections and analyzing of bio-chemical reaction. The LSPRs occurrence happens if the light interacts with Nano-scales metals structure, resultant in spectral shifts in the resonant frequencies that is sensitivity to the RIs change in adjacent mediums. To growth the sensitivities, selectivity, and versatilities of LSPRs sensor, the geometric configurations of fibers probes is continuous modify. Classically, the LSPRs' sensing performance could be efficiently realized by using diverse types of optical fiber, optimizing the geometric structures of fiber probes, and adopting diverse optical transmission modes. This geometry provides unique advantage in term of sensitivities, stabilities, and multiplexes capability, depend on the definite designing. Generally, the geometric formations of FOLSPRs sensor play vital roles in determine the sense performances and enable preparation application in biomedical sense, environment monitor, and chemical analyzing.

4.1 Propagations paths of lights

A LSPR phenomenon in a fiber-optic sensor is created by the interactions among light and metallic nanoparticles or nano-arrays immobilized on a fiber. The LSPRs' effects occur if the incident lights match the resonant frequencies of the nanostructure in the passing fields, resulting in a robust absorption or light scattering. These interactions are determined by the plasmatic property of the nanostructure and could be quantified by using the Mie theories. Through monitor the spectral responses of the scatter lights, change in the nearby RIs could be detects, enable the sensitive detections of many analytic or environment parameter. The two key formations for FOLSPRs sensors are based on the propagation paths of light: straight transmissions [23] and flathead reflections [24]. Figure 1 shows the straight trans missive FOLSPRs sensor system. Incident lights are coupled into one end of the fibers and propagated over the fibers' cores. The LSPRs-active nanostructure is immobilized on the side-outers surfaces of fibers as the sense zone. The lights are received by signals-receive devices at the other ends. As the lights interact with nanostructure along the transmission paths, the LSPRs effects induce a change in the transmitted light's intensity or wavelengths, which could be measured at the output ends.

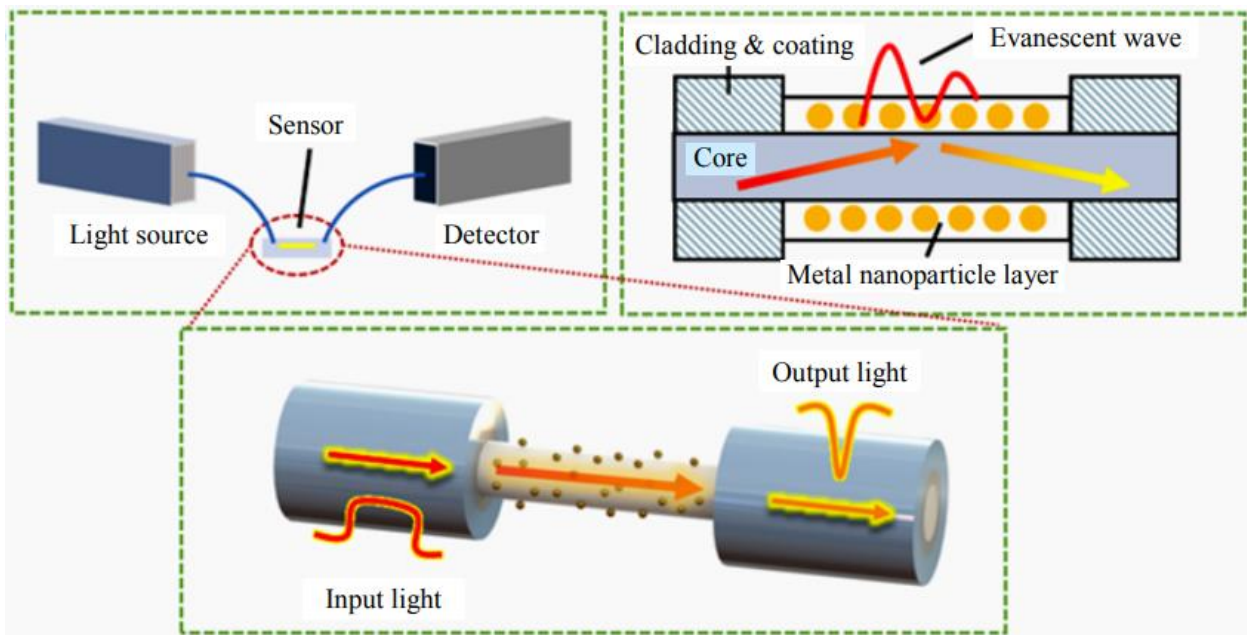


Figure 2: Configuration of straight Tran's missive [24]

In difference, as shown in Figure 3, the flat head reflected configurations use one side of fibers to transmitted the incidents lights and received the end-faces reflects signals over a fibers-optics couplers. The LSPRs-active nanostructure is immobilize on the fibers ends-faces or on the side-outers surfaces nearby the ends of the fibers probes, while the reflect lights from the sense areas are collects and analysis to determined change in the intensity or wavelengths. The flats head reflective configurations allow for integrations with external system, like spectrometer or detector, and is appropriate for application where directs accessing to the samples are desire, such as in implantable medical diagnostic [25].

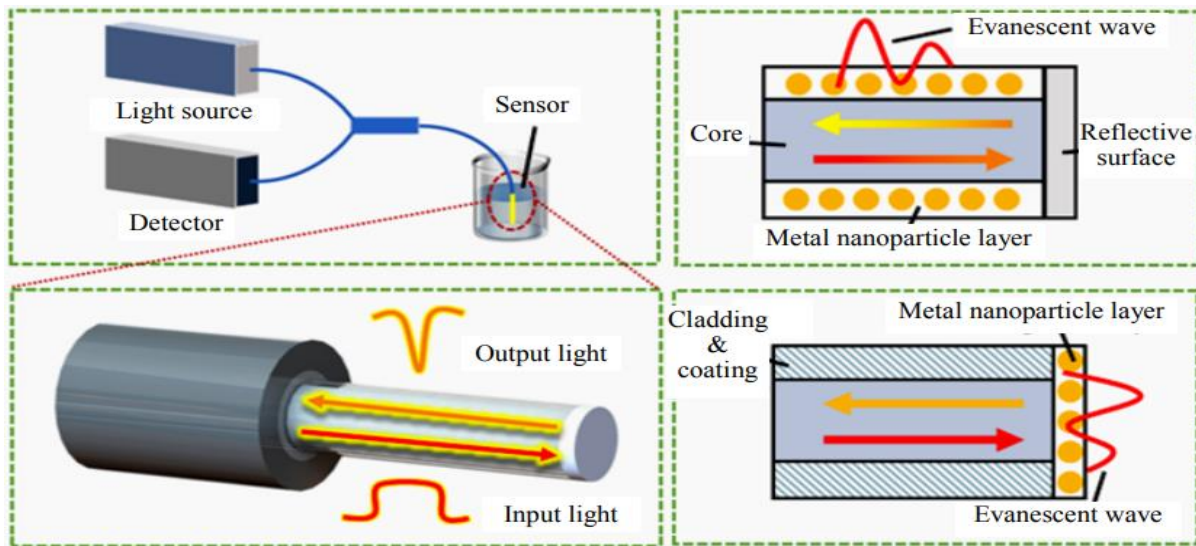


Figure 3: Configuration of flat head reflected FOLSPRs sensor [25]

The selection between these structures depends on numerous aspects. One vital aspect to deliberate is a characteristic of samples being analyzing. As examples, if the samples are sensitive to contact or require non-invasive approaches, the straight transmission structure will be more appropriate as it permits sensing over long distances without direct contact with the samples. These are mainly advantage in biological or hazardous environment. When a direct access to the samples is preferred, like in implantable medical diagnostics, the flat head reflector structure will be desired. These structures allow for easy integration with an outward system, like a spectrometer or detector, enabling effective analysis of reflected light from the sensing areas on the end faces or side surfaces of the fiber probes. Other serious considerations in case of selecting the structure are the definite sense requirement. All configurations could be measured by the change in the transmit lights' intensity or wavelengths induced by LSPRs effects. Though, the straights transmissions structure might offer improved stabilities and repeatability's because of a long interactions paths of lights with the LSPRs-actives nanostructure beside the fibers cores. The flat head reflects structure might offer improved sensitivities in measurement, as it relies on the precise assembly of reflected lights from the smaller bottom sense areas. Compatible with measurements system is vital factors. The straight transmission configuration is moderately simple, requiring signal-receiving devices at one end of the fibers to measure changes in transmitted light. The flat head reflect configurations with the addition Y-shape fibers-optics couplers impose high requirement on the smoothness of the fibers ends faces to ensures the suitable optic couple effectiveness.

4.2 Category of Optic Fibers

Substituting the traditional prisms with the optical fibers as Plasmon component could overcome the limitation of the relative bulk sizes, complex optical and mechanical structures, and incapability for remote and on-site sensing. In addition, it offers advantages like mobility and implant situ detection. Subsequently,

the major reports of the fiber-based SPR sensors were introduced in 1993 with many types of optical fibers as presented in Figure 4 (a), which applies in the Plasmon resonances sense, containing SMF, MMF, hollow-core fibers (HCFs), PCF, micro/Nano fibers (MNF), and FBG. The conventional SMFs and MMFs are extensively use because of their matured manufacture processing. Though, these types of sensors primarily realize LSPRs sense by use the method of cores mismatches, decreasing the width of the clad, or use the fibers ends faces, then the passing field cannot penetrated the entails big width clad to excited the metals nanoparticle on the surfaces of the fibers to produce the LSPRs. A metallic particles monolayers act as a plasma nanostructure that enhance the passing field interactions with the targets analytic. The geometric could varying, include straight, tapered, or U-shape configuration, depend on the preferred sense outcome. Compared to another fibers structure, the SMFs-LSPRs sensors utilize the passing fields of guide modes to interrelate with the analytic, provided solidity, simplicities, and compatibilities with present fibers-optics system. Though, the elimination of SMFs clad requires the uses of robust acid design or polished procedure that hazardous and composite. This process has the probable for resultant in rough on the sense surfaces, afterward decreasing the sensitivities of the sensors. Else, the MMFs are the greatest wide uses in LSPRs sensor since it offers numerous benefits over the conventional SMFs-LSPRs sensors. The MMFs allow for propagations of multiples mode of lights, resultant in enhance sense capability as illustrated in Figure4 (c). The collective processing of eliminating the plastics coat from MMFs only required a modest physic strip. Compare with SMFs-LSPRs sensors, these simplify processing is beneficial in attaining a stabled structures for senses performances. In addition, its greater cores diameters facilitate the couple of lights to the sensors, make it more effectual and improve the signals-to-noise ratio (SNR) [26].

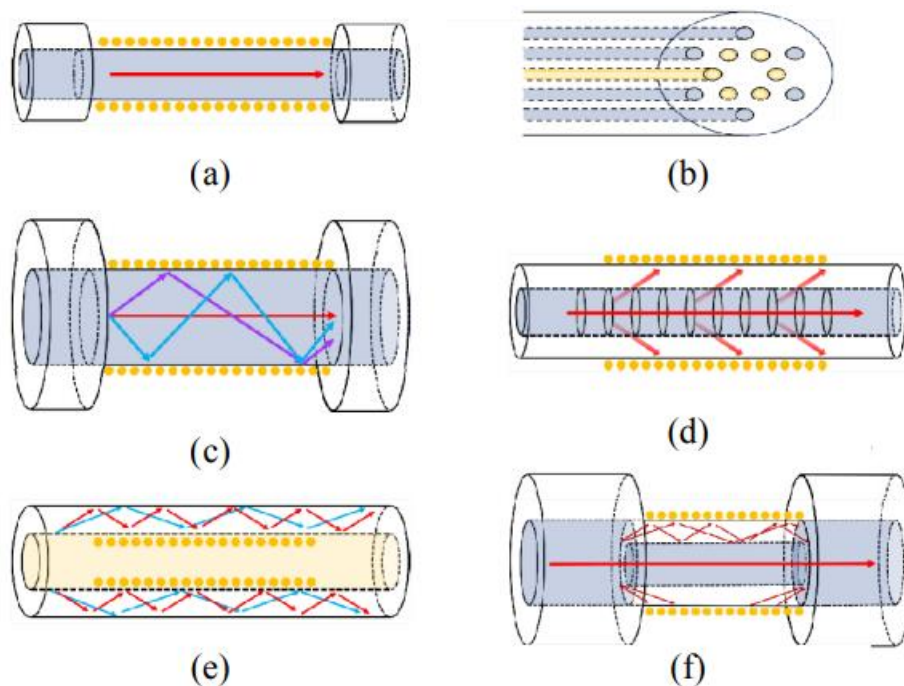


Figure 4: fiber optics types (a) SMFs, (b) PCFs, (c) MMFs, (d) FBGs, (e) HCFs structures fibers [26]

The HCFs is a field fiber with not solid cores structures. The sense structures of HCFs-LSPRs sensor considerably different from the other, as shown in Figure 4(e). Moreover being capable to create sense regions on the outer surfaces of fibers, which allow for the alteration of metals nanoparticle on inners walls of the HCFs [27]. The single structures of HCFs enable the internals air channels to serve as the fluid flows channels [28]. These designing help to minimize the influences of the externals environments on the fluid. Particularly, for PCFs-LSPRs sensor in Figure 4(b), the mixture of PCFs with LSPRs could converts the transverse magnetics (TMs) model establish in conventional plan waveguide into hybrid mode. These

transformations could be facilitating by adjust the air hole-base structures of PCFs itself, permitting for easy phases match among the cores modes and LSPRs modes, and thus producing the LSPRs under exact wavelengths condition [29]. Additionally, PCF offers the advantage of the compacts sizes and different internals air holes design. The sense regions of this fiber could be configures to accommodates metals nanoparticle with diameter lesser than or significant small than the air hole [30]. Otherwise, metals nanoparticle could be place outsides the PCFs or selective occupied within parts of the air hole [30-35]. Though, the fabrications processing for satisfying the air hole present enormous challenge, and the detections ranges are narrow. Consequently, the present researches on PCF-LSPRs sensor is mainly in the theoretic analyzing [36]. There are an sufficient scopes for enhance structure designing and detections stabilities. In its place of eliminating a sections of clad to accessing the cores-guide lights, grating that have been photo-inscribe in the cores could instead be utilize to diffracts a portions of the lights into the clad as show in Figure 4 (d). in this case the major advantage utilized the FBGs are least impacts on mechanic resistances of the fibers and couple of grating is a resonant spectacle that only occur at definite wavelength in guide configuration. Then the related to a couple resonators systems, diverse fibers mode coupled at diverse wavelength where the gratings couple two fibers mode and the metal particle layers couple a fibers modes to a localize surfaces Plasmon portion. If the two resonance overlapping and gratings resonances becomes sensitive to change in the LSPRs, therefore, because of mode couple limitations, longer periods fibers grating (LPFG) and tilted FBG (TFBG) could be direct use for LSPRs sense, while conventional shorted periods fibers grating required clad detached. The FBGs-bases LSPRs sensor [37] could offer the greatly narrow bandwidths compare to the traditional FOLSPRs sensor. Nevertheless, it is challenge to stimulate the LSPRs in the communication wavelength range use metals nanoparticle, requiring the uses of unusual design like nanowire or periodically array. The LPFG base LSPRs biosensors operate in the noticeable spectral ranges reaches a limitation of detections (LODs) lower than to $0.02\mu\text{m}$ for glyphosates [38]. The interactions of cyst amine and glyphosates lead to the changes in the operative RIs of LPFGs clad mode, producing spectral shifts in LPFGs attenuations band. The entire effects are bases on the resonances among the LPFGs attenuations band and LSPRs induce by nanoparticle that increase the sensitivities. Additionally, some strategy utilize honorable metals nanoparticle to improve the sense signal of TFBG base sensor is claim as FOLSPRs sensor. The surfaces modifications of TFBG with golden nanoparticle or golden Nano cages could realize many-folds to numerous ten-fold enhancements in the detections sensitivities of molecule, like protein and glucoses [39-42]. Though, because of the important differences in excitations wavelength among the detections spectral ranges (classically about 1500nm) and LSPRs of metal nanoparticle (classically in the observable lights ranges), we prefers to refers to this strategies as the localize electromagnetic fields enhancements for sense. Presently, some superior optical fiber or hetero-cores fiber show in Figure 4(f) are uses in the creation of LSPRs sensor. The MNFs-based LSPRs biosensors offer larger fraction of evanescent field and higher surfaces fields intensity, creating it high sensitive to disturbance in the nearby mediums, particularly for the LSPRs sense structures [43-45]. These structures facilitate the formation of a Plasmon-enhance is nearby-fields fibers probes for LSPRs sensors. Through adjusted the tips designing, the resonances wavelengths of the probes can be tune in the ranges of (500 – 850) nm, exhibit a smaller full widths at half supreme (FWHMs) of 90nm. Also, the hetero-cores fiber such as MMFs-SMFs-MMFs [46], MMFs-PCFs-MMFs [47], PCFs-FBGs [48], and curved fibers-taper seven-cores fibers-convex fibers [49] splice structure adopting the cores mismatches schemes to realized higher sensitivities exterior biomasses sense, and numerous usual hetero-cores fiber base on LSPRs sense structure is show in Figure 4 [50]. The LSPRs excite by nanoparticle play significant roles in improve the sensitivities and reduced the LODs for bio-sense. A fragment of the multicores fibers comprise 7 core arrange in a hexagonal shapes splice with SMFs is employ as LSPRs biosensors for cancer cell detection as show in Figure 5(a). The propose sensors structures is etch in a controlling manners to increases the evanescent waves and couple of mode among the core of the multicores fibers. The sensitivities are added increase by immobilize diverse nanomaterial, like optimize sizes of gold nanoparticle, grapheme oxide, and coppers oxides Nano-flower on the multicores fibers.



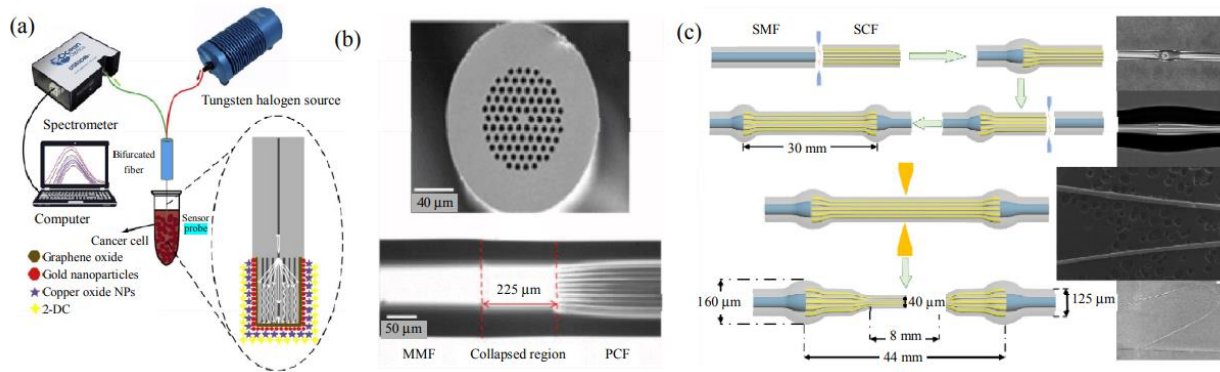


Figure 5: Hetero-cores fiber base LSPRs sense structure: (a) multicores fibers and SMFs base structures [46], (b) MMFs-PCFs-MMFs structures [47], and (c) convex fibers-taper 7-cores fibers-convex fibers structures [48].

4.3 Geometrical of Optical Fibers Probes

Altered method of splice numerous diverse type of optical fiber collected, the methods of properly modify the geometrical shapes and structures of optical fibers to improves the performances of LSPRs fibers-optics biosensor is attract widely attentions. Depend on this distinct shape, LSPRs biosensor with superior geometry could be mostly categorize into numerous commonly type: the tapering, U-types, Ω -types, and D-types. Figure 6 shows the classifications of LSPRs biosensor with singular geometric, and an example of a representative structure corresponds to every class. The SMFs are strongly able to restrict the incident lights. The energies carried by high-order modes leak into the clad as a passing wave propagates. Though, this high-orders mode carrying lower energies and it is hard to forms strongly passing fields [51]. Therefore, the intensities of the passing wave produced by the feeble passing fields are lowest; creation the phenomenon of excited the LSPRs lesser clearly. In contrasts, if a fibers is taper as illustration in Figure 6 (a), the capability of cores to confined lights is importantly reduces, resultant in a massive changes in the modes of the transmit lights. The energies of the transmit lights are couple into the clad, creating a strongly passing fields with a larger penetrations depths, that in turns excite the LSPRs [51]. Three main techniques for fabricating taper optical fiber include grinding [52], chemical etching [53], and fusion taper [54, 56]. Amongst that, the grinds technique is relative primitives, solitary utilize mechanic tool to polishes and creation a taper shapes nonetheless with high mechanic strengths. Though, it suffering from deprived repeatable that required high processing accuracies. The chemicals etch methods are involve by uses a fluorides-base solvents with a accurate ratio for corrosions. Regardless of its simplicities and costly-effective, accurate control the tapers angles prove challenge, leads to dispersions issue. In disparity, the fusions taper methods, the greatest effectual and wide employ techniques for creating taper fiber. It involves heat the fibers to a melted states by use flames or arcs discharges, shadowed by gradual taper under the apply tensions. These approaches facilitate detailed controlling over tapered and shapes, remnants modest by externals factor, and yield the greatest repeatability and accuracies. Besides, academics have openly explore the SMFs-LSPRs sensor with numerous design base on the solitary tapers units [57-60], include the periodical taper structures, tapers-in-tapers structures, truncate semi-tapers structures, and even serials quadruples tapers structures [61]. The sensor structure offers high sensitivities, though, as a numbers of taper increased, the fibers become further breakable and easy to breaks than the origin fibers structures, that need to more overcomes. Structures of U-shape fibers LSPRs sensor appearance in Figure 6(b) is bend the sense region to U-shapes and the angles of lights perpendiculars to the cores-clad interfaces could be changes. In order to optimizing and enhancing the sensitivities, the outers bend radius could be attuned. As the bend radius of the fibers decreased, the RIs sensitivities increased also. When the radius decreased to definite values, the sensitivities reach to maximal. Though, additional reducing the bend radiuses could

results in a decrease of the sensitivities. Then, explore the optimum bend radius could efficiently improves the sensitivities of U-shapes fibers LSPRs sensors [62].

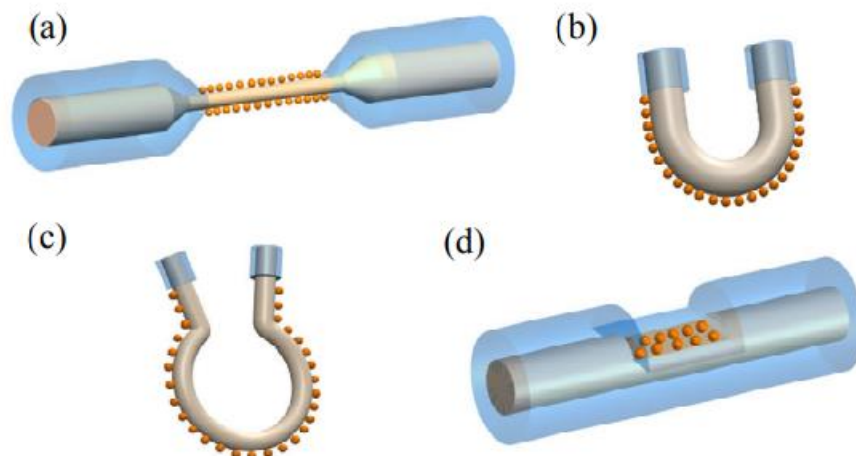


Figure 6: Classifications of LSPRs biosensor and geometric with classic structure: (a) taper, (b) U-types, (c) Ω -types, (d) D-types [61].

This approaches propose U-shape LSPRs sensors depend on AuNP which is proficient of detects bulks refractive indexes change with sensitivities and a resolutions of 540nm/RI and 3.8×10^{-5} RIUs, correspondingly. The result achieves in biosensors application is promise with slightest LODs of 0.8nM of anti-IgG. The U-shape fibers sensor is informal to fabricated and appropriate for penetrate in a narrow gap. Though, they could easy breaks throughout the bend processing, and the smallest bend diameters are limits, make it hard to more improve the sense performances. Depend on the sensitivities enhancements principles of the U-shape optical fibers sensors, to more increase the bend radius and bend lengths; S-shape sensor was projected by [63]. Compare with the solitary bend structures of U-shape sensors, the S-shape sensors with two bend structure has high sense sensitivities because of the small bend radiuses and long bend lengths. Rendering to the experiments conclusions in [64], an RIs sensitivities S-shape fiber are about 1.5 times the U-shape fibers as illustration in Figure 6. While S-shape fibers are high sensitive, its breakable structures with numerous bend make it easy damage by faster fluid flows, resultant in deprived practical. Additionally, the Ω -shape LSPRs sensors show in figure 6(c) exhibit enhance performances with small radiuses and long bend lengths, meanwhile the Ω -types fibers cause lights attenuations in bend parts because of its interactions with nearby environments, resultant in the bend losses [65].

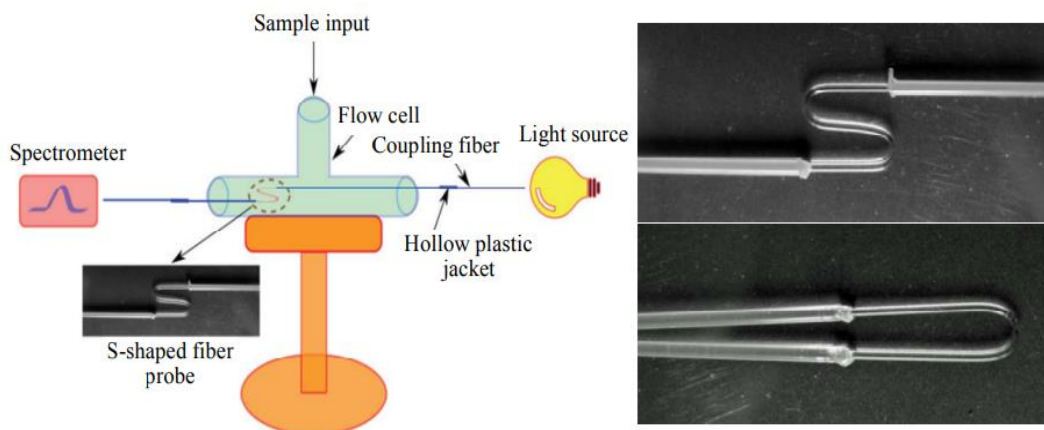


Figure 7: S-shape FOLSPRs sensors and SEMs image of S-shape fibers and U-shape fibers [66-70]

Amongst to another bents fiber like U-shape and S-shape, the Ω -shape fibers permits further fundamentals mode to transfers from the fibers cores into the clad and induce a transitions of the propagation modes from fundamentals modes to a high-orders modes, thus considerably enhance the excitements of LSPRs to attain 2.5 time peak RIs sensitivities than the U-types [66-70].

The type of fiber explained above contains stretch and bend fibers into diverse shape without varying the fibers structures. In disparity, D-shape fiber is shaped by partly removes the clad or removes the clad and portions of fibers cores to forms the structures [71] as show in Figure 6(d). These structures could exposed further passing fields and provided a flat detections planning to the investigative environments, thus induce a strong LSPRs signals and offer a steady platforms for bio-molecular analyzing [72]. Though, the grind and polish of the D-shape fibers might introduce surfaces unevenness, that cause a possible decreases in the sensitivities. In addition, conducts taper treatments on D-shape fibers could be more enhanced the sensitivities, increases it to over 10 times that of a consistent fibers LSPRs sensors [73]. Besides, the expand planar sense zone of D-shape fibers enable the creations of periodical nanostructure [74] or the gathering of 3-dimension (3Ds) mixture multilayers structure [75] to facilitated sensitize and multiplexes in LSPRs sensors. This numerous type of optical fiber, geometrical structure, and transmissions scheme mention overhead could be free combine, and even multiples geometrical structure and type could be uses to realize high sensitivities and encounter the definite applications requirement. In practice application, we also want to considered factor like manufacture costs and complexities, sensors stabilities and durable, and transmissions distances, and then adapt the designs of LSPRs sensor systems according to these conditions.

5. Fabrication techniques of Isprsr sensor area

Additional to the geometrical parameter of the optic fibers, the performances of the optic fibers LSPRs sensors are influence by the nanostructures configurations of the sense regions. The nanostructures configurations of sensor regions include the shapes, sizes, and arrangements of the metals nanoparticle that plays vital roles in regulation the interactions among the nanoparticle and lights, therefore impacts the intensity and frequencies of LSPRs effects. Through the optimization of nanostructures configurations, the sensitivities, choosiness, and constancy of sensors could be attuned, assisting further accurses and reliable bio-analyze and environment observing. Diverse applications requirement might need many nanostructures configuration. Therefore, in case of design optic fibers LSPRs sensors, it is vital to widely considering the relationships among the nanostructures parameter and sensors performances to chance particular applications requirement.

5.1 Nanoparticle Self-assembly

Presently, honorable metals nanoparticle, like AuNP [76], gold Nano rod [77], and silvers Nano-particle [78], are common use for optic fibers LSPRs sensor. Amongst this, gold-base nanoparticle is particular advantage because of their outstanding structure steadiness, oxidations resistances, and bio-compatible. As results, they are extensive utilize in experiment study. The predominates approaches for immobilize nanoparticle in the sensor regions of fibers involve chemical bond the nanoparticle to the modify sense surfaces by use chemical reagent and function group, therefore realizing the self-assemble of sensor structures. In current year, there is considerable report on the applications of self-assemble old nanoparticles layer in optic fibers LSPRs sensor, and all study mainly relying on two method. The furthestmost common employ approaches involve hydroxyl salinization on a glasses substrate by use saline couple agent. That permits the captured of AuNPs over the amino or Thiel terminals group of self-assemble films, facilitate the preparations of the sensor regions as show in Figure 8(a). The saline methods encompass two modifications scheme: amine salinization and Thiel salinization. The mine salinization is depend on the principles of positives and negatives adsorptions effect. It involves the uses of solution like (3-aminopropy) [79] (APTESs) or (3-aminopropy) trim [80] (APTMSs) to amino functionalizes the surfaces of the optic



fibers over an animation reactions, therefore impart a positives charges. Therefore, the negative charge nanoparticle could be bounds to the positive charge optic fibers surface over electrostatics forces, particular the interactions of ionic bond. Thiel salinization, involve functionalize sensors regions by usage (3-mercaptopropy) MPTMSs [81]. The principles of these methods are as follow: the methyl group (Si-OCH₃) of MPTMSs could be hydrolyze into silently group (Si-OH). The interactions amongst Si-OCH₃ and moderately hydrolyze silanol group result in the realization of a self-assemble films with Thiel group cover the surfaces of the optics fibers. The AuNP could be captures by the thiol group on surfaces to monolayers on optics fibers. Other frequently use technique rely on electrostatics adsorptions effects, utilize electrostatics layers-by-layers self-assemble of polyelectrolyte and surfaces charges of nanoparticle for self-assemble of nanostructure [82] as show in Figure 8(b).

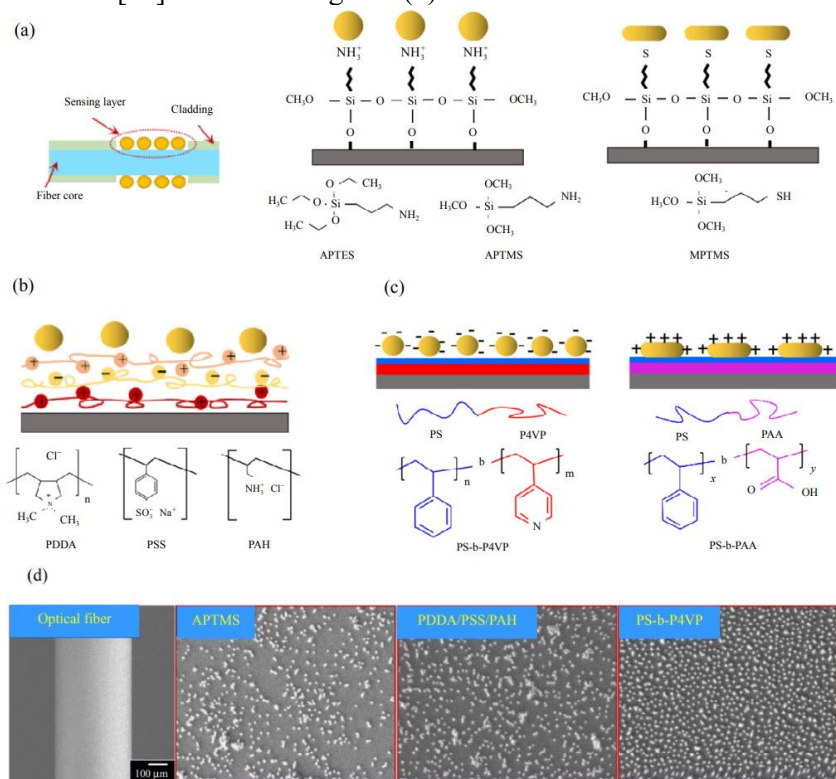


Figure 8: Nanoparticle-based self-assemble method for fibers optics LSPRs sensors fabrications [82]

Additionally, experiments data indicates a relative lower analysis of nanoparticles monolayer gotten via self-assemble, that slightly restrict its possible for applications in fabrications of highs-performances, larger-scales, and costs-effectives fibers sensor. Equally, the layers-by-layers self-assemble technique employ polyelectrolyte demonstrates a fast electrostatics adsorptions rates, resultant in a considerable reductions in depositions times and operation difficulty whereas improving the particles surfaces coverage's. These procedures capably addressed the limitation of these methods [83]. Though, it is connected with challenges like an unpredictable particles diameters and added additional difficulty preparations processing. A novel and multipurpose self-assembling method was recommended for the fabrication of fiber LSPR sensors by [84]. Their method utilize blocks copolymers-base templates to conductor the self-assemble of nanoparticle on the templates surfaces, resultant in the higher analysis, lower aggregations, and control nanostructure as illustrated in Figure 8(c). As the solutions concentrations decreased, the copolymer follow to the substrates as Nano-scale film, enabling the uniforms self-assemble of nanoparticle on the polymers films surfaces which lead to lower aggregations and higher analysis monolayers nanostructure. The well-behaved and detailed self-assemble is depend on facts the multiples

hydrogen bond site on the hydrophilic segment binds to the hydroxylase substrates, whereas the metals nanoparticle is bounded to the hydrophilic segment over surfaces charge, like electrostatics adsorptions and ionic bond. The incidence of freely hydrophobic polystyrenes (PSs) chain prevents particles aggregations. These approaches result in nanostructure with wanted surfaces morphologies characterize by higher attention and lower aggregations. It is value mention that it permits for uses of numerous type and blocks lengths ratio of blocks copolymer for templates fabrications. For example, PSs-b-P4VPs and PSs-b-PAAAs could be employ to yield order template where P4VPs chain binds negative charge nanoparticle via protonate amino group, and PAAAs chain binds positive charge nanoparticle over deprotonate carboxyl group, correspondingly [85]. Therefore, these enable operative surfaces self-assemble of negative and positive charges golden Nano-sphere-Nano-rod [86]. If this compare to the conventional method mention above in Figure 8(d), the result demonstrated that golden Nano-spheres assemble by use APTMSs or PDDAs/PSSs/PAHs could covers the whole surfaces nonetheless exhibits non-uniforms dispersions and aggregations. In difference, golden Nano-spheres assemble by use PSs-b-P4VPs don't realize the completed surfaces treatment, nonetheless exhibits uniform dispersions without particles aggregations and forms monolayers nanostructures. In term of surfaces treatment, the PSs-b-P4VPs methods demonstrate the significant high performances compare to another method for APTMSs and for PDDAs/PSSs/PAHs. The blocks copolymers templates methods efficiently reduce particles aggregations, enhance particles surfaces coverage, and hold abundant possible to improve sensor sensitivities and stabilities, simplify the preparations processing, and reduce cost.

5.2 Assemblies and transfers of periodical arrays of nanostructures

From the traditional chemical self-assembly method, academics have examined non-chemical bond strategies to fabricate a sensor region. Technique like focused ion beams (FIBs) milling, micro-electromechanical systems (MEMSs), and electron beams lithography (EBLs) were employed to generate periodic nano-arrays, which could be efficiently utilized in fiber LSPRs sensors.

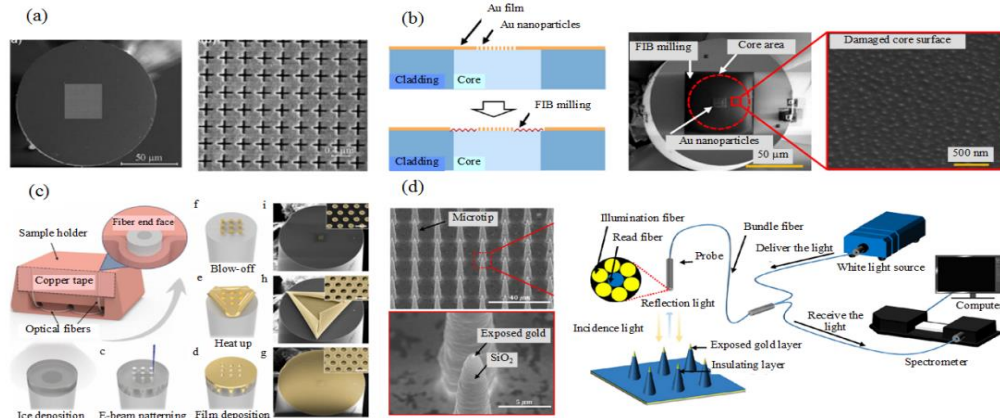


Figure 9: Non-chemicals bond strategy to fabrications of sense region: (a) cross-shape Nano-array [79], (b) AuNP array [80], (c) Nano-disks array [81], (d) arrays of metal nanostructure micro tips [82], ends and faces of fiber.

Amongst this strategy, FIBs millings is mainly utilize for fabrications of periodical nanostructure like Nano-holes, disk, and pillar on ends faces of optic fiber. The crosses-shape nanostructures are fabricates on the ends faces of fibers, as show in Figure 9(a) [87-90] successful employ FIBs millings to produce an AuNP array on the cores ends faces of an optic fibers as show in Figure 9(b), realizing a refractive indexing sensitivities of 5700/RIUs. Though, FIBs millings enable the productions of uniform structure Nano-array with stabled sense performances and its lower succession rates, higher costs, and difficult manufacture processing limits appropriateness for larger-scales process application. Y. Hong et al. [91] propose a solvent-freely Nano-fabrications methods depend on the emerge ice-assist electrons beams lithograph

(iEBLs) techniques, that offer a streamline and eco-friendly approaches for implement e-beams pattern on substrate with arbitrary shape as show in Figure 9(c). They effectively fabricate periodical Nano-structure; include silvers concentric ring, V-shapes Nano-antenna array, bowtie array, and rings array. This technique allow for productions of varied and high uniform structure, and offer low costs and high success rates compare to FIBs millings. Though, the fabrications processing remain relative difficult. The MEMSs techniques is employ to fabricates a uniform distribute arrays of nobles metals nanostructure on a silicon micro tips on the ends faces of an optic fibers [92], as exposed in Figure 9(d). The resultant LSPRs sensors demonstrate the outstanding reproducible, steady reliabilities and promising optic property in measurements systems. The periodical and longer-lasts particles arrays achieve over MEMSs skill position it promise methods for commercialize LSPRs application. In decision, self-assemble and periodical arrays assemble method have advantage and disadvantage. The self-assemble technique is characterizes by simplest preparations processing and low costs. Though, it is challenges to precise controlling the self-assemble of nanoparticle throughout the bind processing, resultant in distributions of particle in disperse and disorder structures. Additionally, issue like locally particles sheds and aggregations could have impacts on the performances of sensors. Hence, the periodical arrays assemble methods enable the making of high order periodical Nano-array, lead to sensor with higher sensitivities, repeatable, and stabilities. Conversely, this technique needs the utilizations of advance micro/Nano fabrications technique, that significant elevate the manufacture cost. Moreover, the substrate use in these methods is most flat, that restrict the fabrications of structure to D-types or fibers ends face, thus presented implementations challenge.

6. Folsprs biosensors applications

The FOLSPRs sensors have emerge as a promise tools for biosensors application. It offer numerous advantage over others sensor configuration. The LSPRs is a phenomenon occurs in case of nobles metals nanoparticle is excite by lights, resultant in strongly absorptions and scatter at precise wavelength. Through immobilize biomolecule on surfaces of this nanoparticle, change in locally RIs cause by bimolecular interaction could be detects. The single property of FOLSPRs sensors made it appropriate for numerous biologic detections scenario. The smaller sizes and flexibilities of optics fiber enabling relaxed integrations into complexes biologics system, like implant device or labs-on-a-chips platform. These allow for real-times, distant, and slightly aggressive monitor of bio-molecules interaction.

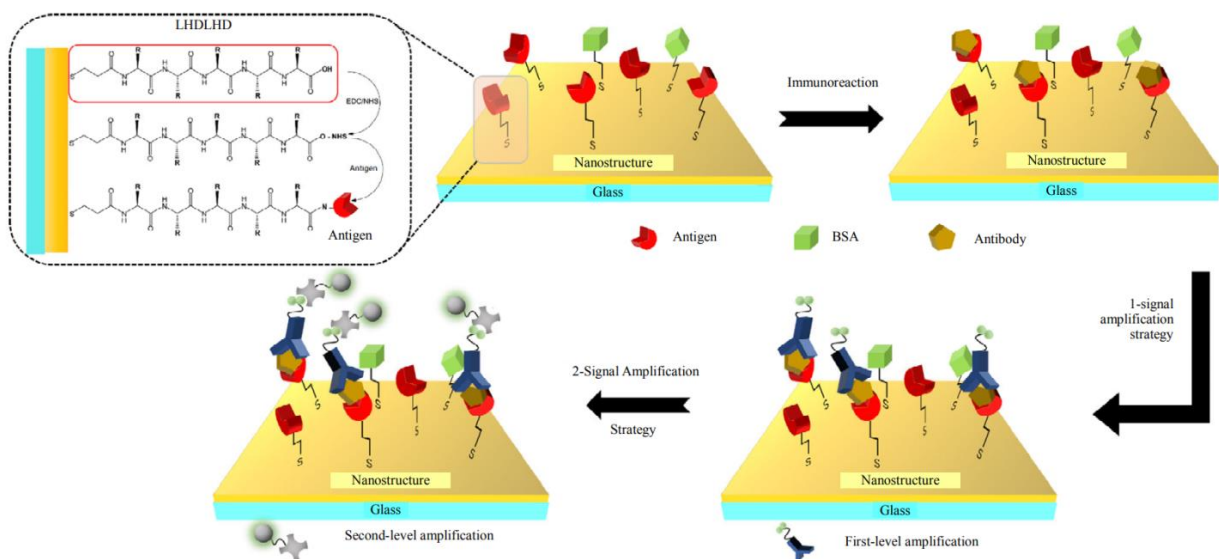


Figure 10: Schematics diagrams of classic antigen-antibody immunoassaying sense processing.

Furthermore, the localize natures of LSPRs in Nano-scales region ensure a higher sensitivities and labels-freely detections. These eliminate the needs for bulk label or tag makes it appropriate techniques for multiplex assay and higher-throughputs screen. Moreover, the tailor designs and fabrications of metals nanoparticle or Nano-array could improve the sensitivities and selectivity of sensors for exact targets molecule. The adaptability of fibers optics LSPRs sensor allow for detections of a widely ranges of analyses, include protein, pathogen and cell, nucleic acid (DNAs and RNAs), and another smaller biomolecule (organics compound and heavy metals ion). Proteins immunoassaying is presently the almost wide studies applications of FOLSPRs biosensor. The overall proteins molecular detections and signals amplifications strategy is show in Figure 10. Naturally, the sensor regions of the nanoparticle/periodical structures surfaces are modify by thiol via golden sulfur bonds with a carboxyl groups at another ends. sulfur bonds with a carboxyl group at the other end.

The anti-bodies or antibodies fragments is immobilize as a bio-recognitions elements on monolayers throughput the carboxyl groups that has been pre-activate by use EDCs/NHSs carbodiimide hydrochlorides (EDCs), N-hydroxysuccinimide (NHSs) solutions. If the correspond antigens are bounds to the surfaces-immobilize antibodies inside the electric fields ranges, these interactions disrupt the Plasmon and consequences in a changed the reflections intensity, permitting to determine the analytic concentrations. Additionally, to thiol, other reagent like peptide and dextran are modify on the sense regions surfaces to produce further anchor point. Because of larger difference in the molecular weights of numerous protein, the locally fields change induce by binds a targets protein with captured probe also differ, leads to altered detections sensitivity. For larger protein, like IgG, their higher masses are adequate for sensitive sense and could be direct monitor [93, 94]. Equally, a smaller molecules immunoassaying presentation is challenge. The smaller sizes of targets proteins itself is incapable to produce adequate LSPRs signals, the antibodies-antigens bind induce a smaller masses variations, that cannot offer sensitive analyzing. Consequently, amplifications strategy, like sandwich assay [95], is requiring improving the signals [96]. H. M. the report of sandwiches assays for ultrasensitive thyroglobulin (Tg) detections via implementation of second antibodies and a second golden nanoparticles signals amplifiers, as illustrated in Figure 10 [97]. The limitation of detections (LODs) is improved by around 15 times from (97.6fg- 6.6fg)/mL Nucleic acid served as reservoirs of genetics data in the humans bodies, and their polymorphisms analyze and mutations detections could efficiently identify condition such as tumor and infectiousness disease. Naturally, the doubles-strand structures of dioxin ribonucleic acids (DNAs) is disrupt via higher temperatures or higher PHs, and the classification is determine over hybridizations with singles-strand DNAs fragment. Therefore, the FOLSPRs has been introduce as a movable and high sensitively sensors for labels-free detections of DNAs, yield capable result. In these techniques, the capture DNAs is immobilizes on sensors surfaces thru golden-sulfur bond. When the conforming complementary targets DNAs are presents in the samples, it will hybridize with captured DNAs [98].

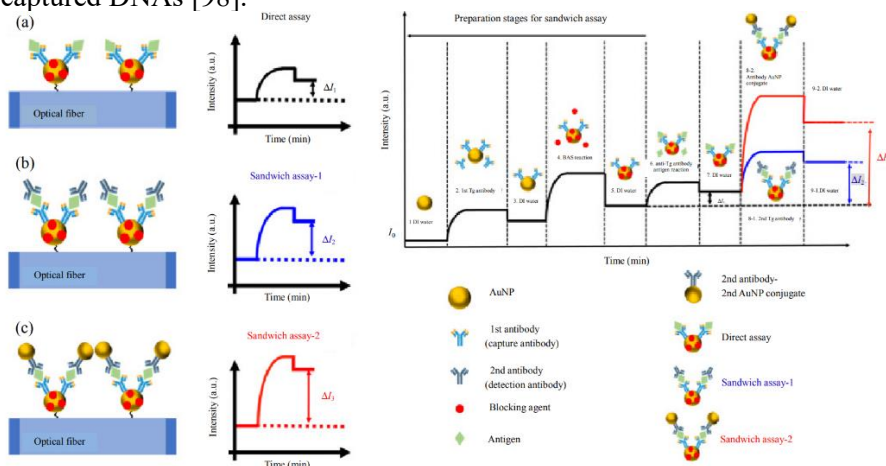


Figure 11: Schematics diagrams of thyroglobulin by direct antibodies, secondary antibodies sandwiches assays, and antibodies-golden nanoparticles conjugated sandwiches assays [98]

These binds happening on nanoparticle disturb localize surfaces Plasmon, varying the resonances condition and producing change in optical signal. Though, when the quantities of targets DNAs is inadequate to induced the LSPRs, a sandwiches construction is employ to improve the detections signals. Figure 11 shows the captured DNAs only hybridizes with one half of the targets DNAs, whereas another half of the targets DNAs is then hybridizing with other probes DNA. The probes DNA is pre-modify with signals amplifications molecule on one ends to realize the secondary signals amplifications. The signals amplifications molecule could be glowing dye, protein, AuNP, or other substance, depend on the definite requirement of spectroscopy, image, and another detections method [99]. Furthermore, certain reports nucleic acids detections strategy shows in Figure 11 use for SPRs sensor is appropriate to fibers LSPRs sensor, include modest detections of micron ribose nucleic acids (miRNAs), sandwiches-base detections of DNAs, and tamer-base detections, amongst other [100]. As show in Figure 12(a), in attendance of targets cfDNAs, the hairpin H1-AuNP and H2 is trigger by the hybridizations chains reactions (HCRs), and then the Ω -shape FOLSPRs biosensors fabricate with the captured DNAs capture the HCRs products for synergistically amplify the LSPRs signals [101]. As in [102], they suggested a phenyl boronic acids (PBAs) probes for miRNAs detections, as show in Figure 12(b), the targets miRNAs and subsequent opposite DNAs were hybridize with captured DNA. The PBAs-AuNP can added binds with ribose in miRNA rather than dioxin ribose in balancing DNA to amplified the sense signals.

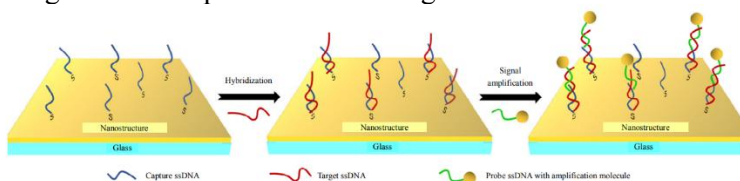


Fig. 10 Schematic diagram of the ssDNA sensing detection process.

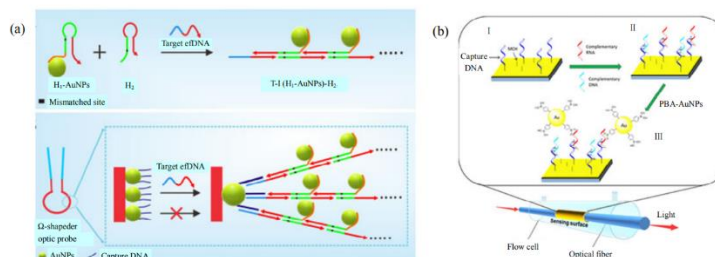


Figure 12: Scheme of signals amplifications strategy for nucleic acids detections: (a) multi stage nanoparticles amplifications [101] and (b) boric acid-golden nanoparticles sandwiches assays [102].

Additionally, detections strategy for another molecule is comparable to protein and nucleic acid as mentions before. The detections strategies can determine depend on size of targets molecule. Particularly, detections of microorganism like living cell, bacteria, and worms could be used to direct capture them onto the surfaces of fibers sensors for detections. The development of a U-shape FOLSPRs biosensors for the colorectal cancers cells detections have been proposed by [103] as show in Figure 12(a), the cells can captures by immobilize Con A onto the fibers over exact binds amongst Con A and the N-glycan expressions on the cells surfaces. The crypto sensors afford the ultra-sensitivities for cancers cells detections with the LODs of 30cells/mL with high linearity in widely ranges of $1 \times 10^2 - 1 \times 10^6$ cells/mL. Moreover, the FOLSPRs biosensors could be employ to inactivate tumors cell by in-site lasers heats or another photo thermal therapy, therefore realizing therapeutics purpose. The Ω -shape FOLSPRs biosensors show in Figure 12(b) is design for real-times and label-freely microscopic detections [104]. The surfaces-immobilize a tamers explicitly captured the salmonella type hymenium, resultant in LODs down to 128 CFU/mL in a linear ranges from $5 \times 10^2 - 1 \times 10^8$ CFU/mL, that demonstrate an improved selectivity for the salmonella type hymenium detections compare to another microbes. The LSPRs biosensors that uses MCFs with 7-core organized in a hexagonal patterns proposed by [105] which splice with SMFs for shigella bacteria detections, and display

a widely linearization detections ranges from [106] CFU/mL with a lower LODs of 1.56 CFU/mL. Figure 12(c) show the design processing of increase passing wave and model couple among MCFs core, whereas the coatings with AuNP and molybdenum disulfides improves the excitations of localize Plasmon's. The J-shape optic fibers is gotten by fold an Ω shapes as illustrated in Figure 12 (d), a spacers nucleic acids with shorter stems-loops structures are adopts to controlling concentration and additional improve the LSPRs signals responses .

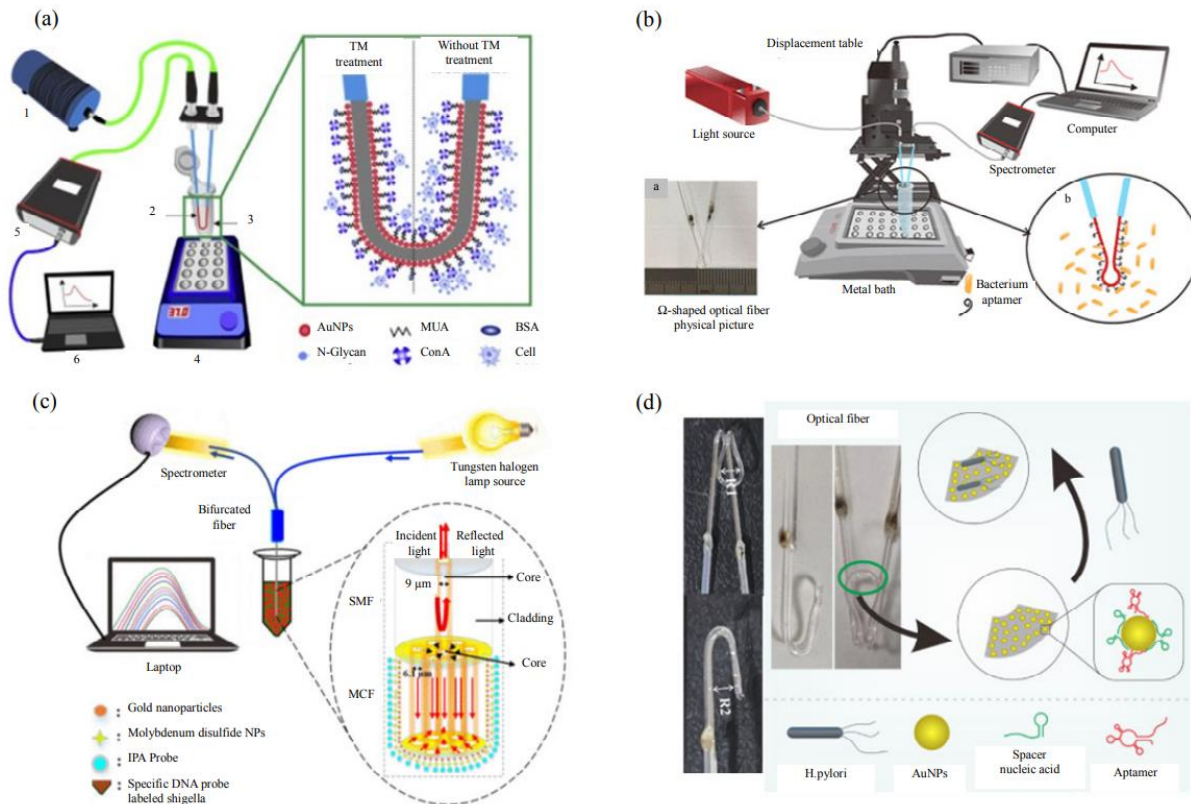


Figure 13: FOLSPRs biosensor diagrams for the microorganism detections: (a) U-shape FOLSPRs biosensors for the cancers cells detections [83], (b) Ω -shape FOLSPRs biosensors for the salmonella type hyemium detections [105], (c) MCFs-SMFs FOLSPRs biosensors [106].

In smaller molecule like cholesterol, ascorbic acids, cretonne, and glucoses, definite captures probe could directly immobilize on the surfaces of fibers to attain the detections by exact bindings among the captures probes and targets molecules. Usually use captures probes molecule in this case included the boronic acids, streptavidin, and enzyme. Through select the suitable enzymes as recognitions elements for targets molecules, high specificities and selectivity could be realized. Glucoses oxidase is an enzyme that catalyzes the oxidations of glucoses. Through immobilize glucoses oxidases on the surfaces of a U-shape FOLSPRs sensors, blood glucoses level could be measure quickly in shorter periods of times [107]. These methods required around 150 μ L of blood samples. For small molecule like weighty metals ion, secondary signals amplifications strategy is necessary to detect molecular interactions at ultra-lowest concentration. Comparable to nucleic acids detections structure, sandwiches assay, nanomaterials improvement approach, and more technique could be utilize to attain the detections of molecular interaction at very little concentration. An wavelengths-modulate FOLSPRs sensors coating by golden Nano-sphere for high sensitively Hg^{2+} detections (LODs: lower to 0.7nM) base on thymine- Hg^{2+} -thymine based couple mismatch systems have been proposed by [108] as show in Figure 14 (a). an ZENs nucleic acids antimere

is modify on cross-sections of FOSPRs ends to ZENs detections illustrated in Figure 14 (b) with lower LODs of 0.102ng/mL.

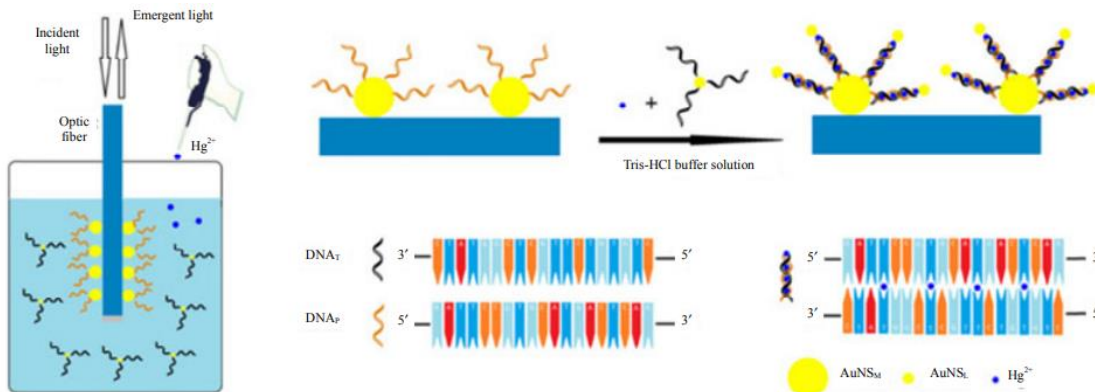


Figure 14: Schematic diagram of FOLSPR biosensors for small molecules including (a) heavy metal ion Hg²⁺ and (b) food toxin ZEN [108].

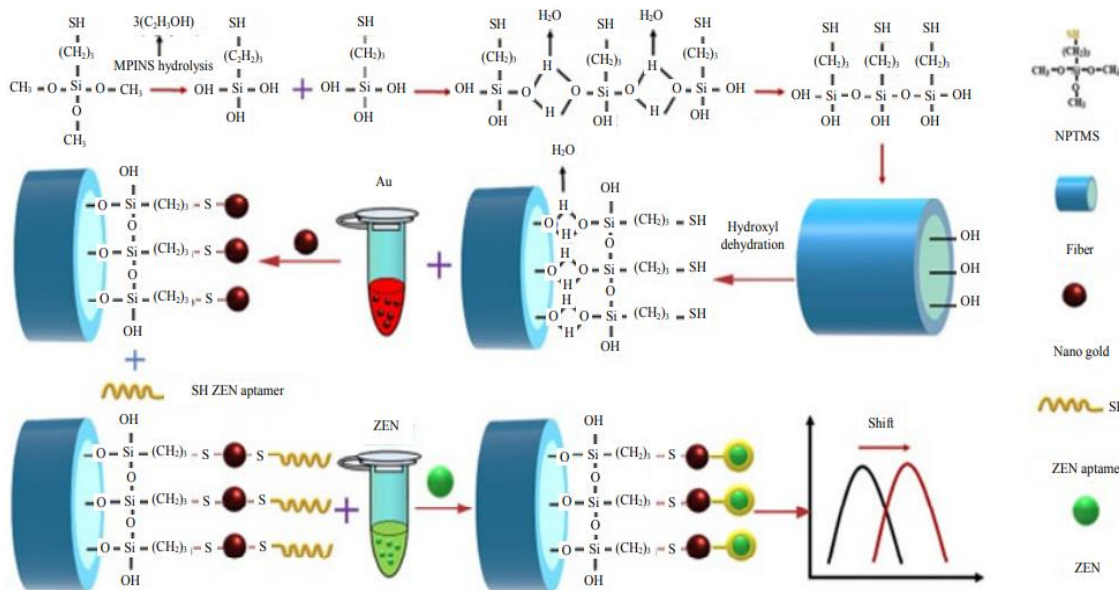


Figure 15: FOLSPRs biosensor scheme for smaller molecule include (a) heavyweight metals ions Hg²⁺ (b) foods toxin ZENs [109].

Amongst them, the grapheme oxides (GOs) has receive the utmost wide attentions. The developing GOs have been widely presented into FOLSPRs bio-sense due to their plentiful oxygen functional groups and larger surface areas, which efficiently enhance the functionalization of biomolecules and improve the sensing performance of biomolecules. Higher tilt fiber grating LSPRs sensors by decorating golden Nano-shell on ExTFGs surfaces and depositing functionalized GOs on sensor surfaces to identify PD-L1 monoclonal antibody in human serum of liver cancer patients have been proposed [110]. Table 1 shows the

performances of recognition techniques with different fiber-optic LSPRs biosensors. Many other approaches have been introduced in this field, such as [111-117].

Table 1: Performances of recognition techniques with different fibers optics LSPRs biosensors approaches.

References	performance	Techniques	Target	Direction
[79]	LOD: 14.0 pM	Ω -type MMF	MCF-7 cancer cells	Direct
[50]	LOD: 12 cells/mL	Ω -type MMF	E.coli B40	Phage T4
[91]	LOD: 1.56 CFU/mL	U-bend MMF	Shigella bacteria	MoS2-DNA
[77]	LOD: 25.5 μ M	SMF-PCF	Cholesterol	Sandwich
[80]	LOD: 15.12 μ M	Ω -type MMF	Ascorbic acid	enzyme
[89]	LOD: 128.4 μ M	SMF-HCF	Creatinine	enzyme
[88]	LOD: 1.06 nm/mM	SMF-photosensitive	Glucose	enzyme
[67]	LOD: 0.8 nM	Straight MMF	Human IgG	Direct
[93]	LOD: 0.85 ng/mL	U-bend MMF	AFP	Direct
[20]	LOD: 14.0 pM	HCF	Transferrin	Direct
[94]	LOD: 0.19 pg/mL	Straight MMF	Thyroglobulin	Direct
[95]	LOD: 100 fg/mL	SMF	f-PSA	Direct
[39]	LOD: 96 ng/mL	MMF	Cardiac troponin I	Sandwich
[82]	LOD: 67 pM	Straight MMF	rop B DNA	Sandwich

7. Conclusions

The fibers optics LSPRs depend on well-order nanoparticle monolayers or periodical nanostructure under definite condition lead to better improvements of localize electric field compare to SPRs without the Nano-material and provide the suitable solutions for micro-smarts biologic integration sensors. To improve the sense performances of FOLSPRs sensor, numerous methods could be use include diverse type of fiber with optimize geometrics structure and the shape include taper U-types, Ω -types, and D-types) and utilize advance surfaces assemble scheme to realize order monolayer of nanoparticle or periodical nanostructure to improve the sensitivities and constancy of sensors, and customize recognitions and measurable analyzing strategy could be design to definite biomolecule. In fields of biomedical diagnostic, they could be used for labels-freely detections of biomarker, DNAs hybridizations, proteins-proteins interaction, and pharmaceutical analyzing. Furthermore, the current developments of the compacts, portables, and costs-effectives instrumentations are expects to facilitated the widely adopt of those biosensor in numerous field. Therefore, FOLSPRs biosensor is composed to revolutionize the fields of biosensors, permitting the quick and correct biomolecule detections, diseases diagnosing, and environments monitor in real times. Though FOLSPRs biosensor has originated widespread structure, manufacture, and bio-application, there are ongoing researches to more improve their performances. Resultant in much area in developments of FOLSPRs biosensor is expected.

1. Progress and applications of the multi-channels FOLSPRs biosensor. Presently, utmost bio-application required measurable detections of multiples biomolecule or removal of interference from un-relate molecule. To decrease the complexities and costs of measurements system and enabling simultaneousness assessments of multiples parameter relate to disease or the environments, the designing of FOLSPRs biosensor that could concurrently measures multiples biomolecule or performs multiples measurement of similar biomolecules in a multi-channels FOLSPRs biosensors will be an operative developments approaches in practice application.

2. Utilizations of newer material and technology innovation for improving the sensitivities of FOLSPRs biosensor. We discuss the promise advancement in enhancing the sensitivities of FOLSPRs biosensor by use two dimensions material, like molybdenum disulfide and graphene oxides. Through joining advance



material likes carbons nanotube, it is probable to improve the contacts areas among the sense surfaces and targets molecule over the optimize designing of the sense layers structures. In addition, thru manipulate the parameter of sense layers of two-dimension material like tunable bands gaps and outstanding electronics transportation property of blacks phosphorus, the locally electromagnetic fields effects on the sense surfaces which could be intensify. Those methods have the possible to offers newer possibility for more improving the sense performances.

References

- [1] J. Y. Guang, M. D. Lu, Y. Liu, R. Z. Fan, C. Wang, R. Liu, "Flexible and speedy preparation of large-scale polystyrene monolayer through hemispherical-depression-assisted self-assembling and vertical lifting," *ACS Applied Polymer Materials*, 2023, 5(4): 2674–2683.
- [2] Qi WANG, Dianyun ZHANG², Yizhuo QIAN², Xiangyu YIN², Lei WANG², Shushuai ZHANG², and Yuyang WANG², Research on Fiber Optic Surface Plasmon Resonance Biosensors: A Review, *PHOTONIC SENSORS* / Vol. 14, No. 2, 2024: 240201
- [3] Ananna Chaki Chaity, Highly Sensitive Photonic Crystal Fiber Biosensor Based on Surface Plasmon Resonance for Six Distinct Types of Cancer Detection, Rajshahi University of Engineering and Technology, October 12th, 2023
- [4] X. Yang, C. Gong, C. Zhang, Y. Wang, G. F. Yan, L. Wei, "Fiber optofluidic microlasers: structures, characteristics, and applications," *Laser & Photonics Reviews*, 2022, 16(1): 2100171.
- [5] C. Liang, J. Lai, S. Lou, H. Duan, and Y. Hu, "Resonant metasurfaces for spectroscopic detection: physics and biomedical applications," *Advanced Devices & Instrumentation*, 2022, 2022: 9874607.
- [6] P. Mohankumar, J. Ajayan, T. Mohanraj, and R. Yasodharan, "Recent developments in biosensors for healthcare and biomedical applications: a review," *Measurement*, 2021, 167.
- [7] A. Rezaabakhsh, R. Rahbarghazi, and F. Fathi, "Surface plasmon resonance biosensors for detection of Alzheimer's biomarkers; an effective step in early and accurate diagnosis," *Biosensors & Bioelectronics*, 2020, 167: 112511.
- [8] P. S. Pandey, Y. Singh, and S. K. Raghuwanshi, "Theoretical analysis of the LRSPR sensor with enhance FOM for low refractive index detection using MXene and fluorinated graphene," *IEEE Sensors Journal*, 2021, 21(21): 23979–23986.
- [9] F. Mumtaz, B. Zhang, M. Roman, L. G. Abbas, M. A. Ashraf, and Y. Dai, "Computational study: windmill-shaped multi-channel SPR sensor for simultaneous detection of multi-analyte," *Measurement*, 2023, 207: 112386.
- [10] B. Hossain, A. Kumar Paul, M. Arefin Islam, M. Faruk Hossain, and M. Mahabubur Rahman, "Design and analysis of highly sensitive prism based surface plasmon resonance optical salinity sensor," *Results in Optics*, 2022, 7: 100217.
- [11] S. Long, E. Wang, M. Wu, H. Zhu, N. Xu, Y. Wang, "Sensing absorptive fluids with backside illuminated grating coupled SPR sensor fabricated by nanoimprint technology," *Sensors and Actuators A: Physical*, 2022, 337: 113416.
- [12] F. Mumtaz, M. Roman, B. Zhang, L. G. Abbas, Y. Dai, M. A. Ashraf, "MXene (Ti₃C₂T_x) coated highly-sensitive D-shaped photonic crystal fiber based SPR-biosensor," *Photonics and Nanostructures – Fundamentals and Applications*, 2022, 52: 101090.
- [13] J. Gao, S. Jiang, W. Yang, R. Liu, J. Feng, Z. Zha., "Design a D-shaped single mode fiber SPR sensor with a composite nanostructure of HMM/monolayer graphene for DNA hybridization detection," *Optics & Laser Technology*, 2023, 158: 108854.
- [14] Q. Wang, H. Song, A. Zhu, and F. Qiu, "A label-free and anti-interference dual-channel SPR fiber optic sensor with self-compensation for biomarker detection," *IEEE Transactions on Instrumentation and Measurement*, 2021, 70: 1–7.
- [15] W. Zhang, M. Wu, X. Wang, Z. Tong, M. Dong, and G. Yan, "Temperature insensitive salinity sensor with U-shaped structure based on few-mode fiber," *Optical Fiber Technology*, 2023, 76.
- [16] Z. H. Ren, Q. Wang, X. W. Cong, W. M. Zhao, J. R. Tang, L. Wang, "A fiber SPR sensor with high comprehensive evaluation indicator based on core mismatched U-shaped and tapered arm," *Measurement*, 2023, 206: 112248.
- [17] R. A. Kadhim, A. K. K. Abdul, and L. Yuan, "Advances in surface plasmon resonance-based plastic optical fiber sensors," *IETE Technical Review*, 2020, 39: 442–459.
- [18] C. Teng, M. Li, R. Min, S. Deng, M. Chen, M. Xue, "A high-sensitivity SPR sensor based on MMF-tapered HCF-MMF fiber structure for refractive index sensing," *IEEE Sensors Journal*, 2022, 22(19): 18517–18523.



- [19] Z. Yang, L. Xia, C. Li, X. Chen, and D. Liu, "A surface plasmon resonance sensor based on concave-shaped photonic crystal fiber for low refractive index detection," *Optics Communications*, 2019, 430: 195–203.
- [20] L. Li, Y. Wei, X. Zhao, C. Liu, R. Wang, T. Jiang, "Dual-channel step multimode fiber SPR sensor based on sawtooth structure," *Optical Fiber Technology*, 2022, 71: 102897.
- [21] N. Cennamo, F. Arcadio, M. Seggio, D. Maniglio, L. Zeni, and A. M. Bossi, "Spoon-shaped polymer waveguides to excite multiple plasmonic phenomena: a multisensor based on antibody and molecularly imprinted nanoparticles to detect albumin concentrations over eight orders of magnitude," *Biosensors & Bioelectronics*, 2022, 217: 114707.
- [22] L. Li, Y. Wei, W. Tan, Y. Zhang, C. Liu, Z. Ran, "Fiber cladding SPR sensor based on V-groove structure," *Optics Communications*, 2023, 526: 128944.
- [23] S. Zhang, Y. Peng, X. Wei, and Y. Zhao, "High-sensitivity biconical optical fiber SPR salinity sensor with a compact size by fiber grinding technique," *Measurement*, 2022, 204: 112156.
- [24] Y. Wei, X. Zhao, C. Liu, R. Wang, T. Jiang, L. Li, "Fiber cladding dual channel surface plasmon resonance sensor based on S-type fiber," *Chinese Physics B*, 2023, 32(3): 030702.
- [25] X. Jiang and Q. Wang, "Refractive index sensitivity enhancement of optical fiber SPR sensor utilizing layer of MWCNT/PtNPs composite," *Optical Fiber Technology*, 2019, 51: 118–124.
- [26] C. Liu, Y. Gao, Y. Gao, Y. Wei, P. Wu, and Y. Su, "Enhanced sensitivity of fiber SPR sensor by metal nanoparticle," *Sensor Review*, 2020, 40(3): 355–361.
- [27] Q. Wang, X. W. Cong, W. M. Zhao, Z. H. Ren, N. N. Du, X. Yan, "High figure of merit SPR sensor based on raspberry-like silica," *IEEE Transactions on Instrumentation and Measurement*, 2022, 71: 1–8.
- [28] M. Luo and Q. Wang, "A reflective optical fiber SPR sensor with surface modified hemoglobin for dissolved oxygen detection," *Alexandria Engineering Journal*, 2021, 60(4): 4115–4120.
- [29] M. F. Naief, Y. H. Khalaf, and A. M. Mohammed, "Novel photothermal therapy using multi-walled carbon nanotubes and platinum nanocomposite for human prostate cancer PC3 cell line," *Journal of Organometallic Chemistry*, 2022, 975: 122422.
- [30] Q. Wang, A. Zhu, F. Qiu, L. Wang, X. Y. Yin, W. M. Zhao, "High sensitivity coreless fiber surface plasmon resonance sensor based on Au Nano biconical particles," *IEEE Sensors Journal*, 2022, 22(1): 256–263.
- [31] Q. Wang, X. Jiang, L. Y. Niu, and X. C. Fan, "Enhanced sensitivity of bimetallic optical fiber SPR sensor based on MoS₂ nanosheets," *Optics and Lasers in Engineering*, 2020, 128: 105997.
- [32] T. Li, L. Zhu, L. Lu, R. You, X. Bian, G. Ren, "Highly sensitive optical fiber plasmonic sensors by integrating hydrogen doped molybdenum oxide," *IEEE Sensors Journal*, 2022, 22(8): 7734–7742.
- [33] H. M. Kim, J. H. Park, and S. K. Lee, "Fabrication and measurement of fiber optic localized surface plasmon resonance sensor based on hybrid structure of dielectric thin film and bilayered gold nanoparticles," *IEEE Transactions on Instrumentation and Measurement*, 2021, 70: 1–8.
- [34] G. Li, Q. Xu, R. Singh, W. Zhang, C. Marques, Y. Xie, "Graphene oxide/multiwalled carbon nanotubes assisted serial quadruple tapered structure-based LSPR sensor for glucose detection," *IEEE Sensors Journal*, 2022, 22(17): 16904–16911.
- [35] H. Zhang, Y. Chen, X. Feng, X. Xiong, S. Hu, Z. Jiang, "Long-range surface plasmon resonance sensor based on side-polished fiber for biosensing applications," *IEEE Journal of Selected Topics in Quantum Electronics*, 2019, 25(2): 1–9.
- [36] Q. Wang, J. Y. Jing, X. Z. Wang, L. Y. Niu, and W. M. Zhao, "A D-shaped fiber long-range surface plasmon resonance sensor with high Q-factor and temperature self-compensation," *IEEE Transactions on Instrumentation and Measurement*, 2020, 69(5): 2218–2224.
- [37] W. Luo, J. Meng, X. Li, D. Yi, F. Teng, Y. Wang, "Long-range surface plasmon resonance sensor based on side-polished D-shaped hexagonal structure photonic crystal fiber with the buffer layer of magnesium fluoride," *Journal of Physics D: Applied Physics*, 2021, 54(50): 505106.
- [38] Y. X. Tang, X. Zhang, X. S. Zhu, and Y. W. Shi, "Dielectric layer thickness insensitive EVA/Ag-coated hollow fiber temperature sensor based on long-range surface plasmon resonance," *Optics Express*, 2021, 29(1): 368–376.
- [39] Q. Wang, X. W. Cong, Z. Cheng, W. M. Zhao, L. Wang, X. Y. Yin, "Low dimensional nanostructure-assisted long-range surface plasmon resonance sensors with high figure of merit," *IEEE Transactions on NanoBioscience*, 2023, 22(1): 45–51.
- [40] Z. Dai, J. Tan, K. Zhou, L. Zhang, X. Zhou, and Y. Tan, "Optical fiber SPR biosensor with frequency multiplexing compensated laser heterodyne feedback for ultrasensitive detection of fluoroquinolones," *Sensors and Actuators B: Chemical*, 2023, 393: 134335.
- [41] Y. Wang, C. Gong, X. Yang, T. Zhu, K. Zhang, Y. J. Rao, "Photonic bandgap fiber microlaser with dual-band emission for integrated optical tagging and sensing," *Laser & Photonics Reviews*, 2023, 17: 2200834.



- [42] A. Azzouz, L. Hejji, K. H. Kim, D. Kukkar, B. Souhail, N. Bhardwaj, "Advances in surface plasmon resonance-based biosensor technologies for Qi WANG et al.: Research on Fiber Optic Surface Plasmon Resonance Biosensors: A Review Page 29 of 30 cancer biomarker detection," *Biosensors & Bioelectronics*, 2022, 197: 113767.
- [43] H. Torun, B. Bilgin, M. Ilgu, N. Batur, M. Ozturk, T. Barlas, "Rapid nanoplasmonic-enhanced detection of SARS-CoV-2 and variants on DNA aptamer metasurfaces," *Advanced Devices & Instrumentation*, 2023, 4: 0008.
- [44] R. Wang, C. Liu, Y. Wei, Z. Ran, T. Jiang, C. Liu, "Fiber SPR biosensor sensitized by MOFs for MUC1 protein detection," *Talanta*, 2023, 258: 124467.
- [45] Q. Wang, J. Y. Jing, and B. T. Wang, "Highly sensitive SPR biosensor based on graphene oxide and staphylococcal protein a co-modified TFBG for human IgG detection," *IEEE Transactions on Instrumentation and Measurement*, 2019, 68(9): 3350–3357.
- [46] H. Song, Q. Wang, and W. M. Zhao, "A novel SPR sensor sensitivity-enhancing method for immunoassay by inserting MoS₂ nanosheets between metal film and fiber," *Optics and Lasers in Engineering*, 2020, 132: 106135.
- [47] M. Chen, T. Lang, B. Cao, Y. Yu, and C. Shen, "D-type optical fiber immunoglobulin G sensor based on surface plasmon resonance," *Optics & Laser Technology*, 2020, 131: 106445.
- [48] S. Dai, X. Li, Y. Chen, J. Zhang, and X. Hong, "Highly reproducible fiber optic surface plasmon resonance biosensors modified by CS2 for disposable immunoassays," *Sensors and Actuators B: Chemical*, 2023, 374: 132801.
- [49] W. Yang, Y. Cheng, M. Jiang, S. Jiang, R. Liu, J. Lu, "Design and fabrication of an ultra-sensitive Ta₂C MXene/Au-coated tilted grating sensor," *Sensors and Actuators B: Chemical*, 2022, 369: 132391.
- [50] J. Zhang, X. Mai, X. Hong, Y. Chen, and X. Li, "Optical fiber SPR biosensor with a solid-phase enzymatic reaction device for glucose detection," *Sensors and Actuators B: Chemical*, 2022, 366: 131984.
- [51] Y. Wang, J. Li, L. N. Guo, M. Tian, and F. Meng, "Development of fabrication technique and sensing performance of optical fiber humidity sensors in the most recent decade," *Measurement*, 2023, 215: 112888.
- [52] V. P. Prakashan, G. George, M. S. Sanu, M. S. Sajna, A. C. Saritha, C. Sudarsanakumar, "Investigations on SPR induced Cu@Ag core shell doped SiO₂-TiO₂-ZrO₂ fiber optic sensor for mercury detection," *Applied Surface Science*, 2020, 507: 144957.
- [53] E. Siyu, Y. N. Zhang, B. Han, W. Zheng, Q. L. Wu, and H. K. Zheng, "Two-channel surface plasmon resonance sensor for simultaneous measurement of seawater salinity and temperature," *IEEE Transactions on Instrumentation and Measurement*, 2020, 69(9): 7191–7199.
- [54] M. Yang, Y. Zhu, and R. An, "Underwater fiber-optic salinity and pressure sensor based on surface plasmon resonance and multimode interference," *Applied Optics*, 2021, 60(30): 9352–9357.
- [55] G. An, L. Liu, P. Hu, P. Jia, F. Zhu, Y. Zhang, "Probe type TFBG-excited SPR fiber sensor for simultaneous measurement of multiple ocean parameters assisted by CFBG," *Optics Express*, 2023, 31(3): 4229–4237.
- [56] X. Wei, Y. Peng, X. Chen, S. Zhang, and Y. Zhao, "Optimization of tapered optical fiber sensor based on SPR for high sensitivity salinity measurement," *Optical Fiber Technology*, 2023, 78: 103309.
- [57] Y. C. Xu, M. Xiong, and H. Yan, "A portable optical fiber biosensor for the detection of zearalenone based on the localized surface plasmon resonance," *Sensors and Actuators B: Chemical*, 2021, 336: 129752.
- [58] S. M. Chen, Y. Liu, Q. X. Yu, and W. Peng, "Microcapillary-based integrated LSPR device for refractive index detection and biosensing," *Journal of Lightwave Technology*, 2020, 38(8): 2485–2492.
- [59] Y. Liu, N. Zhang, P. Li, L. Yu, S. M. Chen, Y. Zhang, "Low-cost localized surface plasmon resonance biosensing platform with a response enhancement for protein detection," *Nanomaterials*, 2019, 9(7): 1019.
- [60] J. Zhang, J. Yuan, Y. Qu, S. Qiu, C. Mei, X. Zhou, "Graphene coated micro-channel fiber sensor based on localized surface plasmon resonance," *Journal of the Optical Society of America B – Optical Physics*, 2023, 40(4): 695–704.
- [61] M. A. Mollah and M. S. Islam, "Novel single hole exposed-suspended core localized surface plasmon resonance sensor," *IEEE Sensors Journal*, 2021, 21(3): 2813–2820.
- [62] M. S. Islam, M. R. Islam, J. Sultana, A. Dinovitser, B. W. H. Ng, and D. Abbott, "Exposed-core localized surface plasmon resonance biosensor," *Journal of the Optical Society of America B – Optical Physics*, 2019, 36(8): 2306–2311.
- [63] R. Singh and S. Dewra, "Performance analysis of localized surface plasmon resonance sensor with and without Bragg grating," *Journal of Optical Communications*, 2019, 41(1): 45–50.
- [64] J. X. Zhang, T. M. Liang, H. Y. Wang, Z. L. Huang, Z. J. Hu, K. Xie, "Ultrasensitive glucose biosensor using micro-nano interface of tilted fiber grating coupled with biofunctionalized Au nanoparticles," *IEEE Sensors Journal*, 2022, 22(5): 4122–4134.
- [65] B. B. Luo, Y. J. Wang, H. F. Lu, S. X. Wu, Y. M. Lu, S. H. Shi, "Label-free and specific detection of soluble programmed death ligand-1 using a localized surface plasmon resonance biosensor based on excessively tilted fiber gratings," *Biomedical Optics Express*, 2019, 10(10): 5136–5148.



- [66] L. Singh, R. Singh, B. Y. Zhang, B. K. Kaushik, and S. Kumar, "Localized surface plasmon resonance based hetero-core optical fiber sensor structure for the detection of L-cysteine," *IEEE Transactions on Nanotechnology*, 2020, 19: 201–208.
- [67] M. Y. Li, R. Singh, M. S. Soares, C. Marques, B. Y. Zhang, and S. Kumar, "Convex fiber-tapered seven core fiber-convex fiber (CTC) structure-based biosensor for creatinine detection in aquaculture," *Optics Express*, 2022, 30(8): 13898–13914.
- [68] Y. Wang, R. Singh, S. Chaudhary, B. Y. Zhang, and S. Kumar, "2-D nanomaterials assisted LSPR MPM optical fiber sensor probe for cardiac troponin I detection," *IEEE Transactions on Instrumentation and Measurement*, 2022, 71: 9504609.
- [69] R. Singh, S. Kumar, F. Z. Liu, C. Shuang, B. Y. Zhang, R. Jha, "Etched multicore fiber sensor using copper oxide and gold nanoparticles decorated graphene oxide structure for cancer cells detection," *Biosensors & Bioelectronics*, 2020, 168: 112557.
- [70] V. Semwal and B. D. Gupta, "Experimental studies on the sensitivity of the propagating and localized surface plasmon resonance-based tapered fiber optic refractive index sensors," *Applied Optics*, 2019, 58(15): 4149–4156.
- [71] Z. Wang, R. Singh, C. Marques, R. Jha, B. Y. Zhang, and S. Kumar, "Taper-in-taper fiber structure-based LSPR sensor for alanine aminotransferase detection," *Optics Express*, 2021, 29(26): 43793–43810.
- [72] G. Zhu, N. Agrawal, R. Singh, S. Kumar, B. Zhang, C. Saha, "A novel periodically tapered structure-based gold nanoparticles and graphene oxide – immobilized optical fiber sensor to detect ascorbic acid," *Optics & Laser Technology*, 2020, 127: 106156.
- [73] W. Zhang, R. Singh, Z. Wang, G. R. Li, Y. Y. Xie, R. Jha, "Humanoid shaped optical fiber plasmon biosensor functionalized with graphene oxide/multiwalled carbon nanotubes for histamine detection," *Optics Express*, 2023, 31(7): 11788–11803.
- [74] G. R. Li, Q. Xu, R. Singh, W. Zhang, C. Marques, Y. Y. Xie, "Graphene oxide/multiwalled carbon nanotubes assisted serial quadruple tapered structure-based LSPR sensor for glucose detection," *IEEE Sensors Journal*, 2022, 22(17): 16904–16911.
- [75] Z. W. Luo, Y. Xu, L. He, F. He, J. Wu, Z. J. Huang, "Development of a rapid and ultra-sensitive cytosensor: Ω -shaped fiber optic LSPR integrated with suitable AuNPs coverage," *Sensors and Actuators B: Chemical*, 2021, 336: 129706.
- [76] Y. Li, X. Wang, W. Ning, E. L. Yang, Y. X. Li, Z. W. Luo, "Sandwich method-based sensitivity enhancement of Ω -shaped fiber optic LSPR for time-flexible bacterial detection," *Biosensors & Bioelectronics*, 2022, 201: 113911.
- [77] L. He, F. He, Y. T. Feng, X. Wang, Y. X. Li, Y. H. Tian, "Hybridized nanolayer modified Ω -shaped fiber-optic synergistically enhances localized surface plasma resonance for ultrasensitive cytosensor and efficient photothermal therapy," *Biosensors & Bioelectronics*, 2021, 194: 113599.
- [78] P. Dimpi and R. Biswas, "Clad modified varying geometries of fiber optic LSPR sensors towards detection of hazardous volatile liquids and their comparative analysis," *Environmental Technology & Innovation*, 2022, 25: 102112.
- [79] J. K. Virk, S. Das, R. S. Kaler, H. Singh, and T. Kundu, "D-shape optical fiber probe dimension optimization for LSPR based bio-sensor," *Optical Fiber Technology*, 2022, 71: 102903.
- [80] A. K. Pathak, B. M. A. Rahman, V. K. Singh, and S. Kumari, "Sensitivity enhancement of a concave shaped optical fiber refractive index sensor covered with multiple Au nanowires," *Sensors*, 2019, 19(19): 4021.
- [81] J. B. Maurya, Nikki, J. P. Saini, A. K. Sharma, and Y. K. Prajapati, "A localized SPR D-shaped fiber optic sensor utilizing silver grating coated with graphene: Field analysis," *Optical Fiber Technology*, 2023, 75: 103204.
- [82] J. Feng, J. Gao, W. Yang, R. Liu, M. Shafi, Z. Zha, "LSPR optical fiber sensor based on 3D gold nanoparticles with monolayer graphene as a spacer," *Optics Express*, 2022, 30(6): 10187–10198.
- [83] Q. Yang, X. Zhang, S. Kumar, R. Singh, B. Zhang, C. Bai, "Development of glucose sensor using gold nanoparticles and glucose-oxidase functionalized tapered fiber structure," *Plasmonics*, 2020, 15(3): 841–848.
- [84] V. T. Huong, N. T. T. Phuong, N. T. Tai, N. T. An, V. D. Lam, D. H. Manh, "Gold nanoparticles modified a multimode clad-free fiber for ultrasensitive detection of bovine serum albumin," *Journal of Nanomaterials*, 2021, 2021: 1–6.
- [85] H. M. Kim, D. H. Jeong, H. Y. Lee, J. H. Park, and S. K. Lee, "Improved stability of gold nanoparticles on the optical fiber and their application to refractive index sensor based on localized surface plasmon resonance," *Optics and Laser Technology*, 2019, 114: 171–178.
- [86] M. D. Lu, H. Zhu, C. G. Bazuin, W. Peng, and J. F. Masson, "Polymer-templated gold nanoparticles on optical fibers for enhanced-sensitivity localized surface plasmon resonance biosensors," *ACS Sensors*, 2019, 4(3): 613–622.



- [87] M. D. Lu, H. Zhu, M. Lin, F. Wang, L. Hong, J. F. Masson, "Comparative study of block copolymer-templated localized surface plasmon resonance optical fiber biosensors: CTAB or citrate-stabilized gold nanorods," *Sensors and Actuators B: Chemical*, 2021, 329: 129094.
- [88] M. D. Lu, H. Zhu, L. Hong, J. J. Zhao, J. F. Masson, and W. Peng, "Wavelength-tunable optical fiber localized surface plasmon resonance biosensor via a diblock copolymer-templated nanorod monolayer," *ACS Applied Materials & Interfaces*, 2020, 12(45): 50929–50940.
- [89] H. M. Kim, M. Uh, D. H. Jeong, H. Y. Lee, J. H. Park, and S. K. Lee, "Localized surface plasmon resonance biosensor using nanopatterned gold particles on the surface of an optical fiber," *Sensors and Actuators B: Chemical*, 2019, 280: 183–191.
- [90] Y. Hong, D. Zhao, J. Wang, J. Lu, G. Yao, D. Liu, "Solvent-free nanofabrication based on ice-assisted electron-beam lithography," *Nano Letters*, 2020, 20(12): 8841–8846.
- [91] H. M. Kim, H. J. Kim, J. H. Park, and S. K. Lee, "High-performance biosensor using a sandwich assay via antibody-conjugated gold nanoparticles and fiber-optic localized surface plasmon resonance," *Analytica Chimica Acta*, 2022, 1213: 339960.
- [92] S. Das, B. Mandal, V. R. Rao, and T. Kundu, "Detection of tomato leaf curl New Delhi virus DNA using U-bent optical fiber-based LSPR probes," *Optical Fiber Technology*, 2022, 74: 103108.
- [93] F. Tukur, B. Bagra, A. Jayapalan, M. Liu, P. Tukur, and J. Wei, "Plasmon-exciton coupling effect in nanostructured arrays for optical signal amplification and SARS-CoV-2 DNA sensing," *ACS Applied Nano Materials*, 2023, 6(3): 2071–2082.
- [94] W. Ning, C. Y. Zhang, Z. Y. Tian, M. F. Wu, Z. W. Luo, S. M. Hu, "Ω-shaped fiber optic LSPR biosensor based on mismatched hybridization chain reaction and gold nanoparticles for detection of circulating cell-free DNA," *Biosensors & Bioelectronics*, 2023, 228: 115175.
- [95] M. D. Lu, W. Peng, M. Lin, F. Wang, and Y. Zhang, "Gold nanoparticle-enhanced detection of DNA hybridization by a block copolymer-templating fiber-optic localized surface plasmon resonance biosensor," *Nanomaterials*, 2021, 11(3): 616.
- [96] Z. Luo, Y. Wang, Y. Xu, X. Wang, Z. Huang, J. Chen, "Ultrasensitive U-shaped fiber optic LSPR cytosensing for label-free and in situ evaluation of cell surface N-glycan expression," *Sensors and Actuators B: Chemical*, 2019, 284: 582–588.
- [97] S. Kumar, Z. Guo, R. Singh, Q. L. Wang, B. Y. Zhang, S. Cheng, "MoS₂ functionalized multicore fiber probes for selective detection of shigella bacteria based on localized plasmon," *Journal of Lightwave Technology*, 2021, 39(12): 4069–4081.
- [98] W. Ning, S. Hu, C. Zhou, J. Luo, Y. Li, C. Zhang, "An ultrasensitive J-shaped optical fiber LSPR aptasensor for the detection of *Helicobacter pylori*," *Analytica Chimica Acta*, 2023, 1278: 341733.
- [99] Y. C. Xu, M. Xiong, and H. Yan, "A portable optical fiber biosensor for the detection of zearalenone based on the localized surface plasmon resonance," *Sensors and Actuators B: Chemical*, 2021, 336: 129752.
- [100] B. B. Luo, Y. J. Wang, H. F. Lu, S. X. Wu, Y. M. Lu, S. H. Shi, "Label-free and specific detection of soluble programmed death ligand-1 using a localized surface plasmon resonance biosensor based on excessively tilted fiber gratings," *Biomedical Optics Express*, 2019, 10(10): 5136–5148.
- [101] H. M. Kim, D. H. Jeong, H. Y. Lee, J. H. Park, and S. K. Lee, "Improved stability of gold nanoparticles on the optical fiber and their application to refractive index sensor based on localized surface plasmon resonance," *Optics and Laser Technology*, 2019, 114: 171–178.
- [102] P. Halkare, N. Punjabi, J. Wangchuk, S. Madugula, K. Kondabagil, and S. Mukherji, "Label-free detection of *Escherichia coli* from mixed bacterial cultures using bacteriophage T4 on plasmonic fiber-optic sensor," *ACS Sensors*, 2021, 6(7): 2720–2727. Page 26 of 26 *Photonic Sensors*
- [103] S. Kumar, R. Singh, B. K. Kaushik, N. K. Chen, Q. S. Yang, and X. Zhang, "LSPR-based cholesterol biosensor using hollow core fiber structure," *IEEE Sensors Journal*, 2019, 19(17): 7399–7406.
- [104] S. Kumar, R. Singh, Q. S. Yang, S. Cheng, B. Y. Zhang, and B. K. Kaushik, "Highly sensitive, selective and portable sensor probe using germanium-doped photosensitive optical fiber for ascorbic acid detection," *IEEE Sensors Journal*, 2021, 21(1): 62–70.
- [105] M. Y. Li, R. Singh, C. Marques, B. Y. Zhang, and S. Kumar, "2D material assisted SMF-MCF-MMFSMF based LSPR sensor for creatinine detection," *Optics Express*, 2021, 29(23): 38150–38167.
- [106] Q. S. Yang, G. Zhu, L. Singh, Y. Wang, R. Singh, B. Y. Zhang, "Highly sensitive and selective sensor probe using glucose oxidase/gold nanoparticles/graphene oxide functionalized tapered optical fiber structure for detection of glucose," *Optik*, 2020, 208: 164536.



- [107] S. Long, E. Wang, M. Wu, H. Zhu, N. Xu, Y. Wang, "Sensing absorptive fluids with backside illuminated grating coupled SPR sensor fabricated by nanoimprint technology," *Sensors and Actuators A: Physical*, 2022, 337: 113416.
- [108] F. Mumtaz, B. Zhang, M. Roman, L. G. Abbas, M. A. Ashraf, and Y. Dai, "Computational study: windmill-shaped multi-channel SPR sensor for simultaneous detection of multi-analyte," *Measurement*, 2023, 207: 112386.
- [109] B. Hossain, A. Kumar Paul, M. Arefin Islam, M. Faruk Hossain, and M. Mahabubur Rahman, "Design and analysis of highly sensitive prism based surface plasmon resonance optical salinity sensor," *Results in Optics*, 2022, 7: 100217.
- [110] F. Mumtaz, M. Roman, B. Zhang, L. G. Abbas, Y. Dai, M. A. Ashraf, "MXene (Ti₃C₂T_x) coated highly-sensitive D-shaped photonic crystal fiber based SPR-biosensor," *Photonics and Nanostructures – Fundamentals and Applications*, 2022, 52: 101090.
- [111] Munaf K. Khalaf, Shaymaa R. Tahhan, Hanan J. Taher, Sobhy M. Ibrahim, Kawsar Ahmed, Au-TiO₂ coated dielectric micro-channel based plasmonic refractive index senso, *Optical and Quantum Electronics* (2023) 55:612 <https://doi.org/10.1007/s11082-023-04856-z>
- [112] Munaf K. Khalaf, Hanan J. Taher, Shaymaa R. Tahhan, Kawsar Ahmed, Fahad Ahmed Al-Zahrani, Design and Numerical Analysis of Refractive Index-Based Reproductive Hormone Sensor, Springer, *Plasmonics*, 24 feb. 2024 <https://doi.org/10.1007/s11468-024-02208-5>
- [113] Dalya H. Abbas, New Refractive Index Sensor Depend on Resonance Effect, The Mattingley Publishing Co., Inc., TEST-engineering & management, Vol. 83, PP.9988 – 9995 May - June 2020
- [114] Ghufraan Mohammed Jassam and Soudad S. Ahmed, D-Shaped Photonic Crystal Fiber Toxic Metal Ions (Arsenic) Sensor Based on Surface Plasmon Resonance, *Iraqi Journal of Physics*, 2023 Vol. 21, No.2, PP. 91-98, <https://doi.org/10.30723/ijp.v21i2.1120>
- [115] Ghufraan Mohammed Jassam and Soudad S. Ahmed, Estimating concentration of toxic ions Arsenic in water by using Photonic Crystal Fiber based on Surface Plasmon Resonance (SPR) , *Baghdad Science Journal*, July, 2023, <https://dx.doi.org/10.21123/bsj.2023.7651>
- [116] Hiba Kh. Abbas and Zainab F. Mahdi , Fabricate a highly sensitive surface plasmon resonance optical fiber sensor based on a D-shape fiber coated with gold (Au) nano-layer, *Results in Optics* 12 (2023) 100497, <https://doi.org/10.1016/j.rio.2023.100497>
- [117] Hiba Kh. Abbas and Zainab F. Mahdi, D-shape Optical Fiber Development and Enhancement as a Refractive Indices Sensor Using Surface Plasmon Resonance, *IJL, Issue 2, Vol. 22, 2023*, <https://doi.org/10.31900/ijl.v22i2.401>
- [118] Ammar M. Tuaimah, Hanan J. Taher, Shaymaa R. Tahhan, Fahad Ahmed Al Zahrani and Kawsar Ahmed. " Plasmonic D-shape Biometallic Coating Refractive index Sensor. *Plasmonics*, 2023,18,2393-2404.
- [119] Ammar M. Tuaimah, Hanan J. Taher, Shaymaa R. Tahhan, Kawsar Ahmed Fahad and Ahmed Al Zahrani. "Multi Analyte Detection Based on D-Shaped PCF Sensor for Glucose Concentrations Sensing'. *Optical and Quantum Electronics*, 2024,56,3,319.
- [120] Sally K. Abbas, Soudad S. Ahmed.' Photonic Crystal Fiber Drug Sensor Based on Surface Plasmon Resonance. *Iraqi Journal of Laser*, 2024,23,123-130.
- [121] Namaa Salem Rahim, Soudad S. Ahmed, Murtadha Faaiz Sultan, " Optical Fiber Biomedical Sensor Based on Surface Plasmon Resonance, 2020,61,1650-1656.
- [122] Fatima Fadhil Abbas, Soudad S. Ahmed." Photonic Crystal Fiber Pollution Sensor based on Surface Plasmon Resonance". 2023,64,658-667.

الاستشعار بواسطة الالياف البصرية المعتمدة على الرنين البلازمي السطحي: مراجعة شاملة

اداليا حسين عباس¹, احنان جعفر ظاهر², بشرى رزوقي مهدي

¹معهد الليزر للدراسات العليا، جامعة بغداد، بغداد، العراق

²وزارة العلوم والتكنولوجيا، بغداد، العراق

البريد الإلكتروني للباحث: dalia.abbas2201p@ilps.uobaghdad.edu.iq

الخلاصة:



تستخدم أجهزة استشعار الطلاء البلازماني Surface Plasmon على نطاق واسع في مجالات الكيمياء والأحياء والبيئة. ينبع هذا النوع من أجهزة الاستشعار من الآثار الناتجة عن الاهتزازات السطحية للبلازما (SPRs) أو الاهتزازات المحلية للبلازما السطحية (LSPRs)، والتي لها تطبيقات تجارية. في هذه المراجعة، نقدم التقدم الحالي في مجالات أجهزة استشعار البلازما السطحية، ولا سيما في تكوين البنية المستوية المتراسة والموجهات الضوئية الألياف البصرية. في منصات البنية المتراسة، يعتمد المستشعر الضوئي على آثار LSPRs والانتشارات الفائقة والاهتزازات فانو والتكامل مع مواد ثنائية الأبعاد (2D). يتم تلخيص دمج المستشعر الألياف البصرية مع هياكل LSPRs/SPRs ومواد الأبعاد الثنائية. بالإضافة إلى ذلك، نقدم التقدم الحالي في مستشعرات البلازما الكمومية ما وراء قيود الضوضاء الكلاسيكية. تم مناقشة التحديات والفرص في هذا المجال. تمكن مستشعرات LSPR البيولوجية من الحد النطاقي النانوي وتلاعب الضوء، مما يؤدي إلى زيادة الحساسية وتركيز الطاقات الكهرومغناطيسية. إن الجمع بين LSPR وتقنيات الألياف البصرية قد ساعد في تقدم المستشعرات المدمجة وخفض الكشف عن بُعد. تستكشف هذه المراجعة الشاملة العديد من تكوينات المستشعرات وفئات الألياف والتخطيطات الهندسية، وتسلط الضوء على فوائدها من حيث الحساسية والتكامل وتحسين الأداء. تُناقش جهود تقنيات التصنيع المتعلقة باستراتيجيات الروابط غير الكيميائية والتجميع الذاتي للجزيئات النانوية، وتوفر التحكم في أشكال النانو هياكل وتحسين أداء المستشعرات. يُعطي التطبيق البيولوجي لمستشعرات LSPR الألياف البصرية (FOLSPRs) بالتفصيل، خاصةً في تفاعلات البيومولكولات وتحليل البروتينات والجراثيم والخلايا والأحماض النووية (DNA) و (RNA). يتم التركيز على تعديلات السطح وهياكل التعرف لإمكاناتها في أنظمة الاستشعار البيولوجي بدون علامات. وفي الوقت الحقيقي. يتم معالجة تحديات وفرص مستشعرات FOLSPR، مع التطورات في الحساسية وتقنيات التصنيع وموثوقية القياسات. يتم تسليط الضوء على التكامل مع التقنيات الناشئة مثل المواد النانوية كاتجاه واعد للأبحاث المستقبلية. توفر هذه المراجعة رؤى في التقدم والتطبيقات المحتملة لمستشعرات FOLSPR، وتمهد الطريق لمنصة استشعار بيولوجي بصري حساسة ومرنة في العديد من المجالات.



A comparative Efficacy of 635 nm and 980 nm Low-Level Laser Therapy in Treating Temporomandibular Disorders

Noor Qasim Mohammed^{1, *}, Zainab F. Mahdi¹, Balsam S. Abdulhameed²

¹ Institute of Laser for Postgraduate Studies, University of Baghdad, Baghdad, Iraq

² Al-Imamen Al-Kadmen Medical City, Ministry of Health, Baghdad, Iraq

* Email address of the Corresponding Author: noor.qasem2202m@ilps.uobaghdad.edu.iq

Article history: Received 7 Oct. 2024; Revised: 3 Feb. 2025; Accepted: 10 Mar. 2025; Published online: 15 Jun. 2025.

Abstract:

Background: Temporomandibular disorders (TMDs) are a complex group of conditions impacting the temporomandibular joint (TMJ) and masticatory muscles, leading to pain, reduced jaw mobility, and other debilitating symptoms. These conditions often result from multifactorial causes, including malocclusion, trauma, stress, and parafunctional habits. Effective treatment is challenging, necessitating innovative therapeutic approaches.

Aim: This study compares the efficacy of two low-level laser therapy (LLLT) modalities with wavelengths of 635 nm and 980 nm in managing TMD symptoms. The goal is to determine which wavelength provides superior short-term and long-term therapeutic outcomes in pain relief, improved mouth function, and reduction of tender points.

Materials and methods: Fifty patients with diagnosed temporomandibular disorder (TMD) were randomized into two groups. Group 1 received 635 nm low-level laser therapy (LLLT), while Group 2 was treated with 980 nm low-level laser therapy (LLLT). Pain levels, mouth opening range, and the number of tender points were measured before each treatment and at a one-month follow-up. The treatment was administered in continuous mode, with a power output of 0.3 Watts (W). Irradiation time was 30 seconds per tender point, with a total of four treatment sessions (two sessions per week). A follow-up assessment was conducted one month after the completion of the treatment protocol. Data was analyzed using appropriate statistical methods to evaluate the efficacy of the treatments.

Result: The 635 nm laser group experienced significantly greater reductions in pain intensity ($p = 0.025$) and fewer tender points in the masseter muscle ($p = 0.048$) compared to the 980 nm laser group during the short-term evaluation. However, no significant differences were observed between the two groups at the one-month follow-up.

Conclusion: The 635 nm laser demonstrated superior short-term efficacy in reducing pain and masseter tender points, whereas both wavelengths were equally effective in the long term. These findings highlight the importance of wavelength selection in optimizing low-level laser therapy (LLLT) protocols for temporomandibular joint disorder (TMD) management. Further research is needed to explore the mechanisms underlying these differences and to identify the optimal parameters for sustained therapeutic outcomes.

Keywords: (Laser635nm), (Laser980 nm), Temporomandibular disorders (TMDs), pain, mouth opening.

1. Introduction



Temporomandibular disorders (TMDs) represent a diverse group of conditions affecting the temporomandibular joint (TMJ) and associated masticatory muscles, significantly impairing jaw function and causing pain. Common symptoms include headaches, limited jaw mobility, joint clicking, and tenderness in the facial muscles [1]. These conditions are often linked to factors such as malocclusion, trauma, emotional stress, and parafunctional habits [2]. TMDs predominantly affect women aged 20-40 years, with studies showing a 2:1 female-to-male ratio [3]. Diagnosis often involves imaging, physical examinations, and patient history [4]. According to the diagnostic criteria for temporomandibular disorder (DC/TMD), TMD patients are categorized into three groups: Group I includes muscle disorders (e.g., myofascial pain with and without limitation of mouth opening (Group II involves disc displacement with or without reduction and mouth opening limitation), and Group III: arthralgia, arthritis, and osteoarthritis [5]. Despite advancements in diagnostic techniques, including imaging and clinical evaluations, effective treatment remains challenging due to the multifactorial nature of TMDs. Treatments range from conservative approaches (medication, splints, physical therapy) to advanced methods like low-level laser therapy (LLLT) [6]. Recent studies have highlighted the potential of low-level laser therapy (LLLT) as a non-invasive treatment modality for managing TMD symptoms. LLLT operates through photobiomodulation, a process that stimulates cellular activity, promoting pain relief, reducing inflammation, and enhancing tissue repair. Different wavelengths, particularly 635 nm and 980 nm, have demonstrated therapeutic benefits, yet their comparative efficacy remains underexplored [7]. The optical properties of different wavelengths of light significantly influence their interaction with human tissues, affecting absorption, penetration depth, and therapeutic outcomes. To evaluate the effectiveness of light-based treatments, it is essential to measure the path length and absorption coefficients of the masseter and temporalis muscles at two distinct wavelengths (980 nm and 635 nm). The path length (x) (0.4-0.5 cm) and adsorption coefficients (α) for masseter and temporalis muscle, respectively, were (0.24-0.43 cm^{-1}) and (0.27-0.51 cm^{-1}) at 980 nm, and the path length (x) (0.2-0.3 cm) and absorption coefficients (α) for masseter and temporalis muscle, respectively, were (1.13-1.67 cm^{-1}) and (1.23-1.83 cm^{-1}) at 635 nm [8,9,10,11,12]. This study aims to address this gap by comparing the short-term and long-term efficacy of 635 nm and 980 nm LLLT in reducing pain, improving mouth opening, and alleviating tender points in the masseter and temporalis muscles of TMD patients. By evaluating the outcomes of these two wavelengths, this research seeks to optimize treatment protocols and contribute to evidence-based advancements in TMD management.

New research shows that low-level laser therapy (LLLT) can help people with temporomandibular muscle disorders (TMDs) feel less pain and improve their ability to function. Researchers Da Silva et al. (2023) found that combining low-level laser therapy (LLLT) with exercise helped people with temporomandibular disorders (TMD) feel less pain and be able to do more things than exercise alone. In addition, Kim et al. 2024 [14] found that low-level laser therapy (LLLT) using a 635nm wavelength was better than a 980nm wavelength at reducing pain and improving function in people with temporomandibular disorder (TMD).

2. Materials and methods

2.1 Study design

This randomized clinical trial was conducted at the Department of Oral and Maxillofacial Surgery, AL Imam Ali Hospital, and the oral medicine clinic at a specialized center in Baghdad from January to August 2024. Ethical approval for the study was obtained from the Research Scientific Committee of the Laser Institute (Ref. No. 1329, 23/09/2024). Informed consent was acquired from all participants prior to their inclusion.

2.2 Participant Selection



Fifty patients (43 females and 7 males) aged 20-29 years with a clinical diagnosis of muscular temporomandibular disorder (TMD) were recruited for the study. Inclusion criteria encompassed patients presenting with pain, restricted mouth opening, and tender points in the masseter and temporalis muscles. Exclusion criteria encompassed congenital temporomandibular joint (TMJ) abnormalities, recent trauma, occlusal disturbance, neoplastic conditions, and previous treatments within the last month.

2.3 Laser components

The following are the laser device accessories as shown in Figure 1:

1. Wireless footswitch
2. Front view of the base unit
3. Laser-protective eyewear
4. Therapy hand piece
5. Patient's goggles



Fig. 1: Solase Pro dental laser

2.4 Laser System and Application

The laser system utilized was a Solase Pro diode dental laser device, equipped with wavelengths of 635 nm and 980 nm.

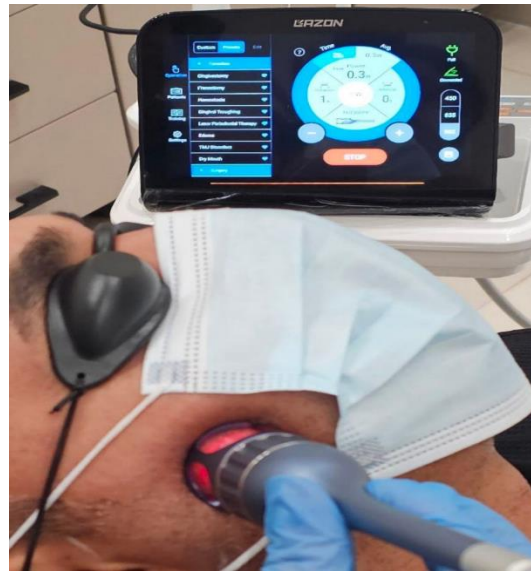
Parameters included:

Power output: 0.3 W

Spot size: 3.14 cm²

Power density: 0.0955 W/cm².

We applied each laser wavelength in continuous mode. We used the therapy handpiece to deliver laser energy to the affected sites, which included the TMJ and tender points in the masseter and temporalis muscles. We administered the treatment in four sessions, two per week, one-month follow-up. Each tender point received 30 seconds of laser application per session. As shown in figures (2b), (2c).



(a)



(b)

Fig.2: (a) Application of laser 980 nm on masseter tender points (b) Application of laser 635 nm on temporalis tender points.

2.5 Outcome Measure

Pain Intensity: Assessed using the Visual Analog Scale (VAS) before and after each session, and at one-month follow-up.

Mouth Opening Range: Measured using a digital caliper before and after each session, and at one-month follow-up.

Number of Tender Points: Evaluated through palpation of the masseter and temporalis muscles before and after each session and at a one-month follow-up.

2.6 Statistical analysis



Data analysis was performed using the statistical package for social science SPSS software, version 26). Descriptive statistics were expressed as mean, standard deviation, and minimum/maximum values. The Mann-Whitney U test was used to compare continuous variables (non-normally distributed data), while Fisher’s exact test was applied to categorical data. Statistical significance was set at $p \leq 0.05$.

3. Result

Participant Characteristics: Most participants were female (86%), with a mean age of 27.5 ± 9.3 years. As shown in Figures 3 and 4. No significant difference between both groups regarding age ($P=0.316$) and gender ($P=1.000$) as shown in Table 1.

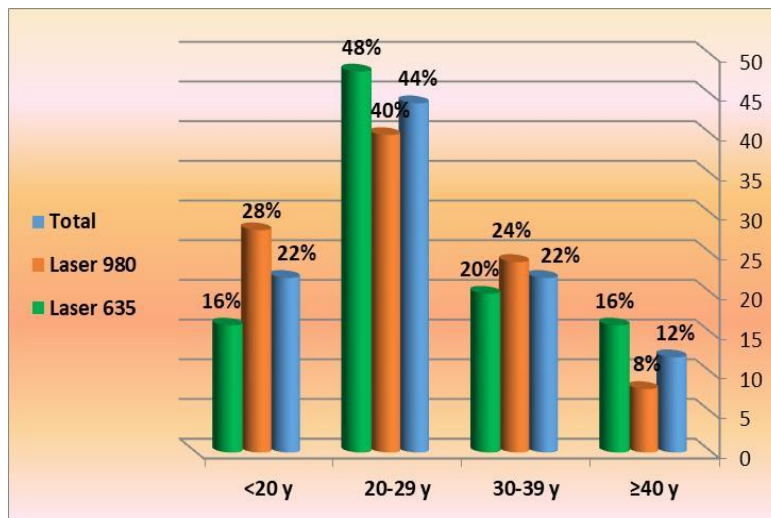


Fig. 3: Distribution of participants according to age groups, Baghdad, 2024.

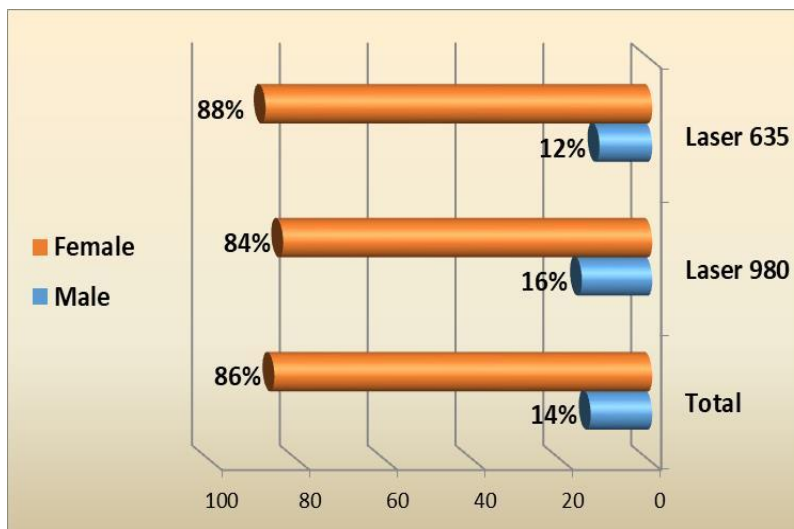


Fig. 4: Distribution of participants according to gender, Baghdad, 2024.

Table 1. Comparison of age and gender of both groups, Baghdad, 2024.

Variable	Groups		P value
	Laser 635 nm	Laser 980 nm	
	N%	N%	
Mean±SD	29.5±8.8	25.6±9.5	0.3161
	Age		
Male	3 (12%)	4 (16%)	1.0002
Female	22 (88%)	21 (84%)	
	gender		

Table 2. Comparison between the variables studied among groups at different time periods

Variable	Laser 635 nm Mean±SD	Laser 980nm Mean±SD	P value
Before first session			
Pain intensity	5.4±1.2	5.9±1.5	0.246
Mouth opening	39.1±7.4	37.6±4.4	0.454
No. of masseter tender points	4.1±1.5	4.3±1.3	0.623
No. of temporalis tender points	0.7±1	0.9±1.1	0.624
Before second session			
Pain intensity	3.9±1.2	4.8±1.4	0.025*
Mouth opening	40.4±6.8	39.9±4.8	0.976
No. of masseter tender points	3.1±1.6	3.3±1.2	0.647
No. of temporalis tender points	0.5±0.9	0.6±0.8	0.616
Before third session			
Pain intensity	3.0±1.1	3.7±1.2	0.021*
Mouth opening	42.0±6.1	40.8±5.8	0.686
No. of masseter tender points	2.8±1.2	2.7±1.3	0.968
No. of temporalis tender points	0.3±0.6	0.5±0.7	0.366
Before fourth session			
Pain intensity	2.2±1.1	2.8±1.2	0.145
Mouth opening	57.8±71.4	42.8±3.9	0.419
No. of masseter tender points	1.7±1.4	2.3±1.2	0.048*
No. of temporalis tender points	0.3±0.7	0.4±0.7	0.37
One month follow-up			
Pain intensity	1.3±1.3	1.1±0.9	0.754
Mouth opening	43.6±4.8	42.9±3.8	0.767
No. of masseter tender points	0.9±0.9	1.1±0.9	0.351
No. of temporalis tender points	0.1±0.3	0.2±0.4	0.127

The results of this randomized clinical trial revealed distinct differences in the short-term and long-term efficacy of the two laser wavelengths (635 nm and 980 nm) for the management of temporomandibular disorders (TMDs). As shown in Table 2

Short-Term Outcomes Pain Intensity: Patients in the 635 nm laser group reported significantly lower pain levels compared to the 980 nm group by the second session ($p = 0.025$) and third session ($p = 0.021$). These findings highlight the superior analgesic effects of the 635 nm wavelength in the short term.

Tender Points: A significant reduction in the number of tender points in the masseter muscle was observed in the 635 nm laser group before the fourth session ($p = 0.048$). No significant differences were detected in temporalis muscle tender points during the short-term evaluation.

Mouth Opening: Both groups showed slight improvements in mouth opening range over the short-term, but the differences between the two wavelengths were not statistically significant ($p > 0.05$).

Long-Term Outcomes (One-Month Follow-Up) Pain Intensity: No significant differences in pain intensity were observed between the two groups after one month ($p = 0.754$), indicating comparable long-term efficacy.

Tender Points: Both groups demonstrated reductions in the number of tender points in the masseter and temporalis muscles, with no statistically significant differences between them ($p > 0.05$).

Mouth Opening: Improvements in the range of mouth opening were sustained in both groups, with no significant differences between the two wavelengths ($p = 0.767$).

Summary of Findings While the 635 nm laser provided superior short-term pain relief and reduction in masseter tender points, both wavelengths exhibited equivalent long-term outcomes in all measured parameters. These results underscore the potential of wavelength-specific laser therapy in tailoring TMD management strategies.

4. Discussion

This study highlights the potential of low-level laser therapy (LLLT) as an effective treatment for temporomandibular disorders (TMDs), with particular emphasis on the comparative efficacy of 635 nm and 980 nm wavelengths. The findings provide insights into the therapeutic advantages and limitations of each wavelength, offering a foundation for optimizing temporomandibular disorder (TMD) management protocols. Regarding age, the study found that the highest incidence of temporomandibular joint disorders (TMD) was in the 20-29 age group (44.0%). This aligns with previous research, such as Valesan et al., 2021 [15], which reported that 41% of TMD patients were over 18, and Al-Jewair et al., 2021 [16] which reported that 41% of TMD patients were over 18, and noted that TMD peaks between 20 and 40 years.

Regarding gender, our study revealed that the highest incidence of TMD was observed in females (86.0%) compared to males (14.0%). This finding was nearly consistent with most other studies, which also found a predominance of females to males in TMD, including the studies such as Lei et al., 2021 [17]. The impact of sex steroid hormones, like estrogen, on condylar shape and health was recently reviewed by Stinson et al., 2019 [18]. Furthermore, the study of Nauru et al., 2024 demonstrated how low amounts of estradiol altered proteoglycan levels in the mandibular condyle cartilage [19].

Neurological, inflammatory, and psychosocial factors significantly impact pain in patients with Temporomandibular Joint Disorders (TMDs). Neurological mechanisms include central sensitivity, abnormal pain processing, peripheral sensitivity, and neuroimmune interactions. Inflammatory mediators like cytokines and prostaglandins contribute to pain, while stress and anxiety exacerbate it by causing muscle tension and altering perception [20,21].

Temporomandibular Joint Disorders (TMJDs) patients often experience limited mouth opening, often less than 40 mm, which affects their ability to eat, speak, and maintain oral hygiene. Joint inflammations, muscle spasms, neurotransmitter imbalance, stress, and anxiety contribute to this issue by affecting the masseter and temporalis muscles [22,23,24,25].

LLLT, a low-level laser therapy, can alleviate pain and mouth discomfort by increasing tissue adenosine triphosphate (ATP) production. This process, called photo biomodulation, raises nerve growth factors,



balances neurotransmitters, and lowers substance P, which stops the transmission of pain [26, 27, 28]. The treatment also improves membrane permeability, reduces oxidative stress, accelerates tissue repair, offers pain relief, improves function, reduces inflammation, and increases mobility. The treatment's effects on cells include improved membrane permeability, reduced oxidative stress, faster tissue repair, and reduced inflammation [22, 23, 24].

The study compares the effects of two different laser wavelengths (635 nm and 980 nm) on pain intensity and tender points in the masseter and temporalis muscles. The results indicate that the 635 nm laser, which delivers higher transmitted intensities (0.7618–0.5786 W/cm² for the masseter and 0.7467–0.5515 W/cm² for the temporalis), is more effective in reducing pain and the number of tender points in the masseter muscle. In contrast, the 980 nm laser, with lower transmitted intensities (0.8676–0.7702 W/cm² for the masseter and 0.8572–0.7400 W/cm² for the temporalis), results in less energy delivery to the tissue, leading to diminished therapeutic outcomes. The superior short-term effects of the 635 nm laser can be attributed to its higher absorption in superficial tissues, enhancing photobiomodulation effects. These findings align with previous research, suggesting that shorter wavelengths are more effective in modulating inflammatory processes and reducing nociceptive signaling in superficial tissues [29,30].

In contrast, the 980 nm laser exhibited deeper tissue penetration due to its longer wavelength but showed comparatively less impact on superficial tissues. This limitation may explain the reduced efficacy in addressing masseter tender points in the short term, as the energy may have been dispersed beyond the target tissues[31,32]. Long-Term Outcomes Interestingly, the long-term results revealed no significant differences between the two wavelengths in terms of pain intensity, tender points, or mouth opening[33,34,35]. This finding suggests that while the 635 nm laser provides superior immediate relief, the 980 nm laser achieves comparable therapeutic outcomes over time. The deeper penetration of the 980 nm laser may contribute to sustained effects by targeting deeper structures, including the TMJ capsule and associated nerves [36,37].

Clinical Implications The findings underscore the importance of wavelength selection in tailoring LLLT protocols to individual patient needs. The 635 nm laser may offer a more effective short-term solution for patients with acute pain and localized tenderness. Conversely, the 980 nm laser may be preferable for patients requiring treatment of deeper tissue structures or those with chronic conditions. Combining both wavelengths or integrating LLLT with other modalities, such as physical therapy, could further enhance treatment efficacy [38].

5. Limitations and Future Directions

This study is limited by its relatively small sample size and short follow-up duration. Future research should explore the long-term effects of LLLT with larger, more diverse patient populations and investigate optimal treatment parameters, such as session frequency and duration. Additionally, mechanistic studies are needed to elucidate the cellular and molecular pathways underlying the differential effects of 635 nm and 980 nm lasers.

6. Conclusions

The 635 nm laser offers superior short-term benefits for TMD management, particularly in pain reduction and tender point alleviation. However, both wavelengths demonstrate equivalent long-term efficacy, emphasizing their role as viable options for LLLT in clinical practice. Tailoring treatment protocols based on individual patient characteristics and integrating multimodal approaches may maximize therapeutic outcomes.

Acknowledgment

I would like to thank Dr. Mustafa Mohammed Hussein, Oral and Maxillofacial surgeon at AL Imam Ali Hospital in Al-Sadr City, and Asst. prof. Dr. Muhassad Al-Mudhafar, Oral medicine, College of



dentistry/University of Kufa for their help in diagnosing and referring TMD patients to me for LLLT treatment.

References

- [1] Al-Kufi, H.M. and A.M. Al-Bayati, Efficacy of photobiomodulation therapy (PBMT) in management of temporomandibular disorder (TMD). *Lasers in Dental Science*, 2023. 7(2): p. 77-83.
- [2] Alshamaa, A. and T. Aldelaimi, Treatment of myogenic temporomandibular joint disorders with diode laser and pharmacotherapy (comparative study). *Int Med J*, 2020. 25: p. 461.
- [3] Noor Q. Mohammed, Zainab F. Mahdi, Balsam S. Abdulhameed. Application of low level laser therapy (laser 980 nm) and ultrasound therapy and a combination of (US/Laser 980 nm) therapy in patients with temporomandibular joint disorders (TMDs). (2024). *African Journal of Biomedical Research*, 27(3S), 5569-5578. <https://doi.org/10.53555/AJBR.v27i3S.271>.
- [4] Zhang, JM., Yun, J., Zhou, TQ. et al. Arthrocentesis for temporomandibular joint disorders: a network meta-analysis of randomized controlled trials. *BMC Oral Health* 24, 1108 (2024).
- [5] Ahmed Fadhel Al Quisi1, Firas A. Jamil, Baseem Natheer Abdulhadi and Salah Jassim Muhsen. The reliability of using light therapy compared with LASER in pain reduction of temporomandibular disorders: a randomized controlled trial 1,2023.
- [6] Ali, O.A., Z.F. Mahdi, and B.S. Abdulhameed, Efficacy of low-level laser therapy on postoperative sequelae following extraction of impacted mandibular third molars. *Iraqi Journal of Laser*, 2024. 23(1): p. 1-11.
- [7] Al-Mamgani, M. (2021). Photobiomodulation laser therapy in dentistry. *Iraqi Dental Journal*, 43(2), 1-8.
- [8] Hassan et al. (2020). Reduced scattering coefficients of human temporalis muscle at 980 nm. *Journal of the Iraqi Academy of Sciences*, 21(2), 1-9.
- [9] Abdulrahman et al. (2021). Optical properties of human masseter muscle at 635 nm. *Al-Mustansiriya Journal of Science*, 32(1), 1-10.
- [10] Mohammed et al. (2022). Scattering coefficient of human temporalis muscle at 635 nm. *Iraqi Journal of Physics*, 20(1), 1-12.
- [11] Al-Saadi et al. (2020). Path length of human masseter muscle at 980 nm. *Iraqi Journal of Physics*, 18(2), 1-8.
- [12] Hassan et al. (2021). Path length of human temporalis muscle at 980 nm. *Journal of the Iraqi Academy of Sciences*, 22(1), 1-9.
- [13] Da Silva RF, et al. Effects of low-level laser therapy combined with exercise on pain and function in patients with temporomandibular disorders: a randomized controlled trial. *J Oral Rehabil.* 2023;50(3):257-265.
- [14] Kim J, et al. Comparison of the effects of 635nm and 980nm low-level laser therapy on pain and function in patients with temporomandibular disorders: a randomized controlled trial. *Lasers Med Sci.* 2024;39(2):347-354.
- [15] Valesan, L.F.; Da-Cas, C.D.; Réus, J.C.; Denardin, A.C.S.; Garanhani, R.R.; Bonotto, D.; Januzzi, E.; de Souza, B.D.M. Prevalence of Temporomandibular Joint Disorders: A Systematic Review and Meta-Analysis. *Clin. Oral Investig.* 2021, 25, 441–453.
- [16] Al-Jewair, T.; Shibeika, D.; Ohrbach, R. Temporomandibular Disorders and Their Association with Sleep Disorders in Adults: A Systematic Review. *J. Oral Facial Pain Headache* 2021, 35, 41–53.
- [17] Lei J, Yap AU, Zhang M, Fu KY (2021) Temporomandibular disorder subtypes, emotional distress, impaired sleep, and oral health-related quality of life in Asian patients. *Commun Dent Oral Epidemiol* 49:543–549.
- [18] Stinson, C.; Bellinger, L.L.; Puri, J.; Ahuja, N.; Bender, S.D.; Kramer, P.R. Estrogenic effects on temporomandibular disorder and pain. *J. Appl. Biobehav. Res.* 2019, 24, e12164.
- [19] Nauru, R.; Rieppo, L.; Tuomisto, T.; Yu, J.; Laaksonen, S.; Saarakkala, S.; Raustia, A.; Pirttiniemi, P. Fourier-transform infrared study on effects of ageing, oestrogen level and altered dietary loading on rat mandibular condylar cartilage. *Orthod. Craniofac. Res.* 2024, 27, 151–164.
- [20] Yin, Y., He, S., Xu, J. et al. The neuro-pathophysiology of temporomandibular disorders-related pain: a systematic review of structural and functional MRI studies. *J Headache Pain* 21, 78 (2020).
- [21] DeLorey DS and Clifford PS (2022). Does sympathetic vasoconstriction contribute to metabolism: Perfusion matching in exercising skeletal muscle? *Front. Physiol.* 13:980524.
- [22] Gürbüz, R. (2023). The effect of low-level laser therapy on myofascial pain and tender points in patients with temporomandibular disorders. *Journal of Clinical and Experimental Dentistry*, 15(3), e245-e250.
- [23] Santos, R. F. (2022). Low-level laser therapy in the treatment of temporomandibular disorders. *Journal of Oral Science*, 64(1), 1-6.



- [24] Hamblin, M. R. (2020). Photobiomodulation: A light-based therapy. *Journal of Clinical and Translational Research*, 6(3), 1-12.
- [25] Dantas, P. R. (2022). Effects of low-level laser therapy on mouth opening and pain in patients with temporomandibular disorders. *Journal of Photomedicine and Laser Surgery*, 22(2), 1-6.
- [26] Al-Ameri, L.M., Laser Biostimulation Effect on Human Sperm Motility. *Iraqi Journal of Laser*, 2021. 20(1): p. 39-42.
- [27] Haidar Flayyih Hasan, Layla M. H. Al-ameri, Ammar Saleh Alalawi, Impact of Low Level Laser Therapy on Mandibular Range Motion in Temporomandibular Joint Disorder in Iraqi Patients , *Iraqi Journal of Laser: Vol. 23 No. 2* (2024).
- [28] Assi, A.A., R.A. Faris, B.S. Abdulhameed, and S.S. Almalki, The Effect of Dual Diode Laser:(810,980) nm in Acceleration of Orthodontic Tooth Movement: A Case Report. *Iraqi Journal of Laser*, 2023. 22(2): p. 19-26.
- [29] Al-Saadi et al. (2022). Effects of 635 nm laser therapy on collagen synthesis and wound healing in diabetic rats. *Iraqi Journal of Laser*, 21(1), 1-8.
- [30] Hassan et al. (2023). Evaluation of 635 nm laser therapy on fibroblast proliferation and skin texture in patients with acne scars. *Journal of the Iraqi Academy of Sciences*, 24(1), 1-9.
- [31] Al-Abdullah, K. (2021). Effect of low-level laser therapy on pain and function in patients with temporomandibular disorders. *Journal of Oral and Maxillofacial Surgery*, 30(2), 100-105. (Scopus, DOI: 10.21608/ajns.2021.200944).
- [32] Buduru S, Oprea DM, Manziuc MM, Leucuța DC, Almășan O. Effectiveness of Laser Therapy in Treatment of Temporomandibular Joint and Muscle Pain. *J Clin Med*. 2024 Sep 9;13(17):5327.
- [33] Al-Tae, A. (2022). Comparative study between ultrasound and laser therapy in treatment of temporomandibular disorders. *Journal of Baghdad College of Dentistry*, 34(1), 23-28. (Scopus, DOI: 10.33899/jbcd.2022.166849).
- [34] Al-Saadi, 2022. Effect of low-level laser therapy on pain and function in patients with temporomandibular disorders. *Journal of Clinical and Diagnostic Research*, 16(9), ZC01-ZC05.
- [35] Al-Khateeb, T. (2023). Efficacy of low-level laser therapy in treatment of temporomandibular disorders. *Iraqi Journal of Dental Sciences*, 21(1), 45-50.
- [36] Al-Rawi, N. (2020). Photobiomodulation therapy in dentistry. *Iraqi Journal of Dental Sciences*, 18(1), 15-20.
- [37] Al-Mamgouter, A. (2023). Efficacy of low-level laser therapy in treatment of temporomandibular disorders. *Journal of Dental and Medical Sciences*, 22(3), 12-18. (Scopus, DOI: 10.4103/jdms.jdms_115_22).
- [38] Yeladandi M, Chavva S, Padala SB, Khanam S, Vemula H, MoparthiH. Effects of Transcutaneous Electrical Nerve Stimulation, Laser Therapy, and Ultrasound in Managing Temporomandibular Disorders: A Randomised Clinical Study *J Clin of Diagn Res*. 2024; 18(3):ZC01-ZC06.

دراسة مقارنة بين استخدام جهاز (ليزر 635) وجهاز (ليزر 980) في علاج اضطرابات الصدغية الفكية

نور قاسم محمد¹، زينب فاضل مهدي¹، بلسم سعدي عبد الحميد²

¹معهد الليزر للدراسات العليا، جامعة بغداد، بغداد، العراق.

²مستشفى مدينة الامامين الكاظمين التعليمي، بغداد، العراق.

البريد الإلكتروني للباحث : noor.qasem2202m@ilps.uobaghdad.edu.iq

الخلاصة: مقدمة: ان اضطرابات المفصل الصدغي الفكى هي مجموعة معقدة من الحالات التي تؤثر على المفصل الصدغي الفكى وعضلات المضغ مما يؤدي إلى الألم وانخفاض حركة الفك وأعراض أخرى منهكة. غالبًا ما تنشأ هذه الحالات عن أسباب متعددة العوامل بما في ذلك سوء الإطباق والصدمات والإجهاد والعادات غير الوظيفية. ان العلاج الفعال لهذه الاضطرابات من الامور الصعبة مما يستلزم اتباع أساليب علاجية مبتكرة.



الهدف: تهدف هذه الدراسة الى مقارنة وتقييم فعالية طريقتين من طرق العلاج بالليزر منخفض المستوى بطول موجي 635 نانومتر و980 نانومتر في علاج أعراض اضطراب المفصل الصدغي الفكي. والهدف هو تحديد الطول الموجي الذي يوفر نتائج علاجية قصيرة وطويلة الأمد متفوقة في تخفيف الألم وتحسين وظيفة الفم وتقليل النقاط المؤلمة.

المواد والطرق: تم تقسيم خمسين مريضاً تم تشخيصهم باضطراب المفصل الصدغي الفكي (TMD) بشكل عشوائي إلى مجموعتين. تلقت المجموعة الأولى علاجاً بالليزر منخفض المستوى 635 نانومتر بينما عولجت المجموعة الثانية بالليزر منخفض المستوى 980 نانومتر. تم قياس مستويات الألم ونطاق فتح الفم وعدد النقاط المؤلمة قبل كل علاج وفي متابعة بعد شهر واحد من العلاج. تم تحليل البيانات باستخدام الأساليب الإحصائية المناسبة لتقييم فعالية العلاجات.

النتائج: أظهرت النتائج أن مجموعة الليزر 635 نانومتر شهدت انخفاضاً أكبر بكثير في شدة الألم ($p = 0.025$) ونقاط أقل إيلاًماً في العضلة الماضغة ($p = 0.048$) مقارنة بمجموعة الليزر 980 نانومتر أثناء التقييم قصير المدى. غير انه لم تلاحظ أي فروقات كبيرة بين المجموعتين في المتابعة بعد شهر واحد من المعالجة.

الاستنتاجات: أظهر الليزر بطول موجة 635 نانومتر فعالية فائقة على المدى القصير في تقليل الألم ونقاط الألم في العضلة الماضغة، في حين كان كلا الطولين الموجيين فعالين بنفس القدر على المدى الطويل. وتسلط هذه النتائج الضوء على أهمية اختيار الطول الموجي في تحسين بروتوكولات العلاج بالليزر منخفض المستوى لإدارة اضطراب المفصل الصدغي الفكي (TMD). وهناك حاجة إلى مزيد من البحث لاستكشاف الآليات الكامنة وراء هذه الاختلافات وتحديد المعايير المثلى لتحقيق نتائج علاجية مستدامة.



In vitro investigation: the impact of MI varnish and fractional CO₂ laser on demineralized enamel surfaces

Ayat Majid Salih^{1,*}, Aseel Jasim Ali², And Soudad Salman Ahmed³

¹ Institute of Laser for Postgraduate Studies, University of Baghdad, Baghdad, Iraq

² Department of Oral Medicine, College of Dentistry, Al-Mustafa University College, Baghdad, Iraq

³ Department of Physics, Faculty of Science, University of Baghdad, Baghdad, Iraq

* Email address of the Corresponding Author: ayatalsaraj@gmail.com

Article history: Received: 15 Dec. 2024; Revised: 5 Apr. 2025; Accepted: 22 May 2025; Published online: 15 Jun. 2025.

Abstract: To assess the therapeutic efficacy of fractional CO₂ laser and MI varnish alone and their combined effects in two cases (CO₂ Laser before and after the application of MI varnish). Method: 60 enamel samples were prepared, and then the samples were passed through the pH cycling process to induce a demineralized enamel surface. The samples were categorized into five groups: control, CO₂ laser, MI varnish, CO₂ laser with MI varnish, and MI varnish with CO₂ laser. Surface alterations were evaluated using the Vickers microhardness assessment, surface roughness, and the Scanning Electron Microscope (SEM) combined with the Energy-Dispersive X-ray Spectroscopy (SEM-EDX). Results: All of the microhardness results were diminished after the demineralization process, and then subsequently, the different treatments enhanced the demineralized enamel surface with no notable distinction among the treatment groups. The surface roughness data showed improved surface roughness in the CO₂ laser-containing groups. The surface morphology and mineral weight were enhanced after the treatments. All treatment groups were effective in enhancing the microhardness, roughness, and surface morphology in comparison to the control group, preferring the simultaneous application of CO₂ laser and MI varnish in both instances (similar results).

Keywords: MI varnish, fractional CO₂ laser, hardness, roughness, combined use.

1. Introduction

Enamel serves as the protective layer of the tooth. It is a rigid, slender, opaque material that envelops and safeguards the dentin. Enamel comprises 96% inorganic material substances, 4% organic compounds, and water. So, it is the most mineral-rich tissue in the human body [1]. Tooth decay, or dental caries, is caused by germs such as *Streptococcus mutans* in dental plaque, which generate acids that erode the teeth, resulting in demineralization. This bacterium is prevalent in the oral cavity and leads to dental caries [2]. Hypomineralized enamel exhibits diminished mineral content, a disordered structure, expanded prism sheaths, and decreased calcium levels while possessing elevated carbon and protein concentrations compared to healthy dental enamel [3]. This produces a surface that is more porous and less resilient than healthy teeth [3,4]. The probability of developing dental caries is increased [5]. An imbalance between



demineralization and remineralization may result in mineral loss from the outer surface, leading to carious lesions. If remineralization is more effective, these lesions can be stopped and restored(6). The objective of remineralization procedures is to augment the mineral composition of under-mineralized tooth tissues, hence improving their physical qualities and increasing their resistance to decay(7). This process involves reintroducing calcium phosphate ions into the lesion, where they solidify. The concentration must be higher than that in the lesion to ensure the calcium phosphate ions diffuse into the enamel through micropores. However, the concentration should not be so high that it causes surface precipitation, which can block tubules and hinder ion entry into the white spot lesions(8).

The loss of hard tissue in teeth results from two main processes: the degradation of apatite crystals in the enamel and the movement of calcium, phosphate, and hydrogen ions. Demineralization starts with subsurface lesions that can develop into visible clinical lesions if it continues(9). In managing tooth decay, it is important to detect early lesions and employ remineralizing chemicals to avert more decay and cease the demineralization process prior to cavity formation(10). It's been confirmed that high-calcium mineralizing agents can reverse white spot lesions and prevent them from progressing to cavities(11).

Recently, this noninvasive technique was used to maintain the preservation of dental integrity against carious decay and to avoid the occurrence of incipient lesions. Fluoride use is an efficient method to prevent enamel demineralization and facilitate remineralization, even at minimal fluoride doses(12). MI varnish is a commercial formulation consisting of casein phosphopeptide, amorphous calcium phosphate, and fluoride, which possesses mineralizing properties that replenish lost ions in demineralized enamel(13). The effect of varnish on enamel exceeds that of alternative topical fluoride treatments such as toothpaste, gels, and mouthwashes(14). Varnishes are more acceptable, do not require patient cooperation, and cause less discomfort to the patients(15). In a study conducted by Cochran et al.(16), the efficacy of casein phosphopeptide stabilized amorphous calcium phosphate (CPP-ACP) and amorphous calcium fluoride phosphate (CPP-ACFP) in the remineralization of enamel subsurface lesions was evaluated. The CPP sequesters free calcium, fluoride, and phosphate ions and hinders the precipitation of mineral ions at neutral pH. Nonetheless, this binding diminishes when the pH is decreased to 5.5 or below, facilitating the release of mineral ions.

When fluoride is added to HAP, it becomes fluorapatite (FAP), with lower solubility and increased acid resistance(17). The introduction of casein phosphopeptide-amorphous calcium phosphate paste (CPP-ACP) has proven to be a useful method for augmenting enamel resistance to caries; CPP consists of A congregation of phosphoryl residues stabilizes ACP nanoclusters in a metastable solution. It is an adhesive protein that associates with phosphate and calcium ions, stabilizing them in an amorphous state(18).

The CO₂ laser with a 10,6µm wavelength is highly recommended as its penetration depth is tenfold deeper without compromising the pulp tissue or elevating its temperature(19). The absorption of this range occurs at the carbonate, phosphate, and hydroxyl groups that are in hydroxyapatite crystals(20). The absorption of laser light by minerals induces structural and chemical alterations in enamel crystals, evidenced by the thermal disintegration of carbonated hydroxyapatite, which diminishes dissolution and improves resistance to acid assaults(21). The surface alterations penetrate to a depth of 58 µm, thereby diminishing demineralization by up to 98% in the enamel surface(22). If the laser is used improperly with a high dose, this will lead to enamel surface carking and irregularities, which will decrease enamel hardness and increase brittleness(23). When utilizing a laser for caries prevention, it is essential to keep the laser energy below the ablative threshold to effectuate chemical alterations in the enamel surface without inflicting morphological damage(24).

Esteves-Oliveira et al. observed diminished mineral loss and the re-hardening of softened enamel in samples solely treated with CO₂ laser; however, the combination of fluoride and subsequent CO₂ laser irradiation significantly prevented alterations in surface microhardness(25). The enhancement in hardness may be attributed to crystal development associated with temperature fluctuations, resulting in larger crystals and a reduction in crystallographic defects(26). Ramalho et al. discovered that both CO₂ laser irradiation alone and the combination fluoride-laser therapy resulted in reduced mineral loss compared to the fluoride group across all storage durations(27). Laser and fluoride have synergistic effects, improving enamel acid resistance attributable to the elimination of organic matrix, augmented fluoride absorption, and expanded



surface area for ion adhesion(26). Irradiating CO₂ laser with fluoride application may result in the development of fluorohydroxyapatite and calcium fluoride (CaF₂) on the enamel surface. These compositions act as a fluoride reservoir during enamel demineralization and are employed in the subsequent remineralization process(20).

This study assessed and contrasted the efficacy of fractional CO₂ laser, MI varnish, and combined methods in improving the surface characteristics of demineralized enamel. The null hypothesis examined was that none of these methods can improve the surface characteristics, microhardness, and roughness of the demineralized enamel surface.

2. Material and Method

Thirty sound premolar teeth were collected without cracks, demineralization, or filling material. Teeth were collected from patients seeking orthodontic treatment <30 years and maintained in a 0.1% thymol solution at 4°C without modifying the storage media until the commencement of the study(28).

The teeth were washed and cleaned, and all periodontic ligament and soft tissue were removed using an ultrasonic scaler. Then, the dental crowns of the teeth were polished through micropores with non-fluoridated pumice paste with a low-speed handpiece. Then, the teeth were cleaned with an ultrasonic cleaner to remove all pumice residue for 4 minutes. By fixing the root of the tooth with a mechanics vice, the crown was cut mesiodistally with a water-cooled diamond blade and then cut to obtain square pieces of 4*4 mm from the buccal and from the lingual side from the center of the surface. The samples were poured with acrylic in a silicon mold (the samples were placed on top of the resin mix). The external enamel surface was polished using silicon waterproof abrasive paper (P 800, P 1200, P 2000) underwater to provide flat and smooth surfaces. Then, samples were cleaned ultrasonically to remove all smear layers and stored in de-ionized water in a plastic screw cup at 4°C till used to avoid dehydration(29). All samples underwent a pH cycling procedure to induce the demineralized enamel surface before treatment(30). This procedure consisted of two solutions (the demineralizing and remineralizing solutions). Each sample was placed in a separate plastic cup containing a demineralizing solution for 6 hours, then cleaned with deionized water and placed in another plastic container with a remineralizing solution for 18 hours; all samples were placed inside a water path during the pH cycling procedure to mimic the temperature inside the oral cavity, which was about 37°C. This process was continuous for ten days, so a white spot lesion was formed. The samples were divided into five groups (12 samples in each): 1- control group (with no treatment, samples stored in artificial saliva only (31)), 2- varnish group (samples receive MI varnish treatment only), 3- CO₂ laser group (the samples receive laser treatment only), 4- CO₂ with MI varnish group (sample received laser treatment first, then varnish treatment), and 5- MI varnish with CO₂ laser group (samples receive MI varnish treatment first then laser treatment). The MI varnish was applied by utilizing a tiny applicator brush to apply a single layer of varnish over the enamel surface, allowing it to remain undisturbed for 20 seconds to dry. Subsequently, samples were preserved in artificial saliva for a period of four hours; after that, the varnish layer was removed. This is applied to all groups with MI varnish treatments. A pilot study was conducted to select the most suitable fractional CO₂ laser parameters. The most suitable parameters were 2W power, 10 millisecond (ms) pulse duration, 1 ms interval, 1mm distance, and 20 Hz frequency in non-contact mode. The laser treatment was done for all groups with fractional CO₂ laser treatment (on a dry and clean surface for the CO₂ laser group, before MI varnish in the CO₂ Laser with MI varnish group, after applying MI varnish and removed it before laser treatment in the MI varnish with CO₂ laser group). Afterwards, the samples were kept in artificial saliva at 37°C.

The investigations used were the microhardness test (Vickers hardness microscope) and the profilometer roughness test. Hardness and roughness measurements were taken at every study step (sound enamel, demineralized enamel, and treated samples). Three readings were taken at each test for each sample, and the mean was then calculated. A scanning electron microscope has been used to analyze alterations in the sample's surface morphology. The samples were coated with gold to enhance the resolution of the final



image. One sample was examined from each group. The same sample examined for the SEM was used to measure the changes in the element weight of the enamel by using Energy Dispersive Spectroscopy.

3. Results and discussion

3.1. Statistical data analysis

Data were analyzed with statistical analysis software (SPSS). Then, by using Tukey HSD, multiple pairwise comparisons were done between phases of microhardness and surface roughness readings.

The microhardness decreases after demineralization and then increases after the different treatment methods, with significant differences in all phases of demineralization to treatment, except for the control group and the CO₂ laser group, as shown in Table 1.

The microhardness after treatment was higher in the varnish group, followed by the CO₂ laser with varnish group, and lower in all groups with no significant differences. There was a nonsignificant difference between groups in every study phase (Table 1).

In table 2 of the microhardness measurement, there was a significant difference inside each group phase except for the demineralization to the treatment phase of the control group and the demineralization to the treatment phase of the CO₂ group.

Table 1: Descriptive and statistical analysis of surface microhardness across groups, phases, and treatments.

Group	Treatments	H 1		H 2		H 3		F	P value
		Mean	± SD	Mean	± SD	Mean	± SD		
BDT	The Control	337.667	17.607	138.760	39.159	149.600	40.958	162.895	0.000
	MI Varnish	356.775	16.358	145.005	23.307	170.075	28.609	536.974	0.000
	CO ₂ laser	353.892	14.765	141.095	23.846	148.283	18.155	2604.440	0.000
	MI with CO ₂	352.317	16.999	112.651	20.028	147.108	20.214	347.971	0.000
	CO ₂ with MI	376.283	13.304	126.153	17.532	150.292	21.955	1335.657	0.000
P value		0.052		0.051		0.220			

Table 2 Multiple pairwise comparison of SM among phases using Tukey HSD.

Group	Treatments	Phases	Phases			
			D		T	
			MD	p value	MD	p value
BDT	Control	B	198.907	0.000	188.067	0.000
		D			-10.840	0.051
	MI Varnish	B	211.770	0.000	186.700	0.000
		D			-25.070	0.007
	CO ₂ laser	B	212.797	0.000	205.608	0.000
		D			-7.188	1.000
	MI with CO ₂	B	239.666	0.000	205.208	0.000
		D			-34.457	0.000
	CO ₂ with MI	B	250.130	0.000	225.992	0.000
		D			-24.138	0.000



In Table 3, regarding surface roughness analysis data, no substantial differences were seen between the groups in any phase of the treatment. In the varnish with CO₂ group, no significant variances were observed between the phases across the same group.

After the treatment, the higher roughness reading was in the varnish group than the control group, and the lowest reading was in the CO₂ laser with the varnish group.

In table 4, the data were non-significant in all phases in the groups except: sound to demineralization in control, varnish group and CO₂ laser with varnish group and from demineralization to treatment phase in CO₂ laser group and varnish group.

Table 3 Descriptive and statistical analysis of surface roughness across groups, phases, and treatments.

Phases	Treatments	R1		R2		R3		P value
		Mean	±SD	Mean	±SD	Mean	±SD	
BDT	Control	0.596	0.105	0.830	0.251	0.705	0.151	0.030
	MI Varnish	0.675	0.130	0.937	0.251	0.721	0.114	0.025
	CO ₂ laser	0.683	0.066	0.781	0.109	0.674	0.113	0.033
	MI with CO ₂	0.624	0.082	0.748	0.140	0.700	0.100	0.067
	CO ₂ with MI	0.603	0.082	0.729	0.129	0.656	0.126	0.031
P value		0.086		0.062		0.709		

Table 4 Multiple pairwise comparison of SM among phases using Tukey HSD.

Group	Treatments	Phases	Phases			
			D		T	
			MD	p value	MD	p value
BDT	control	B	-0.234	0.022	-0.109	0.166
		D			0.125	0.242
	MI Varnish	B	-0.262	0.018	-0.045	1.000
		D			0.217	0.030
	CO ₂ laser	B	-0.099	0.173	0.009	1.000
		D			0.107	0.025
	CO ₂ with MI	B	-0.126	0.032	-0.053	0.874
		D			0.074	0.832

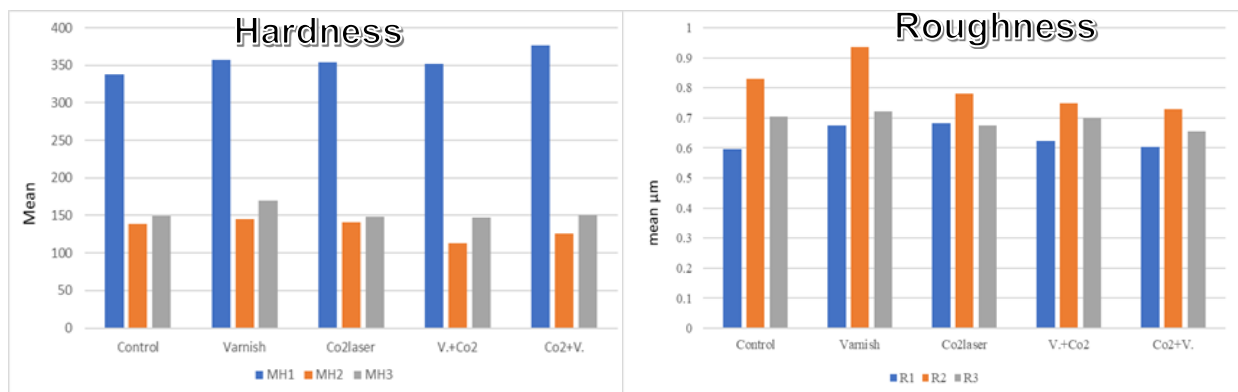


Fig.1 Graphical representation of microhardness and surface roughness data.

3.2. Scanning Electron Microscope and Energy Dispersive Spectroscopy

The sound-polished enamel surface appears smooth and homogenous, with minimal irregularities and debris. The demineralized enamel surface shows porosities and irregularities. The enamel rods lose their organized structure, creating a rough and uneven surface with pitted areas and a loss of the typical prismatic pattern. The surface may also appear more translucent due to reduced mineral content. The group treated with CO₂ laser shows smoother and more uniform characteristics than untreated or demineralized enamel. The laser treatment aids in remineralizing the enamel surface, thereby reducing porosities and irregularities. As a result, you may notice a reformation of the prismatic structure and an improvement in surface integrity. Demineralized enamel surfaces that are treated with an MI varnish typically exhibit fewer porosities and irregularities compared to untreated demineralized enamel. The varnish aids in remineralizing the enamel surface, resulting in a smoother and more uniform appearance. You may also notice a partial reformation of the prismatic structure and an improvement in surface integrity. The synergistic impact of the fractional CO₂ laser and CPP-ACPF varnish on a demineralized enamel surface yields substantial enhancements in surface morphology. SEM images typically show a smoother and more homogeneous surface with fewer irregularities compared to untreated enamel. The prismatic structure of the enamel is partially restored, and the overall integrity of the surface is enhanced, as shown in Fig 2.

The EDX measurement was higher in the sound enamel sample, then decreased after the demineralization process. The calcium weight percentage was the element that decreased; the phosphate decreased slightly. After the treatment, the phosphate weight percentage was slightly changed. The calcium weight percentage was higher in the MI varnish with CO₂ laser group; the rest of the treatment was similar in the results. The carbon weight percentage was higher in sound enamel than in the MI varnish with CO₂ laser group; the rest of the groups were comparable in carbon results, Fig 3 and Table 5.

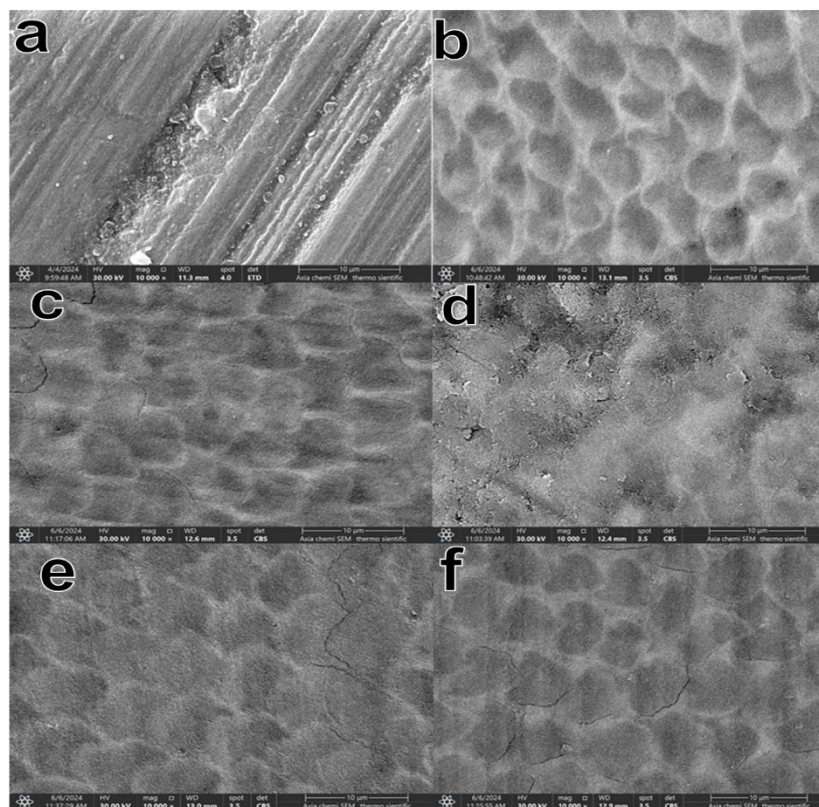


Fig.2 SEM pictures of the enamel surfaces of the groups, **a**: sound enamel, **b**: demineralized enamel, **c**: CO₂ laser varnish treatment, **e**: CO₂ laser with varnish group, **f**: varnish with CO₂ laser group.

Table 5 Elements weight percentage.

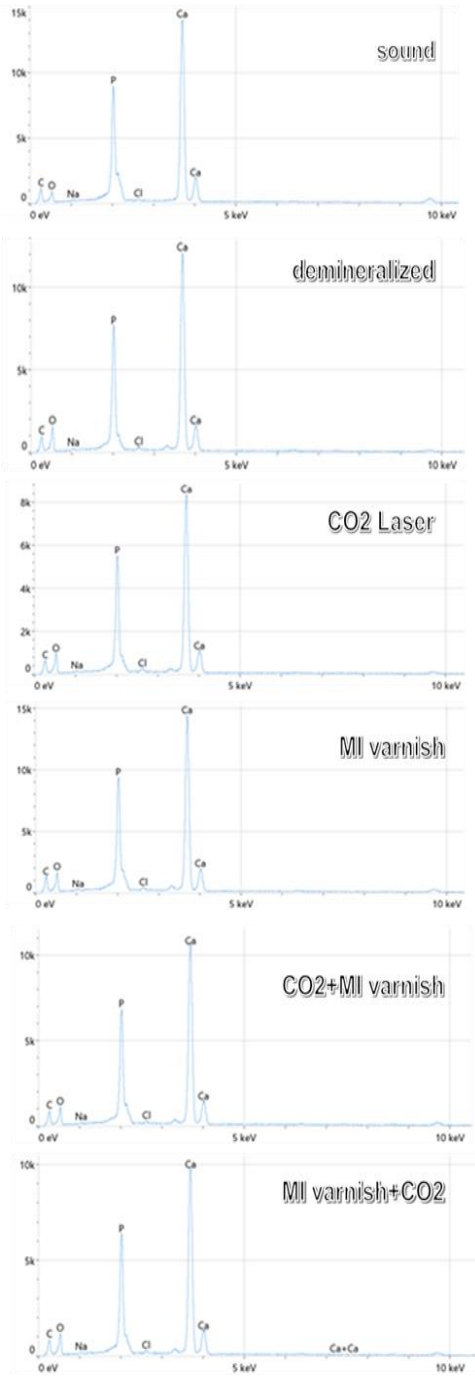


Fig.3 EDX analysis.

samples	Carbon weight %	Phosphate weight %	Calcium weight %
Sound enamel	16.7%	15.9%	44.3%
Demineralized enamel	13.4%	15.2%	35.5%
CO ₂ laser	14.6%	15.4%	36.1%
MI varnish	16.4%	15.1%	36.3%
CO ₂ Laser with MI varnish	14.7%	15.1%	36.8%
MI varnish with CO ₂ Laser	15.1%	15.5%	39

3.3. Discussion

This study assessed and analyzed the treatment efficacy of MI varnish (CPP-ACPF) and fractional CO₂ laser on demineralized enamel surfaces. The results suggest that all the treatment approaches effectively enhanced the hardness characteristics of the demineralized enamel surfaces. The null hypothesis was rejected in this investigation. The Vickers microhardness test effectively assesses tooth enamel's microstructure and detects changes in mineral density, indicating mineral loss or gain(32). The results of microhardness testing indicated that demineralization led to a significant reduction in mean hardness compared to the baseline. This reduction may be attributed to enamel weakness caused by an increase in pore size due to the loss of minerals from the enamel surface resulting from the dissolution of hydroxyapatite.

The absorption peak of hydroxyapatite crystal, the main component of dental enamel, matches the wavelength of the CO₂ laser. This means the laser is absorbed and converted to heat without harming surrounding tissues(33). This process will reduce demineralization by decreasing the permeability and acid diffusion of enamel surfaces (34).

The CO₂ laser has been reported to enhance the crystalline stability of enamel, hence reducing its susceptibility to acid and augmenting fluoride absorption by the enamel (35). Chiang et al. indicated that laser alters the permeability of the enamel matrix. This reduces acid diffusion, while changes in the enamel's organic and inorganic constituents enhance microhardness and diminish acid susceptibility(36). In our present investigation, we employed sub-ablative laser settings. These lasers reduce the solubility of hydroxyapatite and impede the inter-prismatic spaces by melting and recrystallizing enamel prisms on the surface. Furthermore, the administration of fluoride varnish or fluoride gel before radiation exposure might transform enamel hydroxyapatite into fluorapatite, hence reducing enamel solubility. This allows the irradiated surface to retain fluoride ions for a longer duration compared to non-laser irradiated enamel(27).

According to the hardness measurements, there exists a notable disparity in the hardness of combined groups between demineralization measurements and post-treatment assessments, also, the laser's effect on the demineralized enamel surface was not significantly different from the demineralizing measurement in the CO₂ laser group and it's non-significant-from the final measurement that in the control group, in which the samples were placed in artificial saliva only. The use of MI varnish alone demonstrated a high increase in hardness measurement compared to other groups. However, the laser effect significantly decreased surface roughness in the CO₂ laser group and in the CO₂ laser with MI varnish group. The results of EDX show that the sound enamel had a higher mineral percentage, which decreased after the demineralization of the enamel samples. After treatment of different groups, the mineral shows a slight increase after treatment, so it's still far from the sound enamel results. Repeated sessions of treatment are indicated in future works in an attempt to highlight the mineral percentage.

Fluoride products help remineralize teeth by creating more acid-resistant compounds when fluoride ions interact with dental hydroxyapatite crystals(37). This protein nanotechnology incorporates proteins sourced from bovine milk, resulting in the formation of amorphous calcium phosphate (ACP). All calcium phosphates are safe for individuals of all ages, including children, as they dissolve in the stomach upon accidental ingestion, releasing non-toxic calcium and phosphate ions.(38). Numerous dental care products utilizing calcium phosphates are derived from either CPP-ACP or HAP. CPP-ACP sustains a saturated concentration of phosphate and calcium on the enamel surface, hence reducing demineralization and enhancing remineralization(39).

This study employed two combined treatment methods: the application of fractional CO₂ laser before and subsequent to MI varnish on the enamel that was a demineralized surface. The outcomes of these groups were notably comparable; nevertheless, the use of fractional CO₂ laser prior to MI varnish yielded superior results..

The researchers found that using a laser on the enamel surface before applying a remineralizing chemical enhances its effectiveness. One possible explanation is that the laser-created microgaps could be filled with fluoride after application, making it easier to incorporate the ions(40). The concurrent use of CPP-



ACFP and fractional CO₂ laser has been demonstrated to markedly improve tooth microhardness via a potent synergistic effect(22). Laser irradiation enhances fluoride adhesion to dental structures, resulting in elevated fluoride levels in the enamel. Apatite formed in a calcium and phosphorus milieu exhibits reduced carbonate and manganese levels, enhancing its resilience to acid assaults.

Liu et al. assessed the influence of CO₂ laser and fluoride on preventing tooth decay and determined that the laser did not exhibit a synergistic effect with fluoride treatment(41). Farhadian et al. (42) Investigated the impact of CPP-ACP paste and CO₂ laser treatment on the microhardness of demineralized enamel. They found that only the CO₂ laser treatment showed a significant difference from the control group, indicating that CPP-ACP paste was ineffective in preventing demineralization. Additionally, the CO₂ laser alone resulted in higher microhardness values than when combined with CPP-ACP paste, which is incompatible with the present study's findings.

Abufarwa et al. (43) evaluated the impacts of CPP-ACP fluoride varnish and CO₂ laser therapy on enamel demineralization and microhardness. They found that CPP-ACP fluoride varnish is more effective in preventing demineralization. The MI varnish used contains 22000 ppm fluoride, which, along with the CPP-ACP complex, enhances enamel hardness. They reported an increase in hardness to a depth of 60 µm with MI varnish, while the CO₂ laser did not yield encouraging results, which is similar to this study. Baniasad et al. (44) CPP-ACP paste and fractional CO₂ laser, neither alone nor in combination, did not improve the appearance of enamel remineralization compared to the control group. Certain researchers discovered markedly enhanced acid resistance when enamel was subjected to laser irradiation prior to fluoride treatment(45). Conversely, others contended that laser application ought to be conducted subsequent to fluoride therapy(25). Poosti et al. (46) Determined that laser irradiation prior to fluoride treatment significantly enhanced the surface microhardness of enamel, as seen at depths of 30 and 60 µm. Rajendran et al. (47, 48) determined that the concurrent application of CPP-ACP and fluoride exhibits a synergistic impact in the remineralization of enamel samples. Consequently, CPP-ACP with fluoride can be regarded as the preferred material for the remineralization of early enamel carious lesions. The fractional carbon dioxide laser is not explicitly intended for dental use. Additional design enhancements and superior accessories are required to improve comfort during dental treatments.

4. Conclusions

All treatment results had quite similar effects on demineralized enamel by increasing microhardness, decreasing roughness, and enhancing surface morphology, but using a fractional CO₂ laser with MI varnish improved surface roughness more than using them alone.

References

- [1] T. Brown, H. E. Lemay, and B. Bursten, *Chemistry: The Central Science*, 2009.
- [2] A. M. Vinogradov, M. Winston, C. J. Rupp, and P. Stoodley, "Rheology of biofilms formed from the dental plaque pathogen *Streptococcus mutans*," *Biofilms*, vol. 1, no. 1, pp. 49–56, 2004.
- [3] T. G. Fagrell, W. Dietz, B. Jälevik, and J. G. Norén, "Chemical, mechanical and morphological properties of hypomineralized enamel of permanent first molars," *Acta Odontol. Scand.*, vol. 68, no. 4, pp. 215–222, 2010.
- [4] K. Elhennawy et al., "Structural, mechanical and chemical evaluation of molar-incisor hypomineralization-affected enamel: A systematic review," *Arch. Oral Biol.*, vol. 83, pp. 272–281, 2017.
- [5] G. C. Americano, P. E. Jacobsen, V. M. Soviero, and D. Haubek, "A systematic review on the association between molar incisor hypomineralization and dental caries," *Int. J. Paediatr. Dent.*, vol. 27, no. 1, pp. 11–21, 2017.
- [6] J. S. Zhang, C. H. Chu, and O. Y. Yu, "Oral Microbiome and Dental Caries Development," *Dent. J. (Basel)*, vol. 10, no. 10, 2022.
- [7] F. A. Crombie, N. J. Cochrane, D. J. Manton, J. E. Palamara, and E. C. Reynolds, "Mineralisation of developmentally hypomineralised human enamel in vitro," *Caries Res.*, vol. 47, no. 3, pp. 259–263, 2013.
- [8] G. L. Vogel et al., "Composition of plaque and saliva following a sucrose challenge and use of an alpha-tricalcium-phosphate-containing chewing gum," *J. Dent. Res.*, vol. 77, no. 3, pp. 518–524, 1998.



- [9] R. P. Shellis, J. D. Featherstone, and A. Lussi, "Understanding the chemistry of dental erosion," *Monogr. Oral Sci.*, vol. 25, pp. 163–179, 2014.
- [10] H. M. Abbas, H. Hamza, and H. M. A. Ahmed (Eds.), *Minimal Intervention Approaches in Remineralizing Early Carious Lesions*, 2012.
- [11] H. H. Xu, M. D. Weir, L. Sun, S. Takagi, and L. C. Chow, "Effects of calcium phosphate nanoparticles on Ca-PO₄ composite," *J. Dent. Res.*, vol. 86, no. 4, pp. 378–383, 2007.
- [12] T. Rodemer, N. Pütz, and M. Hannig, "Influence of hydroxyapatite nanoparticles on the formation of calcium fluoride surface layer on enamel and dentine in vitro," *Sci. Rep.*, vol. 12, no. 1, 2022.
- [13] D. Dionysopoulos, K. Tolidis, and T. Sfeikos, "Effect of CPP-ACPF and nano-hydroxyapatite preventive treatments on the susceptibility of enamel to erosive challenge," *Oral Health Prev. Dent.*, vol. 17, no. 4, pp. 357–364, 2019.
- [14] M. A. Todd, R. N. Staley, M. J. Kanellis, K. J. Donly, and J. S. Wefel, "Effect of a fluoride varnish on demineralization adjacent to orthodontic brackets," *Am. J. Orthod. Dentofacial Orthop.*, vol. 116, no. 2, pp. 159–167, 1999.
- [15] H. E. Goodis, D. Fried, S. Gansky, P. Rechmann, and J. D. Featherstone, "Pulpal safety of 9.6 µm TEA CO₂ laser used for caries prevention," *Lasers Surg. Med.*, vol. 35, no. 2, pp. 104–110, 2004.
- [16] N. J. Cochrane, P. Shen, Y. Yuan, and E. C. Reynolds, "Ion release from calcium and fluoride containing dental varnishes," *Aust. Dent. J.*, vol. 59, no. 1, pp. 100–105, 2014.
- [17] T. T. Thuy et al., "Effect of strontium in combination with fluoride on enamel remineralization in vitro," *Arch. Oral Biol.*, vol. 53, no. 11, pp. 1017–1022, 2008.
- [18] K. Chokshi et al., "An in vitro comparative evaluation of three remineralizing agents using confocal microscopy," *J. Clin. Diagn. Res.*, vol. 10, no. 6, pp. ZC39–ZC42, 2016.
- [19] M. Esteves-Oliveira, K. F. El-Sayed, C. Dörfer, and F. Schwendicke, "Impact of combined CO₂ laser irradiation and fluoride on enamel and dentin biofilm-induced mineral loss," *Clin. Oral Investig.*, vol. 21, no. 4, pp. 1243–1250, 2017.
- [20] B. R. Zancopé et al., "CO₂ laser irradiation enhances CaF₂ formation and inhibits lesion progression on demineralized dental enamel—in vitro study," *Lasers Med. Sci.*, vol. 31, no. 3, pp. 539–547, 2016.
- [21] P. Rechmann, L. Q. Le, R. Kinsel, C. Kerbage, and B. M. T. Rechmann, "In vitro CO₂ 9.3-µm short-pulsed laser caries prevention—effects of a newly developed laser irradiation pattern," *Lasers Med. Sci.*, vol. 35, no. 4, pp. 979–989, 2020.
- [22] S. M. Adel, E. S. Marzouk, and N. El-Harouni, "Combined effect of Er,Cr:YSGG laser and casein phosphopeptide amorphous calcium phosphate on the prevention of enamel demineralization," *Angle Orthod.*, vol. 90, no. 3, pp. 369–375, 2020.
- [23] N. Yilmaz et al., "Effect of the usage of Er,Cr:YSGG laser with and without different remineralization agents on the enamel erosion of primary teeth," *Lasers Med. Sci.*, vol. 35, no. 7, pp. 1607–1620, 2020.
- [24] S. Ghadimi, M. Khami, and S. Razeghi, "Combined effect of laser irradiation and fluoride application in dental caries prevention," *J. Dent. Med. Tehran Univ. Med. Sci.*, 2015.
- [25] M. Esteves-Oliveira et al., "Rehardening of acid-softened enamel and prevention of enamel softening through CO₂ laser irradiation," *J. Dent.*, vol. 39, no. 6, pp. 414–421, 2011.
- [26] M. Mahmoudzadeh et al., "Effect of CO₂ laser on the prevention of white spot lesions during fixed orthodontic treatment: A randomized clinical trial," *Turk. J. Orthod.*, vol. 32, no. 3, pp. 165–171, 2019.
- [27] K. M. Ramalho et al., "Protective effect of CO₂ laser (10.6 µm) and fluoride on enamel erosion in vitro," *Lasers Med. Sci.*, vol. 28, no. 1, pp. 71–78, 2013.
- [28] A. Secilmis, E. Dilber, N. Ozturk, and F. G. Yilmaz, "The effect of storage solutions on mineral content of enamel," *Mater. Sci. Appl.*, vol. 4, no. 7, pp. 7–12, 2013.
- [29] J. Parry, L. Shaw, M. J. Arnaud, and A. J. Smith, "Investigation of mineral waters and soft drinks in relation to dental erosion," *J. Oral Rehabil.*, vol. 28, no. 8, pp. 766–772, 2001.
- [30] M. Alghazali, F. Abdul-Razzak, M. Al-Bazaz, N. Jafer, M. Radhi, and K. Hubeatir, "Effect of CO₂ laser and selected nanoparticles on the microhardness of human dental enamel in vitro study," *J. Med. Chem. Sci.*, vol. 6, no. 7, pp. 1487–1497, 2023.
- [31] M. Björklund, A. C. Ouwehand, and S. D. Forssten, "Improved artificial saliva for studying the cariogenic effect of carbohydrates," *Curr. Microbiol.*, vol. 63, no. 1, pp. 46–49, 2011.
- [32] W. A. Fried, M. Abdelaziz, C. L. Darling, and D. Fried, "High contrast reflectance imaging of enamel demineralization and remineralization at 1950-nm for the assessment of lesion activity," *Lasers Surg. Med.*, vol. 53, no. 7, pp. 968–977, 2021.



- [33] F. M. Bevilacqua, D. M. Zzell, R. Magnani, P. A. Ana, and C. P. Eduardo, "Fluoride uptake and acid resistance of enamel irradiated with Er:YAG laser," *Lasers Med. Sci.*, vol. 23, no. 2, pp. 141–147, 2008.
- [34] M. Shubbar, A. Addie, and L. Al-Tae, "The effect of a bioactive oral system and CO₂ laser on enamel susceptibility to acid challenge," *Diagnostics (Basel)*, vol. 13, no. 6, 2023.
- [35] A. Mathew et al., "Acquired acid resistance of human enamel treated with laser (Er:YAG laser and CO₂ laser) and acidulated phosphate fluoride treatment: An in vitro atomic emission spectrometry analysis," *Contemp. Clin. Dent.*, vol. 4, no. 2, pp. 170–175, 2013.
- [36] Y. C. Chiang et al., "Microstructural changes of enamel, dentin-enamel junction, and dentin induced by irradiating outer enamel surfaces with CO₂ laser," *Lasers Med. Sci.*, vol. 23, no. 1, pp. 41–48, 2008.
- [37] A. Lussi et al., "The use of fluoride for the prevention of dental erosion and erosive tooth wear in children and adolescents," *Eur. Arch. Paediatr. Dent.*, vol. 20, no. 6, pp. 517–527, 2019.
- [38] J. Enax, F. Meyer, E. Schulze Zur Wiesche, and M. Epple, "On the application of calcium phosphate micro- and nanoparticles as food additive," *Nanomaterials (Basel)*, vol. 12, no. 22, 2022.
- [39] P. Somasundaram, N. Vimala, and L. G. Mandke, "Protective potential of casein phosphopeptide amorphous calcium phosphate containing paste on enamel surfaces," *J. Conserv. Dent.*, vol. 16, no. 2, pp. 152–156, 2013.
- [40] F. A. R. M. Al-Bazaz, M. H. Radhi, N. J. Hubeatir, and M. W. Alghazali, "Effect of CO₂ laser and selected nanoparticles on the microhardness of human dental enamel in vitro study," *J. Med. Chem. Sci.*, vol. 6, no. 7, pp. 1487–1497, 2023.
- [41] Y. Liu, C. Y. Hsu, C. M. Teo, and S. H. Teoh, "Potential mechanism for the laser-fluoride effect on enamel demineralization," *J. Dent. Res.*, vol. 92, no. 1, pp. 71–75, 2013.
- [42] N. Farhadian et al., "Effect of CPP-ACP paste with and without CO₂ laser irradiation on demineralized enamel microhardness and bracket shear bond strength," *Dental Press J. Orthod.*, vol. 22, no. 4, pp. 53–60, 2017.
- [43] M. Abufarwa, A. Noureldin, T. Azimaie, P. M. Campbell, and P. H. Buschang, "Preventive effects of carbon dioxide laser and casein phosphopeptide amorphous calcium phosphate fluoride varnish on enamel demineralization: A comparative, in vitro study," *J. Investig. Clin. Dent.*, vol. 10, no. 2, p. e12400, 2019.
- [44] N. Baniasad, M. Poosti, S. Etemadi, F. Mahmoudi, and K. Mirmohammadi, "Effects of fractional carbon dioxide laser and CPP-ACP paste on remineralization and discoloration of enamel white spot lesions," *J. Res. Dent. Maxillofac. Sci.*, vol. 9, no. 3, pp. 174–183, 2024.
- [45] S. Tagomori and T. Morioka, "Combined effects of laser and fluoride on acid resistance of human dental enamel," *Caries Res.*, vol. 23, no. 4, pp. 225–231, 1989.
- [46] M. Poosti, F. Ahrari, H. Moosavi, and H. Najjaran, "The effect of fractional CO₂ laser irradiation on remineralization of enamel white spot lesions," *Lasers Med. Sci.*, vol. 29, no. 4, pp. 1349–1355, 2014.
- [47] R. Rajendran et al., "Comparative evaluation of remineralizing potential of topical cream containing casein phosphopeptide-amorphous calcium phosphate and casein phosphopeptide-amorphous calcium phosphate with fluoride: An in vitro study," *J. Pharm. Bioallied Sci.*, vol. 16, suppl. 2, pp. S1801–S1804, 2024.
- [48] R. Rajendran et al., "Development of strontium-doped nano hydroxyapatite dentifrice and compare its remineralising potential with a topical cream containing casein phosphopeptide-amorphous calcium phosphate – An in vitro study," *Indian J. Dent. Res.*, vol. 32, no. 1, pp. 92–97, 2021.

دراسة مختبرية: تأثير ورنيش MI وليزر ثنائي أوكسيد الكربون الجزئي على سطح المينا منزوعة المعادن

آيات ماجد صالح¹، اسيل جاسم علي²، سوّدد سلمان احمد³

¹معهد الليزر للدراسات العليا، جامعة بغداد، بغداد، العراق.

²قسم طب الفم، كلية طب الاسنان، الجامعة المستنصرية، بغداد، العراق.

³قسم الفيزياء، كلية العلوم، جامعة بغداد، بغداد، العراق.

البريد الإلكتروني للباحث : ayatalsaraj@gmail.com



الخلاصة: تقييم التأثيرات العلاجية لليزر ثنائي اوكسيد الكربون الجزئي وورنيش MI وحدهما وتأثيراتهما مجتمعة في حالتين (ليزر ثنائي اوكسيد الكربون قبل وبعد تطبيق ورنيش MI). الطريقة: تم تحضير 60 عينة مينا، ثم تم تمرير العينات من خلال عملية تقليل نسبة المعادن للحصول على سطح مينا منزوع المعادن. تم تقسيم العينات إلى خمس مجموعات: مراقبه، ليزر ثنائي اوكسيد الكربون، ورنيش MI، ليزر ثنائي اوكسيد الكربون + ورنيش MI وورنيش MI + ليزر ثنائي اوكسيد الكربون. تم تقييم التغيرات السطحية بواسطة جهاز قياس الصلابة و قياس خشونة السطح و استخدام المجهر الإلكتروني الماسح مع التحليل الطيفي للأشعة السينية المشتتة للطاقة (SEM-EDX). النتائج: انخفضت جميع نتائج الصلابة بعد عملية إزالة المعادن ثم زادت بعد المعالجات المختلفة مع عدم وجود فرق كبير بين المجموعات المعالجة. كانت بيانات خشونة السطح أفضل في المجموعات المحتوية على ليزر ثنائي اوكسيد الكربون. تم تحسين سطح المينا ونسبه المعادن بعد العلاجات. الاستنتاج: كانت جميع مجموعات العلاج فعالة في تعزيز الصلابة وتقليل الخشونة و تحسين مورفولوجيا السطح مقارنة بمجموعة المراقبة، مع تفضيل الاستخدام المشترك لليزر ثنائي اوكسيد الكربون وورنيش MI في كلتا الحالتين (نتائج مماثلة).



Esthetic and Healing Outcomes of Oral Fibroma Excision Using a Diode Laser: A Case Report

Ahmed Ali Shnawa^{1,*}, Hanan J. Taher¹, Afrah A. Khalil²

¹ Institute of Laser for Postgraduate Studies, University of Baghdad, Baghdad, Iraq

² College of Dentistry, University Of Anbar, Ramadi, Iraq.

* Email address of the Corresponding Author: ahmed.ali2201m@ilps.uobaghdad.edu.iq

Article history: Received: 9 Mar. 2025; Revised: 5 May 2025; Accepted: 27 May 2025; Published online: 15 Jun. 2025.

Abstract: This case report evaluates the clinical outcomes of oral fibroma excision using a 980 nm diode laser, focusing on its effectiveness in reducing postoperative discomfort, promoting healing, and improving esthetic outcomes. A 980 nm diode laser was used in CW mode at 2 watts of power to remove two fibrous masses on the buccal mucosa from a 65-year-old male patient who had presented with these lesions. The procedure was performed under local anesthesia using 2% lidocaine with 1:80,000 epinephrine. Postoperative evaluations were performed at follow-up visits on the 3rd day, 1st week, 2nd week, and 4th week to evaluate bleeding, pain, edema, functional interference, mucosal scarring, and healing through standardized clinical indices. At each follow-up visit, photographic documentation was collected to objectively track the healing progress. The procedure resulted in no bleeding, no postoperative swelling, and mild pain that did not necessitate analgesics. The recovery of function was swift. Esthetic evaluation revealed no scarring on the left side and a minor scar on the right side, with excellent overall appearance. The left fibroma site underwent complete healing by the second week, whereas the right site necessitated four weeks for full reepithelialization. The results showed that the 980 nm diode laser is a suitable substitute for traditional scalpels for oral soft tissue surgery, with few complications, mild pain after the procedure, and fast healing time. This case highlights the clinical advantages of diode lasers in minor oral surgical procedures and supports their broader adoption in clinical practice.

Keywords: Diode laser, oral fibroma, Soft tissue surgery, esthetic outcome, healing outcome

1. Introduction

Oral fibromas are the most prevalent types of oral soft tissue reactive hyperplastic lesions. They primarily arise from trauma or persistent irritation and are generally benign, rarely showing aggressive behaviors [1]. In fibroma, a fibrous submucosal mass develops as a consequence of a continuous healing process that involves scar formation and granulation tissue [2]. Because it generally arises from repeated irritation of the mucosa, fibromas are frequently seen on the buccal mucosa, tongue, and lower lip, as these regions are more susceptible to trauma [3]. The fibroma is firm, with a sessile or pedunculated base, normal color, and a smooth surface. Due to decreased vascularity, it manifests as a painless swelling that is lighter in color and more round or oval in shape than the adjacent tissue [4]. Histologically, oral fibromas have a dome-shaped structure that is covered by keratinized stratified squamous epithelium. The submucosa has a low



number of blood vessels and inflammatory cells [5]. Although scalpel-based surgical excision remains a popular option for treating oral fibromas, it is not without its risks, including intraoperative hemorrhage, infection, and slowed healing. The incredible technological breakthroughs in dentistry have made multi-wavelength lasers an essential tool for oral soft tissue surgery, allowing for accurate excision with remarkable hemostasis and field vision [6]. Diode lasers that work in the infrared spectrum are becoming a useful tool for oral soft tissue surgery. Benefits of diode laser treatment include hemostasis, improved visibility, shorter procedures, sterile environments, quicker recovery, and less pain after surgery [7]. This article presents a case report of oral fibroma excision using a diode laser. The focus is on the clinical evaluation of postoperative esthetic and healing outcomes.

2. Clinical case report

2.1 Patient presentation

A 65-year-old edentulous male patient was sent to Basra Teaching Hospital's Department of Oral and Maxillofacial Surgery with two intraoral fibrous masses on the buccal mucosa. A clinical examination identified a firm, asymptomatic, smooth-surfaced, mucosa-colored fibroma on the right buccal mucosa, approximately 0.8 cm in diameter, and a smaller fibroma, about 0.3 cm in diameter, was found on the left buccal mucosa, exhibiting similar clinical characteristics. Both lesions exhibited characteristics associated with traumatic or irritational fibromas based on their clinical presentation (Figure 1a, Figure 2a). The treatment plan was an excisional biopsy using a diode laser.

2.2 The procedure

The surgical procedure was described to the patient in his native language, after which informed consent was obtained. The diode laser (Quicklase 12 W Dual Plus 6" 810+980nm, England, UK), set at a 980 nm wavelength and operated in Continuous Wave mode at 2 W, was used in the procedure. Continuous wave emission refers to the persistent tissue interaction caused by the laser's continuous output of energy when it is turned on. Infiltration anesthesia was delivered with a solution of 2% lidocaine and 1:80,000 epinephrine. The fiber tip was initially activated by using articulating paper to boost heat retention, enabling a more efficient cutting process with reduced lateral thermal damage and improved precision, which also contributed to decreased beam dispersion. All laser safety protocols were strictly followed. Protective eyewear designed for the 980 nm wavelength was provided to the patient, operator, and assistant. Continuous high-volume suction was maintained throughout the procedure to eliminate the vapor plume generated by laser cutting. The fiber tip was maneuvered in a continuous, sweeping motion with minimal contact pressure to prevent carbonization or excessive charring of the tissues. This measure together with short activation times with intermittent cold saline irrigation, and keeping the fiber tip clean aid to prevent collateral thermal damage and protect surrounding tissues. The excised fibrous lesions were immediately preserved in a 10% formalin buffer solution and dispatched for histological investigation to verify the diagnosis; irritation fibroma was confirmed. Postoperatively, the patient was instructed to utilize 0.12% chlorhexidine mouthwash bi-daily, avoid hot, spicy, citrus, and hard foods for a few days, and maintain a soft diet. Furthermore, amoxicillin 500 mg capsules were prescribed three times daily for 3 days as antibiotic coverage, and ibuprofen 200 mg tablets were given to be taken as needed during the postoperative period for pain management.

2.3 postoperative evaluation

Several objective clinical indices were used to evaluate postoperative outcomes through third-day, first-week, second-week, and fourth-week follow-up appointments (Figure 1, Figure 2). For intraoperative bleeding, a bleeding index is used (1 = no bleeding, 2 = spontaneous hemostasis, 3 = needs compression, 4



= needs hemostasis) [8]. For pain after surgery, patients were asked to fill out a form if they had any pain during the first week postoperatively, using a verbal rating scale (VRS) where 0 means no pain, 1 means mild pain, 2 means moderate pain, and 3 means extreme pain [9]. Edema score (0= No swelling, 1= very slight edema, 2= slight edema, 3= moderate edema, 4= severe edema) [10]. Function evaluation using a function interference index (0= no interference, 1= mild, 2= moderate, 3= severe) [11]. The Mucosal Scarring Index (MSI), on a scale from 0 (no scar) to 10 (greatest scar), was utilized to evaluate the surgical sites for mucosal scarring, which serves as an indicator of the esthetic outcome [12]. The Landry Healing Index assesses wound healing by clinical indicators representing the biological phases: inflammatory, proliferative, and remodeling. A score of 1 indicates poor healing characterized by significant inflammation, spontaneous hemorrhage, dehiscence, and infection. A score of 2 indicates inadequate healing characterized by sustained inflammation, bleeding upon palpation, and partial dehiscence of the incision. A score of 3 indicates satisfactory healing accompanied by moderate inflammation and partial epithelialization. A score of 4 indicates excellent healing with minimal inflammation and nearly full closure. A score of 5 indicates exceptional recovery characterized by complete epithelialization, the presence of pink, healthy tissue, and the absence of infection [13].

No bleeding during the surgery, and no edema noted or functional interference experienced postoperatively. Mild discomfort was reported through the first and second day with no need for analgesic (Table 1). By the fourth week, there was a barely noticeable scar on the right surgical site and no scar on the left site (Table 2). Both surgical sites demonstrated "excellent" healing, marked by pink tissue coloration and complete epithelialization, and with no complications noted (Table 3).

2.4 Histopathological findings

The tissue section shows characteristics of an irritational fibroma, which is characterized by the development of thick fibrous connective tissue along with varied blood vessels and moderate chronic inflammatory cells infiltrating the stratified squamous epithelium (Figures 3a, 3b). Although the thermal effect of the laser causes ballooning degeneration in some cells, it generally has no impact on diagnosis (Figure 3c).



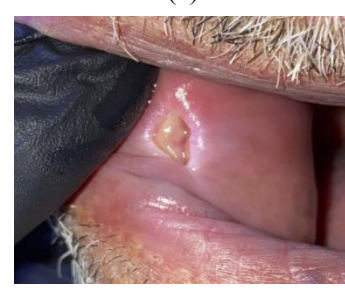
(a)



(b)



(c)



(d)



(e)

Fig.1: clinical progression of right fibroma (a) preoperative (b) immediate postoperative (c) 3rd day postoperative (d) 1st week postoperative (e) 4th week postoperative.



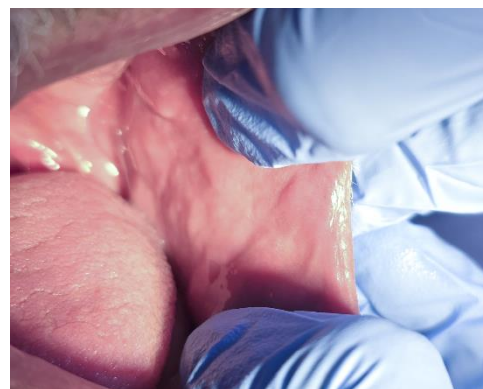
(a)



(b)



(c)



(d)

Fig.2: clinical progression of left fibroma (a) preoperative (b) immediate postoperative (c) 3rd day postoperative (d) 4th week postoperative

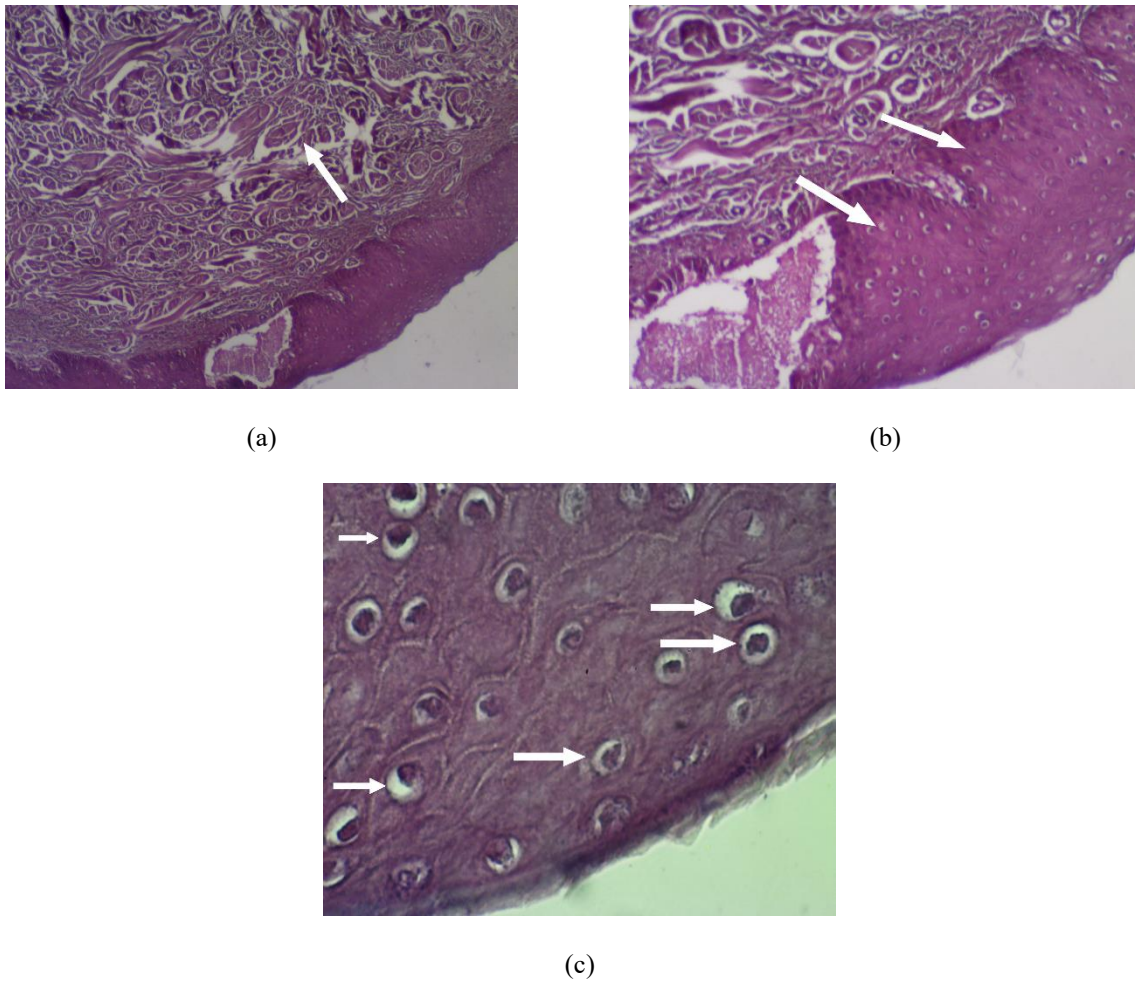


Fig.3: histology section at different magnification (a) the section shows densely collagenized fibrous connective tissue bundles admixed with few chronic inflammatory cells (The magnification power 4x). (b) The section shows stratified squamous epithelium covered by the densely collagenized fibrous connective tissue bundles (magnification power 10x). (c) The section shows the thermal effect of the laser, causing ballooning degeneration in some cells (magnification power 40x).

Table 1. Pain index (VAS) through the first week postoperatively.

Day	Day 1	Day 2	Day 3	Day 4	Day 5	Day 6	Day 7
Score	1	1	0	0	0	0	0

Table 2. Mucosal scarring index for the two fibromas through follow-up visits.

visit	Right fibroma	Left fibroma
3 rd day	8	4
1 st week	7	2
2 nd week	4	0
4 th week	2	0

Table 3. Healing index for the two fibromas through follow up visits.

visit	Right fibroma	Left fibroma
3 rd day	3	4
1 st week	4	4
2 nd week	4	5
4 th week	5	5

3. Discussion

Benign oral lesions are frequently observed in routine clinical practice throughout all age groups. A comprehensive understanding of these lesions is crucial for clinicians to correctly distinguish between illnesses and administer suitable treatment. If neglected, these benign oral lesions may advance to more severe forms, thereby diminishing the patient's overall well-being [14]. In this case report, the patient was suffering from two fibroma lesions on both sides of the buccal mucosa, which interfered with the feasibility of fabricating and fitting a complete denture.

The 980 nm diode laser was chosen for its established clinical benefits in soft tissue surgery, especially within the maxillofacial area. This wavelength exhibits significant absorption by hemoglobin, facilitating efficient photothermal interaction and prompt hemostasis during the procedure. The application facilitated accurate incisions with reduced intraoperative bleeding, thereby obviating the necessity for sutures and enhancing surgical visibility. Furthermore, diminished postoperative pain, edema, and scarring were noted, aligning with outcomes documented in prior clinical studies [15].

In this case, the Continuous Wave mode was employed, since it has demonstrated efficacy in delivering consistent coagulation and precise tissue ablation, particularly with the 980 nm diode laser. A variety of thermal management strategies were implemented to minimize the risks associated with extended continuous wave exposure, which, as shown in the literature, may elevate the potential for thermal injury to adjacent tissues. This was accomplished by optimizing laser power, minimizing exposure duration, and employing fine optical fibers for accurate energy transmission. Local anesthetic and continuous monitoring additionally minimized the risk of overheating. These solutions facilitated the secure utilization of continuous wave mode, consistent with prior research on 980 nm diode laser applications [16].

The variation in healing durations between the left and right fibroma primarily accounted for the disparity in lesion size. The larger fibroma on right side may have resulted in delayed healing relative to the smaller lesion on left side due to the greater surface area requiring epithelial covering and tissue regeneration. Also larger lesions display a more substantial thermal necrosis zone post-laser treatment, potentially hindering tissue regeneration and epithelialization. In contrast, smaller lesions exhibit a reduced necrosis zone, facilitating expedited recovery. This explanation is consistent with previous studies, which reported that larger lesion size and increased thermal necrosis can delay epithelialization and tissue regeneration following laser excision [17] [18]. The use of diode lasers to treat oral lesions is a simple, effective, and risk-free substitute for conventional methods. There are many advantages to this modality over the standard surgical method. For example, it reduces pain, improves vision, expedites recovery, lessens scarring, preserves tissue elasticity, and precisely excises soft tissue abnormalities [19]. Through stimulate the division of epithelial cells, vascular proliferation, collagen production, and fibroblast proliferation the healing process is much faster with the use of diode lasers [20]. Furthermore, hemostasis assistance during soft tissue procedures can lead to less postoperative pain and less need for analgesics [21]. The results from our case were consistent with these findings, demonstrating that diode laser excision facilitated rapid healing, reduced discomfort, and lowered the need for analgesics. During the follow-up appointments, the patient shows a positive outlook for complete recovery. He achieved complete reepithelization of the surgical site. The patient reported no concerns post-surgery. Furthermore, he has received training on



maintaining dental hygiene and caring for his denture, and he currently wears a well-fitting complete denture. The current study offers significant clinical insights into the healing process after diode laser excision of oral fibroma; nevertheless, it is constrained by its classification as a single case report. The findings cannot be generalized to a broader population without further validation via bigger clinical studies or randomized controlled trials. Differences in individual patient characteristics, lesion properties, and surgical techniques may influence healing results. Future studies employing larger sample sizes and comparative analysis with conventional surgical methods are crucial to confirm and improve these findings.

4. Conclusions

Diode laser surgery appears to be a promising substitute to standard scalpel excision of oral fibromas. Minimal bleeding, less discomfort, and quicker recovery are the outcomes of diode laser excision, as shown in this case report. Esthetic and healing outcomes can be enhanced by integrating diode lasers into conventional dental procedures. However, this result relies on a single case report; additional research with bigger sample sizes and comparative clinical trials is essential to verify these first findings and establish definite clinical recommendations.

References

- [1] M. Patait, P. Kulkarni, A. Bezalwar, P. Patekar, K. Saraf, and P. Student, "Management of oral mucosal irritational fibroma with laser therapy: A case report," *Journal of Oral Medicine Oral Surgery Oral Pathology and Oral Radiology*, vol. 4, no. 1, pp. 61–63, May 2018, doi: 10.18231/2395-6194.2018.0015.
- [2] A. Kohli, K. Gupta, M. Pandey, and A. Dwivedi, "Excision of irritation fibroma using a diode laser," *Rama Univ J Dent Sci*, pp. 26–29, Sep. 2016.
- [3] M. Glick, *Burket's Oral Medicine, 12th Edition*. PMPH USA, 2015.
- [4] B. Diwan, U. Shirbhate, P. Bajaj, A. Reche, and A. Pahade, "Conventional scalpel and diode laser approach for the management of traumatic fibroma," *Cureus*, Oct. 2023, doi: 10.7759/cureus.47810.
- [5] F. Nakamura, S. F. Fifita, and K. Kuyama, "A Study of Oral Irritation Fibroma with Special Reference to Clinicopathological and Immunohistochemical Features of Stromal Spindle Cells," *International Journal of Oral-Medical Sciences*, vol. 4, no. 2, pp. 83–91, Jan. 2005, doi: 10.5466/ijoms.4.83.
- [6] A. L. Do-Amaral, M. C. Carneiro, G. De Paula Almeida, and P. S. Da-Silva-Santos, "Surgical Treatment of Oral Fibrous Hyperplasia with Diode Laser: An Integrative Review," *International Journal of Odontostomatology*, vol. 17, no. 2, pp. 136–141, Jun. 2023, doi: 10.4067/s0718-381x2023000200136.
- [7] A. Al-Ani, H. Taher, and A. Alalawi, "Comparative evaluative study of Erbium, chromium YSGG and wavelength-dual Diode lasers in oral soft tissue incision morphology: a histological ex vivo study," *ijl.uobaghdad.edu.iq*, Jun. 2024, doi: 10.31900/ijl.v23i1.446.
- [8] F. E. Musaa, L. G. Awazli, and F. Alhamdani, "Gingival Enlargement Management using Diode Laser 940 nm and Conventional Scalpel Technique (A Comparative Study)," *ijl.uobaghdad.edu.iq*, 2017, doi: 10.31900/ijl.v16iB.38.
- [9] E. I. Marhab and Z. F. Mahdi, "A comparison between diode laser 976 nm and conventional technique in treatment of gingival fibromatosis," *ijl.uobaghdad.edu.iq*, Jun. 2024, doi: 10.31900/ijl.v23i1.412.
- [10] S. R. A. Ghazali, S. S. Ahmed, and Balsam. S. Abdulhameed, "The clinical evaluation of oral fibroma lesion removal utilizing two types of diode lasers 980 nm and 450 nm," *ijl.uobaghdad.edu.iq*, Jun. 2024, doi: 10.31900/ijl.v23i1.431.
- [11] T. N. Aldelaimi and A. A. Khalil, "Clinical Application of Diode Laser (980 nm) in Maxillofacial Surgical Procedures," *Journal of Craniofacial Surgery*, vol. 26, no. 4, pp. 1220–1223, Jun. 2015, doi: 10.1097/scs.0000000000001727.
- [12] R. Wessels *et al.*, "The Mucosal Scarring Index: reliability of a new composite index for assessing scarring following oral surgery," *Clinical Oral Investigations*, vol. 23, no. 3, pp. 1209–1215, Jul. 2018, doi: 10.1007/s00784-018-2535-6.



- [13] Y. Hamzani and G. Chaushu, "Evaluation of early wound healing scales/indexes in oral surgery: A literature review," *Clinical Implant Dentistry and Related Research*, vol. 20, no. 6, pp. 1030–1035, Oct. 2018, doi: 10.1111/cid.12680.
- [14] P. Guerrieri, et al., "Exophytic soft tissue traumatic lesions in dentistry: A systematic review," *Int. J. Appl. Dent. Sci.*, vol. 6, pp. 387-392, 2020.
- [15] I. Pastar et al., "Epithelialization in Wound Healing: A Comprehensive review," *Advances in Wound Care*, vol. 3, no. 7, pp. 445–464, Mar. 2014, doi: 10.1089/wound.2013.0473.
- [16] V. Sotiri, N. Katsoulas, A. C. Lazaris, N. Kavantzias, and E. Agapitos, "Diode type laser in resection biopsies of superficial benign lesions of oral mucosa: a histological analysis," *Journal of Surgical and Molecular Pathology*, vol. 5, no. 1, p. 13, 2020.
- [17] T. N. Aldelaimi and A. A. Khalil, "Clinical Application of Diode Laser (980 nm) in Maxillofacial Surgical Procedures," *Journal of Craniofacial Surgery*, vol. 26, no. 4, pp. 1220–1223, Jun. 2015, doi: 10.1097/scs.0000000000001727.
- [18] M. Michalik, J. Szymańczyk, M. Stajnke, T. Ochrymiuk, and A. Cenian, "Medical Applications of Diode Lasers: Pulsed versus Continuous Wave (cw) Regime," *Micromachines*, vol. 12, no. 6, p. 710, Jun. 2021, doi: 10.3390/mi12060710.
- [19] I. Sufiawati, F. D. Siregar, I. S. Wahyuni, and E. Syamsudin, "Evaluation of diode laser efficacy in treating benign oral soft tissue masses: A case series," *International Journal of Surgery Case Reports*, vol. 114, p. 109075, Nov. 2023, doi: 10.1016/j.ijscr.2023.109075.
- [20] S. R. Tawi, S. S. Ahmed, and B. S. Algharak, "Histopathological evaluation of two diode lasers 450 and 980 nm in excision biopsies of oral benign lesion," *Lasers in Dental Science*, vol. 7, no. 4, pp. 251–258, Nov. 2023, doi: 10.1007/s41547-023-00205-1.
- [21] R. R. Asundaria and A. Tavargeri, "Excision of traumatic fibroma of the tongue in a pediatric patient: a case report," *International Journal of Clinical Pediatric Dentistry*, vol. 16, no. 1, pp. 166–169, Mar. 2023, doi: 10.5005/jp-journals-10005-2492.

عنوان البحث باللغة العربية (النتائج الجمالية والشفائية لاستئصال الورم الليفي الفموي باستخدام ليزر الداويد)

احمد علي شناوه¹، حنان جعفر طاهر¹، افراح عدنان خليل²

¹معهد الليزر للدراسات العليا، الكلية، جامعة بغداد، بغداد، العراق.
²كلية طب الاسنان، جامعة الانبار، الرمادي، العراق.

البريد الالكتروني للباحث: ahmed.ali2201m@ilps.uobaghdad.edu.iq

الخلاصة: هذا التقرير يقيم النتائج السريرية لاستئصال الأورام الليفية الفموية باستخدام ليزر داويد بطول موجي 980 نانومتر، مع التركيز على فعاليته في تقليل الألم بعد الجراحة، وتسريع الشفاء، وتحسين النتائج الجمالية. تم استخدام الليزر داويد في وضع الموجة المستمرة وبقوة 2 واط لإزالة الورم الليفي على كلا الجانبين الداخليين للخد من مريض ذكر يبلغ من العمر 65 عامًا يعاني منهم. تم إجراء التقييمات بعد الجراحة في زيارات المتابعة في اليوم الثالث، الأسبوع الأول، الأسبوع الثاني، والأسبوع الرابع، حيث تم تقييم النزيف خلال الجراحة، الألم، التورم، تأثير الوظيفة، التندب، والشفاء باستخدام مؤشرات سريرية معينة. أسفرت الإجراءات عن عدم وجود نزيف خلال العملية، وعدم وجود تورم بعد الجراحة، وألم خفيف لم يتطلب مسكنات وكان ممارسة الوظيفة سريعًا. أظهرت التقييمات الجمالية عدم وجود تندب على الجهة اليسرى ووجود ندبة طفيفة على الجهة اليمنى، مع مظهر عام ممتاز. تم ملاحظة الشفاء الكامل في موقع الورم الليفي الأيسر في الأسبوع الثاني، بينما استلزم الموقع الأيمن أربعة أسابيع. تظهر النتائج أن ليزر داويد 980 نانومتر هو بديل جيد للمشارط التقليدية في جراحة الأنسجة الرخوة الفموية، مع تقليل المضاعفات، والألم بعد العملية، ووقت شفاء سريع.





Performance Enhancement of Metasurface Grating Polarizer Using Deep Learning for Quantum Key Distribution Systems

Hayder Sami Jassim Al-Dahwi*, Shelan Khasro Tawfeeq

Institute of Laser for Postgraduate Studies, University of Baghdad, Baghdad, Iraq

* Email address of the Corresponding Author: haidar.sami1101a@ilps.uobaghdad.edu.iq

Article history: Received: 25 Feb. 2025; Revised: 20 May 2025; Accepted: 5 Jun. 2025; Published online: 15 Jun. 2025.

Abstract: Metasurface polarizers are essential optical components in modern integrated optics and play a vital role in many optical applications including Quantum Key Distribution systems in quantum cryptography. However, inverse design of metasurface polarizers with high efficiency depends on the proper prediction of structural dimensions based on required optical response. Deep learning neural networks can efficiently help in the inverse design process, minimizing both time and simulation resources requirements, while better results can be achieved compared to traditional optimization methods. Hereby, utilizing the COMSOL Multiphysics Surrogate model and deep neural networks to design a metasurface grating structure with high extinction ration of ≈ 60000 at visible spectral wavelength of 632 nm, could be achieved.

Keywords: metasurface, polarizer, grating, deep learning, neural network and surrogate model.

1. Introduction

Quantum cryptography is an innovative subfield of cryptography that leverages the principles of quantum mechanics in communication to provide distribute encryption keys. Different from classical cryptography, quantum cryptography is based on fundamental physics laws and is therefore highly immune to attacks by the most advanced computing systems. Quantum key distribution (QKD) is a secure communication protocol which utilizes quantum mechanics principles to distribute encryption keys [1]. Polarization encoding is the most used degrees of freedom to encode data in QKD system [2]. Polarizers are considered as essential optical components used in both transmitters and receivers of the QKD systems [3].

Metasurfaces, which are optical devices comprising structures on the nanometer scale and designed to control the wavefront and properties of light, are promising artificial materials to replace conventional optical components such as refractive optical elements (ROEs). Metasurfaces have the ability to manipulate various optical properties, including polarization, amplitude, and phase, within a single component. Besides, they provide the capability to reduce the form factor of bulky systems by replacing conventional optical elements [4].

The design of microscopic structures remains a major topic in metasurface optics research. Even though optical structure performance is typically straightforward to predict, through sophisticated simulation



algorithms such as finite element method (FEM) and finite different time domain (FDTD), the problem of inverse designing an on-demand optical metasurface device is not that simple. At the early research, the prototypical designs were mostly based on educable guesses such as the split ring, V-shaped antenna, and gammadions. However, limited by the prior knowledge of humans and the sophisticated light-matter interaction mechanisms, exceptional functionalities and extremely high efficiencies may have never been discovered by intuitively guessed geometries. In order to overcome the difficulty of metasurface and optical design, inverse design methodologies, such as adjoint methods and evolutionary algorithms, have become one of the main themes of research in recent years. These algorithms have successfully been implemented for the design of different unconventional optical devices, such as power splitters, light trapping structures, and dielectric nano antennas. To further develop the capabilities of machine-aided design approaches, and to avoid some problems of traditional optimization, such as the local minimum problem and expensive computations, the optical community started to look at data-driven and machine learning methods as alternative approaches to resolve the inverse design problem. Hence, machine learning became the central research theme in computer vision, natural language processing, speech recognition, and more. The optical community has been increasingly migrating the techniques of machine learning and data science into optical research, with various successful applications including ultrafast optics, optical communication, and optical microscopy [5] [6].

Artificial intelligence (AI) recently became a global concept in various physical sciences. Specifically, there are a diversity of challenging tasks in optics that can be effectively analyzed and solved without directly solving Maxwell's equations but by utilizing these novel approaches. Meanwhile, the direct solution of Maxwell's equations can be utilized to generate enormous amounts of training data required for executing various AI algorithms. Thus, a remarkably powerful AI methodology which complements many typical analytical and numeric techniques finds many key applications in optics. Such approaches are used for inverse design, optimization, big-data processing, underpinning the fast development of optics. The concept of all-dielectric metasurface is motivated by the idea to utilize subwavelength dielectric Mie resonant nanoparticles as "meta-atoms" to build high efficient optical metasurfaces and meta devices [7]. Those can be defined as optical devices having exclusive functionalities because of a smart structuring the meta-atoms at the subwavelength scale merged with the use of functional and high-refractive-index materials. Differs from classical optics, where the electromagnetic response is totally defined by electric polarization, the metasurface is frequently termed "meta-optics" highlighting the importance of optically induced magnetic response of the artificial subwavelength-patterned structures. The high-refractive-index materials provide exceptional confinement of electromagnetic fields making even subwavelength particles resonant. The interference between these resonances results in a sort of scattering effects not existing in classical optics. Dielectric nanoscale structures are supposed to complement or even replace several plasmonic components in a range of potential applications. Furthermore, many concepts which had been developed for plasmonic structures, but fell short of their potential due to high losses of metals at optical frequencies, can now be used based on low-loss dielectric structures [8].

It's supposed that highly efficient all-dielectric metasurfaces with the extraordinary capability of polarization control can be commonly applied in areas of polarization detection and imaging, data encryption, display, optical communication and quantum optics for ultracompact and miniaturized optical systems realization [9]

Deep learning (DL) is a subcategory of machine learning (ML) which is based on layered structures described as artificial neural networks (ANNs). ANNs derive their name from the neural structures found in biological beings. This structure can be mathematically emulated as a node, denoted as a neuron, which may contain many input and output connections with correlated weightings. These neurons have a non-linear activation function that serves to map the inputs to an output and provides the switching behavior similar to that in biological neurons. These neurons are packed into layers which are connected to successive layers. The functionality of this is to construct a necessarily deep neural network such that any arbitrary function would be estimated. At the same time, the higher the ANN complexity the larger datasets is required for suitable prediction accuracy. ANNs can be considered as a mapping between input and output spaces which can be arbitrarily defined. For different tasks, ANNs can have complicated structures. The



dataset features are automatically learnt to set up the desired mapping from input to output. To perform a given task, the DL models should experience a process known as training [10].

Training a model requires the introduction of the so-called loss function, that provides feedback on the difference between the real output (or "ground truth") and the output predicted by the network for the same given input data. Training the ANN intends to minimize the loss function by adjusting the weight values at each layer. These tasks are commonly accomplished through some form of stochastic gradient descent which may be done effectively over the network with backward propagation [11]. The training is labeled complete when the model can predict the output with some required quality metric. After the training, the ANN can accurately map the input to the wanted output, implying that it has "learned" the necessary mapping from the given data. It should be known that this mapping is not essentially unique while differences in training procedure may lead to a failure to converge. Generally, a dataset is divided into training and validation sets. Due to high dimensional networks structure, over-fitting possibly occurs which should be mitigated. Over-fitting can be examined through the loss function applied to validation set. When the model is trained and over-fitting is overcome, the model considered to be capable of generating an output based on a sample input. This supposes that the training data provided is characteristic of the problem that one is trying to learn [12].

One of the major challenges of ML is the amount of data needed for the training procedure, which is typically determined by the complexity of the problem.

DL is useful for tasks that require repeated resolution with different parameters or for creating complex feature extraction tasks. In photonics, ML is mainly used for forward and inverse design. Forward design predicts physical responses (e.g., scattering spectra, polarization) for a given structure using tools like T-matrix calculations and full wave simulations to solve Maxwell's equations. While ML can serve similar purposes, its greatest advantage lies in inverse design problems, where it determines structure parameters for a desired response. DL supports this through surrogate modeling, offering data-driven approximations instead of simulations [13].

Surrogate models (SMs) are used to replace expensive simulation models of engineering problems. Although computers are becoming faster and more powerful, the demand for computational complexity is still outpacing the improvements in computer power and speed. Additionally, using computer simulations can be challenging due to their high fidelity, regardless of how fast or powerful computers are. Even methods like parallel computing, where many calculations or processes are executed simultaneously, do not fully address these issues [14].

Surrogate models trained on limited data accurately predict unit cell properties and speed up microscopic optimization. These models replace full-wave simulations to quickly predict meta-atom properties [15].

In previous work, deep learning has been utilized in metasurface design and response verification. CHRISTIAN et al. have demonstrated modeling of complex all-dielectric metasurface systems with deep neural networks achieving an average mean square error of only 1.16×10^{-3} and is over five orders of magnitude faster than conventional electromagnetic simulation software [16]. A data preprocessing approach based on the governing laws of the physical problem to eliminate dimensional mismatch between a high dimensional optical response and a low dimensional feature space of metasurfaces was proposed by Ibrahim et al. They trained forward and inverse models to predict optical responses of cylindrical meta-atoms and to retrieve their geometric parameters for a desired optical response, respectively. Using their inverse model, they designed and demonstrated a focusing meta lens as a proof-of-concept application [17]. A deep learning-based metasurface/meta-atom modeling approach was introduced by SENSONG et al. to significantly reduce the characterization time while maintaining accuracy. Based on a convolutional neural network (CNN) structure, the proposed deep learning network was able to model meta-atoms with nearly freeform 2D patterns and different lattice sizes, material refractive indices and thicknesses [18]. To reach the highest working frequency for training the DNN, Fardin et al. have considered 8 ring shaped patterns to generate resonant notches at a wide range of working frequencies from 4 to 45 GHz. They proposed two network architectures. In one architecture, they restricted the output of the DNN, so the network can only generate the metasurface structure from the input of 8 ring shaped patterns. This approach drastically reduces the computational time, while keeping the network's accuracy above 91%. They showed that the



model based on DNN can satisfactorily generate the output metasurface structure with an average accuracy of over 90% in both network architectures [19]. Xiaoshu et al. used deep learning methods to build a metamaterial database to achieve rapid design and analysis methods of metamaterials. They proposed a method to calculate the electromagnetic properties of metamaterials using DNNs. Effectively simulate the electromagnetic properties of periodic metamaterial structures [20]. VLAD et al. proposed an alternative data-free DL method using a physics-informed neural network (PINN) to enable more efficient computation of light diffraction from 3D optical metasurfaces, modeling of corresponding polarization effects, and wavefront manipulation. Once trained, the PINN-based electromagnetic field (EMF) solver simulates light scattering response for multiple inputs within a single inference pass of several milliseconds. This approach offers a significant speed-up compared to traditional numerical solvers, along with improved accuracy and data independence over data-driven networks [21].

In this paper, we have rebuilt the metasurface grating structure in [22] and used the surrogate model and DNN built-in COMSOL Multiphysics software, to optimize geometrical dimensions instead of the Monte Carlo optimization method used by Baki and Tawfeeq [22], to improve the performance by obtaining higher polarization extinction ratio (*ER*). Thus, improving its capability to function as a polarization modulator that is used in QKD systems. Simulation results of the obtained design show excellent extinction ratio of the polarizer. Thus, by utilizing COMSOL Multiphysics Surrogate model deep neural networks can help in optical component design improvement over conventional design methods.

2. Theory

DL ANN consists of an input layer, hidden layers and an output layer, as illustrated in Figure 1. Each layer is made of multiple nodes, those are fully or partially connected to the subsequent layer nodes. Each node has weight, that is tuned based on training. Biased parameter is added to the connection between two nodes too. The output y_i is a function of node input x_i , weight w_i and bias b_i , as in the following equation [23]:

$$y_i = \sum(x_i - w_i) + b_i \quad \dots\dots (1)$$

In a supervised NN learning algorithm, input data comes with corresponding labels. The training process compares predicted results with these labels, continuously optimizing the network for better performance. It learns the relationships between metasurface structures and optical responses to perform specific optical functions. One of the main and fundamental supervised ANN algorithms is the multilayer perceptron (MLP) shown in Figure 1 [23].

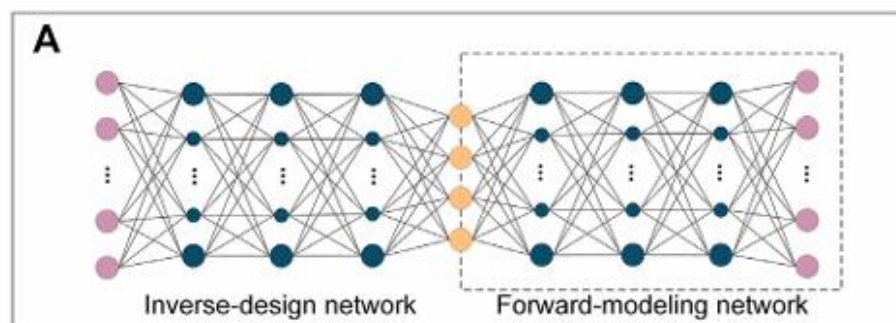


Fig. 1: Schematic illustration of typical deep learning model algorithm multiple perceptron [23]

The MLP is a key model in deep learning, forming the basis of all other ANNs. It links inputs to outputs through hidden layers with nonlinear activation functions. This model optimizes many parameters, allowing it to learn complex, nonlinear relationships in optical data. In training, a cost function based

on variance or cross entropy is defined, and weights are adjusted using back propagation to minimize this cost. Then, target optical functions like scattering spectra are fed into the network to predict photonic structures. Adding more hidden layers increases feature learning and accuracy but can lead to over-fitting. The tandem network model solves non-uniqueness by combining inverse-design and forward-modeling networks, as shown in Figure 2 [24].

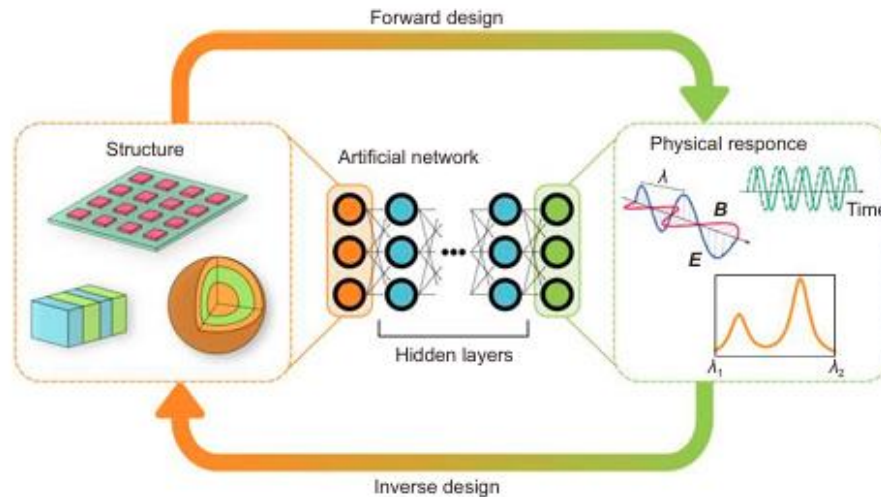


Fig. 2: Inverse and forward designs based on DL techniques [24]

2.1 Metasurface Polarizers

Metasurfaces generally consist of subwavelength structures (meta-atoms) arranged in a 2D plane. By adjusting the shapes, sizes, orientations, or positions of meta-atoms, a phase gradient can be introduced at the interface to mold the optical wavefront as needed. In addition to phase manipulation, metasurfaces leverage strong light–matter interactions at the subwavelength scale to regulate light across various degrees of freedom (DoFs) such as amplitude, frequency, chromatic dispersion, and polarization, using mechanisms like electric dipole resonance, magnetic dipole resonance, or guided mode resonance [9] [25] [26].

Polarization manipulation at the subwavelength scale is a unique capability of all-dielectric metasurfaces (ADMs), achieved by engineering the anisotropy of the media in contrast to traditional refractive and diffractive optical components. ADMs can be engineered to have much higher refractive index contrasts by introducing asymmetric meta-atoms compared to the principal refractive indices along two orthogonal axes (extraordinary and ordinary) difference in natural materials. Meta-atoms that are designed as birefringent elements can be used to achieve subwavelength polarization control for applications such as polarization conversion, polarization-dependent multiplexing, and complex vector beams. Combining these capabilities with phase and amplitude regulation allows for the realization of more complex functions [9] [25] [26].

In QKD systems, such as, the BB84 protocol two basis sequences are used, i.e. rectilinear and diagonal. The rectilinear basis includes horizontal 0° and vertical 90° polarization, while the diagonal basis has 45° and 135° polarization states. To generate these polarization states in the transmitter, optical polarizers are needed. With the high transmittance, high extinction ratio, compactness and integrability in optics, compared to bulk polarizers, metasurface polarizers are used in QKD transmitting systems [1] [2] [3] [27].

2.2 Deep Learning for Metasurface Structure Design

Metasurface optics have rapidly advanced over the past decades, demonstrating strong capabilities in controlling light-matter interactions. Recently, deep learning has revolutionized this field [23]. Traditional

design methods, such as trial-and-error, parameter sweeps, and optimization algorithms, require extensive computational resources and time-consuming simulations. These simulations must be repeated if design requirements change, limiting user focus on actual needs. To address these issues, deep learning offers a faster, more efficient, and automated design approach [19].

3. Methodology

Over the past two decades, the explorations of metasurfaces have led to the discovery of exotic light–matter interactions, such as anomalous deflection, asymmetric polarization conversion and wave-front shaping. An inverse metasurface design is taking place by providing the structure optical response vs. its geometric parameters as a dataset to NN, the network can be trained to learn the relationship between the input and output [23] [19].

Nanowire periodic structure lattice of the metasurface grating polarizer is designed in the visible region [22]. Based on the effect of guided-mode resonance. Guided-mode resonance involves structures composed of a substrate, a waveguide layer, and a grating layer. When illuminated by an incident light beam, a portion of the beam is directly transmitted through the structure while another portion is diffracted by the grating and trapped within the waveguide layer. Subsequently, some of the trapped light is rediffracted, causing destructive interference with the transmitted part of the light beam. At specific wavelengths and angular orientations of the incident beam, the structure resonates, resulting in complete interference and no transmission of light. The critical factor is the relative phase shift between the incident and diffracted waves, leading to destructive interference. Figure 3 illustrates this process. The grating layer (layer 2), assumed to be infinitely thin, is positioned at the interface between the high refractive index waveguide layer and the surrounding medium. Most of the incident plane-wave, denoted by t , is transmitted through the structure as b . The grating diffracts a small fraction of the incident plane-wave into the first-order wave [28].

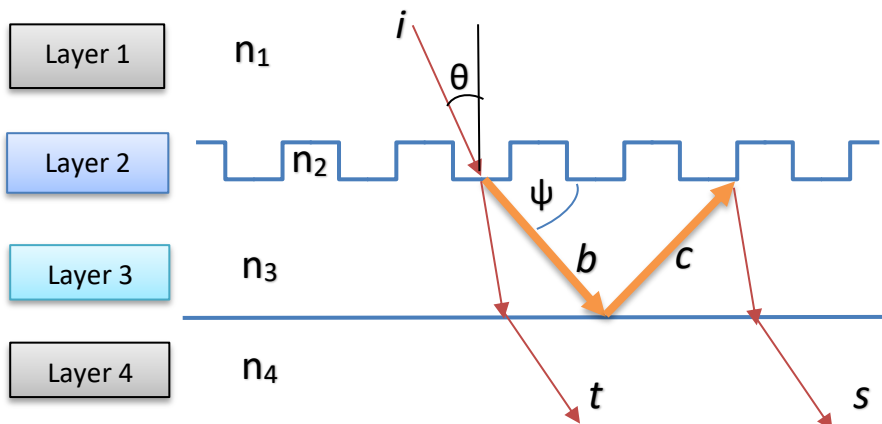


Fig. 3: Basic geometry of grating waveguide structure and relevant interference waves. Transmitted wave t and diffracted wave S originating from the incident wave i destructively interfere at resonance [28].

Here in this work, the metasurface structure passes the TM polarized light and blocks the TE one. Grating structure dimensions must be designed to ensure having the best polarizer performance, i.e., high ER can be obtained [22]. Hereby, deep learning neural networks algorithms can be utilized to perform dimensions optimization.

Then by applying a condition to restrict the required response, i.e., $\max|T_{TM}|$ and $\min|T_{TE}|$ at a specific wavelength, a linearly polarized light with maximum extinction ratio ER can be obtained as in Eq. (2) [22]. Thus, the trained network can propose the optimal geometrical dimensions of the structure which meet the requirements.

$$ER = \frac{T_{TM}}{T_{TE}} \dots\dots (2)$$

The structure in [22] consists of TiO_2 grating on a SiO_2 substrate of 1000 nm thickness. TiO_2 is chosen as the base material because it exhibits no loss $\kappa \approx 0$ and high index of refraction for strong light-matter interactions at visible wavelength spectrum [29]. The grating is covered by SiO_2 as in Figure 4, was built and simulated using COMSOL Multiphysics software as shown in Figure 5. The refractive indices of TiO_2 and SiO_2 are 2.5824 and 1.4570 respectively at $\lambda = 632$ nm.

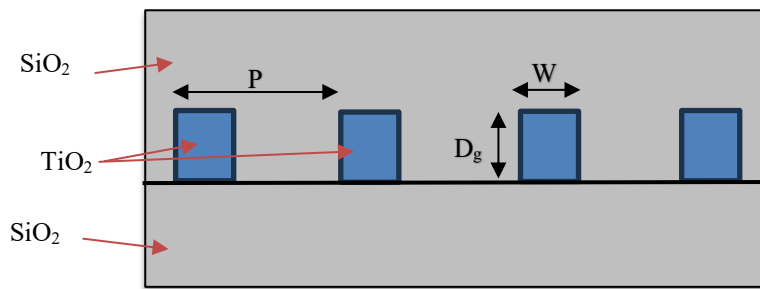


Fig. 4: Metasurface grating structure

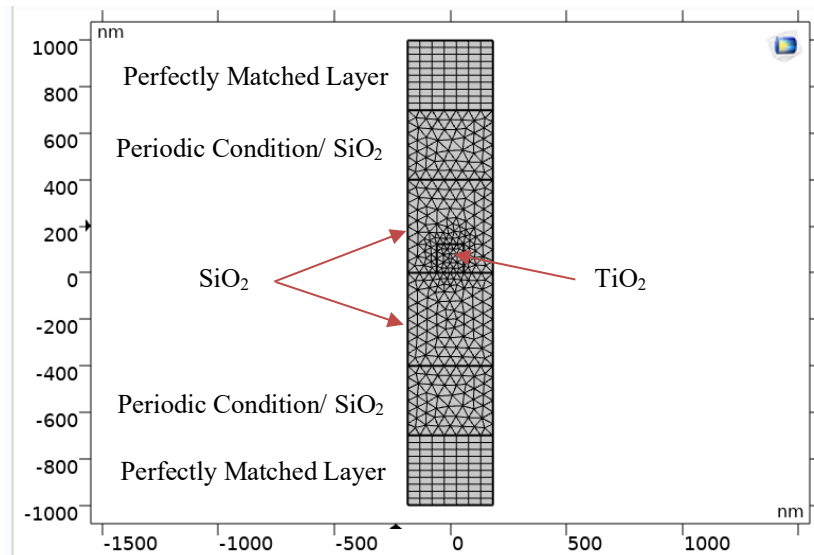


Fig. 5: Grating structure unit mesh configuration

Deep neural network, illustrated in Figure 6, was used to optimize the geometrical structure dimensions such as grating thickness D_g , grating period P and fill factor FF which is the ratio of grating width W to the grating period P . Thus, $FF = W / P$.

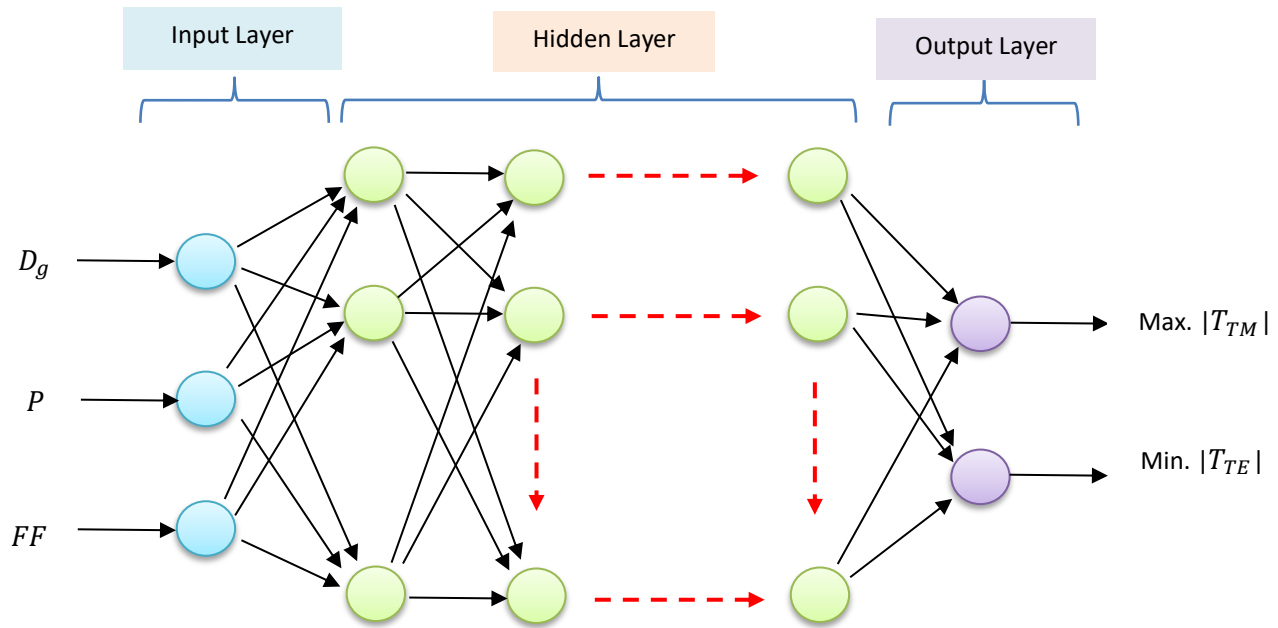


Fig. 6: ANN structure of the used model

Instead of Monte Carlo optimization method that was used in [22], where $ER = 1800$ was obtained in [22], the Surrogate model, a COMSOL Multiphysics software built-in tool, has been used to build and train an ANN with the dataset generated by specifying the input parameters limits and wavelength range, as listed in Table 1. The Surrogate model was trained on simulation data generated from a parametric sweep of structure geometry (P , D_g and FF , in addition to λ) to simulate the response (T_{TE} and T_{TM}), and was fed directly to DNN. For validation, 20% random samples (not used for training) of generated dataset were used.

Table 1. Surrogate Model Parameters Limits

Parameter	Lower limit	Upper limit
D_g	100 nm	390 nm
P	200 nm	400 nm
FF	0.1	0.9
λ	400 nm	800 nm

After execution of the model training, optimal structure dimensions were obtained that meet the output condition for higher ER . The loss function used to evaluate the learning capability of the neural network is calculated using mean square error MSE as the loss function (L), defined as in Eq. (3) [12]:

$$L(w_i, b_i) = \frac{1}{n} \sum_{i=1}^n (Y_i - \hat{Y}_i)^2 \quad \dots\dots (3)$$

Then the whole wavelength range, 400- 800 nm, T_{TM} and T_{TE} responses were simulated to calculate ER using the obtained structure dimensions. The process was repeated, as illustrated in the block diagram shown in Figure 7.

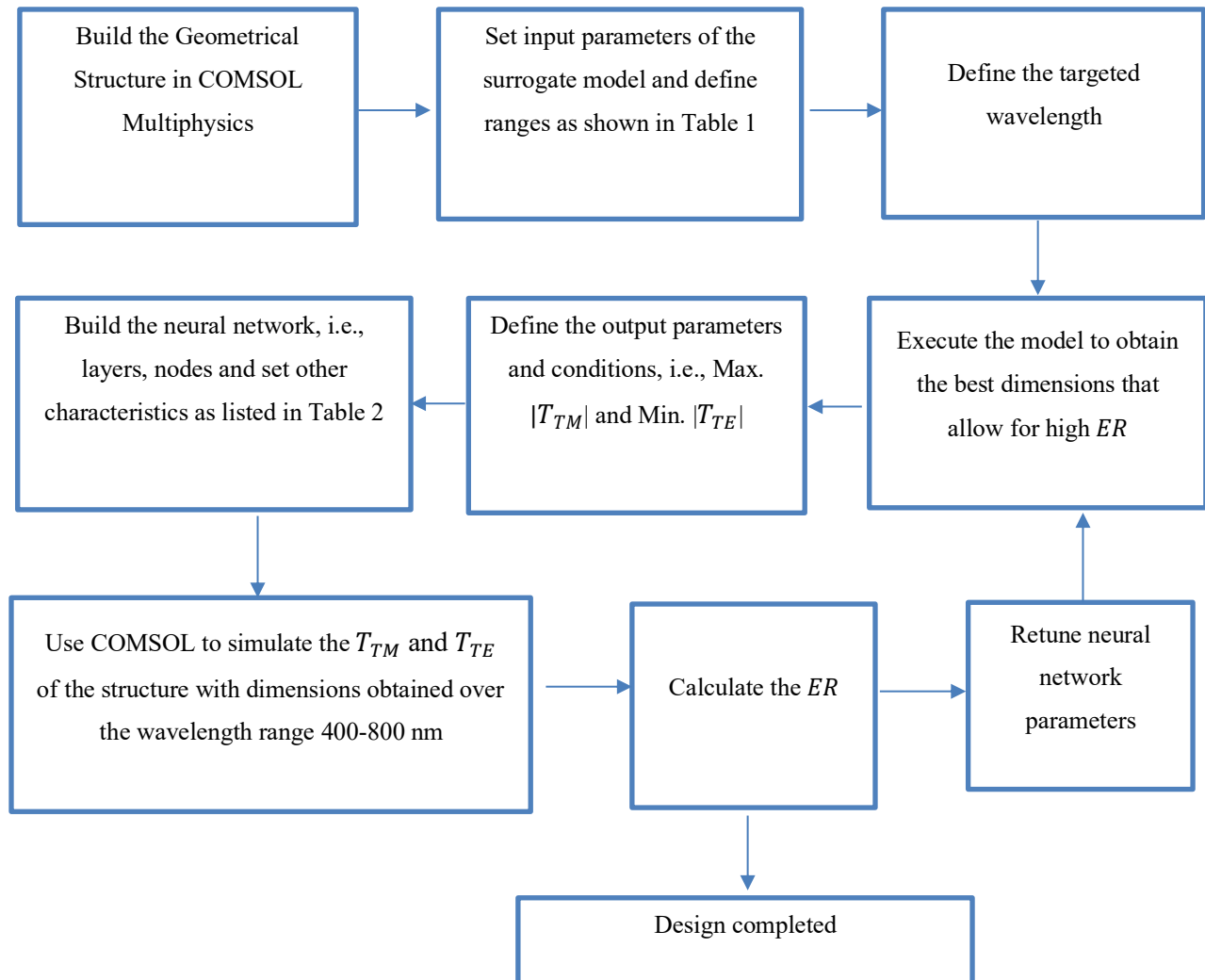


Fig. 7: Process block diagram

Table 2 Neural Network Parameter Setting

Parameter	Value	Description
Number of input nodes	3	Number of nodes of Neural network input layer, i.e. input parameters D_g , P and FF
Number of layers	10	Number of layers in Neural Network
Number of nodes per layer	512	Number of nodes per each hidden layer in neural network
Epoch size	1000	Determines how many times the model sees the entire dataset
Batch size	128	the size of the data subset passed through the network before the model's internal parameters are updated
Number of input points	500	Number to train the surrogate model to a sufficient degree of accuracy
Activation function	ReLU	Rectified linear unit
Output layer activation function	Linear	
Optimizer	Adam	Optimizer is the element that fine-tunes a neural network's parameters during training
Loss function	MSE	Measures how good a neural network model is performing a certain task
Validation	20%	random samples of dataset unused for training.
Number of output nodes	2	Number of nodes of Neural network output layer, i.e. TM and TE

4. Result and discussion

Based on block diagram illustrated in Figure 7, collected results were compared to tune the ANN parameters. Optimal obtained parameters were set for the final results, as illustrated in Table 2, based on the assessment of the training progress of the prediction, it can be noticed that validation loss did not drop similarly as much as the training loss curve did, as shown in Figure 8. This may indicate a kind of overfitting of ANN. Although, several tuning processes were made to NN parameters that improve the curve, yet



difference is distinguished. However, the resulting performance parameter (ER) showed excellent results. Sample results of tuning process are shown in Figure 9. The higher obtained ER was considered as the optimal design of the grating metasurface as shown in Figure 10, while EM field distribution for both T_{TM} and T_{TE} are plotted as shown in Figure 11.

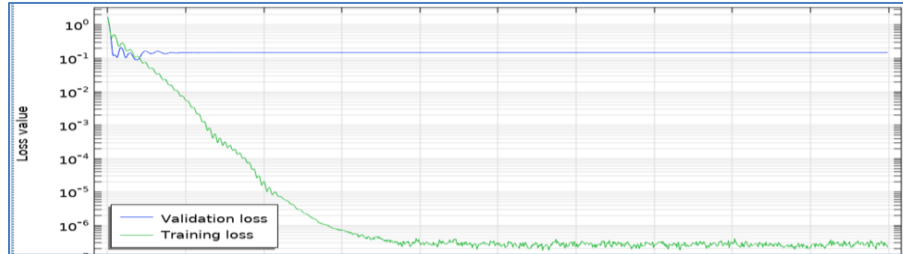


Fig. 8: Training progress graph of ANN

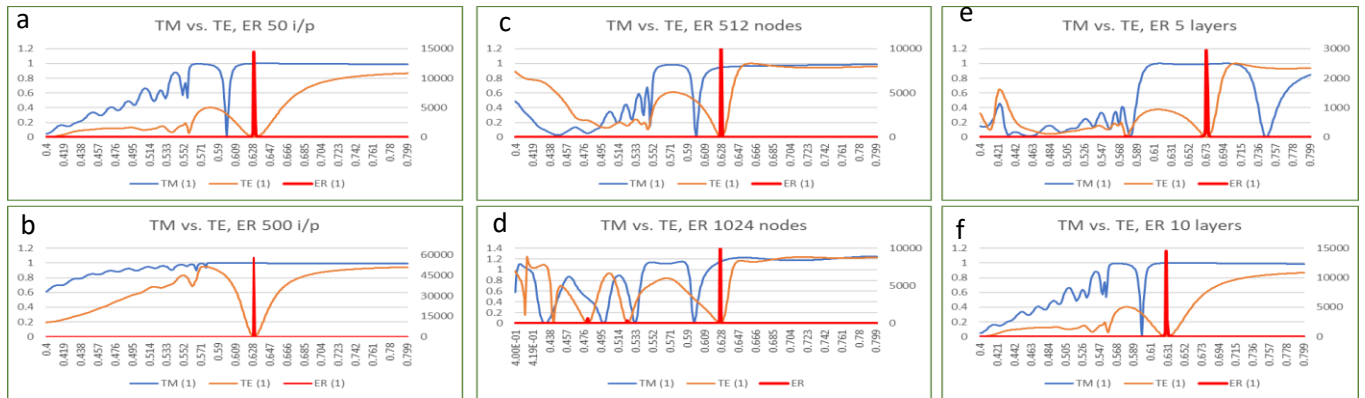


Fig. 9: Plot of T_{TM} , T_{TE} and ER vs. wavelength for different Surrogate Model parameter tuning samples. a and b, different inputs number. c and d, different hidden layers' number of nodes. e and f, different number of hidden layers.

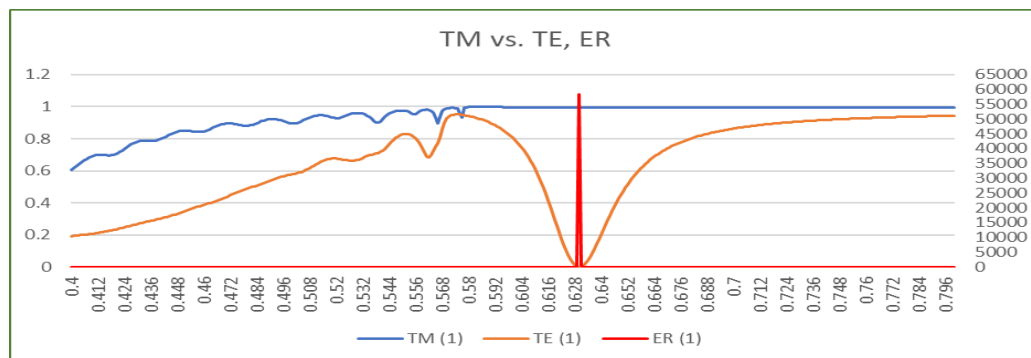


Fig. 10: Metasurface grating structure response based on the optimal Surrogate model proposed dimensions

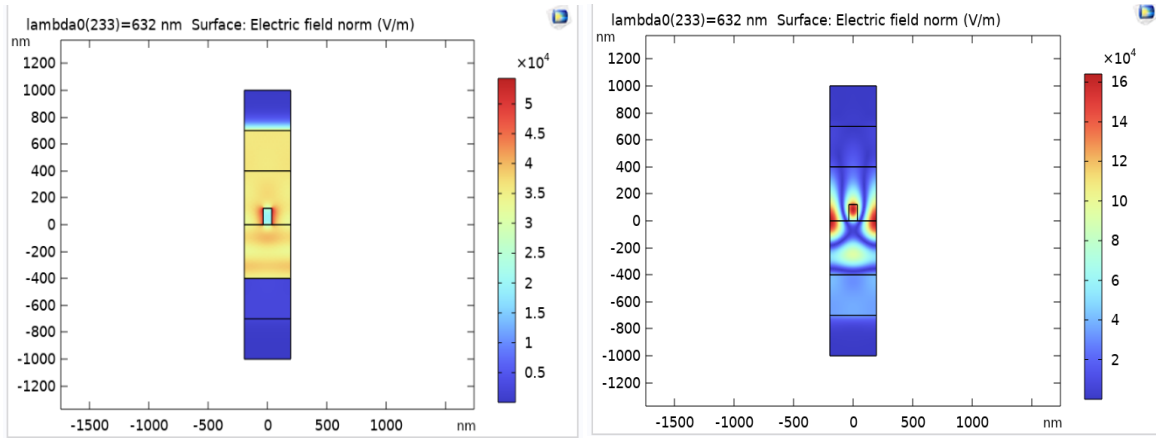


Fig. 11: The electric field distribution of the Surrogate metasurface grating structure. (a) T_{TM} (b) T_{TE} .

The result from COMSOL Multiphysics simulation is consistent with the predictions of the DL Surrogate model which validates the accuracy of the approach used.

Surrogate model and ANN proposed the dimensions, $D_g = 121.71$ nm, $FF = 0.18302$ and $P = 390.83$ nm, as the optimal grating structure at $\lambda = 632$ nm, to achieve high ER .

Optical response of the metasurfaces grating was simulated using the COMSOL Multiphysics over the wavelength 400–800 nm, resulting into an $ER \approx 60000$, at the wavelength of interest, as illustrated in Figure 10, compared to 1800 using Monte Carlo optimizer in [22]. The response T_{TM} and T_{TE} of the polarizer grating structure are simulated with dimensions change tolerance of $\pm 10\%$ to demonstrate the fabrication error. Results show good tolerance for D_g , good tolerance for P and very good tolerance for FF as illustrated in Figure 12, a, b and c respectively.

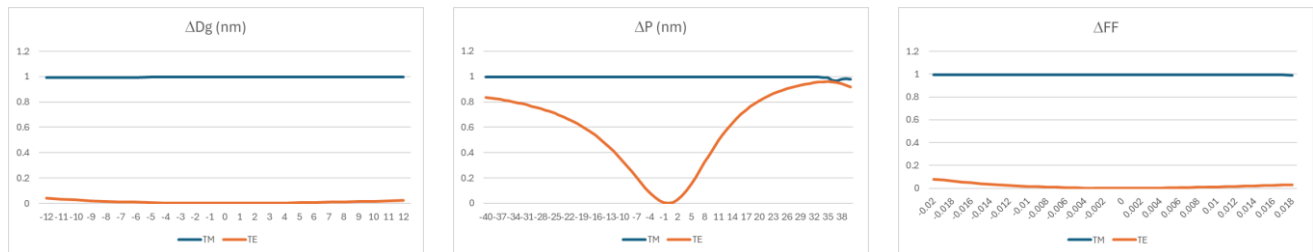


Fig.12: Structure dimensions response with $\pm 10\%$ tolerance. (a) grating thickness D_g (b) grating period P (c) fill factor FF .

5. Conclusions

Utilizing the DL technique, Surrogate model, and DNN built-in COMSOL Multiphysics software, have been used to optimize dimensions of TiO_2 metasurface grating structure, to obtain high quality polarizer with high ER of ≈ 60000 at $\lambda = 632$ nm, in visible spectral region. Thus, by using the Surrogate model and DL, the design process results were highly improved compared to conventional iterative optimization techniques such as Monte Carlo used in [22]. Hence, this polarizer can be used for photon polarization state encoding in QKD systems.

Acknowledgement: The authors are grateful to Dr. Ali Q. Baki for his support.

References

- [1] S. K. Reddy, S. Mandal and C. Mohan, "Comprehensive Study of BB84, A Quantum Key Distribution Protocol," *IRJET*, pp. 1023-1034, Mar Mar 2023.
- [2] S. Mantey, N. Silva, A. Pinto and N. Muga, "Design and implementation of a polarization-encoding system for quantum key distribution," *Journal of Optics*, 13 Jun 2024.
- [3] C. H. Bennett and G. Brassard, "QUANTUM CRYPTOGRAPHY: PUBLIC KEY DISTRIBUTION AND COIN TOSSING," in *International Conference on Computers, Systems & Signal Processing*, Bangalore, Dec 1984.
- [4] M. Choi, J. Park, J. Shin, H. Keawmuang, H. Kim, and J. Yun, "Realization of high-performance optical metasurfaces over a large area: a review from a design perspective," *npj Nanophotonics*, 2024.
- [5] Z. Liu, D. Zhu, L. Raju, and W. Cai, "Tackling Photonic Inverse Design with Machine Learning," *Advanced Science*, vol. 8, no. 2002923, 2021.
- [6] C. Yi, Z. Chen, Y. Gao and Q. Du, "Designing high efficiency asymmetric polarization converter for blue light: a deep reinforcement learning approach," *Optics Express*, vol. 30, no. 6, pp. 10032-10049, Mar 2022.
- [7] I. Brener, S. Liu, I. Staude, J. Valentine and C. Holloway, *Dielectric Metamaterials Fundamentals, Designs, and Applications*, Duxford, UK: Woodhead Publishing (an imprint of Elsevier), 2020.
- [8] S. Krasikov, A. Tranter, A. Bogdanov and Y. Kivshar, "Intelligent metaphotonics empowered by machine learning," *Opto-Electronic Advances*, vol. 5, no. 3, 2022.
- [9] Y. Hu, X. Wang, X. Luo, X. Ou, L. Li, Y. Chen, P. Yang, S. Wang and H. Duan, "All-dielectric metasurfaces for polarization manipulation: principles and emerging applications," *Nanophotonics*, vol. 9, no. 12, p. 3755–3780, 2020.
- [10] W. Ji, J. Chang, H. X. Xu, J. R. Gao, S. Gröblacher, H. P. Urbach and A. J. L. Adam, "Recent advances in metasurface design and quantum optics applications with machine learning, physics-informed neural networks, and topology optimization methods," *Light: Science & Applications*, vol. 12, no. 169, 2023.
- [11] M. K. Chen, X. Liu, Y. Sun and D. P. Tsai, "Artificial Intelligence in Meta-optics," *Chemical Reviews*, vol. 122, pp. 15356-15413, 2022.
- [12] P. R. Wiecha, A. Arbouet, C. Girard, and O. L. Muskens, "Deep learning in nano-photonics: inverse design and beyond," *Photonics Research*, vol. 9, no. 5, pp. B182-B200, May 2021.
- [13] Z. Liu, Z. Dang, Z. Liu, Y. Li, X. He, Y. Dai, Y. Chen, P. Peng and Z. Fang, "Self-design of arbitrary polarization-control waveplates via deep neural networks," *Photonics Research*, vol. 11, no. 5, pp. 695-711, May 2023.
- [14] R. Alizadeh, J. K. Allen and F. Mistree, "Managing computational complexity using surrogate models: a critical review," *Research in Engineering Design*, Apr 2020 .
- [15] P. Naseri, "Inverse Design of Metasurfaces Using Machine Learning Techniques," A Ph.D. thesis submitted to Graduate Department of The Edward S. Rogers Sr. Department of Electrical and Computer Engineering, University of Toronto, 2023.
- [16] C. C. Nadell, B. Huang, J. M. Malof, and W. J. Padilla, "Deep learning for accelerated all-dielectric metasurface design," *OPTICS EXPRESS*, vol. 27, no. 20, pp. 27523-27535, Sep 2019.
- [17] I. Tanriover, W. Hadibrata, and K. Aydin, "Physics-Based Approach for a Neural Networks Enabled Design of All-Dielectric Metasurfaces," *ACS Photonics*, pp. 1957-1964, Jul 2020.
- [18] S. AN, B. Zheng, M. Y. Shalaginov, H. Tang, H. Li, L. Zhou, J. Ding, A. M. Agarwal, C. Rivero-Baleine, M. Kang, K. A. Richardson, T. Gu, J. Hu, C. Fowler, and H. Zhang, "Deep learning modeling approach for metasurfaces with high degrees of freedom," *Optics Express*, vol. 28, no. 21, pp. 31932-31942, Oct 2020.
- [19] F. Ghorbani, S. Beyraghi, J. Shabanpour, H. Oraizi, H. Soleimani and M. Soleimani, "Deep neural network-based automatic metasurface design with a wide frequency range," *Scientific Reports*, vol. 11, no. 7102, Mar 2021.



- [20] X. Zhou, Q. Xiao and H. Wang, "Metamaterials Design Method based on Deep Database," *Journal of Physics: Conference Series*, vol. 2185, no. 012023, 2021.
- [21] V. Medvedev, A. Erdmann, and A. Roskopf, "Physics-informed deep learning for 3D modeling of light diffraction from optical metasurfaces," *Optics Express*, vol. 33, no. 1, pp. 1371-1384, Jan 2025.
- [22] A.Q. Baki and S.K. Tawfeeq, "Numerical study of single-layer and interlayer grating polarizers based on metasurface structures for quantum key distribution systems," *Semiconductor Physics, Quantum Electronics & Optoelectronics*, vol. 27, no. 1, pp. 109-116, 2024.
- [23] B. Duan, B. Wu, J. Chen, H. Chen and D. Q. Yang, "Deep Learning for Photonic Design and Analysis: Principles and Applications," *Frontiers in Materials*, vol. 8, Jan 2022.
- [24] S. Krasikov, A. Tranter, A. Bogdanov and Y. Kivshar, "Intelligent metaphotonics empowered by machine learning," *Opto-Electronic Advances*, vol. 5, no. 3, 2022.
- [25] C. ZHANG, J. HU, Y. DONG, A. ZENG, H. HUANG, and C. WANG, "High efficiency all-dielectric pixelated metasurface for near-infrared full-Stokes polarization detection," *Photonics Research*, vol. 9, no. 4, pp. 583-589, Apr, 2021.
- [26] J. Zheng, Zhi-Cheng Ye, Nan-Ling Sun, Rui Zhang, Zheng-Ming Sheng, Han-Ping D. Shieh and Jie Zhang, "Highly anisotropic metasurface: apolarized beam splitter and hologram," *SCIENTIFIC REPORTS*, vol. 6491, no. 4, 29 Sep 2014.
- [27] Anusuya Devi V. and Kalaivani V., "Enhanced BB84 quantum cryptography protocol for secure communication in wireless body sensor networks for medical applications," *Personal and Ubiquitous Computing*, no. 27, pp. 875-885, 18 March 2021.
- [28] D. Rosenblatt, A. Sharon, A. A. Friesem, "Resonant Grating Waveguide Structures," *IEEE JOURNAL OF QUANTUM ELECTRONICS*, vol. 33, no. 11, pp. 2038-2059, Nov. 1997.
- [29] S. M. Choudhury, D. Wang, K. Chaudhuri, C. DeVault, A. V. Kildishev, A. Boltasseva and V. M. Shalaev, "Material platforms for optical metasurfaces," *Nanophotonics*, p. 959-987, 2018.

تحسين الأداء لمستقطب محرز من الأسطح الفعالة باستخدام التعلم العميق لمنظومات توزيع المفتاح الكمومي

حيدر سامي الدهوي*, شيلان خسرو توفيق

معهد الليزر للدراسات العليا، جامعة بغداد، بغداد، العراق.

البريد الإلكتروني للباحث*: haidar.sami1101a@ilps.uobaghdad.edu.iq

الخلاصة: المستقطبات المصنوعة من الأسطح الفعالة هي مكونات بصرية أساسية في دوائر البصريات المتكاملة الحديثة وتلعب دوراً حيوياً في العديد من التطبيقات البصرية بما في ذلك منظومات توزيع المفتاح الكمومي في التشفير الكمومي. ومع ذلك، يعتمد التصميم العكسي للمستقطبات المصنوعة من الأسطح الفعالة ذات الكفاءة العالية على التخمين الجيد للأبعاد الهيكلية بناءً على الاستجابة البصرية المطلوبة. يمكن لشبكات التعلم العميق أن تساعد بشكل فعال في عملية التصميم العكسي، مما يقلل من الوقت والمتطلبات المتعلقة بالمحاكاة، بينما يمكن تحقيق نتائج أفضل مقارنة بطرق التحسين التقليدية. وبالتالي، يمكن استخدام نموذج Surrogate والشبكات العصبية العميقة في برنامج COMSOL Multiphysics لتصميم هيكل مستقطب محرز من الأسطح الفعالة مع نسبة فصل عالية تبلغ حوالي 60000 عند طول موجي مقداره 632 نانومتر ضمن الطيف المرئي.

